



**Design and performance investigation of
Flux – Concentrated Tubular Linear Generator for an
External Combustion Free Piston Engine**

Aslan Sabahaldeen Jalal

B Sc., M Sc.

A thesis submitted for the degree of
Doctor of Philosophy

School of Electrical and Electronic Engineering

Newcastle University

United Kingdom

November 2017

DECLARATION

I hereby declare that this thesis is a record of work undertaken by myself, that it has not been submitted anywhere for any award, and other sources of information used in this work have been duly acknowledged.

Aslan Sa. Jalal

CIRTIIFICATE OF APPROVAL

I confirm that, to the best of my knowledge, this thesis is from the student's own work and effort, and all other sources of information used have been acknowledged. This thesis has been submitted with my approval.

Nick J. Baker

Newcastle upon Tyne, November 2017

Abstract

The increasing global desire for highly fuel efficient power systems and the need for environmentally friendly energy sources is driving much present research in electrical power. A linear power system, where a linear machine is driven directly by a free piston engine, offers scalability and a wide range applicability. Standalone power units, hybridised power systems and range extenders in electrified vehicles are all potential applications for this technology.

This thesis explores the application of a Linear Joule Engine driving a Permanent Magnet Linear Machine for electrical power generation. Whereas most Joule cycle engines have a rotary compressor and expander, at smaller scale this configuration suffers from leakage around the blades. The linear engine uses a double acting free piston configuration running on the external combustion Joule-cycle, overcoming the low efficiency inherent in small scale gas turbines. The key element for electrical power generation, and the main focus of this thesis, is the development of a linear machine operating as a generator, the design of which is heavily constrained by the geometrical and the operational characteristics of the engine.

Using specific constraints for an 5kW engine and by using two dimensional finite element analysis, a novel design methodology of tubular PM linear machine with modular armature winding and feasible arrangements of magnets on the translator member is outlined. The effect of core material, pole number and power conversion system on the machine design are investigated, highlighting the effect of the interconnected design variables on the resulting performance and material use, all satisfying design objectives. A Flux – Concentrated PM configuration is selected for further development.

In order to accomplish an overall system performance investigation tool, at first the development of a general novel linear machine model is introduced and tested in a feedforward manner with accounts for all machine interacting electromagnetic forces. Then, a novel dynamic model incorporating both the linear machine model driven by the linear Joule engine model, coupled together in a closed loop form, is realized. The coupled model bridges mechanical and electrical parts of the engine-generator, and provides a solid dynamic performance prediction of the system focusing on identifying the effect of cogging force on system performance and the resultant electrical power loss and electrical efficiency.

Compared with the reported cogging force reduction techniques, a novel structural technique and a selection criteria are presented with two dimensional axisymmetric finite element analysis verification showing the effectiveness of the proposed technique.

Finally, a machine prototype of the selected design model is manufactured and tested on a bespoke test rig to validate the design model findings. Manufacturing recommendations and future achievable steps are reported for future development of the existing work.

Dedication

To the loving memory of my father

Your life was a blessing, your memory is a pleasure

You are loved beyond words & missed beyond measure

Acknowledgements

First and foremost, I would like to dedicate my deepest gratitude to Dr Nick J. Baker for his enduring advice, support and guidance during the course of this research preparation and patiently read and commented on this thesis.

Secondly, I highly appreciate the input from Dr Dawei Wu, the co-supervisor on this interesting research project, particularly in exporting the critical thinking about the driving engine modelling and the related problem solving.

Financial support from The Iraqi Ministry of Higher Education and Scientific Research – University of Baghdad made this research possible and is gratefully acknowledged.

A great deal of work has gone into the construction and the adept assembly of the machine prototype and the test rig, special thanks to Jack Noble, Chris Manning, Allan Wheatley and the rest of engineering workshop and the Electrical Power Group – UG laboratory staff members.

Many office and UG lab friends, past and present, made conducting a PhD bearable at Newcastle University. Particular thanks to Liam, Yang, Sana, Osama and Mehmet Kulan for the time spent in discussion about some certain problems during research years which created an amiable social friendship.

To save the best for last, I must give huge thanks to my family for supporting me during these years of PhD study. I cannot imagine being able to reach this time writing these words without my wife and children being with me at Newcastle City supporting and allowing me to dedicate four years of my life to this research. Of course, having the best mother, mother in law and the lovable sisters had given me a lot of support no matter how it was. Their love and support have made it possible for me to get it done.

Table of Contents

Abstract.....	v
Dedication.....	vii
Acknowledgements	ix
Table of Contents	xi
List of Figures.....	xv
List of Tables.....	xxii
List of Acronyms.....	xxiii
List of Symbols.....	xxiv
Chapter 1 : Introduction.....	1
1.1 Introduction	1
1.2 Objective.....	2
1.3 Methodology.....	2
1.4 Overview of thesis	3
1.5 Contribution to knowledge	5
1.6 Published and submitted works	6
Chapter 2 : Background	7
2.1 Introduction	7
2.2 Free Piston Engine background.....	7
2.2.1 Operational concept.....	8
2.2.2 Single – Stroke	8
2.2.3 Two – Stroke	9
2.2.4 Opposed pistons.....	10
2.3 Linear Machines Background.....	11
2.4 Use of Permanent Magnet in Linear Machines	13
2.5 Permanent Magnet Linear Machines for FPE application.....	13
2.5.1 Longitudinal Flux machines	14
2.5.2 Transverse Flux Linear Machines	21
2.6 Selection of topology criteria	26
2.7 Background on system modelling	29
2.8 Background on cogging force in PM Linear Machines.....	30
2.9 Summary.....	33
Chapter 3 : Linear Joule Engine Specification.....	34

3.1 Introduction.....	34
3.2 Linear Joule Engine operation concept.....	34
3.3 Case study engine model.....	36
3.4 Engine performance	37
3.5 Machine design constraints.....	40
3.6 Summary	44
Chapter 4 : Selected Machine Topology Design.....	45
4.1 Introduction.....	45
4.2 Slot / Pole number combination.....	45
4.3 Machine topology	46
4.4 Design variables and PM orientation	47
4.5 Optimisation methodology and results	48
4.5.1 Details of 2D FEA model.....	49
4.5.2 Methodology	49
4.5.3 Stator outer diameter.....	51
4.5.4 PM Dimensions.....	52
4.6 Performance comparison.....	57
4.7 Weighting Criteria.....	58
4.8 Conclusion	60
Chapter 5 : Flux – Concentrated Tubular Machine Detailed Design	61
5.1 Introduction.....	61
5.2 Core material investigation	61
5.3 Investigation of air-gap length based magnet grade	63
5.4 Pole number investigation.....	65
5.5 Power conversion technology investigation	68
5.6 Conclusion	77
Chapter 6 : Integrated System Model	78
6.1 Introduction.....	78
6.2 System description	78
6.3 Linear Generator reacting force components.....	79
6.3.1 Cogging force.....	79
6.3.2 Armature reaction (reluctance) force	81
6.3.3 Back EMF and phase inductance	82

6.3.4 Equivalent circuit and phase resistance	83
6.3.5 Losses	83
6.3.6 Electrical power generated and efficiency.....	84
6.4 Analytic model validation	84
6.5 Electromagnetic force comparison	87
6.5.1 Effect of cogging force on machine performance	90
6.6 Coupled system model	92
6.6.1 Operational performance	94
6.6.2 System frequency and electrical power generated	96
6.7 Energy conversion system.....	98
6.8 Conclusion.....	99
Chapter 7 : Novel Cogging Force Reduction Technique	101
7.1 Introduction	101
7.2 Ends cogging force analysis	101
7.2.1 Novel technique description	103
7.2.2 Flux Gathering Ring optimisation procedure	104
7.2.3 Optimal dimensions selection criteria	106
7.3 Selected Model performance	108
7.4 Effect on total power generated.....	113
7.5 Conclusion.....	113
Chapter 8 : Construction of Prototype Machine and System Test Rig	114
8.1 Introduction	114
8.2 Stator construction.....	114
8.3 Translator construction.....	119
8.4 Machine assembly	121
8.4.1 Electrical Circuit and power connection	125
8.5 Experimental test rig.....	126
8.5.1 Limitation of available test rig.....	126
8.6 Conclusion.....	128
Chapter 9 : Testing and Results	129
9.1 Introduction	129

9.2 Resistance measurement	129
9.3 Inductance measurement.....	130
9.4 Cogging force measurement	131
9.5 Force production	133
9.6 Thermal analysis	134
9.7 No – Load EMF induced.....	135
9.8 Magnetic pole damage	137
9.9 Conclusion	139
Chapter 10 : Conclusion and Future Work.....	140
10.1 Introduction.....	140
10.2 Design constraints and investigated topology.....	140
10.3 Optimisation method and investigated topology	140
10.4 Detailed machine design	141
10.5 System modelling.....	142
10.6 Cogging force reduction technique	142
10.7 Constructed model and test results.....	143
10.8 Importance of the technology	144
10.9 Future work	144
10.9.1 Future electromagnetic machine design.....	144
10.9.2 Future thermal analysis	146
REFERENCES.....	147
Appendix A: Tubular Machines FEA Modelling Techniques	156
Appendix B: B-H curves of the Materials used in FEA modelling	159
Appendix C: Machine mechanical drawings	160

List of Figures

Figure 2-1: 3D view of FPE set up showing fundamental components	8
Figure 2-2: 2D view showing single-stroke FPE and load arrangement	9
Figure 2-3: 2D view of two – stroke FPE set up showing major components	10
Figure 2-4: (a) 2D view of opposed pistons with shared combustion chamber and two loads; (b) Double acting or opposite chambers arrangement	11
Figure 2-5: Linear Machines classes based on geometrical variation and member length (a) Flat Long Rotor One Sided; (b) Flat Long Stator One Sided; (c) Flat Long Rotor Two Sided; (d) Flat Long Stator Two Sided; and (e) Tubular Long Rotor One Sided	12
Figure 2-6: Rare-Earth PM energy product development [42].....	13
Figure 2-7: Longitudinal Flux paths in a Linear Machine of cylindrical geometry	14
Figure 2-8: 2D structure view of MCM (a) Ref. [46]; (b) Ref. [47]	15
Figure 2-9: Samples of MIM configurations (a) Tubular [51]; (b) Flat [52]	15
Figure 2-10: Flux Switching MIM machine models (a) Three-phase model [53]; (b) Comparison results [54]	16
Figure 2-11: Surface mounted MMM classes (a) Axial (AM); (b) Radial (RM); and (c) Quasi- Halbach (QHM)	16
Figure 2-12: AM tubular model (a) Conventional [59]; (b) Modified [61]	17
Figure 2-13: 9 slot/10 poles tubular QHM for FPE use (a) Topology [69]; (b) Prototyping in FPEC unit [10]	18
Figure 2-14: QHM partial irreversible demagnetisation [74] (a) FE modelling of demagnetised PM corners; (b) Effect of demagnetization on machine force capability; (c) Axial air gap between QHM segments; and (d) Effect of axial air gap on machine force capability ..	18
Figure 2-15: Square shape of one sided MMM configuration [77] (a) One side stator model; (b) Cross sectional 2D view; and (c) 3D view of stator and coil.....	19
Figure 2-16: Yokeless dual mover LF-MMM topology [78] (a) 3D view; (b) Flux path.....	20
Figure 2-17: Magnetic gear machine topology [80] (a) 2D view; (b) Flux distribution	20
Figure 2-18: Flat topology of TFLM with RM (a) 3 poles structure; (b) 6 poles structure	21
Figure 2-19: Tubular TFM topology [82] (a) 3D FEA model; (b) Radial cut view showing separate flux path; (c) Axial magnets shift to achieve three – phase design and; (d) Final translator structure.....	22

Figure 2-20: TFM topologies (a) Stator lamination; (b) 3-D view of flat stator core structure [88]; (c) Staggered teeth lamination; (d) TF with staggered teeth and three – phase design [89]; (e) Major and leakage flux paths in the staggered teeth; (f) TF with staggered teeth and single – phase assembly [90]	23
Figure 2-21: TTFLM topologies and flux paths for short stroke FPE application (a) Initial MITFLM design [92, 93]; (b) RMMTFLM design variation [94];(c) Dual stator RMM design variation [95]; and (d) QHMM design variation [96]	25
Figure 2-22: New TFM for FPE application showing flux paths [99] (a) Moving Magnet TFM; and (b) Moving Iron – Flux Switching TFM.....	26
Figure 2-23: Structural modification to reduce cogging force in various linear machines.....	32
Figure 3-1: (a) First design of the Linear Joule Engine [107]; (b) PV diagram of an ideal Joule cycle; and (c) System integral length description.....	35
Figure 3-2: Linear Joule Engine dynamic model implementation in LMS [106].....	37
Figure 3-3: Instantaneous time variation of (a) Velocity; and (b) Damping force	38
Figure 3-4: Two steady-state mechanical cycles time variation of (a) Velocity; and (b) Damping force	38
Figure 3-5: Steady–state velocity versus position trajectory ($5s < \text{time} \leq 10s$).....	39
Figure 3-6: Linear Joule Engine steady–state piston displacement compared with sinusoidal displacement	39
Figure 3-7: Half cycle piston motion with a ratio of (1/2 : 1) between active machine length to stroke amplitude	41
Figure 3-8: Thrust density of single – sided LIMs and LSMs at different cooling systems [126]	43
Figure 3-9: Physical active dimensions of any tubular LM topology.....	44
Figure 4-1: Three – Phase linear machine of three stator slots and two translator poles.....	46
Figure 4-2: 3D quarter cut view clarifying the general investigated topology parts	47
Figure 4-3: Longitudinal view illustrating optimisable parameters in machine topology	48
Figure 4-4: Investigated machine topologies and connected load (a): Axially Magnetised magnets; (b) Radially Magnetised magnets; (c) Quasi-Halbach Magnets arrangement, and (d) Resistive Loading.....	49
Figure 4-5: (a) 2D FEA general machine model used in optimisation; (b) Mesh size of the general model	50
Figure 4-6: Optimisation methodology framework	51
Figure 4-7: Variation of electromagnetic force with stator outer diameter (2ROS).....	52

Figure 4-8: Variation of electromagnetic force with PM dimensions (a) PM height effect; (b) PM width to pole ratio (τ_m/τ_p) effect 53

Figure 4-9: Variation of electromagnetic force with dimensional ratios (a) Tooth width effect (TW); (b) Stator and translator core backs effect (SCBH, TCBH)..... 54

Figure 4-10: Rated force variation over one electrical cycle of alternative optimal Longitudinal Flux Moving Magnets Machine topologies 55

Figure 4-11: Rated load flux distribution showing saturation regions in optimal models of (a) AM machine; (b) QHM machine; and (c) RM machine 56

Figure 4-12: Scoring system results 59

Figure 5-1: 2D view of flux distribution in the machine geometry 62

Figure 5-2: Stator yoke and tooth structure using (a) Laminated steel for both components; (b) Laminated steel for tooth and Soft Magnetic Composite for stator core back..... 62

Figure 5-3: Effect of core material on rated load force over one electrical cycle (2D FEA) ... 63

Figure 5-4: Variation of rated load force over electrical cycle with air gap and magnet grade changes 64

Figure 5-5: Configurations of the competing machines (a) 7 pole design; and (b) 5 pole design 66

Figure 5-6: Variation of rated electromagnetic force over electrical cycle with 5 & 7 magnetic poles 67

Figure 5-7: Variation of no-load cogging force over a half electrical with 5 & 7 magnetic poles 67

Figure 5-8: Power circuit for Grid Interface scenario and FEA software circuit implemented 69

Figure 5-9: Power circuit for Unity power factor controlled converter scenario 70

Figure 5-10: The effect of teeth width and stator core back height variation on the force capability (a) 2-D view for optimal tooth width; and in 3-D view for (b) Resistive Loading; (c) Grid Interface; and (d) Unity Power Factor Controlled Converter 72

Figure 5-11: Cogging force variation based power conversion method 74

Figure 5-12: Rated load force fluctuation based power conversion method 74

Figure 5-13: Grid Interface design circuit diagram clarifying current path at an instant of three phase system operation. 75

Figure 5-14: Variation of phase and line voltage quantities per turn over one electrical cycle for the three selected design models 76

Figure 5-15: Variation of phase and DC link current quantities over one electrical cycle in the machine design model for Grid Interface application 76

Figure 6-1: Simplified schematic diagram of the integrated system 78

Figure 6-2: Short Stator-Long Translator machine topology showing slot and end cogging at (a) Left motion limit; and (b) Arbitrary position between motion limits	80
Figure 6-3: Cogging force variation over one pole pitch due to (a) Stator slotting – case I; and (b) Stator slotting and ends – case II (FEA)	81
Figure 6-4: Armature reaction force variation over one pole pitch due to rated current, FEA	81
Figure 6-5: Variation of air gap flux with translator position over one electrical cycle (FEA)	82
Figure 6-6: Variation of phase inductance with translator position over half an electrical cycle (FEA)	82
Figure 6-7: Per phase equivalent circuit of a Linear Generator supplying variable resistive load	83
Figure 6-8: Core loss and magnets eddy currents loss variation with speed at rated load (FEA)	84
Figure 6-9: General Linear Generator analytic model implementation in MATLAB/SIMULINK	85
Figure 6-10: Detailed Linear Generator analytic model implemented in MATLAB/SIMULINK	86
Figure 6-11: Feedforward investigation against engine’s velocity profile (a) Analytic model; (b) FEA model.....	86
Figure 6-12: One mechanical cycle variation of (a) EMF induced per phase; (b) Phase currents; and (c) Electrical power dumped by the load	87
Figure 6-13: Linear Generator reacting force profile comparison and inductance effect.....	88
Figure 6-14: Linear Generator reacting force profile variation with load over one mechanical cycle.....	89
Figure 6-15: Variation of electromagnetic force and copper loss with current loading (FEA)	89
Figure 6-16: Effect of cogging force due to slot cogging and ignored end effects on the LG efficiency over entire mechanical cycle at different current loading (Case I).....	91
Figure 6-17: End effects on cogging force amplitude and LG efficiency over an entire mechanical cycle at different current loading (Case II)	91
Figure 6-18: Effect of cogging force amplitude on LG efficiency averaged over the entire mechanical cycle at different current loading.....	92
Figure 6-19: Coupled System model in LMS (a) Linear Joule Engine model; (b) Linear Generator model	93
Figure 6-20: System integral model development	94
Figure 6-21: Total system electrical efficiency graph	95
Figure 6-22: Linear Generator efficiency graph	96

Figure 6-23: Linear Generator cyclic electrical power generated variation with time.....	97
Figure 6-24: System cyclic mechanical frequency (fm)	97
Figure 6-25: Averaged electrical power generated versus time	98
Figure 6-26: Peak system velocity versus current loading	98
Figure 6-27: Electrical Energy versus time	99
Figure 7-1: Flux distribution within the selected machine initial design topology (FEA).....	102
Figure 7-2: No – load cogging force variation due to one pole and stator ends.....	103
Figure 7-3: Flux Gathering Rings positioning in stator geometry.....	104
Figure 7-4: Flux Gathering Rings dimensional changes and effects on (a) Normalised force ripple; and (b) Normalised rated force capability (FEA).....	105
Figure 7-5: Proposed rational criterion to identify the effects of changing the dimensions of Flux Gathering Rings on both resultant force capability and consequent force ripple (FEA)	106
Figure 7-6: Variation of rated force over one electrical cycle of initial design, rated averaged force and those of selected FGR designs models (FEA).....	107
Figure 7-7: (a) Modified design model with added Flux Gathering Rings at both ends; (b) Flux distribution in the model after adding Flux Gathering Rings at both ends (FEA).....	108
Figure 7-8: No – load cogging force variation due to inactive poles and stator ends with added FGR.....	109
Figure 7-9: Effect of adding Flux Gathering Rings on total no-load cogging force over an electrical cycle (FEA)	109
Figure 7-10: Effect of adding Flux Gathering Rings on (a) Flux linkage, and (b) Inductance (FEA)	110
Figure 7-11: Variation of normalised force and force ripple in both design models due to changes in (a) Resistive loading; (b) Current density (FEA).....	112
Figure 8-1: Stator parts	115
Figure 8-2: Tools and materials used in constructing stator slots core back.....	116
Figure 8-3: Teeth and mould used in constructing and assembly of stator slots.....	117
Figure 8-4: (a)Thermocouples placement; (b) Stator mass; and (c) Stator in housing.....	118
Figure 8-5: (a)Supporting tube, holding caps and SMC iron-piece; (b) Equilibrium point during assembly.....	119
Figure 8-6: Force nature between moving and stationary magnetic pole sets.....	120
Figure 8-7: (a)Full translator; (b) Mass of full translator	121
Figure 8-8: (a)Machine members' assembly; (b) Oscillating reacting force (FEA)	122

Figure 8-9: (a) Cross section view in machine model describing general translator eccentricity; (b) Effect of eccentricity on airgap total closer force (FEA).....	124
Figure 8-10: Added PTFE bearing to stator structure.....	125
Figure 8-11: Added PTFE bearing to stator structure.....	125
Figure 8-12: (a) Experimental test rig; (b) Low speed measurements showing noise interference	127
Figure 9-1: Measured cogging force variation with translator displaced over two pole pitches with offset.....	132
Figure 9-2: Measured cogging force variation with translator displaced over two pole pitches with removed offset.....	132
Figure 9-3: Electrical circuit phase connection during static force measurement test.....	133
Figure 9-4: Online monitoring of machine coil temperature rise during static test.....	133
Figure 9-5: Static force test at different DC current amplitudes (a) $I = 4.8$ A; (b) $I = 8.0$ A; (c) $I = 16.0$ A; and (d) $I = 24.0$ A.....	134
Figure 9-6: Temperature rise in machine coils over 4 working hours.....	135
Figure 9-7: Measured EMF induced in machine phases.....	136
Figure 9-8: Measured EMF induced in one machine phase.....	136
Figure 9-9: EMF induced in one phase measured comparison with FEA model result.....	137
Figure 9-10: Stator end teeth with fitted Flux Gathering Rings.....	138
Figure 9-11: Stator end teeth with fitted Flux Gathering Rings.....	138
Figure 10-1: Single phase linear machine design proposal.....	145
Figure A-1: FEA machine model using (a) 2D, (b) 2D axisymmetric, and (c) 3D.....	156
Figure A-2: Flux linkage variation over full electrical cycle.....	158
Figure A-3: Flux linkage variation over full electrical cycle.....	158
Figure B-1 : B-H curves of the materials used in FEA machine modelling.....	159
Figure B-2 : Demagnetisation curves of Recoma 26, Sintered Sm ₂ Co ₁₇	159
Figure C-1 : Translator magnetic pole piece made from SMC material (a) Lateral; (b) Interior	160
Figure C-2 : PM dimensions.....	161
Figure C-3 : Translator supporting tube dimensions.....	161
Figure C-4 : Translator end caps.....	162
Figure C-5 : Translator shaft.....	162
Figure C-6 : Translator assembly steps (a) Step 1; (b) Step 2.....	163
Figure C-7 : Linear bushings holder.....	164
Figure C-8 : SMC stator yoke segments without punches.....	164

Figure C-9 : SMC stator yoke segments with punches	165
Figure C-10 : Stator yoke segments cut from SMC discs	165
Figure C-11 : Machine coils (a) Dimensions; (b) Mould used to wind the coils	166
Figure C-12 : Slot components assembly	167
Figure C-13 : Machine housing – lower part.....	167
Figure C-14 : Machine housing – upper part.....	168
Figure C-15 : Machine housing assembly	168
Figure C-16 : LVDT manufacturer calibration certificate	169
Figure C-17 : Load cell calibration certificate.....	170

List of Tables

Table 2-1: Summary of PMLM topologies for FPE applications	27
Table 2-2: Topology marking system	28
Table 3-1: Linear Joule Engine optimal dimensions and steady – state operational characteristics.....	40
Table 4-1: Feasible slot/pole combination	46
Table 4-2: Design variables variance ranges	51
Table 4-3: Optimal machines variables	55
Table 4-4: Optimised machines volume and masses	57
Table 4-5: Optimal machines performance parameters	58
Table 5-1: Optimal machines dimensional, volume and mass parameters	64
Table 5-2: Optimal machines performance parameters	65
Table 5-3: Typical machines dimensional and mass parameters	66
Table 5-4: Typical machines performance parameters	66
Table 5-5: Typical machines dimensional and mass parameters based power conversion method	73
Table 5-6: Typical machines performance parameters based power conversion method	73
Table 6-1: Useful dimensions and machine performance parameters for the resistive loading design model	85
Table 6-2: Total electrical efficiency of the integrated system.....	94
Table 7-1: Flux Gathering rings dimensions and effects on force capability and consequent force ripple of selected design models at $\Delta w = 3.5mm$	107
Table 7-2: Comparative table of machine design models.....	111
Table 7-3: Flux Gathering rings effect on integrated system performance	113
Table 8-1: Dimensions of the machine design model under construction	114
Table 9-1: Predicted and measured resistance in machine phases	130
Table 9-2: Predicted and measured inductance in machine phases	131

List of Acronyms

2D	Two dimensional
3D	Three dimensional
AM	Axial magnetisation
BEC	Bottom end centre
CL	Current loading
DC	Direct current
FEA	Finite element analysis
FGR	Flux gathering rings
FPE	Free piston engine
GI	Grid interface
ICE	Internal combustion engine
IM	Induction machines
LCM	Least common multiple
LFM	Longitudinal flux machine
LG	Linear generator
LIM	Linear induction machines
LJE	Linear joule engine
LM	Linear machine
LV	Low voltage
LVDT	Linear variable differential transformer
MCM	Moving coil machine
MIM	Moving iron machine
MMM	Moving magnet machine
PM	Permanent magnet
PMLM	Permanent magnet linear machine
PMLSM	Permanent magnet linear synchronous machine
PTFE	Polytetrafluoroethylene (Teflon)
QHM	Quasi-Halbach magnetisation
RL	Resistive loading
RM	Radial magnetisation
SMC	Soft magnetic composite
SmCo	Samarium cobalt
TC	Thermocouple
TEC	Top end centre
TFM	Transverse flux machine
UK	United Kingdom
UPFCC	Unity power factor controlled convertor
VA	Volt – Ampere
VBS	Visual basic script

List of Symbols

$\bar{E}_a, \bar{E}_b, \bar{E}_c$	Instantaneous phase voltages, V
\bar{E}_{ph}	Instantaneous induced voltage per phase, V
\hat{F}_{cm}	Peak cogging force amplitude, N
\hat{F}_r	Peak armature reaction force amplitude, N
$\bar{I}_a, \bar{I}_b, \bar{I}_c$	Instantaneous phase currents, A
\sum	Summation operator
Φ_m	Flux linkage amplitude, Wb
$F_y(t)$	Total vertical radial force, N
A_C	Conductor area, m ²
A_W	Slot area, m ²
C_{loss}	Constant representing machine speed dependant losses
D_{active}	Active machine bore diameter, m
\hat{E}	Peak induced EMF, V
\bar{F}	Instantaneous force, N
F_{AR}	Armature reaction force, N
F_C	Compressor reacting force, N
F_E	Expanding force, N
F_L	Load force, N
F_{PMec}	PM eddy currents loss force, N
F_{RD}	Rebound device force, N
F_{cog}	Cogging force, N
$F_{cu\ loss}$	Copper loss force, N
F_{design}	Design force, N
F_{ele}	Electrical power force, N
$F_{iron\ loss}$	Iron loss force, N
F_r	Radial force, N
$F_r(pp)$	Peak-to-peak force ripple, N
F_{rated}	Rated force, N
F_y	Vertical radial force component, N
J_{max}	Maximum current density, A/mm ²
L_a, L_b, L_c	Inductance of phase a, b and c, H
L_{active}	Active machine length, m
L_{ph}	Phase inductance, H
M_{lim}	Mechanical Limit, mm
M_m	Moving mass, kg
N_S	Number of stator slots
Nc_s	Number of turns per slot
N_p	Number of translator poles
P_{ECL}	Eddy currents loss, W
P_{cu}	Copper loss, W
$P_{in(mech)}$	Input mechanical power, W
P_{iron}	Iron loss, W
$P_{out(elect)}$	Output electrical power, W

R_a, R_b, R_c	Resistance of phase a, b and c, Ω
R_c	Periodicity of a function
R_{ph}	Phase electrical resistance, Ω
\hat{V}	Peak velocity, m/s
V_{drop}	Voltage drop, V
a_s	Number of coils connected in series
f_e	Electrical frequency, Hz
f_m	Mechanical frequency, Hz
k_f	Fill factor
x_L	Stroke Amplitude
$\theta_{\tau p}$	Pole pitch, electrical degrees
$\theta_{\tau s}$	Slot pitch, electrical degrees
σ_s	Shear stress, N/m^2
τ_s	Slot pitch, mm
τ_m	Magnet pitch, mm
τ_p	Pole pitch, mm
ω_m	Mechanical translational frequency, rad/s
ϑ_c	Phase shift in cogging force, $^\circ$
\emptyset	Flux linkage, wb
ΔD_{axial}	axial shift, mm
Δh	height increment, mm
Δw	width increment, mm
a	Acceleration, m/s^2
A_g	Air gap length, mm
EMF	Electromotive force, V
I	Circulating current, A
l	Average length of a turn, mm
m	Number of phases
M_H	Magnet height, mm
MMF	Magneto motive force, AT
M_w	Magnet width, mm
pf	Power factor
q	Slots per pole per phase
\mathcal{R}	Magnetic reluctance
R_{os}	Stator outer radius, mm
R_{ot}	Translator outer radius, mm
S	Strand number
SCBH	Stator core back height, mm
TCBH	Translator core back height, mm
T_w	Tooth width, mm
U	Eccentricity, mm
v	Velocity, m/s
V	Voltage, V
VDC	DC link voltage, V
X	Displacement, mm
x	Instantaneous mover position, mm
η	Efficiency
σ	Copper electrical conductivity, S/m

Chapter 1 : Introduction

1.1 Introduction

The quest for highly fuel-efficient engines and the need for environmentally friendly energy sources have played the major part in researching the concept of Free Piston Engines (FPEs). This engine set up has been known for some 200 years, yet the advancement in control and various engineering technologies have contributed in refreshing the research on this family of engines over the last 2-3 decades [1-4].

Conventionally, in a combustion engine, the linear reciprocating motion of the in-cylinder piston is converted to a continuous rotating motion via a crankshaft and the heat energy is derived from combustion within the cylinder. In a FPE, there is no conversion to rotary motion and the mechanical load is derived linearly and is reciprocating. Potential advantages of this include reduced frictional loss, increased thermal efficiency, a physically compact design and the potential for a flexible compression ratio leading to an improved performance at part load. The free piston concept can be applied to many thermodynamic cycles, such as two stroke [5], petrol [6] and diesel [7] engines, assuming a suitable linear load can be designed for the mechanical power take off.

Successful applications in air compressing in the navy during World War II had highlighted FPE high efficiency, low noise and vibration in addition to compactness. Its modern application in hydraulic systems has reported excellent features, most importantly the fuel economy and the high efficiency at part loads [8].

The second potential modern application is the use of the FPE concept for electrical power generation which is the main goal of this thesis. When a linear machine with adequate field excitation is connected to the FPE piston via a connecting rod, electrical energy will be generated in the machine coils and the power starts to flow to any connected electrical load when the engine is working.

Modern applications which energised research in the use of FPE concept in small scale version for electrical power generation fall under the following categories:

- 1- Hybrid Electric and Electric Vehicles [1, 3, 9-13]: to improve the vehicle travelling distance as an auxiliary power unit to charge the on-board battery.
- 2- Standalone or emergency power unit [14, 15]: for multiple use in small scale domestic, industrial and agricultural applications.
- 3- Microgeneration power systems [16, 17]: for use in a hybrid power system.

During the years of researching the promising technology, various linear electrical machine topologies have been reported for use in this system due to its importance as a key element of the system. However, the impacts of system compactness and its relation to the stroke amplitude of the engine, or the effect of the stroke amplitude on the machine design have not clearly been considered and discussed. Additionally, the effect of the electrical machine loading variation and its physical characteristics on shaping its resultant reacting force on the engine operation and overall system stability have not yet been explored elsewhere. These interconnected system design parameters and effects on the electromagnetic design of the machine and system behaviour will be described in detail throughout this thesis.

1.2 Objective

This thesis explores the application of a Linear Joule Engine (LJE) driving a Permanent Magnet Linear Machine for electrical power generation. The engine uses double acting free piston configuration and works on the Joule-cycle with out-of-cylinder combustion in order to improve the low efficiency found in small scale gas turbines. The key element for electrical power generation is the linear machine operating as a Linear Generator (LG), where the machine design is constrained by the geometrical and the operational characteristics of the driving engine. In order to accomplish an overall system performance investigation tool, the development of a general novel linear machine model that accounts for all machine interacting forces is explored. The effect of cogging force on the system performance and energy loss in the system are to be highlighted. A prototype of the selected design model is manufactured and tested to validate the predicted design findings.

1.3 Methodology

The work carried out in this thesis concerns the electromagnetic design of a linear machine operating in the generating mode to satisfy specific constraints for integration with a LJE. The design of the electrical machine and its performance against design variables, material selection, power conversion technology are all explored. For a selected design, innovative machine and system modelling are used to identify the feasibility of the system for electrical power generation. The effect of critical machine performance parameters on the generated power is investigated, including exploring the possible elimination or minimisation of cogging force using innovative techniques. Selected design construction challenges, testing and validation are also discussed.

In order to achieve the research objectives and validate the design model, the following steps have been conducted:

1. Identifying the driving engine steady-state operational point and the corresponding specification, objectives and constraints imposed on the design of the electrical machine.
2. Develop a new optimisation methodology to design moving magnet machines with feasible magnet orientation for any desired force/power rating. Unsuitability and selection of a topology criterion using combined cost-performance function are explained.
3. Investigate the machine interconnected design variables such as core material changes, air gap length, grade of magnet, pole number and power conversion techniques on the machine performance and specific critical parameters.
4. Development of a new linear machine analytical model that accounts for all machine interacting force components including losses and various cogging force origins.
5. Using the novel machine analytical model coupled to the drive engine model to investigate the performance of the system dynamically, and rated load characteristics.
6. Analyse the cogging force due to ends effect using Finite Element Analysis (FEA) model and propose a new structural technique to reduce these effects and total force fluctuation.
7. Construction and testing of best efficiency design model. Results are compared with those obtained using FEA machine model.
8. Recommendation for future work based on both simulations results and those from the experimental model.

1.4 Overview of thesis

This thesis consists of four main parts. The first part introduces the driving engine, describes its operational performance using a damper approximating a linear machine. In this part, the engine geometrical and steady state operational performance and requirement have been identified, and used as constraints to design the electric machine. Over the wide linear machines range, a ranking system is used to adopt a topology to design.

The second part includes the design and modelling of the adopted electrical machine constrained by the engine specification to achieve a specific design force into a limited space envelope. Then, a detailed investigation on the candidate machine has been carried out against selected design variables, material changes and specific power conversion techniques to maximise the efficiency without sacrificing design objectives. A prototype is built and tested for the maximum efficiency design model to validate design findings.

In order to form a solid base for an integrated system model, the third part presents a novel general linear generator model. Then a novel dynamic system model is used to highlight the electrical power generation feasibility and the effect of cogging force on the overall system thermal and electrical efficiencies.

The final part describes a new cogging force reduction technique that has negligible effect on the volumetric dimensions of the adopted machine topology while achieving its objective with an improved power to mass ratio.

A brief description of each chapter is given hereafter.

Chapter 1: The main focus of this chapter was to explain the research as a whole and detail the objectives and the methodology of the thesis.

Chapter 2: This chapter presents the literature review of the research. It is divided into sections. The first section covers, in brief, the demonstration of the possible engine layouts focusing on force balancing equation and load integrity dimensional requirement. The second part focuses on reviewing the development of linear machines with their classifying methods. Then using a proposed classifying method, various machines have been ranked and topology selection is decided.

Chapter 3: Introduces the LJE principle of operation, case study engine operational performance, balancing equation and ends up with a set of design constraints and selection basis.

Chapter 4: Describes the topology selected, possible alternatives and the design methodology using 2D FEA transient solution. Importance of magnet orientation cost and maintainability is considered in which it was used in a weighting system for final machine selection.

Chapter 5: Considers, in detail, the effect of changing some parts of the selected machine topology to investigate a more manufacturable design. General formulas that describe the variation of both the inherent cogging force and that due to the coil driven flux force over translator position are derived.

Chapter 6: Presents a novel dynamic realisation of the LJE integrated with the Linear Generator (LG) model and it aims to obtain transient results for the whole engine-generator system to identify the effect of cogging force on the electrical power generated.

Chapter 7: Describes the novel technique proposed to minimise the cogging force effect, by presenting an analytical expression based flux distribution at both machine ends. Method validation and its effectiveness is quantified using FEA modelling looking at specific parameters.

Chapter 8: Describes the process of building the PM machine prototype along with the assembly process and the encountered challenges. This includes identifying the PM structural weakening actions during poles assembly and the effect of non-concentric machine members on machine assembly. Limitations of the test rig are also explained in this chapter.

Chapter 9: Lists the results of the tests carried out on the machine rig in order to evaluate and validate the design model results. This includes cogging force, static force and monitoring temperature rise in machine coils in addition to open circuit induced EMF test.

Chapter 10: A summary of the research is provided in this chapter along with the recommendations, conclusions and a discussion on the possible future research work and progression.

1.5 Contribution to knowledge

The following contributions to knowledge are made in this study:

1. At first, existing sorting methods of linear machines are clarified. A developed sorting method is then proposed and used in reviewing various up to date machine topologies including less traditional machines in this research field.
2. An innovative manual optimisation method is presented. It offers much saving in time by selecting design variables, starting by those influencing interconnected design objectives, one by one and avoid solving models of the undesired variable changes. Both 2D and 2D axisymmetric FEA machine models can be optimised using this methodology.
3. Development of a new dynamic system model incorporating both the drive engine and the linear generator such that system performance can be investigated against machine variables changes. Effect of cogging force on electrical power loss is identified using this model which is a major contribution in this research area.
4. Designing a new cogging force reduction technique which proved its effectiveness in minimising these effect and the accompanying electrical power loss in the integrated system.
5. Construction and testing of a new power rating flux concentrated linear machine topology. Important recommendations whilst managing prototype construction and assembly are reported. Initial design cogging force, static force and electromotive force validate clearly those obtained from the design model.

1.6 Published and submitted works

The following publications have stemmed from this work;

1. Dawei Wu, Aslan Sa Jalal and Nick J. Baker, “*A Coupled Model of the Linear Joule Engine with Embedded Tubular Permanent Magnet Linear Generator,*” Energy Procedia, Vol. (105), pp. 1986-1991, May 2017.
2. Aslan Sa. Jalal, Nick J. Baker and Dawei Wu, “*The effect of power converter on the design of a Linear Generator for use with a Joule Cycle-Free Piston Engine,*” IEEE International Electrical Machines and Drives Conference IEEE (IEMDC2017), Miami, Florida USA, 2017.
3. Dawei Wu, Aslan Sa. Jalal and Nick J. Baker, “*A coupled model of the Linear Joule Engine integrated with a tubular permanent magnet Linear Generator,*” The 8th International Conference on Applied Energy (ICAE2016), Beijing, China, 2016.
4. Aslan Sa. Jalal, Nick J. Baker and Dawei Wu, “*Electrical Machine Design for use in an External Combustion Free Piston Engine,*” The 5th IET International Conference on Renewable Power Generation (RPG), London, UK, 2016.
5. Aslan Sa. Jalal, Nick J. Baker and Dawei Wu, “*Design of tubular moving magnet Linear Generator for use with an external combustion - free piston engine,*” 8th IET International Conference on Power Electronics, Machines and Drives (PEMD 2016), Glasgow, UK, 2016.
6. Aslan Sa. Jalal, Nick J. Baker and Dawei Wu, “*Performance investigation of Linear Alternator analytical model integrated with Linear Joule -cycle Engine,*” Sustainable Energy, IEEE Transactions on, submitted, 2017.

Chapter 2 : Background

2.1 Introduction

This chapter demonstrates the basic working principle and the most common possible layouts of the Free Piston Engine (FPE) and the corresponding force balance equation to highlight the layout adopted in this work. Also, it presents an overview on the linear motion types, the development of Linear Machines (LMs), the principle of operation for electrical power generation accompanied by demonstrating the most commonly used sorting methods. A classification method of LMs is presented based on the flux path and the mover structure of the considered topology. Afterwards, it considers the LMs that have been reported for use with FPE for the purpose of electrical power generation. Various topologies are reported with discussion on the benefits and drawbacks with each topology.

2.2 Free Piston Engine background

Although the FPE was known centuries ago, its first generation was successfully applied in air compressors and used during World War II. The moving piston was coupled to the air compressing cylinder via a multi-stage configuration, and some of the remaining air was used to push the piston back without the need for any rebounding device. The merits of applying this concept in air compressing at the navy had highlighted its high efficiency, low noise and vibration levels and compactness. After the success of this application in reality and its attractive outcomes, research had been directed towards discovering the use of the FPE concept in gas generators for large scale power plant. Much effort and documented developments have been reported in this application, yet the rapid advancements made to FPE alternatives like the gas turbine and the diesel engines, and because of the low power to weight ratio at part loads compared to gas turbine, had resulted in a reduced or limited success of this application as a practical competitor to the others [8]. Its first modern application was in Hydraulic engines, where the hydraulic cylinder acts as a load and/or a rebound device by using controlled valves. This application had reported excellent features, most importantly are the fuel economy and the high efficiency at part loads [8], and different FPE layouts were investigated to report the major differences. Such operational features yielded engines not only of simple structure, but also with a reduced volume with load integrity, increased system integral reliability, and ease of maintenance. Additionally, these recognisable outcomes nominate its use for electrical power generation as a second modern application, which is the main goal in this thesis.

When a linear machine is connected to the FPE piston via a connecting rod, and the engine operates in a continuous back and forth linear motion, electrical energy will be generated in the machine coils and the power flows to any connected electrical load.

2.2.1 Operational concept

A general 3D view of the FPE set up is shown in Figure 2-1 clarifying its fundamental components. In general, FPE operation is based on converting an energy source, like different fuels and renewables, into a linear form of mechanical energy to drive a directly coupled load. The crank-less load coupling reduces dramatically friction loss and increases the engine's thermal efficiency in comparison to rotating engines counterpart [4]. This is mainly due to the key parameter of FPE's flexible compression ratio combined with the simple mechanism in which engine's ability to operate efficiently, even with part loads, becomes possible.

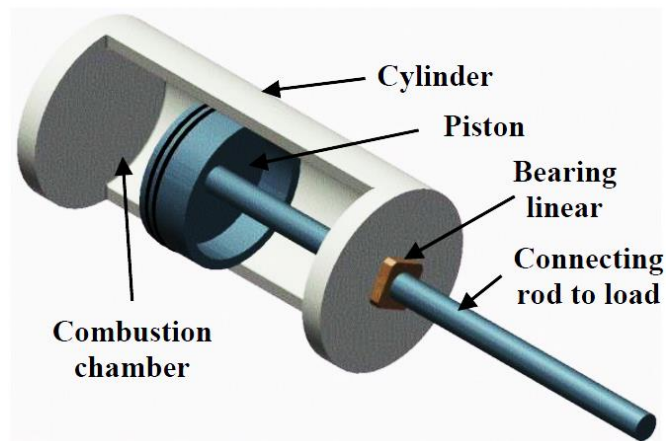


Figure 2-1: 3D view of FPE set up showing fundamental components

In the late 1990's due to the progress of modern engineering technologies, research on FPE had revived to enhance the growing need for more radical redesigns of the existing systems, as well as to follow up with the continuous environmental legislation changes [8]. This resulted in the development and/or the reconstructing of the engine into multiple layouts or assemblies. All share the same operational concept with variation in the working fluid - air mixture, injection timing and the control strategy, if any, and the desired application.

2.2.2 Single - Stroke

Figure 2.2 clarifies the single - stroke FPE layout and the mechanical limits. It can be seen that the engine's stroke amplitude (x_L) is a measure of the distance between the Bottom End Centre (BEC) and the Top End Centre (TEC) of the piston motion inside the cylinder. Motion is permitted only between the mechanical limits (M_{lim}) at cylinder ends.

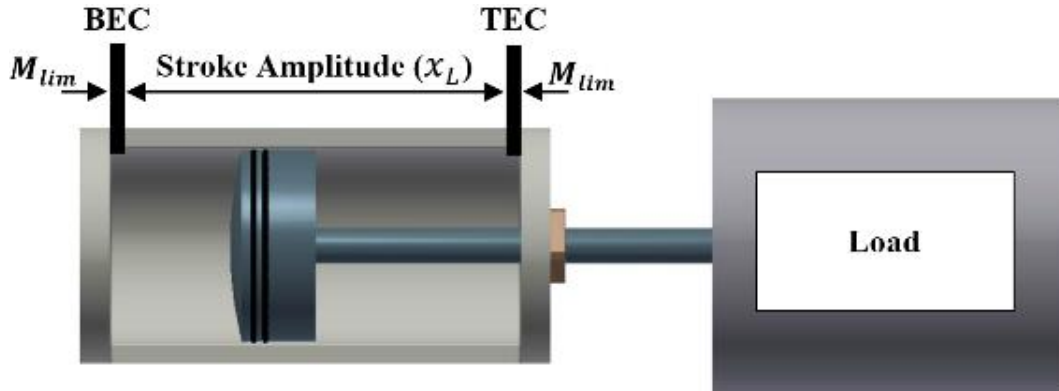


Figure 2-2: 2D view showing single-stroke FPE and load arrangement

Piston motion and spanned distance is fixed and controlled by the types of the connected load and the rebounding device, if any, and their corresponding force profiles. The instantaneous force (F) balancing equation for this configuration is given as:

$$\sum F = a \cdot M_m \leftrightarrow \pm \overrightarrow{F_E} \mp \overrightarrow{F_L} \mp \overrightarrow{F_{RD}} = a \cdot M_m \quad 2-1$$

Where:

- a : system acceleration (m/s^2)
- M_m : moving mass (kg)
- $\overrightarrow{F_E}$: Expanding force (N)
- $\overrightarrow{F_L}$: Load force (N)
- $\overrightarrow{F_{RD}}$: Rebounding device force (N)

To achieve full utilisation of the engine's mechanical cycle, the load axial spacing, in addition to its active and any mandatory fittings' lengths, must at least be equal to the maximum stroke amplitude.

Applications that use this configuration are air compressors, gas generators, in addition to hydraulic which could serve (react) as both load and the rebounding force with a reported system efficiency of 50% [8, 18, 19].

2.2.3 Two - Stroke

Application of the FPE to hybrid vehicle powertrains started to emerge at the end of last century, with several variations in the configuration investigated to achieve robust and compact system integration [3, 14]. This resulted in the development of the two-stroke, or the dual combustion, FPE shown in Figure 2-3.

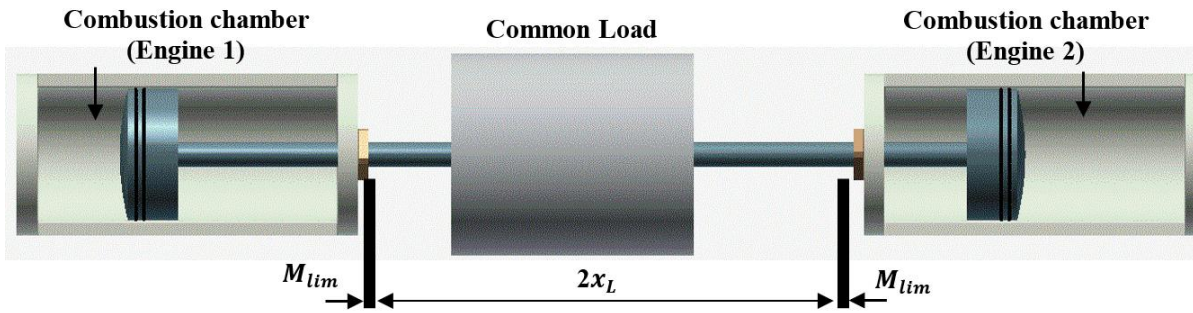


Figure 2-3: 2D view of two – stroke FPE set up showing major components

This configuration has two identical cylinders collinearly arranged to drive a common load located at the midsection of the engine. By performing appropriate control technique to the combustion process in each chamber, the two cylinders work in opposed phases to achieve continuous reciprocating operation. The force balance equation for the two cylinders (1 & 2) arrangement is:

$$\overrightarrow{\pm F_{E1}} \mp \overrightarrow{F_{E2}} \mp \overrightarrow{F_L} = a \cdot M_m \quad 2-2$$

The axial displacement between the two cylinders, ensuring use of full mechanical cycle, needs to be at least twice the maximum stroke amplitude with consideration to allowable mechanical limits and load active length, and this imposes some constraints on the load design when striving for a compact system. However, such a configuration in hydraulic systems applications demands a high degree of controllability incorporating both fuel and load to control the piston position precisely, a complex task to achieve in practice [8], [20]. A 51% efficiency of this configuration was predicted at varying electrical load of a LM of which its reacting force was assumed to vary linearly with system speed, i.e. like a damper [5].

2.2.4 Opposed pistons

The third configuration of FPE is termed the opposed pistons engine, where two pistons share the same combustion chamber, as shown in Figure 2-4 (a). In general, the use of this set up is to manipulate driving two loads and their rebounding device.

The main feature of this FPE configuration is the vibration free operation compared to previous engine types [8]. Each load will require a maximum operating stroke length plus the necessary fittings lengths and its active length. The force balancing equation for this engine layout is given as:

$$\overrightarrow{\pm F_E} \mp \overrightarrow{F_{L1,2}} \mp \overrightarrow{F_{RD1,2}} = a \cdot M_m \quad 2-3$$

This configuration was one of the early FPE designs used to ensure symmetric pistons' vibration free motion featured by perfect balance, nevertheless the requirement to double component sets increase system cost. Further, a synchronisation mechanism is required which adds another frictional loss and reduces overall system efficiency, which is considered the major drawback in this configuration. Yet, this configuration had served well as air compressors and gas generators in large scale plants and have an efficiency of 31% in hydraulic system [8].

One feasible development of this arrangement is the use of the double acting, or opposite chambers, engine arrangement, see Figure 2-4 (b), which does not have much difference except that the separate pistons are replaced by a single free piston driven from both side chambers.

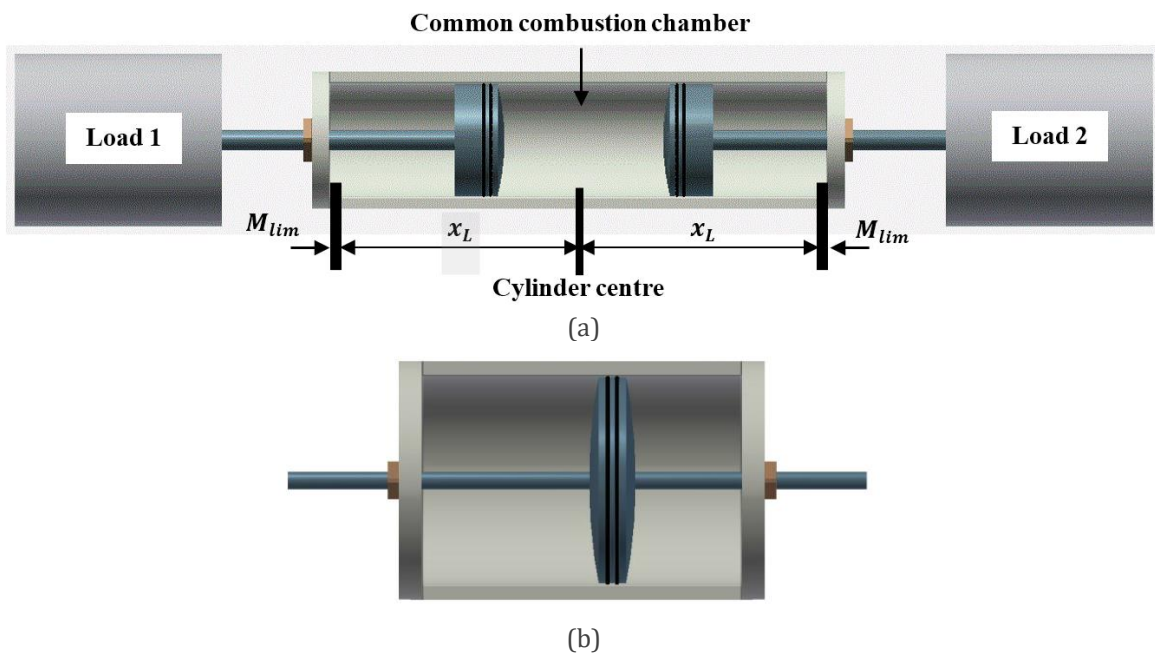


Figure 2-4: (a) 2D view of opposed pistons with shared combustion chamber and two loads; (b) Double acting or opposite chambers arrangement

In such a case a shorter assembly is gained and the engine can drive one side or two sided loads depending on the desired application. The main achievement of this assembly is that it can operate quietly with multi-fuel capabilities which promote it to fit for small scale applications [2]. The driving engine adopted in this thesis considers this arrangement in which the load(s) are placed on one side, as will be explained in next chapter.

2.3 Linear Machines Background

In general, linear motion can be classified as oscillating motion or continuous (as in conveying belts, escalators, or railway transportation). For both motion types, most LMs past studies focused on converting electrical energy into a linear mechanical energy.

Studies on Linear Induction Machines (LIMs) have discussed the differences between conventional rotating IMs and the LIMs in topological variation, standstill, low and high speeds, and self-oscillating applications [21-26].

Some pioneering studies have also been recognised in describing the development that have been made to LIM of synchronous topology and investigated its ability for electrical power generation based on transformer action [27, 28]. Other studies describing LIM principal of operation, and classify it according to the geometrical variation and the industrial applications with the analytic prediction of fields/forces within machine geometry [29-36]. Most LIMs belong to one of the classes sorted according to machine members' lengths and geometry, see Figure 2-5, in addition to desired application speed. From these studies, the range of LIMs application may fall under one of the following:

- (a) Force machines: in which the machine is required to operate at low speed or at standstill in applications like transducing [37], or actuation [38].
- (b) Energy machines: in which the machine is to operate at high speed for accelerating purposes as in systems assisting air craft launching [39, 40].
- (c) Power machines: in which the machine is to work for longer periods compared to previous applications. The speed range is variable during operation period such as in transportation system, or in electrical power generation like the intended use of the machine with the application in the current research.

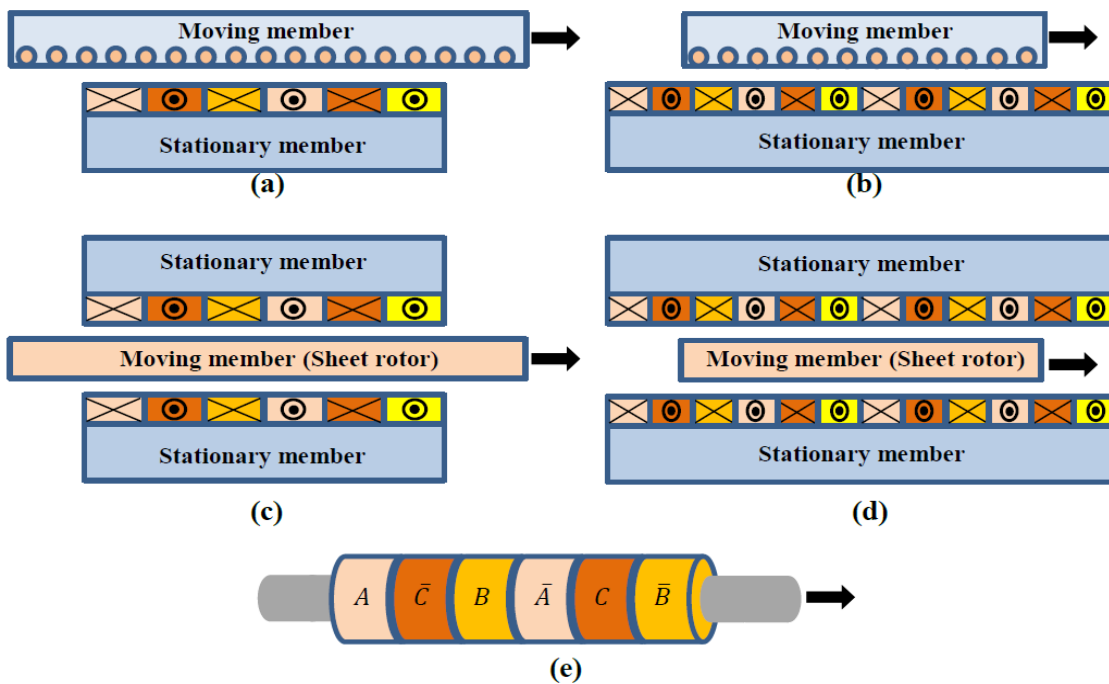


Figure 2-5: Linear Machines classes based on geometrical variation and member length (a) Flat Long Rotor One Sided; (b) Flat Long Stator One Sided; (c) Flat Long Rotor Two Sided; (d) Flat Long Stator Two Sided; and (e) Tubular Long Rotor One Sided

2.4 Use of Permanent Magnet in Linear Machines

Progress in the manufacturing technology of rare – earth Permanent Magnet (PM) accompanied by the improvement in its energy product [41], Figure 2-6, has had a major impact on the design and applications of most electrical machines. In general, using PMs in an electrical machine can result in compactness, high operating efficiency, high torque (force) per unit volume besides offering a more reliable system that consumes less, or produces higher, power ratings. Nevertheless, penalties like cost, weight, and thermal effect on the PMs' operating conditions would add some restrictions and should be considered with care by the machine designer.

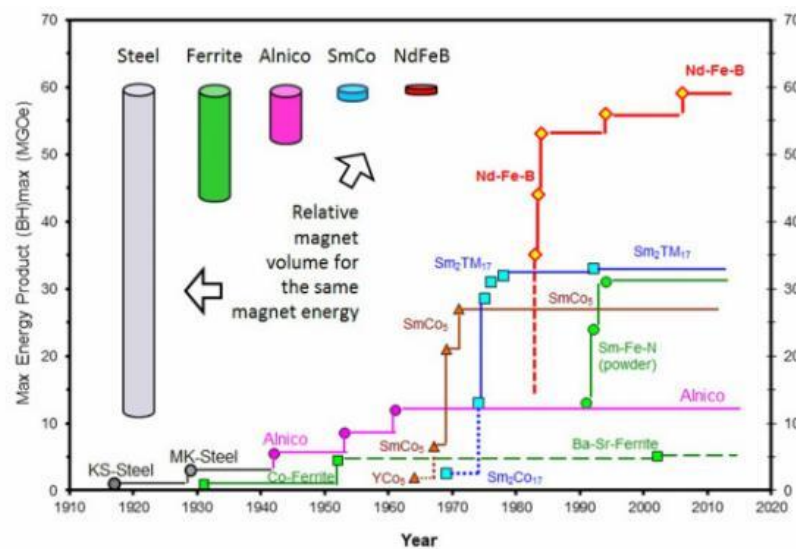


Figure 2-6: Rare-Earth PM energy product development [42]

2.5 Permanent Magnet Linear Machines for FPE application

All rotating machines can be reformed, with attention to electromagnetic behaviour, into their linear counterparts without affecting the operational principals [43, 44]. The following subsections will demonstrate the LMs that have been proposed for use with FPE application focusing on the up to date topologies. The machines are organised according to two kinds of classification categories.

The first category considers the flux path within the machine geometry, where flux path plane in the machine could be:

- (1) **Longitudinal Flux (LF):** in which flux path plane is along the axis of motion.
- (2) **Transverse Flux (TF):** in which flux path plane is perpendicular to the axis of motion.

The second classification method is according to the positioning of magnet/electromagnet onto machine members, of which it gives one of three possible structures [44, 45]:

- (1) **Moving Coil Machine (MCM):** in which the moving member contains only the armature winding.
- (2) **Moving Iron Machine (MIM):** in which the moving member is a pure iron structure which, partially or totally, forms the magnetic circuit.
- (3) **Moving Magnet Machine (MMM):** in which the moving member contains the magnets/electromagnets within its structure.

Combinations of these five classifications are discussed in the following sections.

2.5.1 Longitudinal Flux machines

This group of LMs has a flux that flows in planes parallel to the machine as well as motion axes as shown in Figure 2-7. This LMs family form a common topology for most linear direct drive applications including the FPE application.

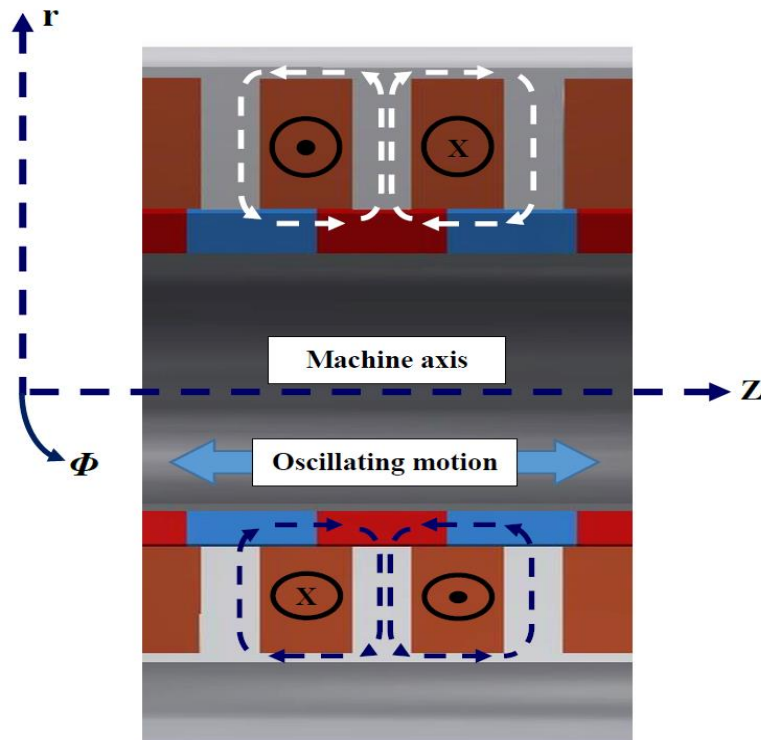


Figure 2-7: Longitudinal Flux paths in a Linear Machine of cylindrical geometry

The MCM version of this group has the main feature of low moving mass which promotes it for applications requiring fast dynamic response, high operating frequency and few Watt ratings, like loudspeakers [44]. On the other hand, the moving coils require flexible leads or commutator/brush set to extract the generated power and this imposes continuous maintenance besides limiting power ratings. Thus, MCMs are rarely used in high power rating applications and in long stroke amplitudes.

However, LF generators of tubular geometry have been proposed and studied for use with an Internal Combustion Engine (ICE), see Figure 2-8, with reporting the merits of low mover mass on system controllability when compared with a MMM and the low efficiencies for low operating speeds [46]. Also, the design and comparison of a three - phase MCM with 6 and 8 poles have been reported with discussion on beneficial use of commutator for system initialising and later electrical power extraction and conversion [47].

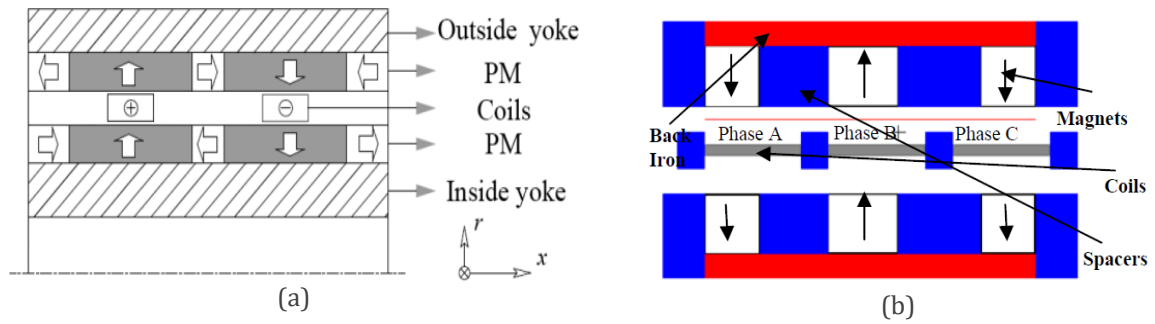


Figure 2-8: 2D structure view of MCM (a) Ref. [46]; (b) Ref. [47]

MIM with its pure iron mover structure are generally characterised by robustness, ease of manufacturing and maintenance procedures, well thermally protected magnets, and applicable in both flat and tubular geometries. Such features promote it for power dense applications ranging from linear transportation, of single and double sided configurations [48, 49], to wave energy conversion application of up to four sides [50] as well as tubular geometries [51].

Figure 2-9 clarifies samples of such machines in both tubular and flat geometries. Also, it can be seen from Figure 2-9 (b) that these machines are suitable for long stroke applications in which case moving short stator of lower mass is more economic.

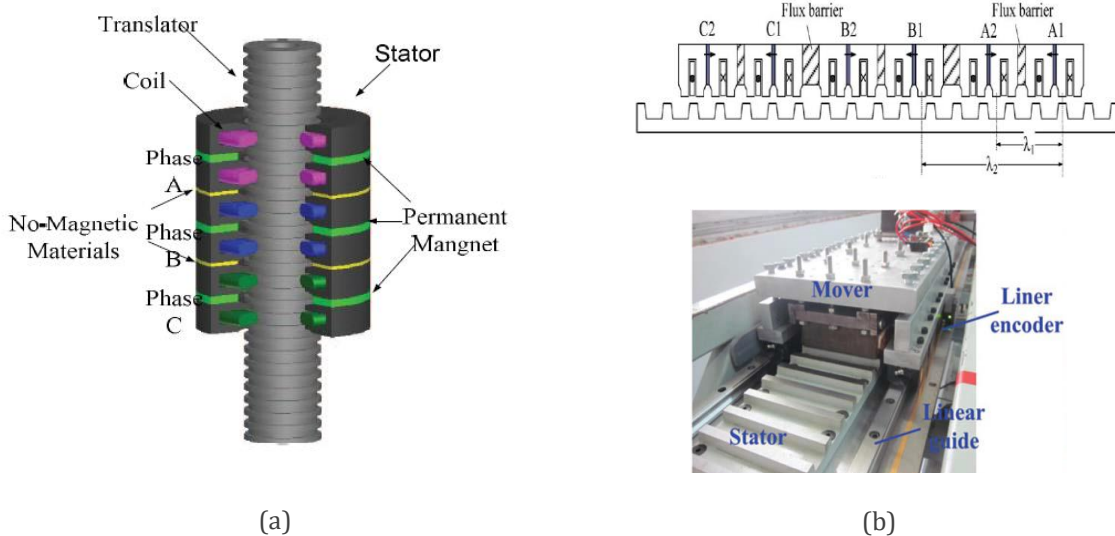


Figure 2-9: Samples of MIM configurations (a) Tubular [51]; (b) Flat [52]

This class of LMs has been proposed for FPE application in three – phases with double layer armature [53], see Figure 2-10 (a), then it showed a heavier mover when compared with an MMM, see Figure 2-10 (b), for a specified design with geometrical constraints [54].

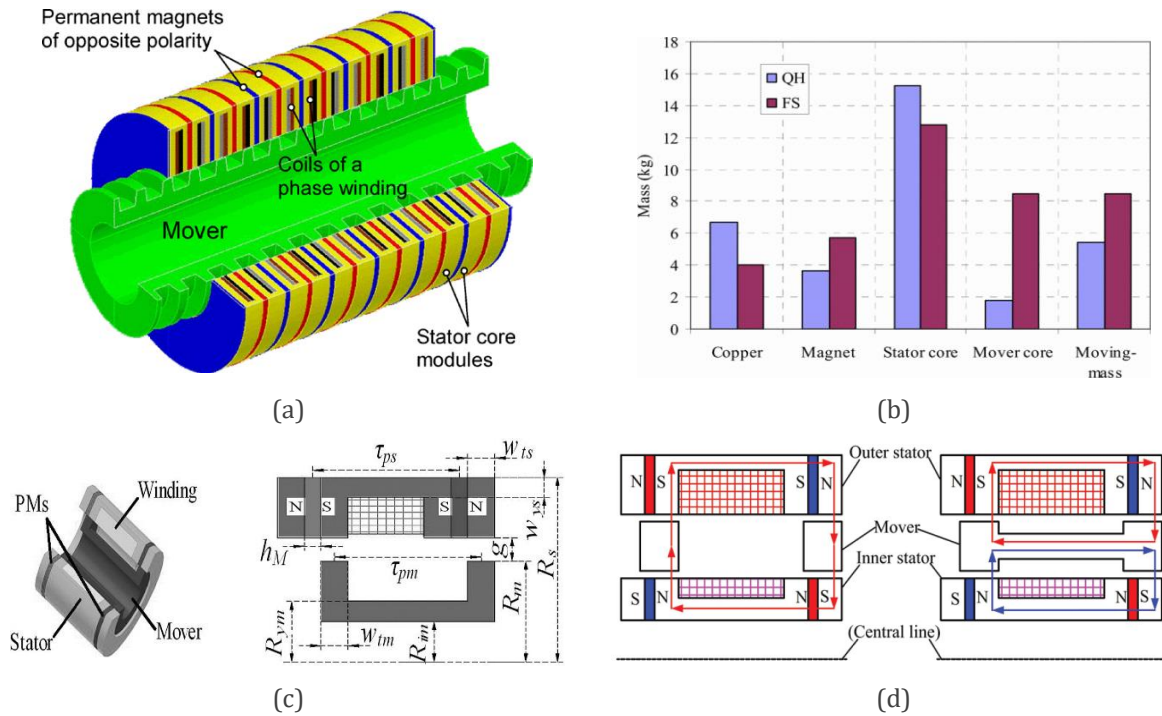


Figure 2-10: Flux Switching MIM machine models (a) Three-phase model [53]; (b) Comparison results [54] (c) Single-phase model [55]; and (d) Dual – stator modified model [56]

The same findings were reported in another MIM topology of single – phase, single coil armature, see Figure 2-10 (c), that has been proposed in [55] and compared with two MMMs, all optimised for another design requirement of 1kW power rating. A modified topology of the later machine with dual stator configuration, see Figure 2-10 (d), can be viewed by visiting [56]. MMMs with LF flux distribution have been widely researched by many research groups worldwide, especially with tubular geometries.

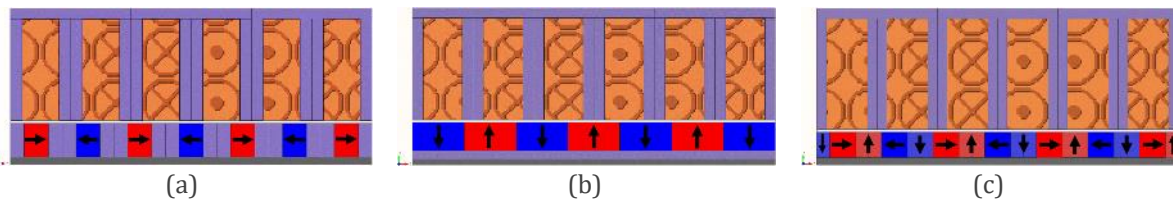


Figure 2-11: Surface mounted MMM classes (a) Axial (AM); (b) Radial (RM); and (c) Quasi-Halbach (QHM)

This family of LMs, requires a supporting moving part for mounting the PMs in which an additional mass is added to the total moving mass. Based on the magnet orientation, these machines are classified as the Flux-Concentrated or the Axial Magnetised (AM), Radial Magnetised (RM) or Quasi-Halbach Magnetised (QHM) all are shown in the cut through view in Figure 2-11 clarifying machine parts and magnets orientation.

Design and testing of a RM machine equipped with slotted conventional windings integrated with an Internal Combustion-FPE has been reported [3, 14, 57]. Reported results showed system ability to generate 313 W dumped by resistive loading until the engine stalled above this value, with no data reported on machine parts weights or the materials used.

At the same time, another team had reported the analytical field solution with 2D FEA verification of this LM family in cylindrical geometry and possible PM arrangements [58]. The field solution was then used for optimising and assessing the performance of three machines equipped with slotless three-phase conventional windings with regard to force capability, associated force ripple and magnet mass [58, 59]. Results showed higher force capability with AM machine, albeit by consuming more magnet mass for the larger air gap assumed. Further AM model modification was carried out by adopting non-magnetic rod to support translator structure, see Figure 2-12, which led to enhancing the force capability, reducing the force ripple and a saving of 4.3% in magnet material [60, 61], with further studies on armature-slotting effects on self-inductance, reluctance force and impacts on performance due to force fluctuation [62].

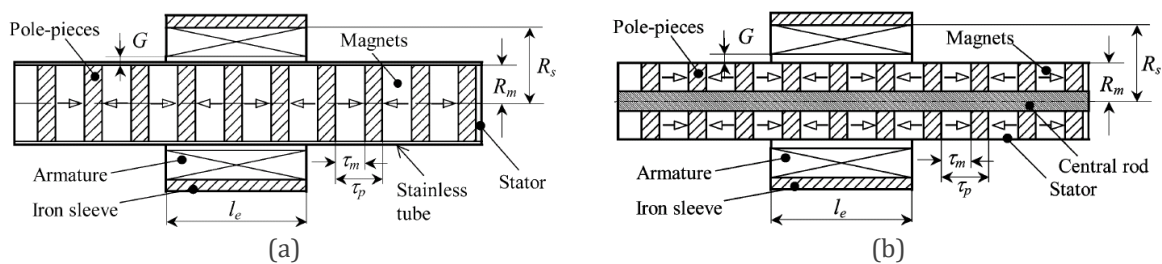


Figure 2-12: AM tubular model (a) Conventional [59]; (b) Modified [61]

Finite stator length end effects on the thrust force, associated ripple and generated EMF harmonics of both RM and QHM excitation has been formulated analytically with FEA verification [63, 64]. Possible elimination of end effects in QHM has been examined with the appropriate choice of armature length, appropriate displacement between stator and translator cores and in order to gain advantageous use of opposition/unidirectional properties of side forces [63, 64]. Additionally, optimisation and performance prediction of an RM machine and conventional winding under the assumption of the power converter's controller ability to align phase quantities in phase have been presented. Impacts of machine key parameters, core saturation, inductance and converter losses on force capability, machine and overall system efficiencies have been demonstrated [65].

Before proposing the QHM machine topology as a candidate for use with FPE application, valuable findings have been reported comprehensively on this machine model.

This includes a description of feasible pole/slot number combinations, introduced the modular winding of which phase coils are displaced in adjacent slots, the effect of supporting tube material on flux distribution and mover weight compared to an RM machine. Key design parameters, converter rating and losses influencing performance have been demonstrated and prototyped, see Figure 2-13, for an optimal 9slots/10 poles dimensions of which the practical model achieved a moving mass of 6.0 Kg [10, 66-74].

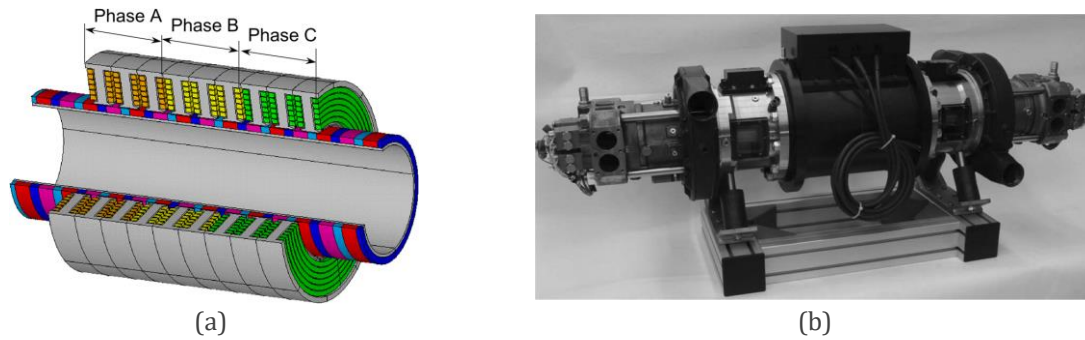


Figure 2-13: 9 slot/10 poles tubular QHM for FPE use (a) Topology [69]; (b) Prototyping in FPEC unit [10]

Additionally the prediction of iron losses, PM eddy currents loss and irreversible PM demagnetisation have been reported [72] highlighting a performance degradation of up to 6.3% in rated force, due to PM demagnetisation, partially and irreversibly at magnet corners due to its temperature rise, and with the increase of armature reaction field, see Figure 2-14 (a, b).

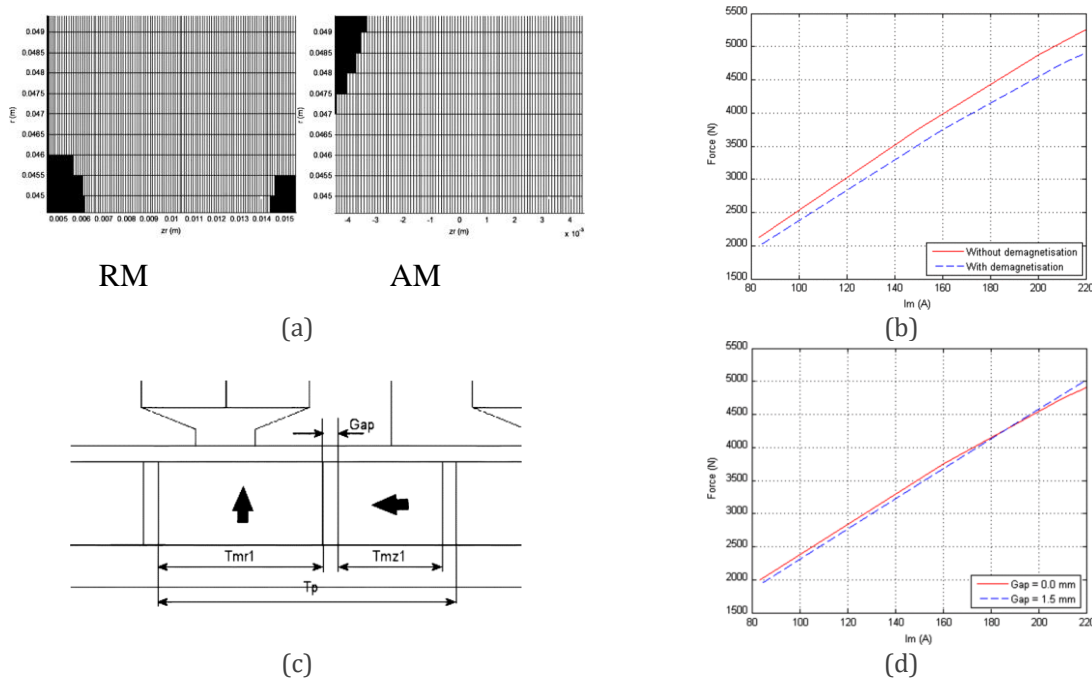


Figure 2-14: QHM partial irreversible demagnetisation [74] (a) FE modelling of demagnetised PM corners; (b) Effect of demagnetization on machine force capability; (c) Axial air gap between QHM segments; and (d) Effect of axial air gap on machine force capability

Also, investigations on the use of Soft Magnetic Composite (SMC) as total slot core material have reported that performance degraded, although it might offer lower cost [73], with reporting its effect on the resulted force capability and machine efficiency. Suggestions like using PMs of trapezoidal cross shape (or chamfered), with associated penalties in cost besides manufacturing complications, might help in the minimising PM demagnetisation problem; or by introducing an additional axial air gaps separating pole segment, see Figure 2-14 (c, d), which have negligible effects on force capability besides offering a save in magnet mass, however, it may cause some mechanical problems in the assembly of magnets sets [74].

Other studies have considered the optimisation by investigating the effect of pole number and PM/lamination materials on an AM machine performance designed for specific FPE demands, thermal constraints and a system of constant speed [13]. The reported results showed that increasing pole number would result in increasing the iron loss.

Yet, for a constant power operation, current could be decreased and hence copper loss decrease. Thus, the resultant specific power can be increased, albeit with decreased efficiency. A machine with 10 poles/9slots, 1.49 kW/kg specific power, and 93.5 % efficiency has been concluded to fit desired specifications.

Few interesting works had considered the use of flat type of MMM machine arrangement. A single – phase, two sided-MMM was proposed to replace a tubular geometry machine scheme, both with RM, for a 500 W power rating and maximum stroke of 37.2mm. The use of the two sided stator was proposed to offset the attraction forces between PMs and salient stator teeth. Reported results showed that the two sided machine topology required an extra (38.4 %) in its translator mass in order to achieve (43.2%) higher power density, and almost (2%) increased efficiency [12].

Another fascinating work of using one sided-MMM with RM in square (cube) shape, see Figure 2-15, has been investigated with experimental validation proposed to reduce cost by simplifying machine manufacturing in comparison with tubular geometry.

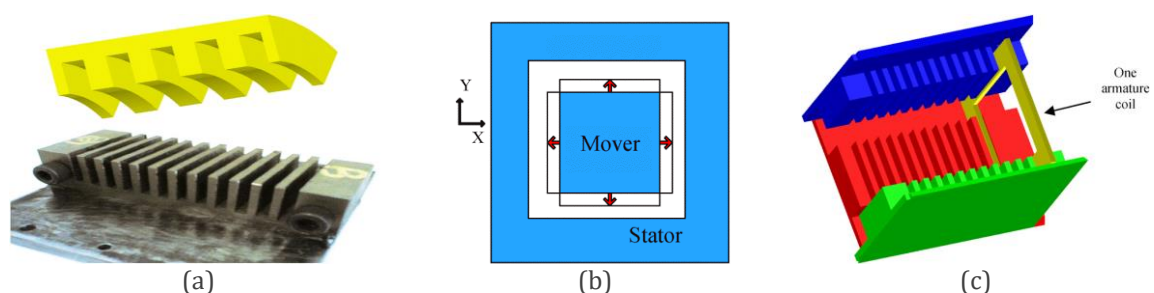


Figure 2-15: Square shape of one sided MMM configuration [77] (a) One side stator model; (b) Cross sectional 2D view; and (c) 3D view of stator and coil

Using this topology also offers much simpler applicability to cogging force reduction techniques suggested earlier for use with other tubular geometries, the pole shifting and end face stepping [75, 76], which can easily be applied together in this flat cube topology. The reported results had clarified the effectiveness of these methods in reducing up to 80% of total cogging force of this geometry.

Recently, a yokeless tubular machine of double movers equipped with QHM and an in between (sandwiched) stator of single-phase winding, see Figure 2-16(a), has been proposed for integration with a Stirling Engine, which has the same mechanical layout as FPE but with shorter stroke amplitude [78]. The machine was proposed with development in order to obtain better coil space utilisation for power rating improvement. The design was compared with an early optimised MMMs of AM and RM magnets arrangement for a 1kW power rating and same drive engine specifications [79]. Higher rated power density was achieved with the proposed topology, albeit with heavier mover/magnet masses compared with the AM machine topology.

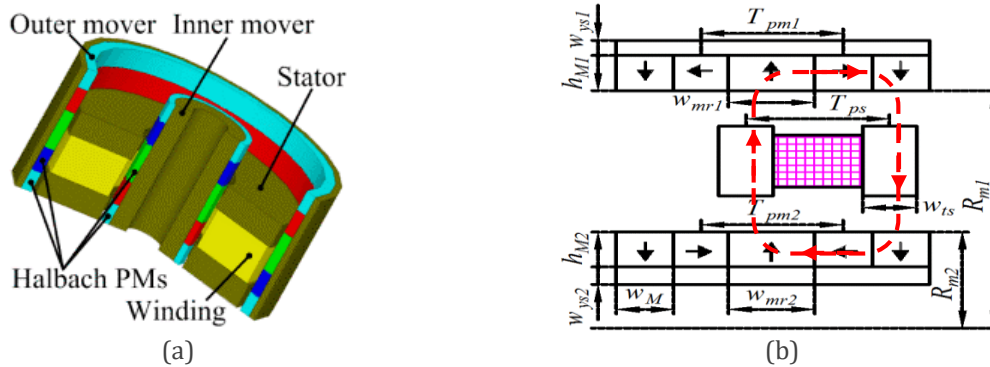


Figure 2-16: Yokeless dual mover LF-MMM topology [78] (a) 3D view; (b) Flux path

A linear magnetic – gear machine topology has also been proposed as a feasible solution for the intended FPE application as shown in Figure 2-17. This topology is composed of double stationary parts and double moving magnet parts which imposes three air gaps.

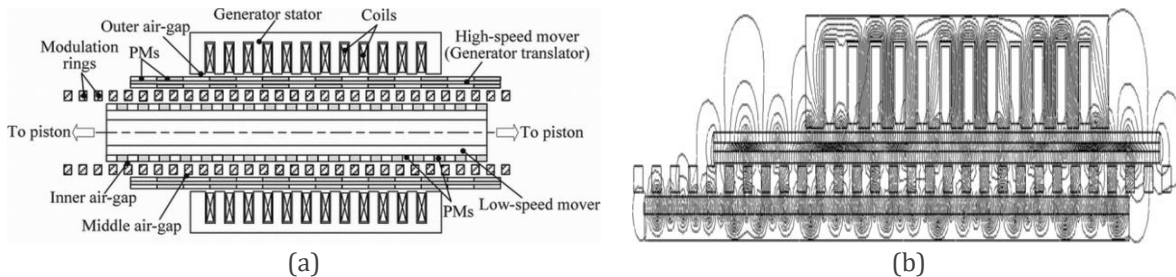


Figure 2-17: Magnetic gear machine topology [80] (a) 2D view; (b) Flux distribution

The machine shows LF field distribution and the topology was described in which it offers a gear ratio of 2.22 between the two movers which contributes to improve the resultant power density, albeit with its structure complications and the associated cost. Further, without reporting the resultant power densities, especially power/mass density, nor comparing with an existing topology designed for same specification, the design and topology still needs detailed analysis to become feasible [80].

2.5.2 Transverse Flux Linear Machines

In general, TFMs are characterised by their high power/torque densities compared to conventional machines of radially distributed flux, due to the perpendicular interaction between the magnetic and electric loadings of the machine. This perpendicular feature has two major effects on machine characterisation. The first effect is a positive one, in which the Volt-Ampere (VA) rating of the machine can be doubled by doubling pole numbers, see Figure 2-18, i.e. doubling the rate of change of magnetic flux for a given geometrical longitudinal dimension and for the same speed [81, 82].

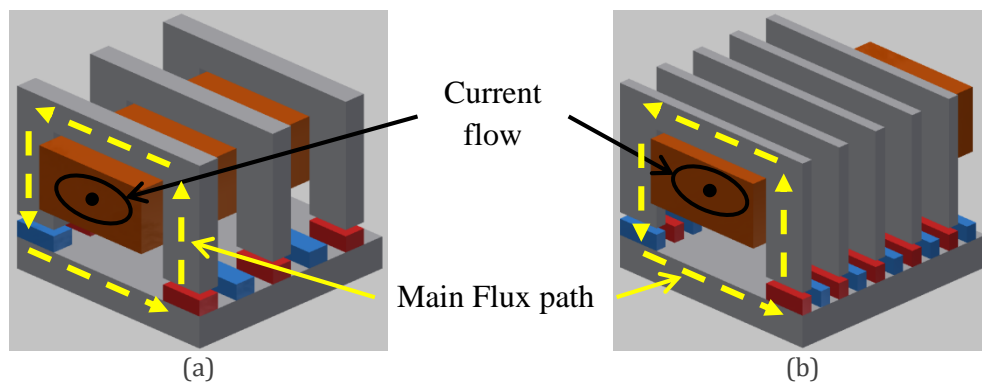


Figure 2-18: Flat topology of TFLM with RM (a) 3 poles structure; (b) 6 poles structure

The second impact is unfortunately a negative interference to flux behaviour, since the increased pole number for a specified fixed length results in a reduced pole pitch and, therefore, two consequences. Firstly, this will cause an increased three – dimensional leakage and fringing fluxes, i.e. a penalty in cost due to poor PM utilisation, within each reduced pole pitch that affects the operating power factor of the machine [81]. Secondly, the low power factor operation impacts on power converter VA rating requirements due to their inverse relationship, which means another penalty in the system cost [83]. However, the positive features had attracted many researchers to explore the design and/or optimisation of TFMs in their linear form and possible geometries as a candidate for FPE application.

An intermediate RM poles, or the Z-TFM, and a modified flux paths had been proposed to compensate the poor PM utilisation in conventional TFM. Yet in a later study it was hesitantly concluded that it requires larger diameter for a specific ratings compared to the original machine, even with 35% improvement in useful air gap flux [84]. A further study had reported an approximated two-dimension analytical solution based on translator position with account for air gap permeances and iron non-linearity in different machine parts.

Dimensioning and 3D FEA modelling of a 5kW prototype machine was performed using iterative solutions of reluctance networks seen by magnets and armature fields. Reported results had showed that a maximum power factor of 0.57, and a specific power of 1.05 kW/kg can be achieved of which it considered high in comparison with other reported values in MMM and MIM [55]. More or less, the poor power factor, manufacturing complications and the highlighted defects in prototyped model due to the shortened pole lengths might have stopped the concept from later studies, even with the buried flux concentrated magnets assembly [9, 85].

Another study considered the tubular TFM topology with surface mounted RMs arrangement, see Figure 2-19, and introduced the analytical solution of a modified reluctance network to account for the axial leakage flux paths due to the inactive magnets that distort the main flux paths and affect the resultant machine performance [86].

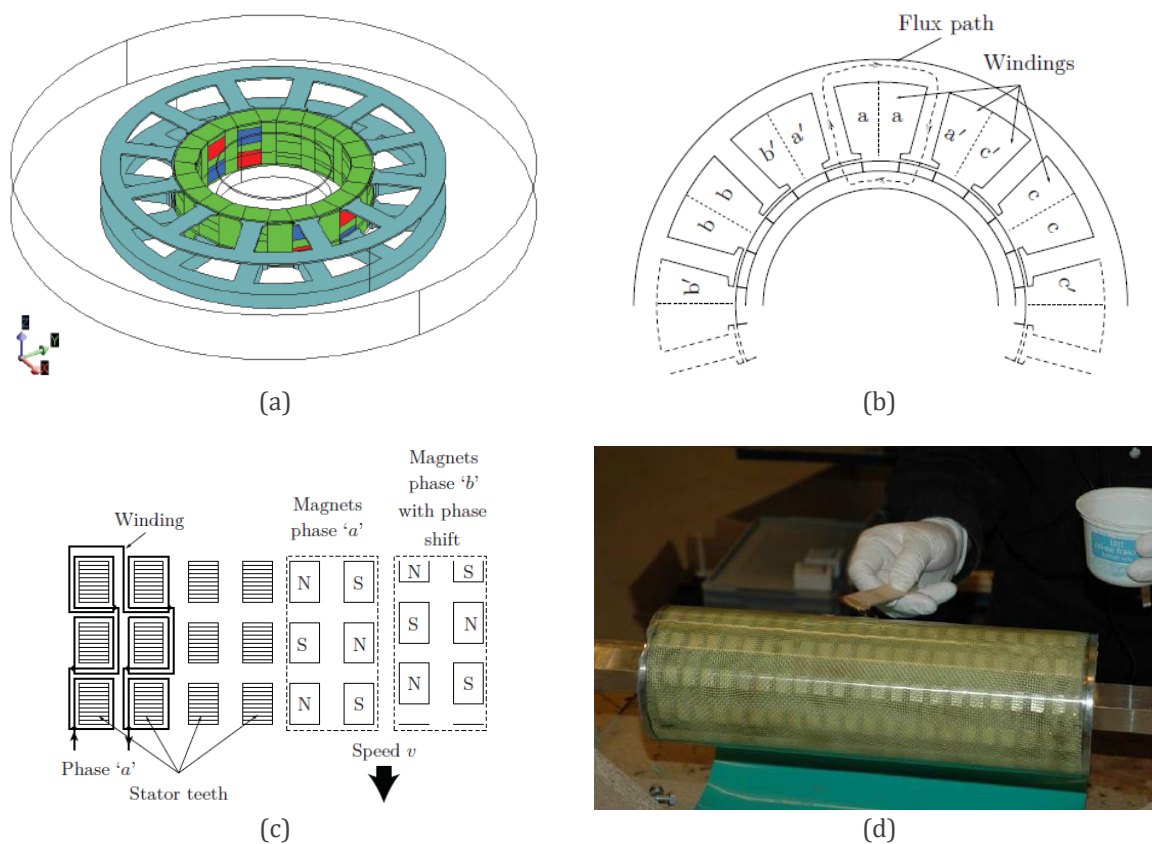


Figure 2-19: Tubular TFM topology [82] (a) 3D FEA model; (b) Radial cut view showing separate flux path; (c) Axial magnets shift to achieve three – phase design and; (d) Final translator structure

The performance of the machine was predicted by 3D FEA performed for a single pole – single-phase topology. A Three – phase TFM design was achieved by setting up an axial shift of 120 electrical degrees between magnet sets that support separate flux paths per phase. As reported in the research, complicated magnet assembly procedures are to be fulfilled with restrictions on bearings selection to avoid any possible misalignment between magnet – stator tooth pole axis and the consequences on machine performance. Therefore, appreciable discussions on magnets gluing type and methods, coating, translator stiffness enhancement, stator pole construction, etc. had been documented in the study [82]. Still however the predicted power factor of 0.38 by the modified adopted analytical method does not exceeded the earlier pronounced values for this family of LMs [83].

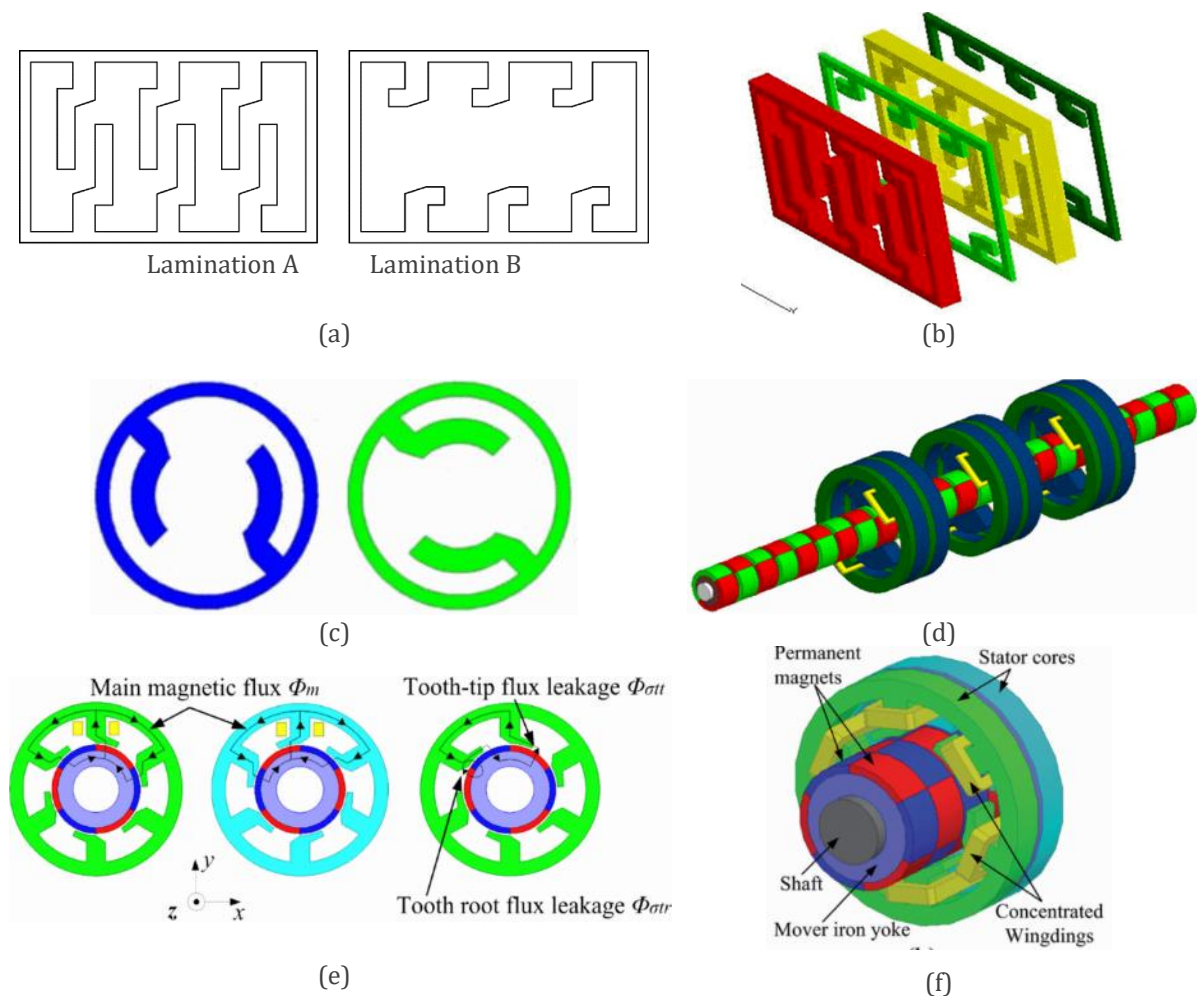


Figure 2-20: TFM topologies (a) Stator lamination; (b) 3-D view of flat stator core structure [88]; (c) Staggered teeth lamination; (d) TF with staggered teeth and three – phase design [89]; (e) Major and leakage flux paths in the staggered teeth; (f) TF with staggered teeth and single – phase assembly [90]

Other work had discussed the Z-TFM design in one side form of which the stator is constructed with two mirrored lamination sets, see Figure 2-20 (a, b), to offer simpler machine mechanical structure.

Again, an axial shift of $2/3$ of the pole pitch had been used to implement the three-phase design with compromised optimisation of important parameters affecting leakage flux paths and performance within the proposed geometry. [87, 88]. Even with its satisfactory characteristics like low cogging force and force ripple, high efficiency and the gained manufacturing simplicity, the reported power factor compared to other MMM topologies was only 0.44, i.e. not exceeding the aforementioned range which indicates that the PMs are still poorly utilised which negatively impacted the resultant power densities. This is mainly due to the leakage fluxes in transversal and longitudinal paths between adjacent stator teeth, and mover magnet poles that had been furtherly inspected and analysed by 3D FEA solution in the study.

Then, by using a tubular geometry, a solution was proposed by staggering stator teeth with a moving magnet mover of multipolar circumferential pair of 1 and 3, see Figure 2-20 (c)-(f), in order to enhance the reluctance between adjacent stator teeth without affecting axial mover pole pitch nor major flux paths. An in depth analysis alongside with a compromised optimisation had been carried out on the topologies that resulted in pronouncing, although theoretically, an improved power factor of (0.52) in the initial proposed design [89], followed by a later jump of up to (0.67) with 3 circumferential pole pairs [91].

Few design studies have considered TFM of single – phase windings and/or stationary magnets that had been optimised using 2D and 3D FEA optimising algorithms to achieve various objectives. The machine was designed for up to 3kW power rating and short stroke applications, and is featured by robustness besides ease of manufacturing and maintainability.

Investigations on a moving iron translator configuration had started with 125W power rating, where optimisation had discussed, with prototyping, possible design cases achieving mass minimising or efficiency maximising [92]. Later study had focused on geometrical machine optimisation to improve the specific power while adhering specific performance constraints with achievement of 0.06 kW/kg specific power by using 3.58 kg mover mass [93].

Specific power had been furtherly improved by replacing the moving iron structure by a surface mounted RM translator, which resulted in an increase of 55% in specific power that utilised 1.78 kg magnet mass [94].

When a dual stator, dual air-gap and moving magnet design replaces the later design, this led to saving almost 41% of total machine mass by utilising 2.0 kg magnet mass for same design specification. A resultant gain of 40% in specific power with a decrease of 51% in mover weight, however, versus the raised drawbacks as increased translator manufacturing difficulties and magnets demagnetising issues related to their internal eddy current losses had been reported [95].

To overcome these issues, the QHM had been investigated for same specification in which it showed good improvements in most of the design aspects, except in the mover and magnet resultant masses and PM losses.

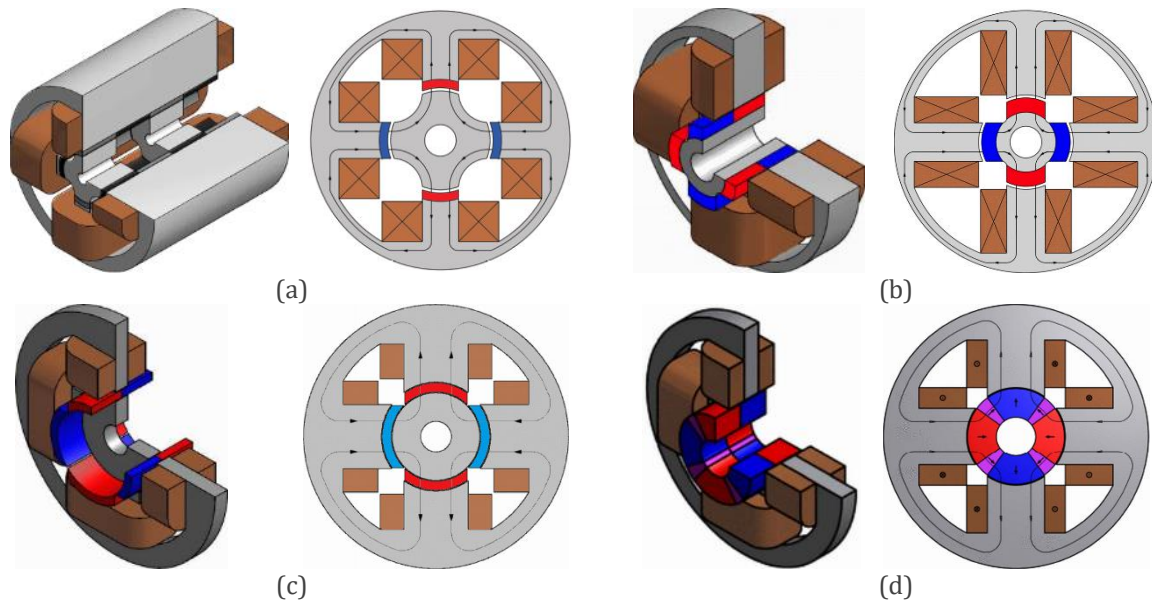


Figure 2-21: TTFLM topologies and flux paths for short stroke FPE application (a) Initial MITFLM design [92, 93]; (b) RMMTFLM design variation [94]; (c) Dual stator RMM design variation [95]; and (d) QHMM design variation [96]

Figure 2-21 clarifies the topological variation of TFM and corresponding transverse flux paths. Addressed reduction of 15% in total machine mass and a 17% gain in power versus a penalty of 45% extra magnet/mover mass can be gained using the QHM design [96].

It is worth mentioning that some of the reported inductances were in the range of (14 – 48 mH) without discussing the resulting power factor and related drive issues, nor the issues related to magnet – mover assemblage as discussed by other works [82, 93, 94].

A new TFM, see Figure 2-22(a), in tubular form has been proposed for this application of which its configuration offsets the problems of PMs - mover assembly by applying the axial shift to the magnetic circuit in order to achieve a three – phase design [43]. Continuous improvement and research, via using both static and dynamic 3D FEA, had showed the efficient use of PMs in this machine topology throughout demonstrating the promising performance parameters that reported an expected improvement in power factor of up to 0.66 [97].

Side by side to the later TFM topology, a new linear flux switching moving iron machine version of a rotating counterpart [98] topology was proposed and added to the TFM family, see Figure 2-22(b), in which the flux paths of both the PM and that driven by coil currents exhibit perpendicular action to the motion direction, i.e. shows transverse flux phenomena, and 100% magnet utilisation is a result [43].

Later investigation on the topology against specified design constraints reported the effect of leakage flux on machine performance and the improvement yielded by modifying tooth structure of initial design, yet not competing for the desired specification [99].

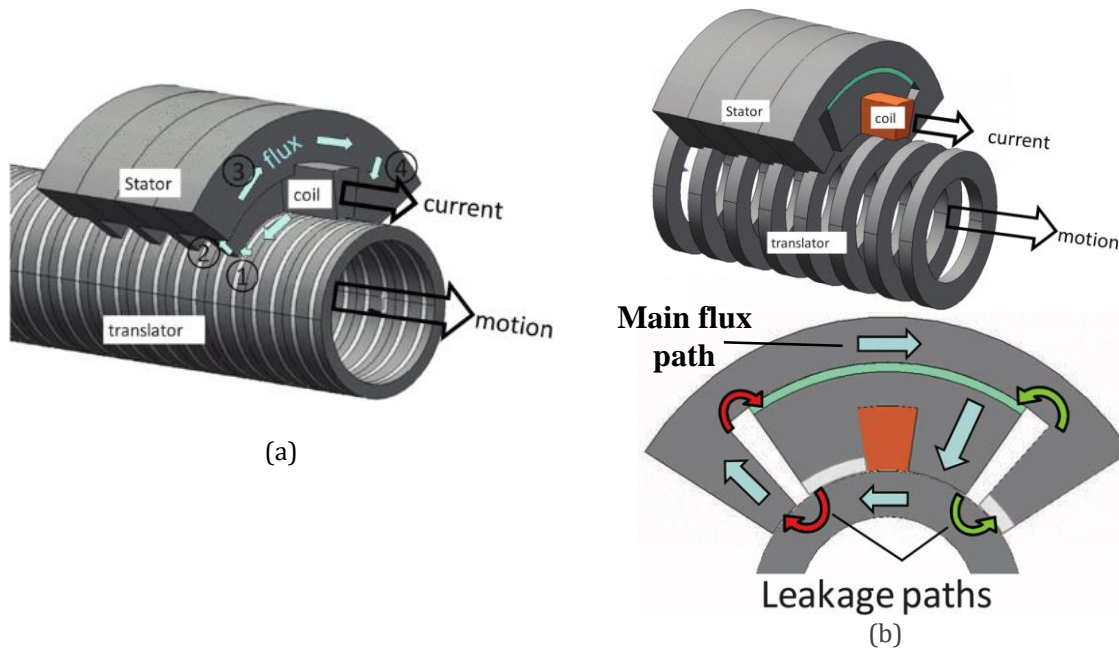


Figure 2-22: New TFM for FPE application showing flux paths [99] (a) Moving Magnet TFM; and (b) Moving Iron – Flux Switching TFM

2.6 Selection of topology criteria

In the system under study, the LG selected topology must interact effectively with the prime mover in order to sustain the maximum efficiency of the integrated system. The initial design stage of the machine topology must satisfy two constraints. Initially, those imposed by the physical and the operational characteristics of the drive engine. Secondly, the machine external characteristics must show high efficiency at various loading conditions as a reflection of the good overall material utilisation and the operational power factor.

Bearing in mind that all machines topologies are equipped with magnets and focusing only on the reported tubular geometries, Table 2-1 summarises a comparison between the machines highlighting the main features of each topology, qualified by the literature review presented in the previous section.

To identify the most suited machine topology, a relative (+/-) marking system was set on specific key factors shared by all topologies in this specific application. When assigning the mark values, a positive mark refers always to a good key factor and the vice versa, and when it is always superior, i.e. even for a feature, the machine is more suited for the application.

The factors were chosen to cover the machines in general as the topology structure and performance, and therefore some factor are related to the structure such as the moving mass and magnet mass utilization; while other factors are selected according to machine operational performance such as the power factor and the power density.

The key factors were mainly dependant on moving mass and materials costs, as expected the topologies that have a lighter moving mass would have a positive mark, which is limited only to moving coil machines MCM. Yet this machine topology needs high amounts of PM mass to achieve a specified power density due to the limited winding volume and the resultant electrical loading, in addition to the limited power abilities of the moving coils and the scheduled maintenance requirement.

Moving iron machines MIM had in general showed a limited resulting force (power) densities compared to moving magnet machines due to poor magnet utilisation, besides the heavier mover mass for a specified design force [53, 54], keeping in focus that moving mass is stroke amplitude dependant. Therefore, it has negative marks in the moving mass, PM mass requirement and power density factors fields.

Table 2-1: Summary of PMLM topologies for FPE applications

Topology		Advantages	Disadvantages
LF	MCM	Light moving mass, PMs well thermally protected, or ease of applying an appropriate cooling technique.	Low stroke amplitudes, limited power ratings due to the low durability of either the coil leads or brushed set, resulting in a short term maintenance.
	MIM	Robust with applicability to long stroke amplitudes, and long term maintenance.	Heavy mover, low power/mass density due to high leakage fluxes, and hence poor material utilisation.
	Single mover	Robust, irrespective of magnets' orientation, with high power density and suitability for various stroke amplitudes, and long term maintainability.	Magnets are not well thermally protected. Mover mass is heavy in general, especially for long stroke applications and for long mover machine with high power ratings.
	MMM	Dual mover	Robust and much suitable for flat geometries, various stroke amplitudes and long term maintainability.
TF	MMM	Robust with high power density and suitability for various stroke amplitudes.	Complicated manufacturing process when axial shift is applied to mover parts and may lead to loss of robustness. In general, most topologies showed poor magnets utilisation with a power factor not exceeding 0.67.
	MIM		

Table 2-2: Topology marking system

Topology	Key factors						Total marks
	Moving mass	PM mass	PM thermal protection	Power density	Power factor (pf)	maintenance	
MCM	+	-	+	-	+	-	+++ ---
MIM	-	-	+	-	+	+	+++ ---
LF	M	Single mover	-	+	-	+	+++ +--
	M	Dual mover	-	-	-	+	++- ---
	M		-	-	-	+	++- ---
TFM – MMM type		-	+	-	+	-	++- ---

The rest of the topologies share the same marks with respect to the moving mass, PM mass and thermal protection as well as power density key factors. The other factors score different marks as regard to machine power factor and maintenance requirement. In this regard, the moving magnet machine in single mover topology is assumed to be easier to maintain compared to the dual mover and the transverse flux machines TFM, therefore it has a positive mark. Also, it has a positive mark in the operating power factor side by side with the dual mover machine compared with the TFM.

Scanning the advantages and disadvantages of both LF and TF machines summarised in Table 2-1 and the total marking score in Table 2-2, the machine topology of longitudinal flux and single moving magnet mover LF-MMM looks like the better option to select as it showed a more convenient candidate for this application and the highest positive marks score compared with other topologies.

However, there still one further problem that may arise in all MMMs, irrespective of the selected machine topology or the type of flux distribution. It is due to the temperature rise in the expanding (compressing) cylinders due to the operation of the inside pistons. This temperature rise will affect the surroundings due to heat conduction, convection and radiation. Should this heat be transferred from the pistons to the connecting rod, the translator and then to the magnets, this will expose the magnets to experience a temperature rise that might degrade their magnetic properties (demagnetisation effect), or cause the permanent loss of magnetic properties at their temperature curie point when accumulated by the heat generated due to the internal eddy currents within the magnets. This is totally dependent on the physical properties of the materials used in the electrical machine. Also, this depends if any insulation is applied to limit the heat transferred to the areas surrounding engine cylinders.

A thermal circuit can be established and the temperature rise in each part of the system can then be assessed. Appropriate ventilating and thermal insulation techniques could be investigated as a means of improving the coupled system performance by eliminating or reducing the heat transfer to the electrical machine, and to avoid the associated fall of PM remanence with the increased temperature [100]. However, this topic is outside the scope of the work considered in this thesis and included as a future step for the development of the current research.

2.7 Background on system modelling

Fundamental operation and performance of various FPEs has been simulated and presented [5]-[7], [8], [101]. Expansion of these works includes combined electrical and dynamic performance using assorted simulation tools [102], [103] and numerical models [104]. High operating efficiency of a compact system with a reduced emissions were the major goals in the work described by Sven and Markus, [102]. Various investigations on some key parameters have been presented in [103, 104] such as the moving mass, spark timing, and equivalence ratio to describe their effects on system performance and the feasibility of optimising these parameters for optimal engine performance. Feng et.al [105] have reported a detailed simulation model of a single cylinder loaded by a Linear Generator and a linear motor acting as the rebounding device. Prototyping of simple structure has been investigated by controlling the rebounding motor force profile to obtain stable system operation and to increase cylinder output power. However, low system efficiency and generating power figures were reported in this work, which promise it to be useful in small scale power applications.

Jia et.al [106] have also presented a study on a spark ignited free – piston engine generator with separation of starting and steady modes of operation of the system. The linear machine was dealt with as a linear motor in the starting mode and as a linear generator in the steady state mode. Developments of sub-models of the system for each mode were carried out using MATLAB/Simulink and results were compared with those of an existing prototype with prediction of the engine efficiency.

In [107] a model of a Linear Joule Engine driving an ideal damper approximating a LG was presented and used to propose an overall optimised engine design.

All these works have simplified the electrical machine to an ideal damper, where the generator force varies linearly with velocity acting against engine's driving force. In electrical terms, this assumption means the machine inductance is ignored, the electromagnetic interconnected forces effects are ignored and there is no force ripple.

Whilst this may be applicable to a constant velocity generator, where inductance can be tuned out with a capacitive load, the variable velocity operation of the FPE gives a variable electrical frequency where no capacitive tuning can be implemented. In addition, a pure damper includes no effects of the combined electromagnetic forces, machine losses, and variation of these parameters to the overall FPE system operation. These important parameters and forces need to be considered in modelling the LG in order to account for their effects on the integrated system operation, sensitivity and the resulting efficiency.

2.8 Background on cogging force in PM Linear Machines

Most LM topologies excited by magnets, except air cored machines, suffer from thrust (force) fluctuations, i.e. force ripple, mainly due to the existence of attraction forces between magnets and slotted armature structure, and partly by the armature reaction and/or reluctance forces. Although employing strong magnets achieves higher force densities, the corresponding force ripple becomes higher and severely affects the performance of the application.

Generally, force ripple has been highlighted to influence the positional controllability and accuracy in all applications incorporating linearly controlled actuating and servo systems. Minimising or eliminating this effect adds complexity to the applied control system, especially for low speed applications requiring precise positioning and complying with its safety standards [75-77, 108-112]. Therefore, in the reported literature many techniques have been employed to reduce these inherent forces and the accompanying effects.

Some of these techniques are applicable in both planer and tubular machine geometries of which some are easy to apply in practice, but with penalties on the resultant machine performance, manufacturing cost or lead to reduce the machine force (power) density due to the increased inactive machine length/volume.

Such techniques include adding auxiliary slots (poles) to the armature of a flat PMLSM [111, 113], see Figure 2-23(a), which achieves a reduction in the rated force fluctuation from 7.2% down to 1.14%. Another technique is the extended end tooth width [110, 114] as shown in Figure 2-23(b) which can effectively reduce the peak-to-peak cogging force scale down to 85% off its initial level. The third technique is the end faces, full or quarter, skewing applied to the armature core of a MMM [76, 77], see Figure 2-23(c), and can achieve a reduction of up to 20% in total resultant cogging forces. Another technique applied to a MMM topology with different magnet orientation of which it considers shortening the length of the end tooth throughout FEA optimisation and was found to significantly reduce force fluctuation to low level margins [79, 115].

Other researchers have reported a solution that dealt with the magnet/pole parts structure. An analytical formulation of cogging force components in an AM-MMM has been presented in [116] to solve the problem by considering iron pole piece slotting, see Figure 2-23(d). The added dummy slots to the iron pole piece proved its effectiveness in reducing or eliminating different cogging force active harmonic components, yet its effect on the resultant machine force capability has not been considered.

Pole shifting [75] is also another technique that can be applied in both flat and cylindrical geometries. It deals with the magnet structure and helped in reducing the cogging force levels down to 65%, 80% and 90% in 4, 6 and 8 poles MMM topologies. Due to the introduced asymmetrical pole distribution, see Figure 2-23(e), this technique introduces a negative impact on the resultant force capability as discussed by the authors.

Other techniques had considered magnets skewing, or V-skewing, applied in a planar synchronous machine, where the V-skewing has reduced effectively the 5th and 6th harmonic components while negligibly affecting other harmonics, see Figure 2-23(f). It is worth mentioning that this technique is hard to apply in a cylindrical machine geometry.

Other research had considered reducing the cogging force using field oriented control with feedforward current compensation, ignored time harmonics and reluctance force. The control technique has been proposed, investigated and applied alongside with added external poles in [112, 117, 118]. Reported simulation and experimental results imply the effectiveness of the control method, even with distorted current waveforms at low speed application [112], and for constant speed operating machine.

Constrained by a specific application requirement and for the same magnet mass, newer design of 9pole/10slot to replace the existing 8pole/10slot design has been proposed in [119]. The new machine model offered lower cogging force and higher thrust force levels for three phase applications, yet it introduced an (0.47%) imbalance to the induced EMF in windings.

In all aforementioned works, cogging force effect in actuating system can be minimised and reduced significantly using applicable classical control methods with the suitable power drive. The effect of cogging force on the performance of a linear machine operating as a generator has never been fully investigated, except in terms of causing vibration, noise and must be minimised to achieve smoother operation of the driving engine [79].

When the machine works as a power source driven by a variable speed driving system, as in this application case, there exists no work that describes cogging force effect on the electrical power generated.

Further, under such continuously transient operation of the system, classical control techniques would fail in achieving the target of controlling the current absorbed by the load. This might enforce proposing newer structural techniques that can be applied easily to the selected machine topology without affecting its resultant power (force) density.

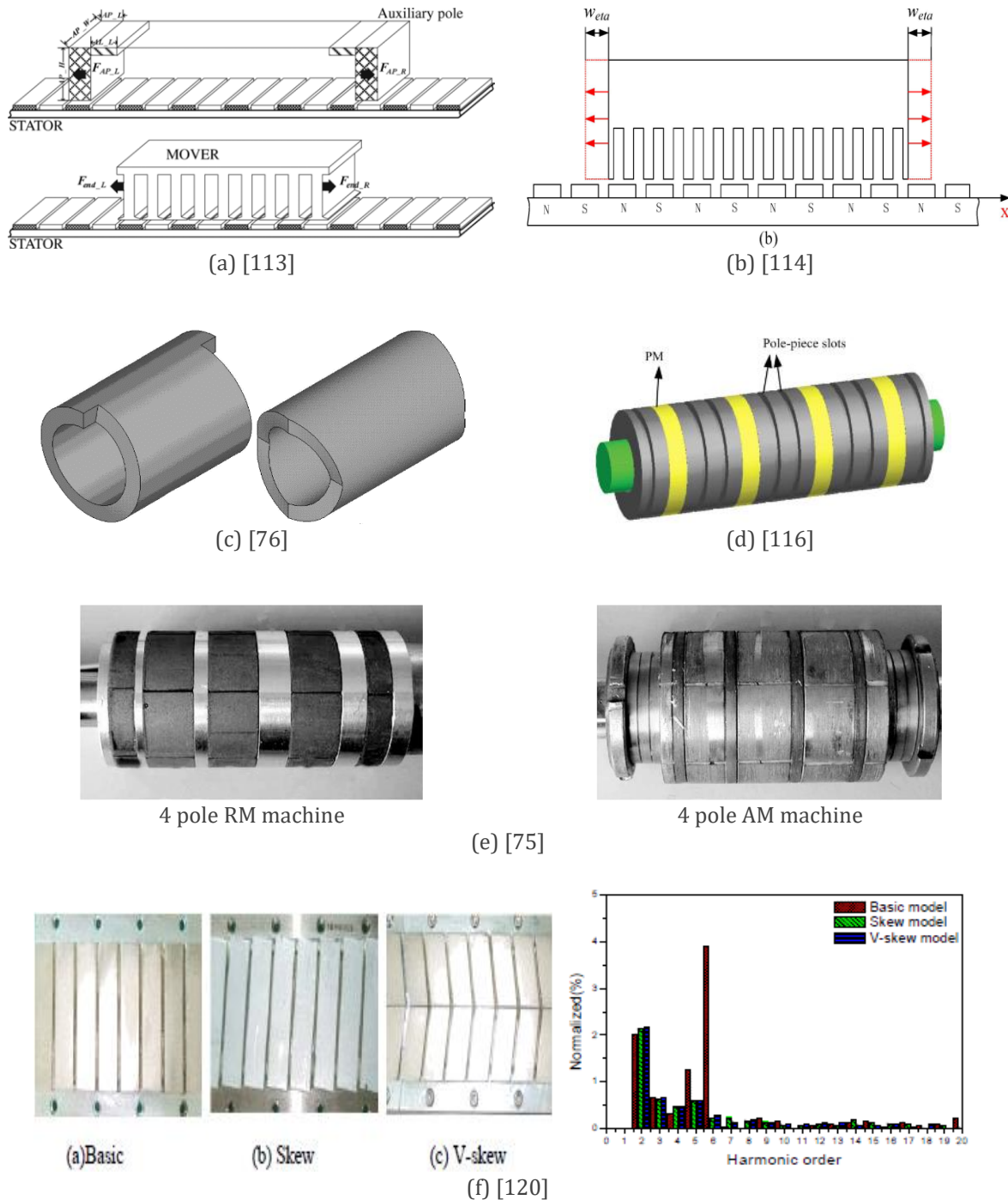


Figure 2-23: Structural modification to reduce cogging force in various linear machines

2.9 Summary

A survey has been presented regarding the principal of operation of FPE, its layout development and applications that have been introduced over the last 2-3 decades. The existing engine configurations were presented with their corresponding force balancing equation of moving bodies. A simple explanation of the necessary load operating axial displacement for each configuration has also been described using two dimensional drawings, in which it is found that this has not been well explained in the existing literature. From the author's point of view, this dimension is required to ensure compactness of system integration and selection of machine topology. The next chapter will clarify why this displacement is important and how it is interconnected to the engine's stroke and affects the resultant system physical dimensions, electrical machine dimensions and performance parameters.

Various machine topologies reported for this application have been reviewed using a new sorting method. The method used was found to be inclusive for the purpose of identifying the most suitable machine topology for this application. Using this method, the single mover, moving magnet machine was selected to design and to study its performance and suitability for the application.

Various modelling methods and assumptions have been reported, in addition to reporting the various cogging reduction techniques, with classification, applicable to a linear machine with tubular geometries to further highlight in this thesis chapters.

As the LG is coupled directly to the piston-moving rod, there is flexibility to the designer to fit the system into limited volumetric envelopes. However, removal of the rotating inertia provided by the crank means the engine is sensitive to the force ripple of the electric machine, potentially impacting the thermal and electrical system efficiencies.

Chapter 3 : Linear Joule Engine Specification

3.1 Introduction

Most heat engine technologies suffer an efficiency penalty when the power rating goes down to a couple of kilowatts. Also, the two major prime movers; internal combustion engine and combustion turbine, have inherent difficulties to be converted to use renewable sources. The Linear Joule Engine (LJE) is an alternative engine technology that can be powered with renewables and has high efficiency at the micro-scale. In most literature discussing similar systems [103] [104] [105], two parts of the system, i.e. mechanical and electrical systems, are separately designed and optimized, therefore, it is impossible to observe dynamic interaction between two systems during simulations investigating their operational performance.

It is important that a coupled model including both mechanical and electrical systems needs to be built for accurate performance prediction and optimal engine-alternator design. Therefore, this chapter presents at first the LJE, with free double acting piston set up, operational principle and characteristics. The Linear Generator (LG) model will then be derived from the designed machine model for the LJE under study, finally the combined integrated models will be investigated.

The LJE model in this chapter works in a closed loop form including thermodynamic, mechanical and control systems integrated into one systematic model to drive a LG approximated to an ideal damper. The dynamic system was constructed using Siemens LMS Imagine. Lab AMEsim and the engine operational features are outlined to conclude the constraints imposed on the design of the intended load, the linear machine.

3.2 Linear Joule Engine operation concept

Thermodynamic power cycles are the basis for the operation of heat engines, which supply most of the world's electric power and run almost all motor vehicles. The most common cycles used in Internal Combustion Engines (ICE) are the Otto cycle, which models gasoline engines and the Diesel cycle, which models diesel engines. Cycles that model external combustion engines include the Brayton, Joule-cycle, which models gas turbines.

At larger machine powers, gas turbine engines become attractive as the continuous steady flow through the combustor avoids the temperature peaks associated with reciprocating engines and can naturally have lower emissions. However, gas turbines do not scale well to low power smaller machines, primarily as leakage around the turbine becomes dominant.

To avoid this, at small engine sizes (1-10kW), it has been proposed to study the Joule cycle using reciprocating cylinders and pistons, [2, 121].

The first design of the LJE is shown in Figure 3-1(a) [107], while Figure 3-1(b) clarifies the ideal pressure – volume diagram of the applied Joule cycle. The split expansion (hot) and compression (cold) cylinders are placed at left and right hand sides of the system.

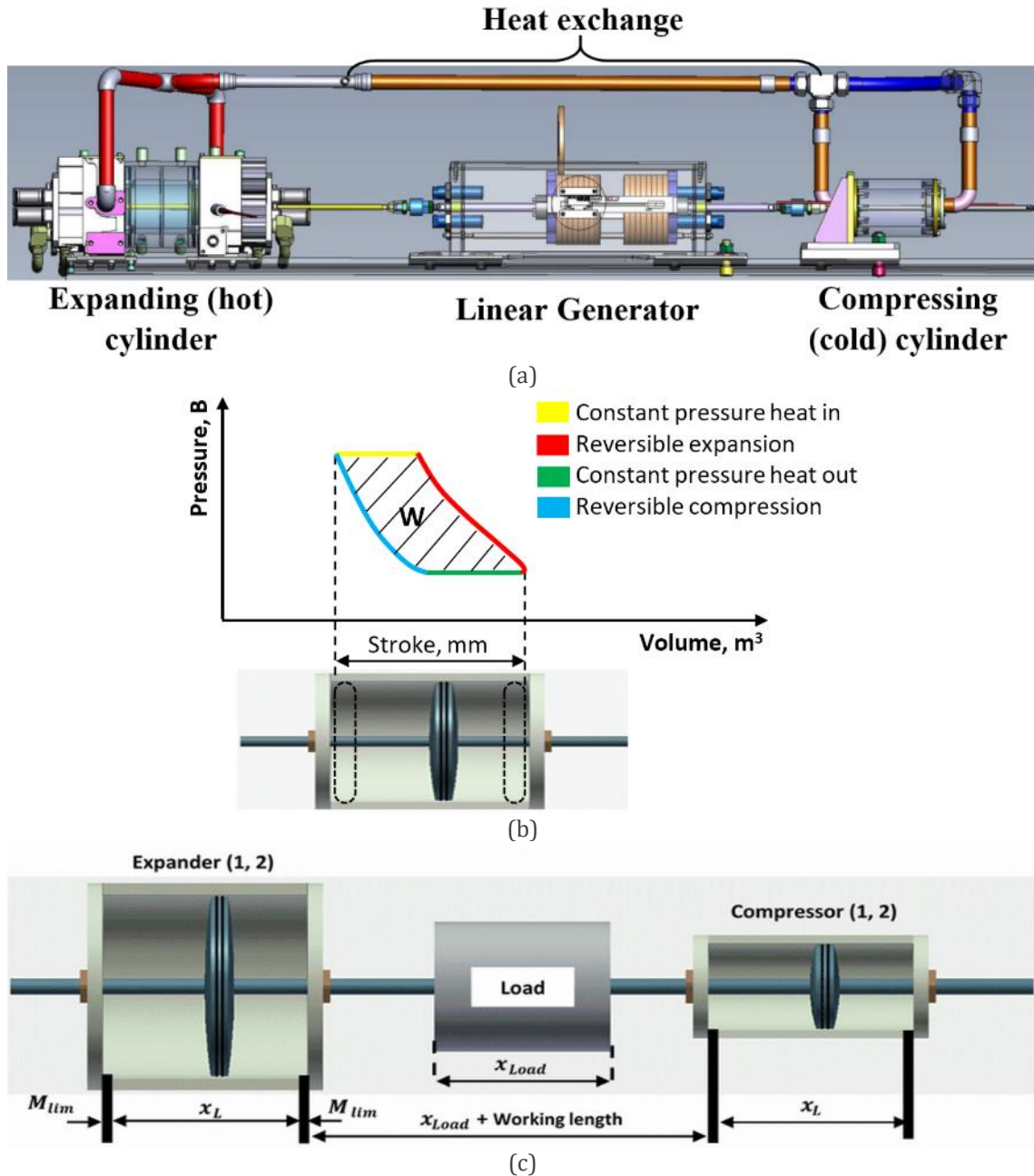


Figure 3-1: (a) First design of the Linear Joule Engine [107]; (b) PV diagram of an ideal Joule cycle; and (c) System integral length description

The LG, approximated by a simplified damper to mimic its reaction force on the engine operation, is centred with its shaft coupled directly with the rods from the compressor and the expander.

With the optimal stroke length generated from the parametrised model presented in [107], the overall length of the engine-alternator has to be at least two times the stroke length in addition to the operational length decided by the peak-to-peak amplitude of the centred linear machine and the gaps left for mechanical safety, couplings and bearings as shown in Figure 3-1(c). In an external combustion FPE, the working fluid is re-circulated in a closed system. By using heat exchangers and any source of heat as solar energy or waste heat from another process, heat is added and removed to the working fluid. Heat is added to the working fluid as it is transferred between the two separate expansion and compression cylinders of different swept volumes. This heat addition can be in the form of external combustion, solar heat, or waste heat from another process – such as in a combined heat and power plant [122], [123]. Compared to the ICE here the working fluid does not contain fuel and can now be any inert gas.

The LJE design offers several advantages compared to rotating-machinery engines. Fuel flexibility becomes possible and hence low carbon dioxide emission levels are now feasible. Power transmitted to the load(s) can be used directly without the need for load – carrying bearings, inherent in the structure of conventional rotating engines between the piston head-crankshaft. The efficiency penalty due to engine scaling is totally omitted as the engine construction becomes much simpler with its fewer moving parts giving a more compact system.

3.3 Case study engine model

A dynamic model of the engine was established using AMESim software, see Figure 3-2, and the main engine geometrical parameters have been parametrised detailing optimal performance [107]. The hot cylinder, the expander, provides the system with linear mechanical power used to drive the directly connected loads, the damper ($\overrightarrow{F_{LG1,2}}$) and the compressor ($\overrightarrow{F_{C1,2}}$) with a total moving mass (M_m , kg). The intake and expel of the working fluid – air mixture at both expander and compressor cylinders were controlled by an algorithm achieved in LabVIEW to control the open/close of the valves at both cylinders. Control timing was a measure of real-time parameters including piston displacement and frequency, working air pressure and temperature. All friction loss components within the system are accounted for by appropriate resisting forces to insure balanced dynamic steady – state operating system. The force balance equation of the reversible system is given in (3-1), where:

$$\sum F = a \cdot M_m \Rightarrow \pm \overrightarrow{F_{E1,2}} \mp \overrightarrow{F_{LG1,2}} \mp \overrightarrow{F_{C1,2}} = a \cdot M_m \quad 3-1$$

With the LG reacting force ($F_{LG1,2}$) approximated by:

$$\overrightarrow{F_{LG1,2}} = \text{Constant } (k) \cdot \text{Velocity}(v) \quad 3-2$$

In (3-1) the focus is on the damping force behaviour, and the velocity as defined in (3-2), over a mechanical cycle as it reflects the expected LG effect on the engine operation. These system performance parameters are obtainable from the LJE model shown to the left of Figure 3-2.

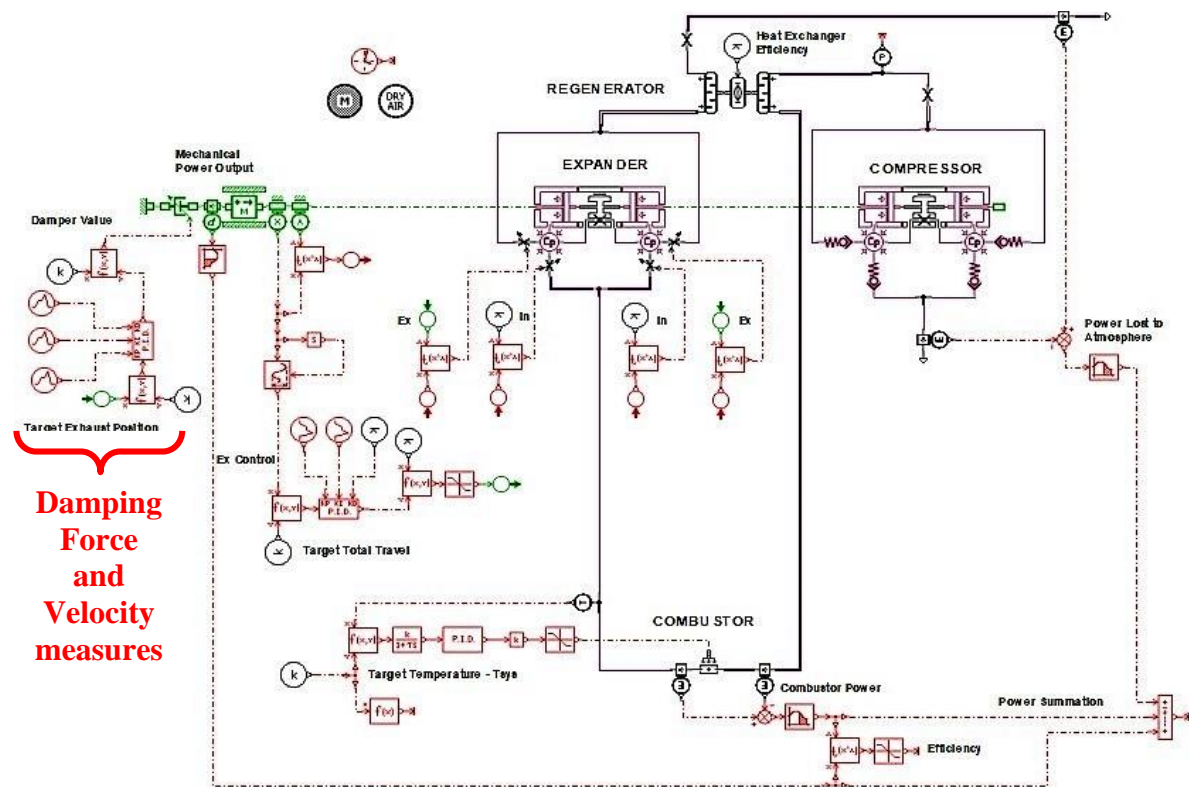


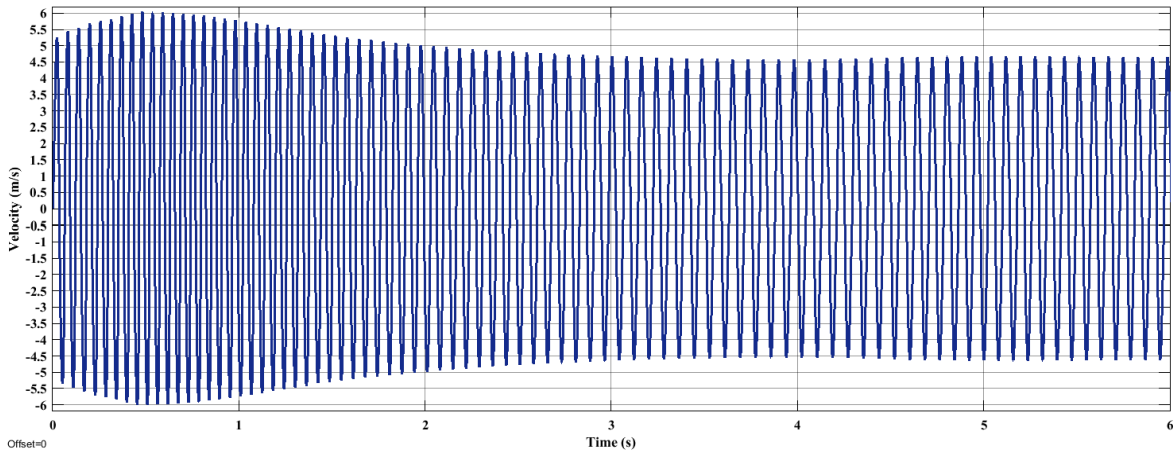
Figure 3-2: Linear Joule Engine dynamic model implementation in LMS [106]

3.4 Engine performance

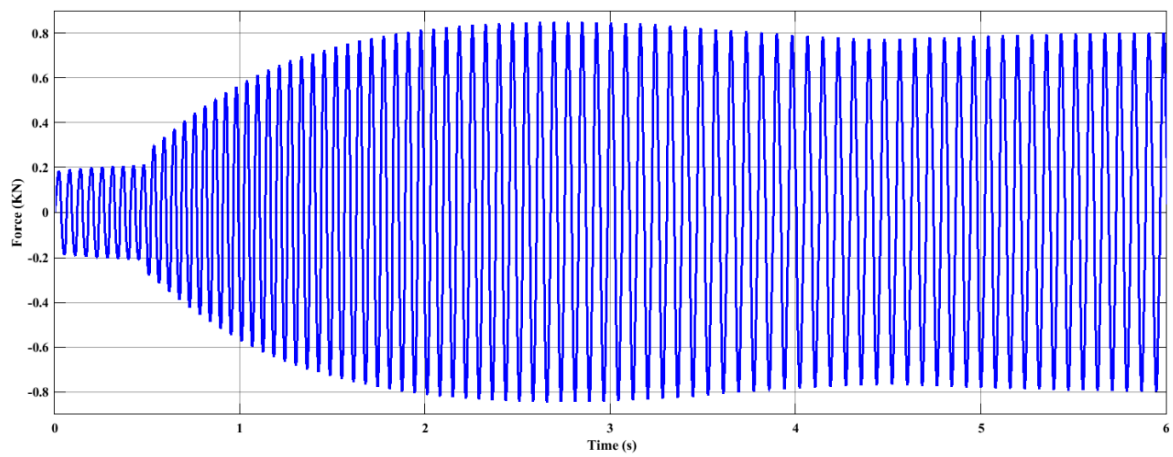
The system was simulated for a running time of (10 seconds), where it was noticed that the system reaches stable operation after a (time > 5 seconds) starting from rest. The parameters that have a direct impact on the LG design were investigated, although with a damper reaction. The variations of the system's velocity and the damping force starting from rest until reaching stable system operation are clarified in Figure 3-3.

In stable steady – state operation of the system, two mechanical cycles of the velocity and the damping force profiles are clarified in Figure 3-4, showing that the force and the velocity profiles are in phase, based on damper operation.

A trace of velocity versus piston position in the steady – state operational region is shown in Figure 3-5, and here it shows the stable operation of the system, i.e. with negligible changes in piston locus.

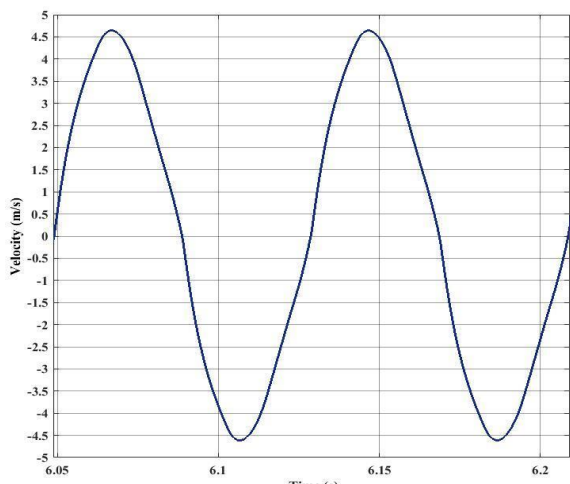


(a)

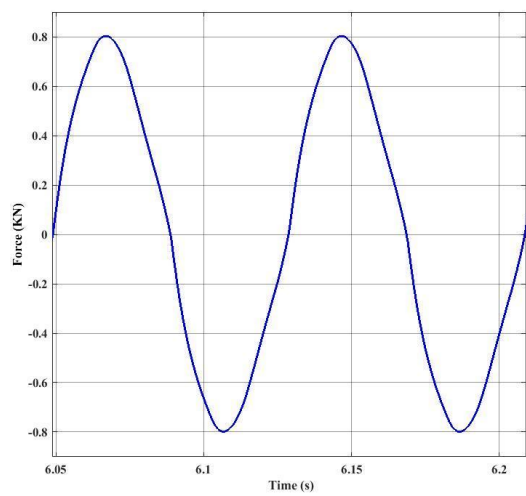


(b)

Figure 3-3: Instantaneous time variation of (a) Velocity; and (b) Damping force



(a)



(b)

Figure 3-4: Two steady-state mechanical cycles time variation of (a) Velocity; and (b) Damping force

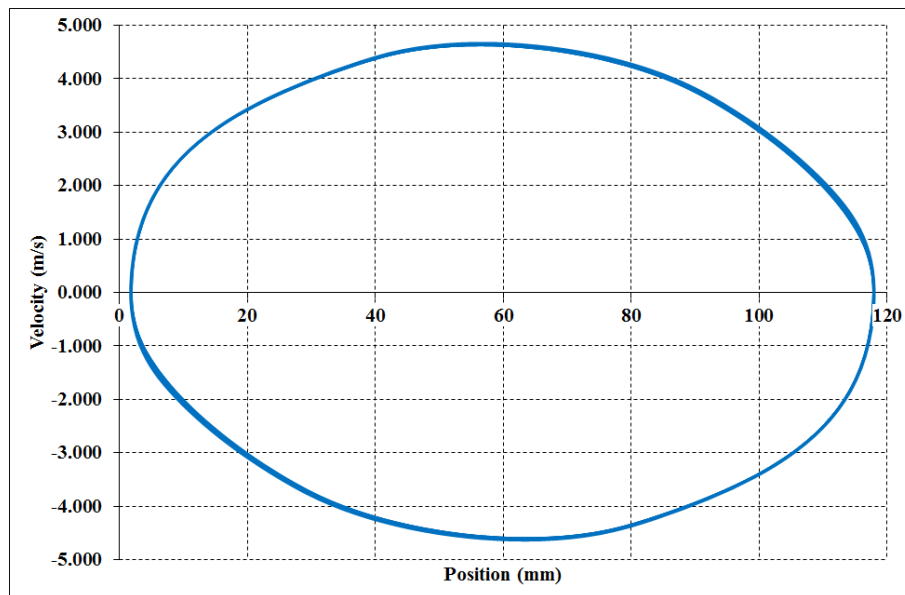


Figure 3-5: Steady-state velocity versus position trajectory ($5s < \text{time} \leq 10s$)

The variation of the piston oscillating motion with time is shown in Figure 3-6 for one mechanical cycle in the steady-state operational region. Compared to a Sine wave, just for clarification of piston motion inside the cylinder, the difference between both displacements can be assumed negligible. Hence, the piston displacement (x) may be expressed in terms of the engine's stroke amplitude as given in (3-3), where:

$$\text{Displacement } (x) = \frac{x_L}{2} + \frac{x_L}{2} \cdot \sin(\omega_m t), (m) \quad 3-3$$

Where: $\omega_m = 2\pi f_m$; and f_m is the mechanical frequency of the system.

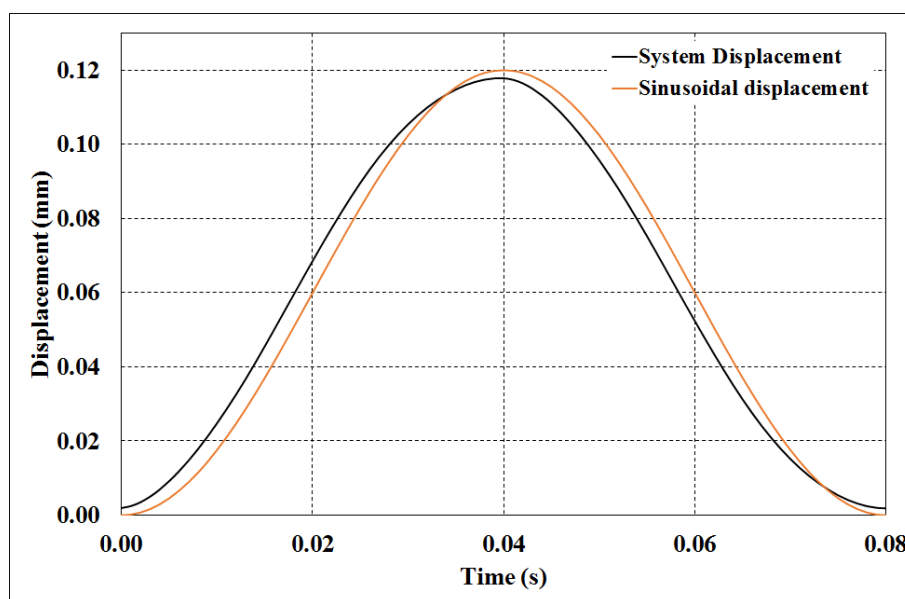


Figure 3-6: Linear Joule Engine steady-state piston displacement compared with sinusoidal displacement

From (3-4), system instantaneous velocity (v) can be obtained and expressed in terms of engine stroke and its mechanical frequency as:

$$Velocity (v) = \frac{dx}{dt} = \hat{V} \cdot \cos(\omega_m t), (m/s) \quad 3-4$$

Where: \hat{V} is the peak velocity and is given as:

$$\hat{V} = \pi \cdot f_m \cdot x_L, (m/s) \quad 3-5$$

3.5 Machine design constraints

The linear machine connected collinearly to the engine oscillating piston rod must interact effectively under the steady – state operating condition. Therefore, the steady - state operational features of the LJE are important. Additionally, the optimal dimensional parameters of the engine are also important for system compactness. Thus, the constraints taken forward to design the linear electric generator, listed in Table 3-1, are a mix of operational (changing) and geometrical (fixed) parameters.

Table 3-1: Linear Joule Engine optimal dimensions and steady – state operational characteristics

Parameter (symbol/period)	Value (unit)	
Expander cylinder outer diameter, (fixed)	200 (mm)	
Stroke amplitude (x_L)	Exact, (fixed)	120 (mm)
	Achieved	116 (mm)
Moving mass (M_m)	8 (kg)	
Peak velocity, (changing)	4.8 (m/s)	
Peak force ($\overrightarrow{F_{LG1,2}}$), (changing)	800 (N)	
Frequency (f_m : start \rightarrow steady – state), (changing)	20 \rightarrow 12.5 (Hz)	

The outer diameter of the large cylinder; the expander, is taken as the geometrical limit perpendicular to system motion imposed on the design of the linear machine. The exact stroke amplitude is taken as a constraint, although it can be noticed that there is a small difference not exceeding 3.35% between the dynamically achieved and the exact stroke decided mechanically, excluding the mechanical limits at both cylinder ends. This difference is due to the combined effects of all interacting engine – load forces, the dead times assumed in controlling the opening/closing of the intake/exhaust valves as well as the total moving mass corresponds to the sum of all moving masses including that of the connecting rod.

As the difference is very small and occurs at both stroke ends where the velocity is almost zero, i.e. load may be assumed inactive, it can be neglected leaving the exact stroke to be used as a constraint.

In order to achieve a full use of the operational stroke, it is preferable in practice to set a ratio between machine active length and the stroke amplitude of the driving engine, and look for the feasible bore dimension.

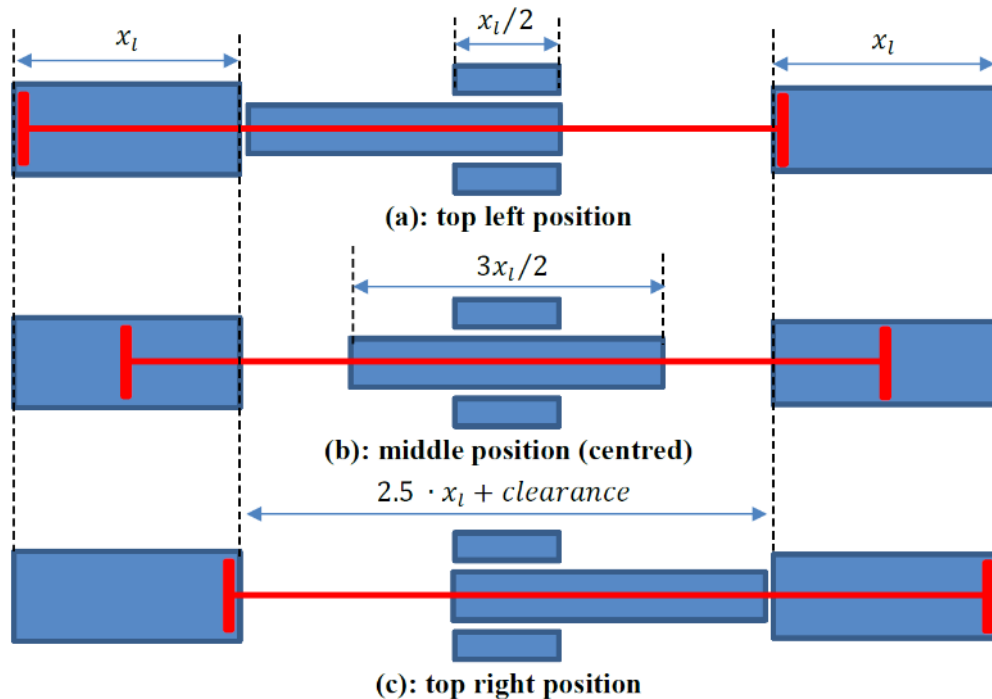


Figure 3-7: Half cycle piston motion with a ratio of (1/2 : 1) between active machine length to stroke amplitude

The effect of setting this ratio has consequences on the percentage utilisation of both stator and translator parts, and the overall system length. If a machine topology is designed to have a (1/2:1) ratio as shown in Figure 3-7, its translator needs to be elongated to maintain the machine full active area during an engine stroke, as illustrated in Figure 3-7. In this short stator machine structure, the required translator elongation must be at least three times that of the stator in order to ensure a 100% utilization of stator parts compared to the 33.33% utilisation of translator parts. This translator's elongation necessity is one of the major factors affecting overall system integral performance due to the factorised moving mass [2, 107]. The displacement required between the two cylinders in this case needs to be five times the active length of the machine, or two and a half times that of the stroke amplitude. A further impact of short ratios (ratio < 1:1) is the larger bore diameter with consequent larger machine diameter, besides that the rate of change of magnetic flux would be higher.

On the other hand, a ratio larger than unity would result in a thinner machine with a lower radial space utilisation and lower rate of change of magnetic flux. In this thesis this ratio is set to be a (1:1) which will impose a translator elongation of twice the machine active length and achieve 50% utilisation of translator parts along the full engine operating mechanical cycle.

During steady-state system operation, the velocity profile reflects the behaviour of the moving mass and the interconnected balanced forces. This profile has the effect of shaping the per phase back electromagnetic force (EMF) and hence the delivered electrical power of the generator. In all LMs configurations as compared to their rotating counterparts, the peak velocity is important and the basis of Faraday's law of electromagnetic induction is applicable, i.e. an EMF is induced per phase (E_{ph}) due to the continuous back and forth motion of the translator and the corresponding interaction between coils and flux lines. This is expressed as:

$$E_{ph} = -N \frac{d\Phi}{dt}, \quad V/ph \quad 3-6$$

Where:

Φ : Flux linkage that varies with translator position, Wb

N : number of turns per phase

Due to the continuous oscillating motion, the useful air gap flux of amplitude (Φ_m, Wb) varies with respect to phase windings, and this variation may be assumed sinusoidal due the translator displacement [44], and hence may expressed as:

$$\Phi = \Phi_m \cdot \sin(x), \quad Wb \quad 3-7$$

Using (3-4) - (3-7) with substitution and rearrangement yields:

$$E_{ph}F = -N \frac{d\Phi}{dx} \frac{dx}{dt} = -\hat{E} \cos(x) \cos(\omega_m t) \quad V/ph \quad 3-8$$

Where:

$\hat{E} = N\Phi_m\hat{V}$, is the amplitude of induced EMF

Equation (3-8) indicates that the induced E_{ph} varies as the velocity varies with translator displacement, i.e. with mechanical frequency (f_m), and with a constant amplitude (\hat{E}) which is a peak velocity dependant, and this clarifies why the peak operational velocity is important and is therefore selected.

The steady – state peak force defines the maximum force level that the engine is able to drive prior to stalling. It is used to decide the active area of the electric machine based on the desired cooling system and the maximum force per active machine area (σ_s). Inspecting the thrust density comparison between LIM and Linear Synchronous Machines (LSM) with various cooling systems, shown in Figure 3-8, it can be seen that the specific thrust of linear machines with natural cooling and thrust force of up to (4250 N), the region highlighted in red in Figure 3-8, fall in the range $\approx (6 \times 10^3 - 26 \times 10^3) \text{ N/m}^2$ [45, 124-126]. Hence, for a given design force (F_{design}), an assumed cooling system and typical thrust density, the active area of the potential machine can be calculated as given in (3-9):

$$\text{Active machine area} = \frac{F_{design}}{\sigma_s}, m^2 \quad 3-9$$

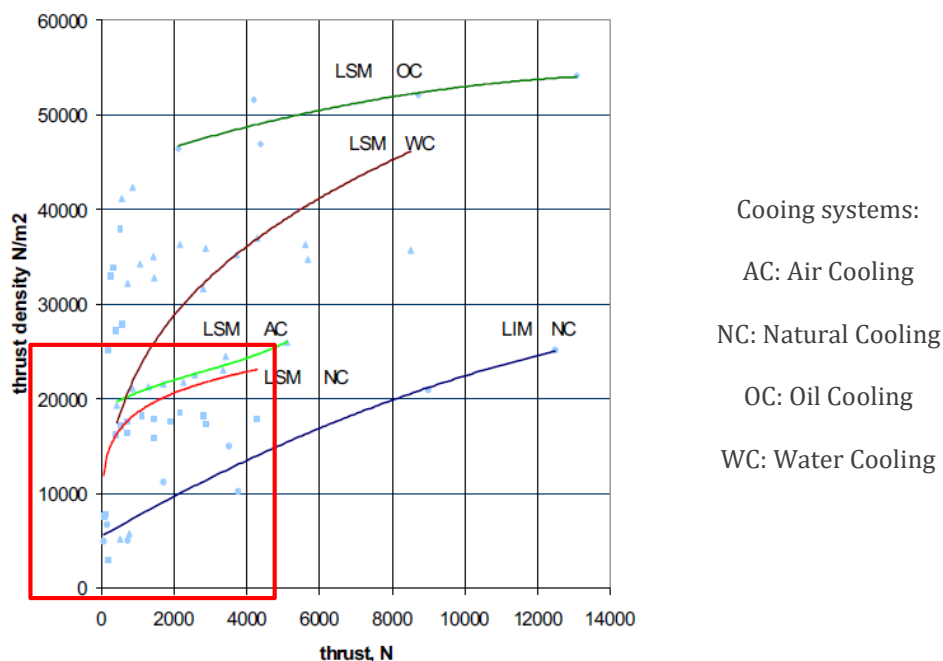


Figure 3-8: Thrust density of single – sided LIMs and LSMs at different cooling systems [126]

For tubular geometry, the active machine surface area defines the effective area required and maintained constant during system operation over the full stroke range, and at the same time it sets the relative relationship between the machine active physical dimensions, i.e. its active length (L_{active}) and the active bore diameter (D_{active}) and is shown in Figure 3-9.

The last design constraint is the mechanical frequency (f_m), the only parameter that has a variation range from the start mode to the steady – state region mode. Design frequency selection needs a discussion, bearing in mind that the damping force represents a LG operating at rated load, and is velocity dependant.

Since the LG is directly connected to the driving engine rod, its electrical frequency (f_e) varies linearly as the mechanical frequency f_m , and vice versa. Therefore, higher system operational speeds, frequency, is a result due to a partially loaded LG. As thus, to achieve optimal system operation even at part loads, the start frequency is taken as the maximum design frequency.

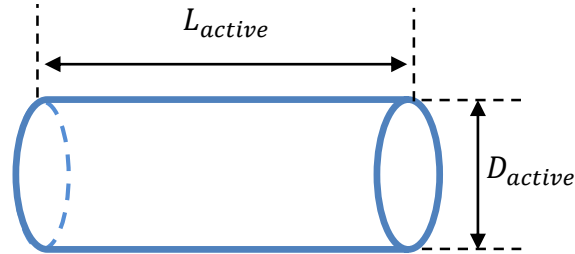


Figure 3-9: Physical active dimensions of any tubular LM topology

3.6 Summary

This chapter has presented the principle of operation of the Linear Joule Engine using free, double-acting piston configuration. Engine performance parameters and operation specification have been demonstrated assuming the Linear Generator acting as a simplified damper.

The tabulated parameters clarifying the constraints imposed on the design of the potential linear machine, operating in the generating mode, have been presented and their effects on the machine design have also been illustrated with discussions.

Chapter 4 : Selected Machine Topology Design

4.1 Introduction

This chapter describes the design methodology used to design a Longitudinal Flux Moving Magnet Machine (LF-MMM) of tubular geometry for use with the Linear Joule Engine (LJE) of the specification detailed in Chapter 3, Table 3-1, to supply a pure resistive loading. Three alternative MMMs are designed throughout manual optimisation to react the same driving force. All machines have similar stator and translator structures and material to study the effect of feasible key design variables on the design. Translator structure with feasible magnet orientation has also been considered as one of the key design variables in order to highlight its effect on the resulting machine parts weights, overall performance and best magnet utilisation. All machines were modelled using 2D FEA with ignored end effects, and by using a transient solution, the results were obtained and the resultant machines achieving design objectives have been compared and conclusions outlined.

4.2 Slot / Pole number combination

In LF-MMM and along the active length of the machine, the combination of stator slots (N_s) and translator poles (N_p) encompassed by the active length are the only effective parts in the electromagnetic energy conversion process. Thus, the active length, the slot pitch (τ_s) and the pole pitch (τ_p), with (q) representing number of slots per pole per phase, are simply related to each other as:

$$L_{active} = q \cdot N_s \cdot \tau_s = N_p \cdot \tau_p \quad 4-1$$

For a basic three phase machine design configuration with $q = 1$ and a minimum combination of three stator slots and two translator poles, see Figure 4-1, the slot pitch (θ_{τ_s}) satisfying three phase requirement, and that of the pole pitch (θ_{τ_p}) satisfying 180 electrical degrees between adjacent translator poles may be defined as:

$$\begin{aligned} \theta_{\tau_s} &= k\pi \pm \frac{2\pi}{3} \\ \theta_{\tau_p} &= k\pi \pm \pi \end{aligned} \quad 4-2$$

By making use of (4-1) and (4-2), and with $k = 1, 2, \dots$, it can be shown that:

$$N_s = N_p \frac{3(k \pm 1)}{(3k \pm 2)} \quad 4-3$$

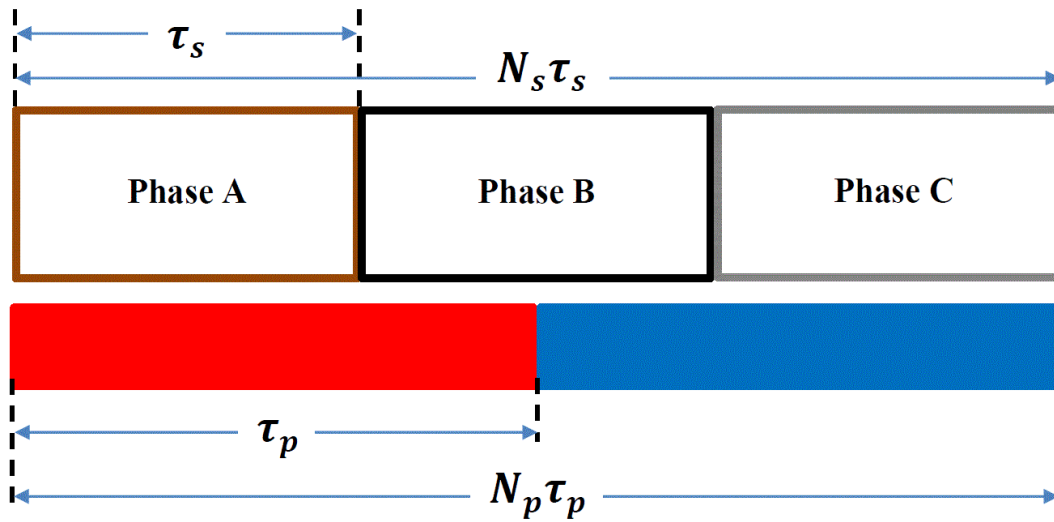


Figure 4-1: Three – Phase linear machine of three stator slots and two translator poles

It must be noted that for the viability of the above relationship, (N_s) must be divisible by three for any given pole number (N_p), and thus the term $\left(\frac{3(k \pm 1)}{3k \pm 2}\right)$ must be a positive integer [100]. Feasible slot-pole number combinations that achieve three phase MMM machine configuration of up to 15 slots are listed in Table 4-1, although a higher slot number is also achievable, it is deduced in here for up to 15 slots.

Table 4-1: Feasible slot/pole combination

Slots (N_s)	Pole number (N_p)
3	2, 4
6	4, 5, 7, 8, 11
9	4, 6, 8, 10, 12, 14
12	2, 7, 8, 10, 11, 13, 14
15	10, 14

4.3 Machine topology

The machine geometry adopted in this study is of tubular geometry due to symmetry offering a theoretical total elimination to the forces perpendicular to the axis of motion. The aim of the design is to investigate the effect of PM orientation on the machine compactness, magnet utilisation for a specific design force and on the overall machine performance.

The design of three machine topologies is presented in here for ($N_s = 6$, and $N_p = 7$) combination, although other combinations can satisfy the design objectives. Figure 4-2 shows a schematic of general machine topology.

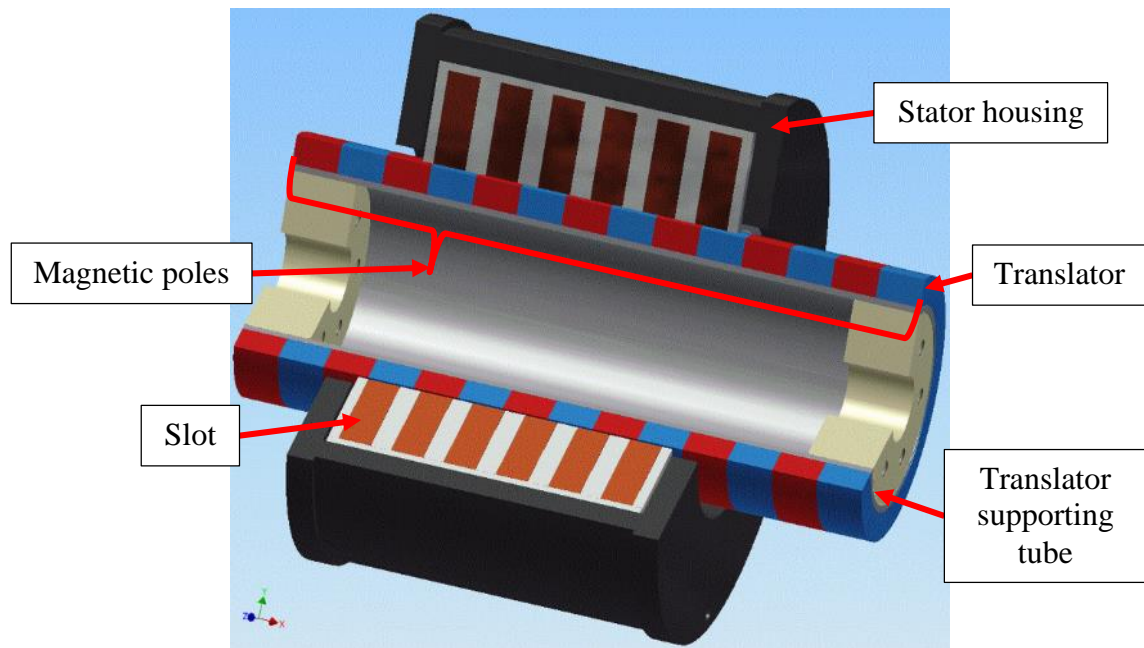


Figure 4-2: 3D quarter cut view clarifying the general investigated topology parts

All machine models are assumed to be naturally cooled and the geometrical constraints imposed by the drive engine are considered as follows:

- Firstly, and as stated before, all models have a (1:1) ratio of active length to engine stroke.
- Secondly, design objectives were set to satisfy the design force as a first objective, then investigate system compactness as the second objective.
- Thirdly, when investigating the effect of stator outer diameter on the machine resultant force capability for a specified bore diameter, the optimal balancing between magnetic and electric loading was taken into consideration [10, 55]. Bearing in mind that the increase or selection of stator outer diameter is kept within certain limits and accounting for the machine housing thickness as clarified in Figure 4-2.

4.4 Design variables and PM orientation

Initial machine dimensional parameters are designed based on classic design theory and elaborating on specific thrust criteria [44, 125, 126]. A longitudinal cut view of the unified machine base model is shown in Figure 4-3, clarifying common key design variables. It also shows that stator slots are occupied by three – phase windings of modular connection which gives higher force capability compared with conventional windings [100, 127, 128].

According to the PM orientation, the three feasible translator magnet arrangements are Axially Magnetised (AM), Radially Magnetised (RM) and Quasi Halbach Magnetised (QHM) as shown in Figure 4-4(a-c) respectively. To achieve a specified force capability, there must be an electrical load to dump the electrical power generated by the machine. Therefore, a simple star Resistive Loading (RL) is connected to the star connection of stator winding as shown in Figure 4-4(d). Each topology has five optimisable variables, except the RM machine topology, where a flux return path is compulsory in the translator core, thus a sixth parameter is added and termed (TCBH) in Figure 4-3.

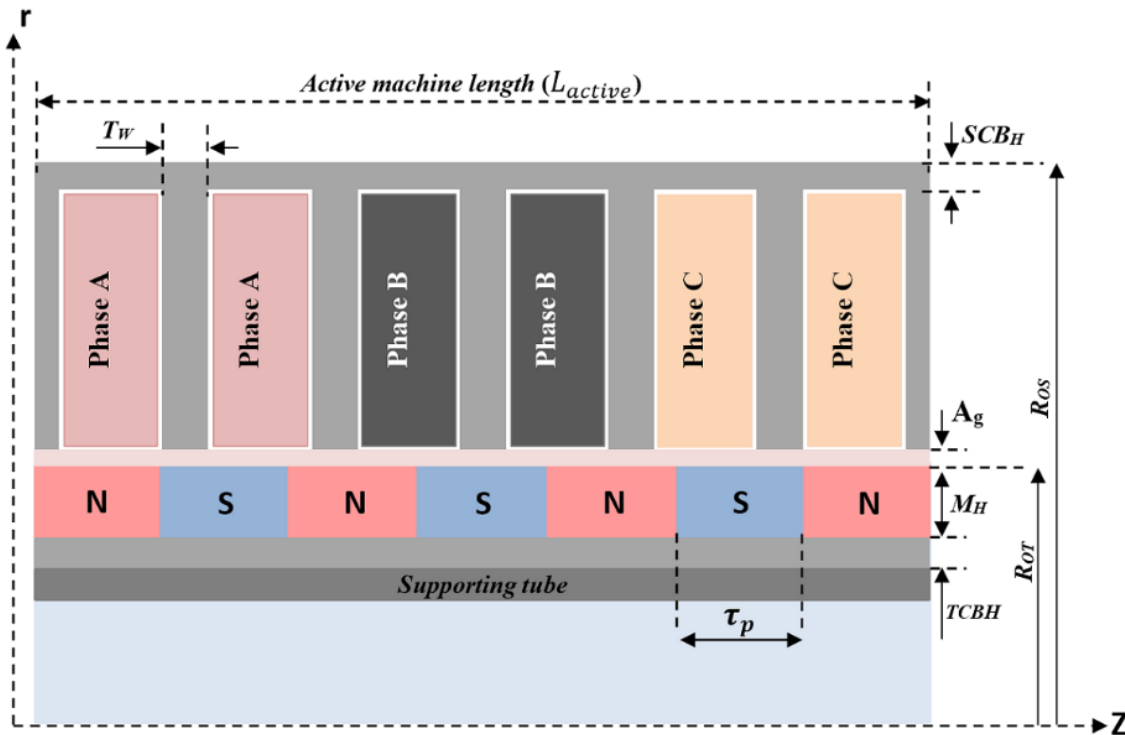


Figure 4-3: Longitudinal view illustrating optimisable parameters in machine topology

In all machine models, stator magnetic circuit composed of teeth and stator core back is modelled by non – oriented silicon steel material graded as M-15 26 Ga that starts to saturate at flux density of 1.6 T, which is also used in translator magnetic circuit when required. The air gap length (A_g) is taken to be (1mm) complying with perceived manufacturing tolerance. The translator is composed of a robust supporting tube (sleeve), surface mounted PMs of grade 5– Samarium Cobalt and/or iron pole segments if required.

4.5 Optimisation methodology and results

All machine topologies were optimised using the transient solution in 2D FEA software. The same speed was used in obtaining the solutions of the three alternative models while supplying the same resistive balanced load.

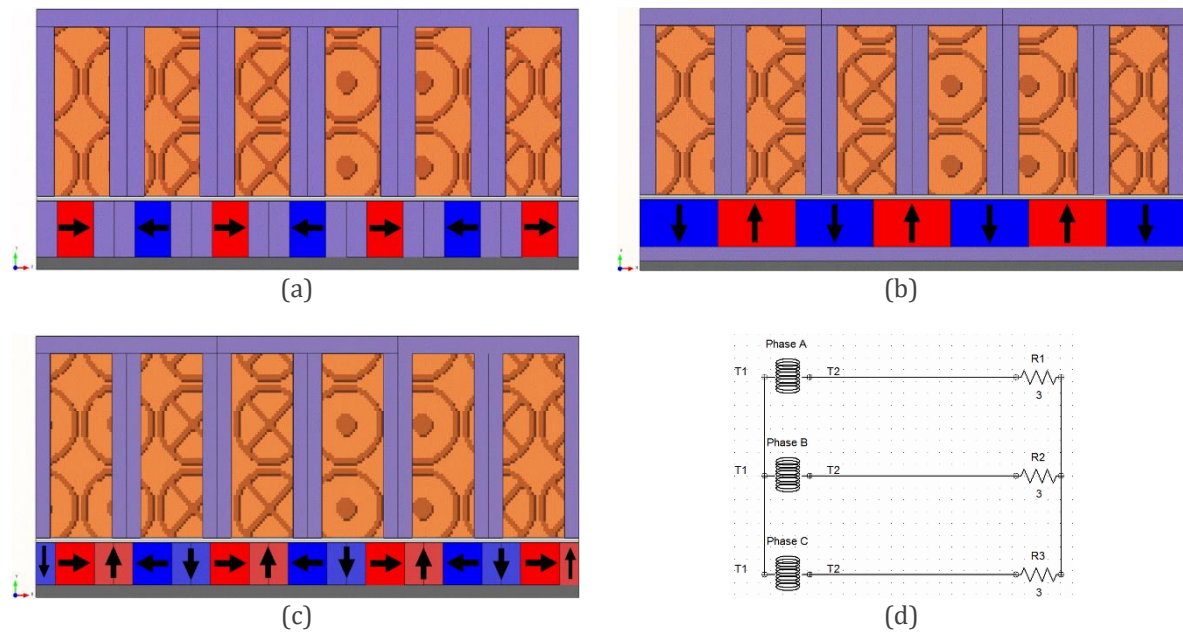


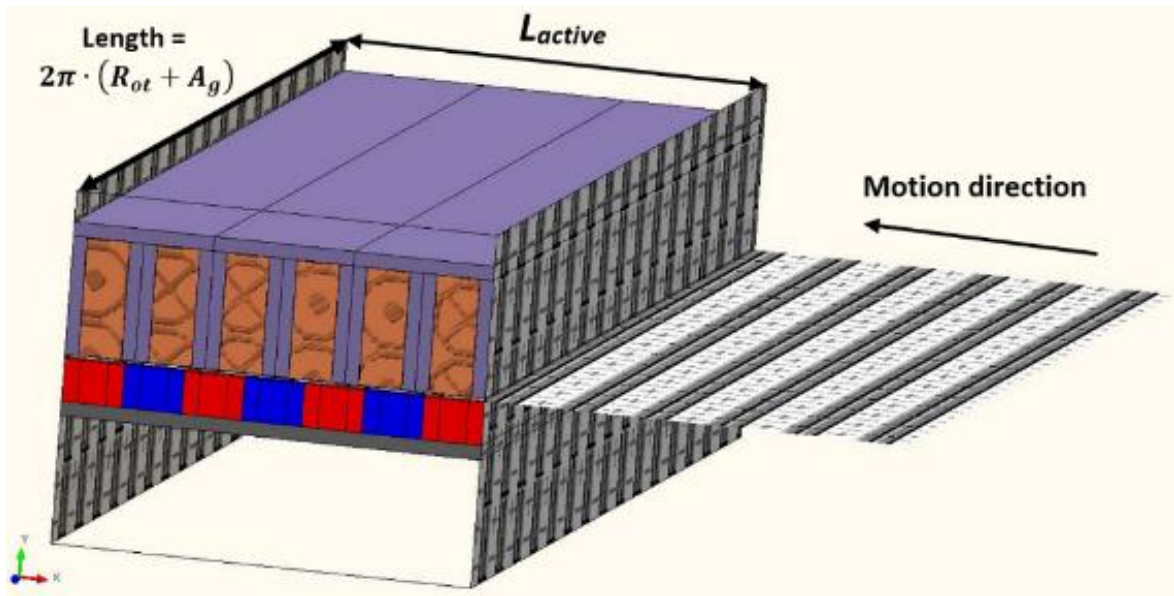
Figure 4-4: Investigated machine topologies and connected load (a): Axially Magnetised magnets; (b) Radially Magnetised magnets; (c) Quasi-Halbach Magnets arrangement, and (d) Resistive Loading

4.5.1 Details of 2D FEA model

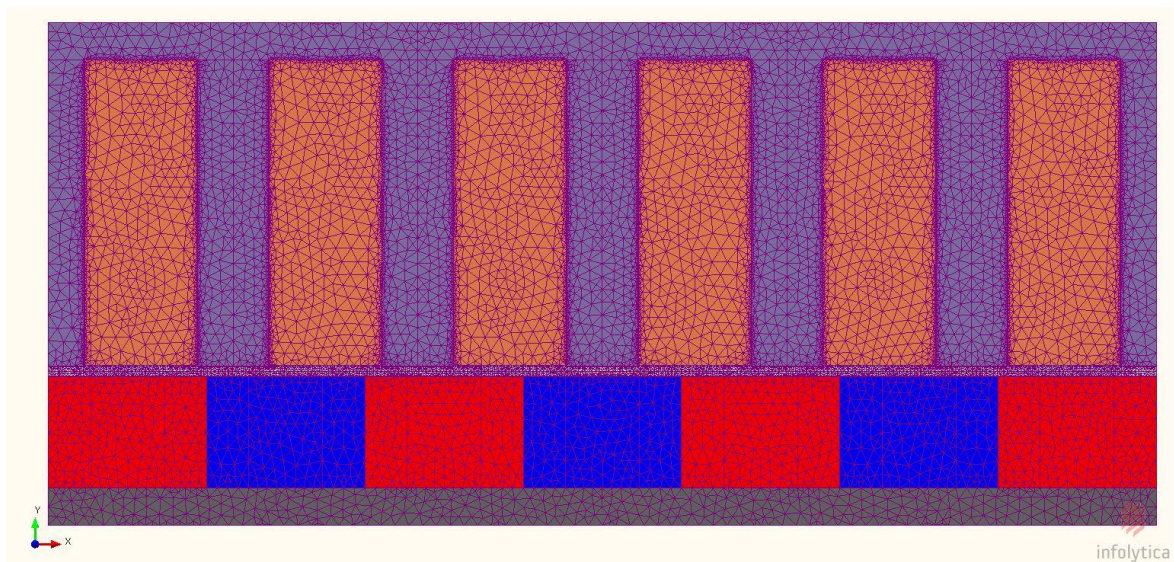
A general 2D FEA machine model is shown in Figure 4-5(a), and the mesh size is shown in Figure 4-5(b). The full machine active length was modelled after cutting the machine longitudinally and extruding it along the full air gap circumferential length. Since the machine has an odd pole number, odd periodic boundary condition was applied to the outer surfaces of the air box enclosing the translator components in addition to stator side faces, which is the case corresponding to ignoring stator end effects. The transient solution was obtained by moving the translator components in the assigned direction shown in Figure 4-5(a) in time steps that achieve the peak driving engine speed (4.8 m/s). The full 7 pole distance was solved transiently while using a 0.25mm mesh size in the remesh regions, and a 2.0mm in the other model regions to obtain the results such as the electromagnetic force, EMF generated, losses, etc.

4.5.2 Methodology

A manual optimisation method using transient solution of 2D FEA models is carried out to optimise, individually, key design variables of each topology. It is implemented by automating Microsoft Excel and the FEA modelling software via Visual Basic Scripting (VBS), as clarified in the framework shown in Figure 4-6. Optimisation addressed towards achieving the design objectives bearing in mind that design variables are entirely coupled by the electromagnetic loadings of the machine.



(a)



(b)

Figure 4-5: (a) 2D FEA general machine model used in optimisation; (b) Mesh size of the general model

Therefore, optimisation started with the variables that influence all objectives at the beginning, then considering remaining variables while keeping the optimised variable unchanged. Individual investigation of the variation of each variable is used to enhance the understanding of how the machine force capability is affected by these changes for each topology. The ranges of different design variables variation are listed in Table 4-2. The results are displayed in per unit (pu) scale while the machine is running at a peak driving engine speed of (4.8 m/s) and at a room temperature of (20°C), assuming a perfect thermal isolation protecting the PM from the heat transferred from the running engine. However, a practical temperature measure could be used to account for the heat in the area surrounding the machine.

For a resulting slot area (A_w , m²), a fill factor in the range ($0.5 < k_f < 0.7$) and a conductor area (A_c , m²), the number of turns per slot (N_{c_s}) is obtainable using the formula:

$$N_{c_s} = \frac{A_w \cdot k_f}{A_c} \quad 4-4$$

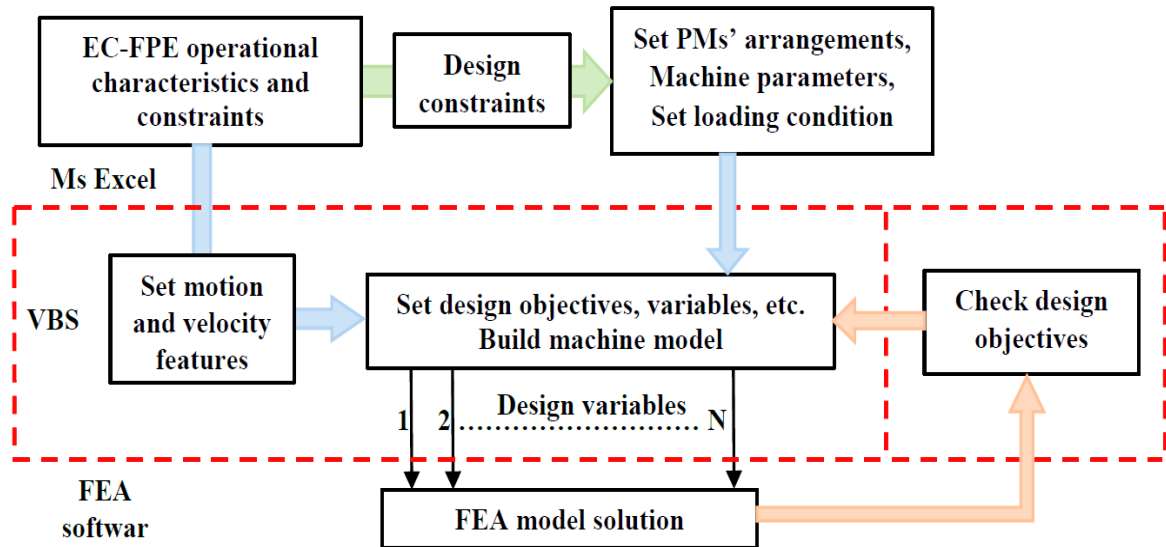


Figure 4-6: Optimisation methodology framework

Table 4-2: Design variables variance ranges

Design variable, unit	PM arrangement		
	AM	RM	QHM
Stator diameter ($2R_{Os}$), mm		175 - 192	
PM height (M_H), mm		7 - 12	
Axial PM width (M_W), mm	7 - 12	---	10.14 - 6.64
Radial PM width (M_W), mm	---	8.14 - 17.14	7 - 10.5
Tooth width (T_W), mm		3.5 - 9.8	
Stator core back height (SCBH), mm		2 - 6	
Translator core back height (TCBH), mm	---	2 - 5	---

4.5.3 Stator outer diameter

Figure 4-7 clarifies the effect of stator outer diameter increase on the machine force. It shows that force capability increases with increasing stator diameter notably in QHM topology compared with other topologies.

Peak force capability is obtained with specific diameter figures in all machines, where further increments have no, or negative impact on the resulting electromagnetic force. Outer diameter is thus selected based on maximum force.

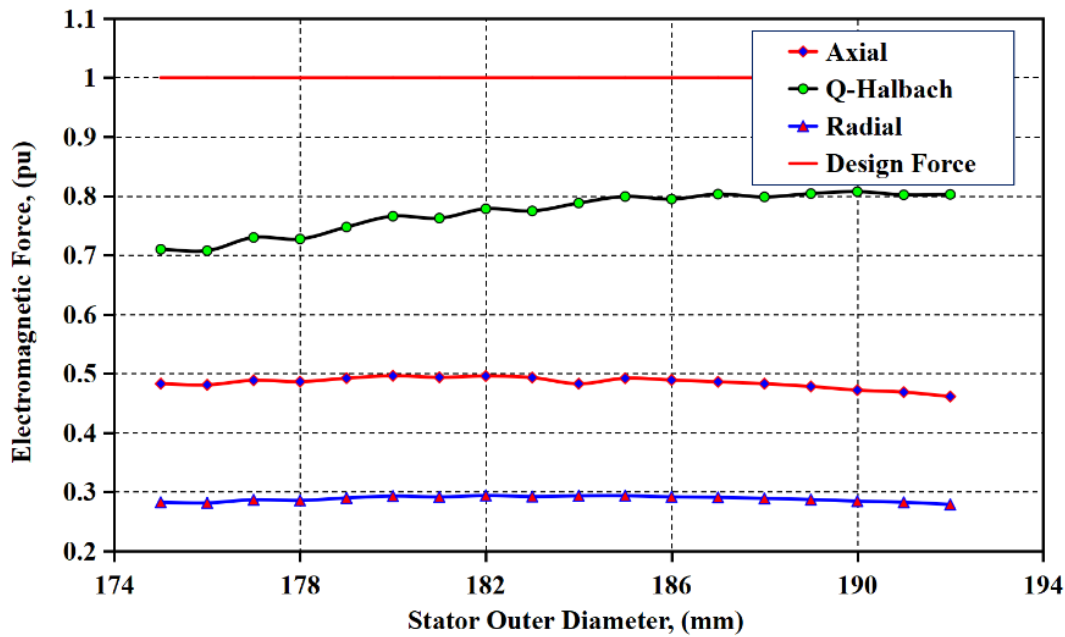


Figure 4-7: Variation of electromagnetic force with stator outer diameter (2ROS)

4.5.4 PM Dimensions

Figure 4-8 (a) illustrates the effect of increasing PM height on the resulting force, where it can be seen that the force increases almost linearly for both AM and QHM machines, whereas in the RM machine this increase is negligible. This indicates that as the PM dimension increment is perpendicular to its orientation, its magnetic energy effect on the force production does not change significantly. This can be seen in the RM force results, where an increase of (5 mm) in magnets height results in only (4%) increase in the force production and fixed translator core back. Figure 4-8 (b) shows the variation of electromagnetic force with dimensional ratio (τ_m/τ_p). Since all translators have the same fixed pole pitch, in order to investigate this dimensional change in the both the AM and QHM machines, the axially magnetised magnet width is changed while the width of the iron part of the pole is a result. In the RM machine topology, the width of the radially magnetised PM is changed with respect to the fixed pole pitch, which introduces air gaps in the pole sides.

Both the AM and the QHM machine models show an increase in force capability until saturation starts to take place in each machine magnetic circuit. QHM machine force capability shows an increase, peak at optimal ratio of ($\tau_m/\tau_p = 0.5$) and then declining with further ratio increase.

The results also clarify that force capability of RM is not feasible even with magnets spanning the full pole pitch with different radial dimension. Tooth width, Stator and Translator core backs The results of changing the tooth width (T_w), stator core back height (SCBH) in all models, and the translator core back in the RM are displayed as ratios with respect to slot pitch (τ_s).

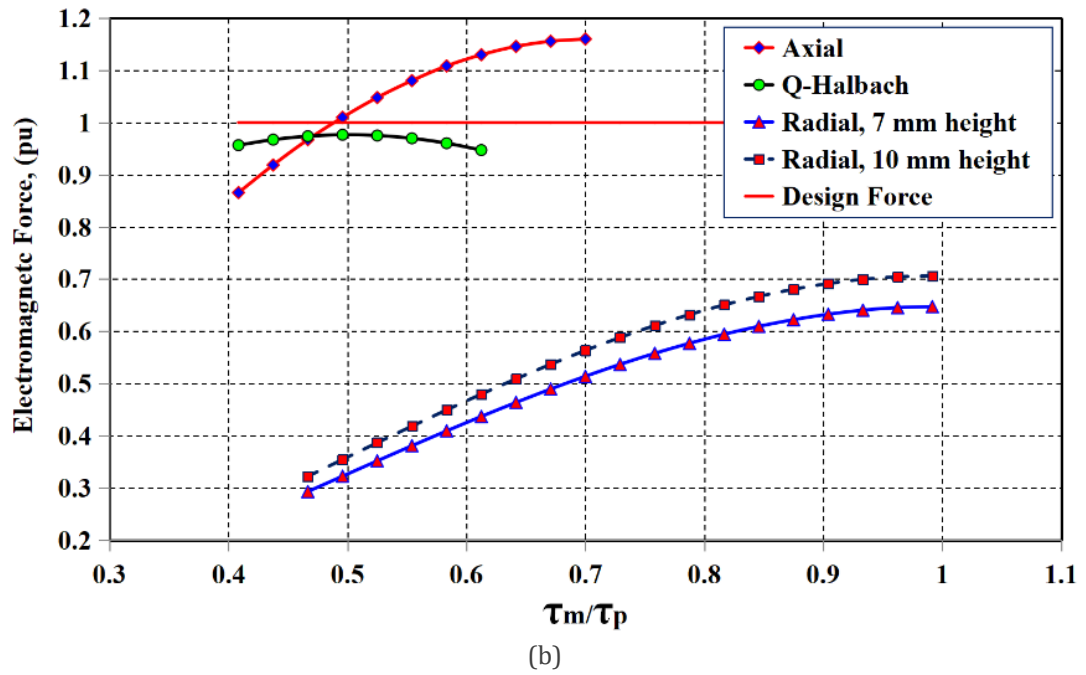
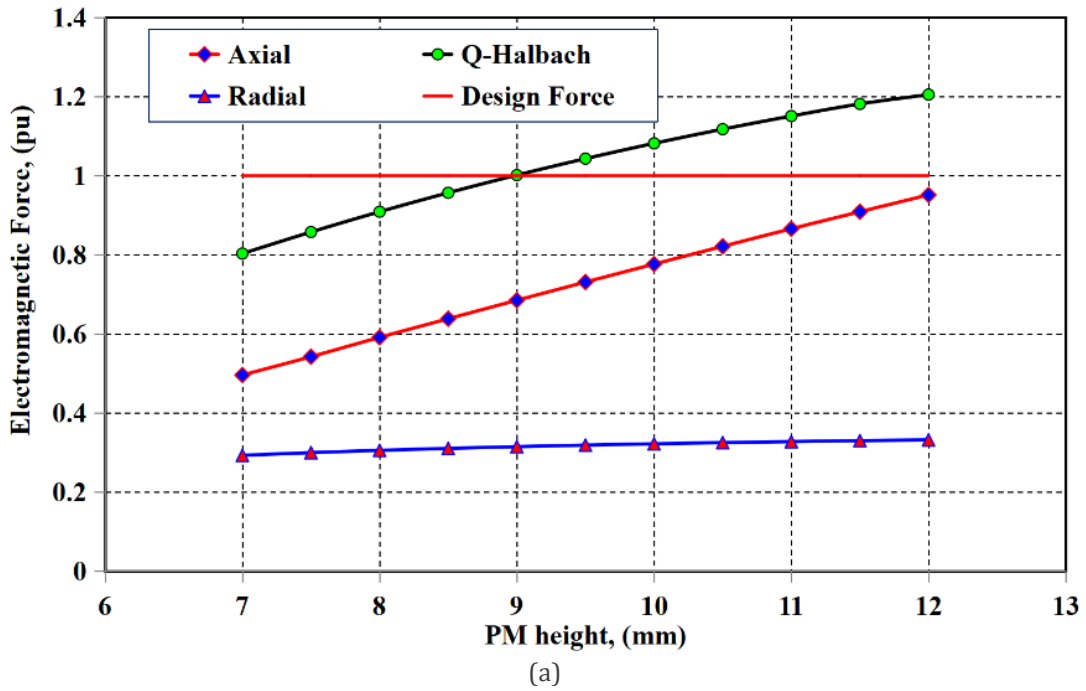
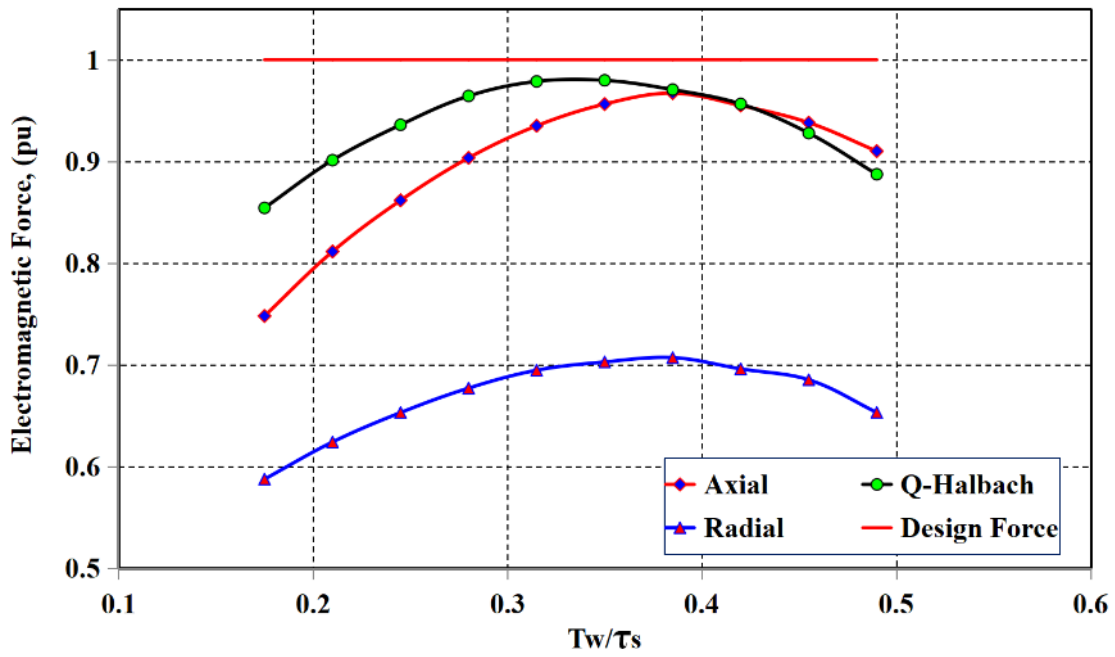
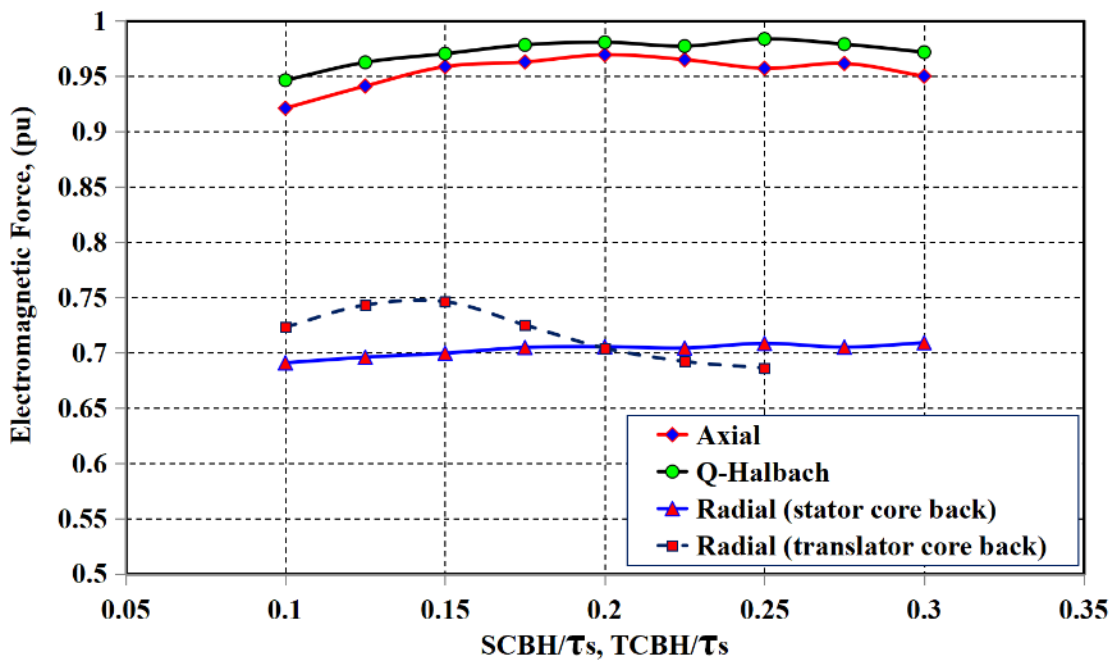


Figure 4-8: Variation of electromagnetic force with PM dimensions (a) PM height effect; (b) PM width to pole ratio (τ_m/τ_p) effect

Figure 4-9 (a) shows the variation of electromagnetic force with the dimensional ratio (T_w/τ_s), where it can be seen for each machine model there exists an optimal ratio for this dimensional ratio variation that corresponds to peak force reflecting the balanced interacting electromagnetic loadings in each topology. This fact is also true in other dimensional ratios variation and their effects on force capability as shown in Figure 4-9 (b).



(a)



(b)

Figure 4-9: Variation of electromagnetic force with dimensional ratios (a) Tooth width effect (TW); (b) Stator and translator core backs effect (SCBH, TCBH)

Figure 4-10 shows the variation of the rated load force profile of the optimal selected machine topologies, while Figure 4-11 shows the flux distribution in these topologies at the rated load. It can be seen from Figure 4-10 that the peak obtainable force in the RM machine configuration does not exceed (0.75 design force) limited by saturation in the translator core back as depicted in Figure 4-11 (c).

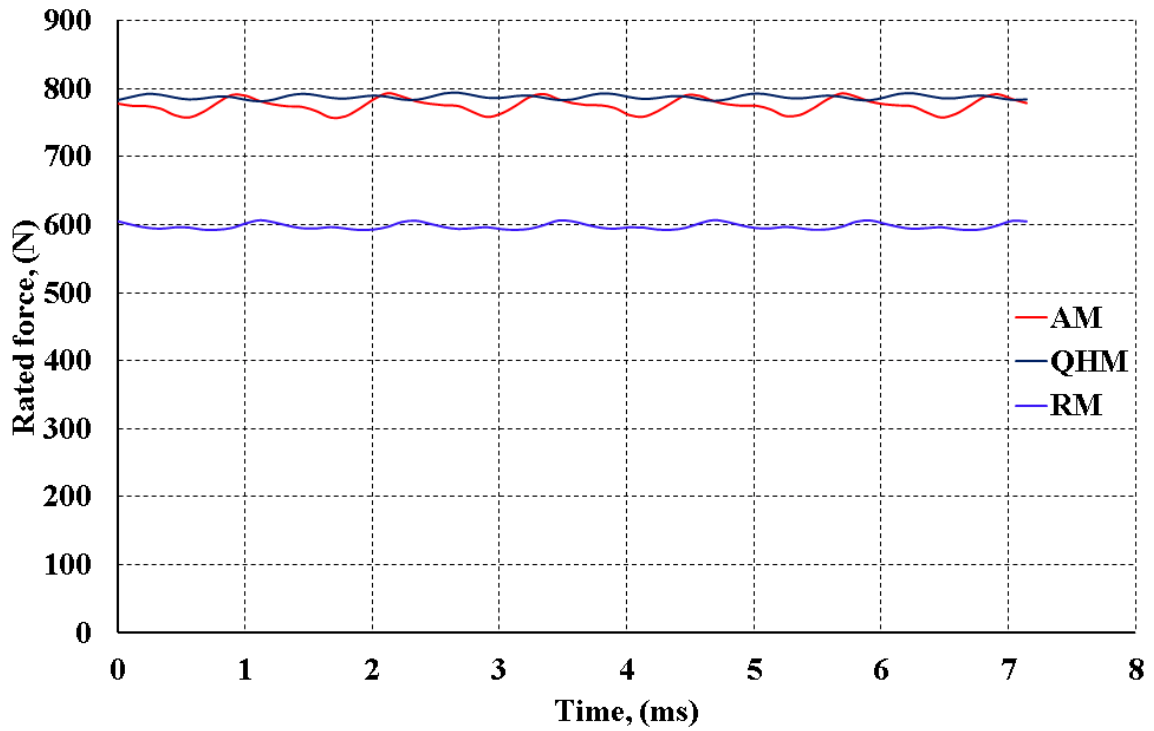


Figure 4-10: Rated force variation over one electrical cycle of alternative optimal Longitudinal Flux Moving Magnets Machine topologies

A flux density of (2.43 T) is detected in the RM translator core back region, exceeding saturation level of the material used. Limited force capability makes the RM machine unsuitable for this application under these running conditions and design geometrical constraints, therefore, it is not considered further in the rest of this work. The final optimal variables of the AM and the QHM machines are listed in Table 4-3.

Table 4-3: Optimal machines variables

Parameter, unit	PM arrangement	
	AM	QHM
Stator diameter ($2R_{OS}$), mm	180	187
PM height – width (M_H, M_W), mm	11- 8	8.5 - 17.143
Tooth width (T_W), mm	7.7	6.3
Stator core back height (SCBH), mm	4	5
Turns per coil (N_C), turns	40	48

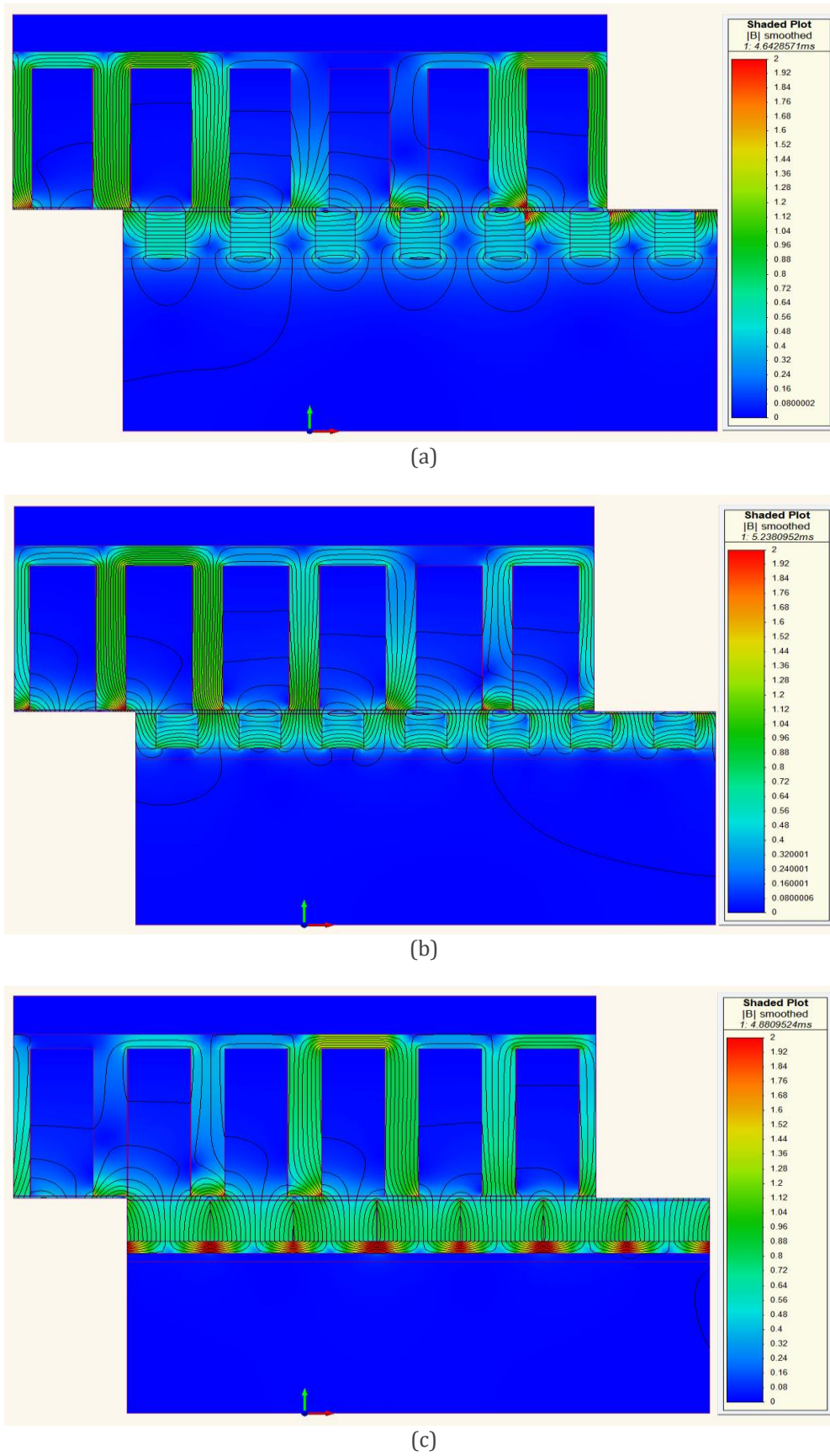


Figure 4-11: Rated load flux distribution showing saturation regions in optimal models of (a) AM machine; (b) QHM machine; and (c) RM machine

4.6 Performance comparison

By recapturing the results of FEA transient solution of the selected optimal machine models, the efficiency (η) is calculated using formulas of both input and output powers, with negligible frictional losses, where:

$$P_{in(mech)} = P_{out(elect)} + P_{losses} \quad 4-5$$

$$P_{losses} = P_{iron} + P_{cu} + P_{ECL} \quad 4-6$$

$$P_{out(elect)} = V_a I_a + V_b I_b + V_c I_c \quad 4-7$$

and

$$\% \eta = \frac{P_{out(elect)}}{P_{in(mech)}} \times 100 \% \quad 4-8$$

In practical consideration of measuring input mechanical power driving the alternator, (4-5) does not retrieve actual results as mechanical driving power is a reflection of driving engine velocity times its boosting force, and thus this principal is used in calculating the machine input power and the corresponding efficiency defined by (4-8). In (4-6), the iron loss (P_{iron}) represents eddy currents and hysteresis losses in the magnetic circuit. The copper loss (P_{cu}) is a reflection of the resulting current density and phase resistance. (P_{ECL}) is a further eddy currents loss in magnets and sleeve due to eddy currents induced by the oscillating movement of the translator, [96].

FEA transient solution accounts for this loss as ohmic losses in PMs and the sleeve. Practically, this loss can be minimised by circumferential segmentation of magnets. Eddy currents power loss in the sleeve is unrecoverable, as segmentation would weaken it and it is a function of the selected sleeve material. The electrical output power ($P_{out} (elect)$) in (4-7) is the sum of the instantaneous power averaged over one electrical cycle in all phases.

Table 4-4: Optimised machines volume and masses

Parameter, unit	PM arrangement	
	AM	QHM
Volume, mm ³	3.6×10^{-3}	3.74×10^{-3}
PM mass, Kg	1.745	2.89
Translator mass, Kg	4.36	3.71
Copper mass, Kg	7.4	8.62
Stator mass, Kg	12.33	13.57
Total mass, Kg	16.69	17.28

Table 4-4 lists a comparison between the remaining optimised machines by considering the volume and materials masses. The translator (moving) mass is of importance above all other component masses as this parameter is a constraint imposed by the drive engine operational constraints. Table 4-5 lists a comparison of performance parameters of the resultant machines at rated loading condition. Force ripple is also included since it is important for smooth operation of the integrated system and its effect on system integral operation will be explained later in Chapter 6.

Table 4-5: Optimal machines performance parameters

Parameter, unit	PM arrangement	
	AM	QHM
P_{Iron} , W	25	19
P_{Cu} , W	57	68
P_{ECL} , W	37.5	39
J_{max} , A/mm ²	5.9	5.93
Rated load force ripple ($F_{r(pp)}$), N	33	10.5
$P_{\text{out(elect)}}$, kW	3.65	3.69
$P_{\text{in(mech)}}$, kW	3.72	3.78
% Efficiency	98.12	97.62
Power density, kW/m ³	1.01	0.97
Power/mass ratio, W/Kg	219.3	213.8

4.7 Weighting Criteria

A weighting score system using specific coefficients and percentage criteria is proposed in deciding the most appropriate machine between the AM and the QHM remaining machines. Three coefficients are selected with consideration to manufacturing cost represented by magnet mass, moving mass and overall machine efficiency from performance parameters. The higher percentage score of a coefficient, the better coefficient; and the machine final score is used to judge the selection of the appropriate topology for this specific application.

Amongst whole machine parts, mass of magnets and orientation type have importance when considering manufacturing cost and maintainability of the machine, and thus this coefficient is evaluated to represent 50% of the total scoring system. The lowest PM mass of the optimised machines tabulated in Table 4-4 is used as a base value in weighing this coefficient.

Furthermore, the limitation of maximum moving mass and the operating mechanical cycle of the engine imposes restrictions to the designer to look for a lighter mover design and adds complexity to the final judgment.

In order to achieve full use of the LJE mechanical cycle, translator length should be twice the machine active length. Therefore, twice the translator mass is also included in the scoring system and evaluated using a base of (6 kg). This base value is selected from Table 3-1, the maximum moving mass constraint, by taking out (2 kg) assumed to represent the connecting rod mass from the constraint. 30% is assumed the contribution of this coefficient in the total scoring system.

Both coefficients are weighed using (4-9), where (*Coefficient value*_{1,2}) defines the value of the coefficient under evaluation; the (Base) defines the base used in evaluating the coefficient under weighing, (*X*) is the weighing coefficient assumed percentage and subscripts (1, 2) refer to the abovementioned coefficients.

$$\% \text{Coefficient}_{1,2} = \left(1 - \frac{\text{Coefficient value}_{1,2} - \text{Base}}{\text{Coefficient value}_{1,2}}\right) \times X_{1,2}\% \quad 4-9$$

The remaining 20% of the scoring system was offered to evaluate the resulting machine overall efficiency which reflects the total design interconnected performance parameters. Figure 4-12 shows the results of the scoring system used and it is clear that the AM topology score is higher than that of the QHM machine topology.

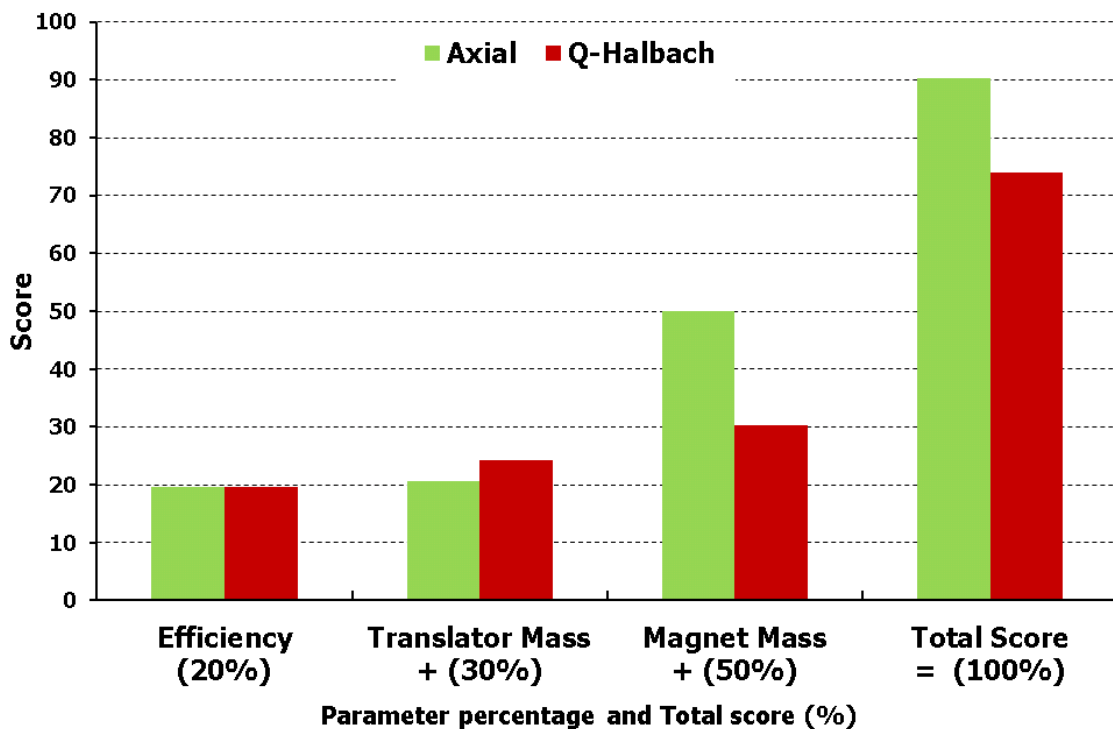


Figure 4-12: Scoring system results

Additionally, from Table 4-4 results, the cost of using magnet and copper materials in the AM topology is cheaper by 40 % and 14 % respectively. Furthermore, the former machine is more compact, that resulting in its higher power density. The only drawback of the AM topology is its resulting rated force ripple. However, as a percentage of the total design force, force ripple of both machine topologies are in the range of (1.3 – 4.1%), which makes it of negligible importance in current design stage without applying any force ripple reduction technique. Thus, based on the scoring system results and the cost of material use, the AM machine is more appropriate for this application.

4.8 Conclusion

This chapter had explained the optimisation methodology based transient solution of 2D FEA modelling technique. The methodology started by defining the design objectives and the design variables, and ended by demonstrating its use in the design of three alternative topologies of Linear Generators of moving magnet and longitudinal flux configuration. The applied methodology is considered as a useful tool in designing this family of linear machines for any desired force rating.

The optimisation results presented show that the machine equipped with radially magnetised magnets (RM) is unsuitable for the application with its resulting force of (0.75*design force) under the considered geometrical constraints.

The comparison made via the suggested scoring system showed that the competing machines have different scores with regard to the selected weighing coefficients and the used percentage criteria. The axially magnetised (AM) machine has a higher score over the Quasi Halbach (QHM) machine, despite its higher translator mass. The lighter magnet mass makes the AM machine cheaper by at least 40 % when considering manufacturing cost of the translator only. Therefore, the AM machine has been adopted in the following chapters for further investigation, development, modelling and prototype construction.

Chapter 5 : Flux – Concentrated Tubular Machine Detailed Design

5.1 Introduction

This chapter considers the effect of changing some parts of the axially (Flux – Concentrated) magnetised tubular machine selected in Chapter 4. This is performed to investigate a more manufacturable design. The following design variables are investigated:

- 1- Core material.
- 2- Air-gap length and grade of magnet.
- 3- Translator pole number (5 versus 7).
- 4- Power conversion method.

General formulas that describe the variation of both the inherent cogging force and that due to the coil driven flux force over translator position are derived. These formulas will be used to implement the modelling of the Linear Generator (LG) taking into consideration the effect of finite stator length end effects on the resultant on load force ripple variation.

These changes and performance parameters investigations have been carried out using 2D axisymmetric, as opposed to 2D FEA used in previous chapter, which was found to give results as close to as a 3D model with much saving in solving and overall design process times. The difference between 2D and 2D axisymmetric machine modelling is described in Appendix A.

5.2 Core material investigation

The initial machine core magnetic material was set in the FE software from Magnet to the available grade M-1526 Ga, a common grade of fully processed non-oriented silicon steel in different lamination thicknesses. Due to adopting a tubular geometry, and the nature of flux distribution pattern shown in Figure 5-1, using laminations means that the formation of stator core back requires radially stacked laminations, while the teeth are formed by axially stacked laminations. In practice, this would result in a complex manufacturing and assembly processes to form the structure shown in Figure 5-2(a). This complexity can be reduced by using Soft Magnetic Composite (SMC) material for the stator core back keeping the teeth formed from lamination as shown on Figure 5-2(b).

Translator pole segments separating the magnets are also modelled by SMC material to provide the necessary two dimensional flux path through each segment which cannot be achieved in the case of radial lamination stacking.

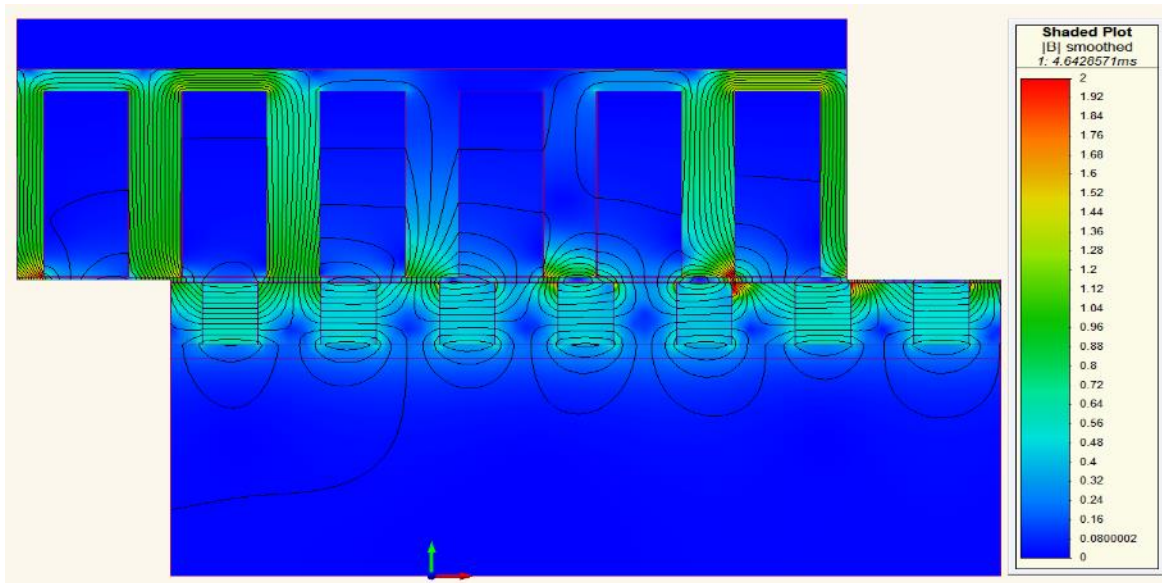


Figure 5-1: 2D view of flux distribution in the machine geometry

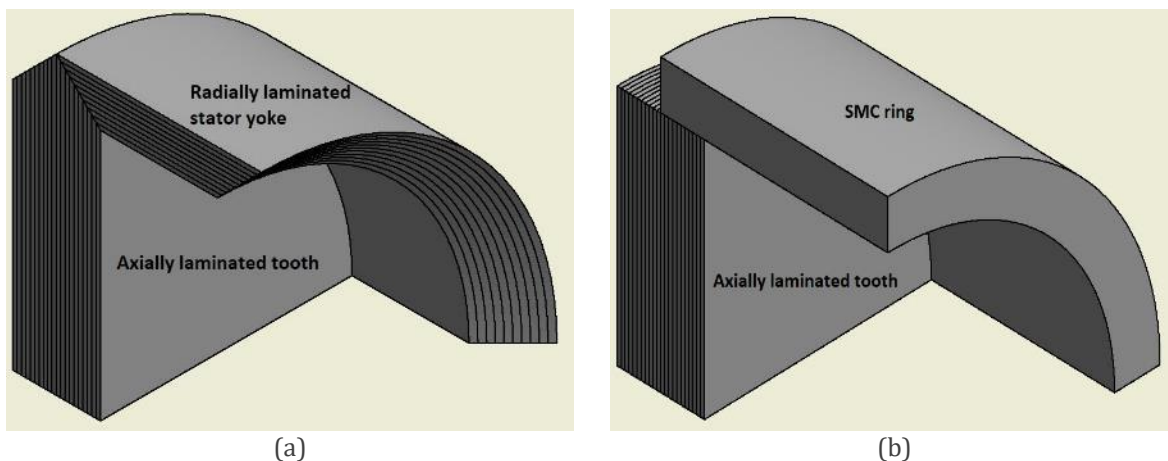


Figure 5-2: Stator yoke and tooth structure using (a) Laminated steel for both components; (b) Laminated steel for tooth and Soft Magnetic Composite for stator core back

Before performing the modelling and FEA analysis using 2D axisymmetric, stator core back and translator pole segments were modelled by the available SMC material grade in the software, Somaloy 700HR 3p from Höganäs¹, corresponding to the same material that will be used in the manufacturing of the actual test rig in Chapter 8. The B-H curves of different core materials used are shown in Appendix B, showing the lower permeability of the SMC material compared to the lamination material, and hence a lower force capability is expected as clearly shown in Figure 5-3. It is clear that the average machine force capability is reduced due to using lower permeability magnetic material, with negligible effect on the peak-to-peak force ripple ($F_r(pp)$) and its cyclic behaviour.

¹ <https://www.hoganas.com/>

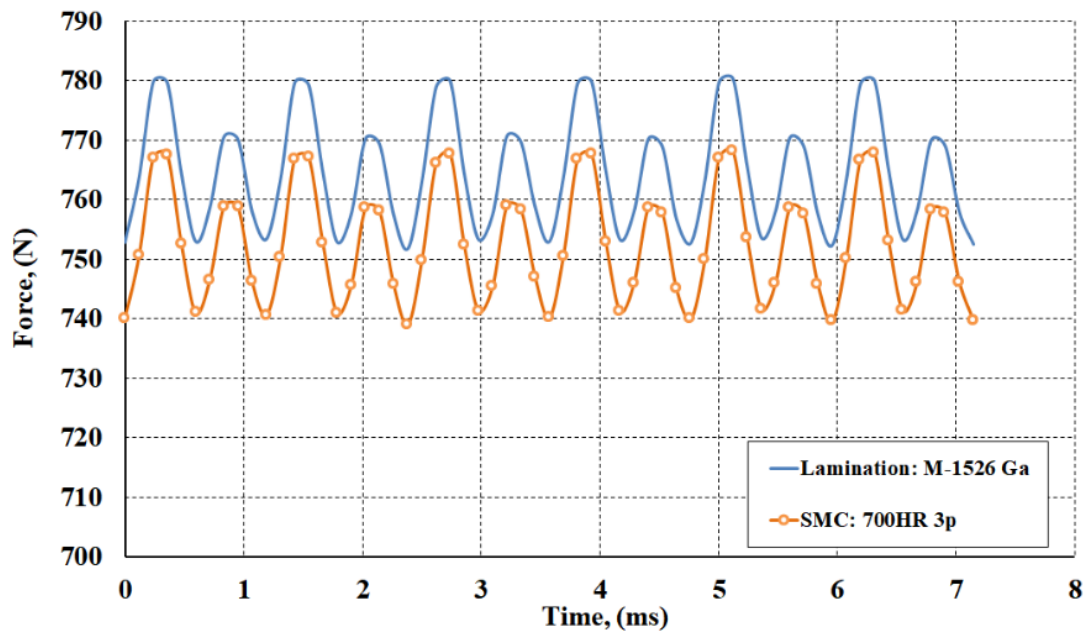


Figure 5-3: Effect of core material on rated load force over one electrical cycle (2D FEA)

The rated force is reduced by 1.5 %, while $F_r(pp)$ is increased by 0.138 % when using the 700HR 3p material.

5.3 Investigation of air-gap length based magnet grade

By keeping the bore diameter and machine loading condition unchanged, the air-gap length and the magnet grade has been changed to overcome the manufacturing difficulties and tolerance issues that may appear in case if magnets are supplied in arcs form instead of a complete ring, a manufacturing fact based magnet grade discussed with supplier during ordering. If the magnets are supplied in segmented arcs to form a ring, an appropriate coating must be used to hold ring segments in position during translator poles assembly to avoid any undesired forces that could act to deform ring segments assembly. Therefore, the initial design air-gap of (1 mm) length is increased to be (1.5mm) to ensure enough room to use magnets coating should necessary [82].

The initial PM grade was (SmCo5) of a 0.87 T remanence and an energy product of 140.8 kJ/m^3 at 20°C , and the replacement grade is (SMCo17) of a 1.08 T remanence and an energy product of 220.3 kJ/m^3 at 20°C , a stronger magnet grade.

For the same magnetic circuit of laminated teeth and SMC material used in stator core back and translator pole segments, the machine design is modified using 2D axisymmetric FEA to react the required design force against the air-gap length and magnet grade changes.

Force capability of both design models is shown in Figure 5-4, and the resulting dimensional, volume, mass and performance comparisons are listed in Table 5-1 and Table 5-2 respectively. It can be seen that stator slot geometry is unaffected, while translator pole structure is largely influenced by these changes. A penalty of 26 % in PM mass was required to achieve the same performance, which consequently increases the translator mass, PM eddy current loss and a slight reduction in efficiency. On the other hand, the load force ripple decreased from 3.24 % to 1.77 % offering partial offset to the aforementioned penalties.

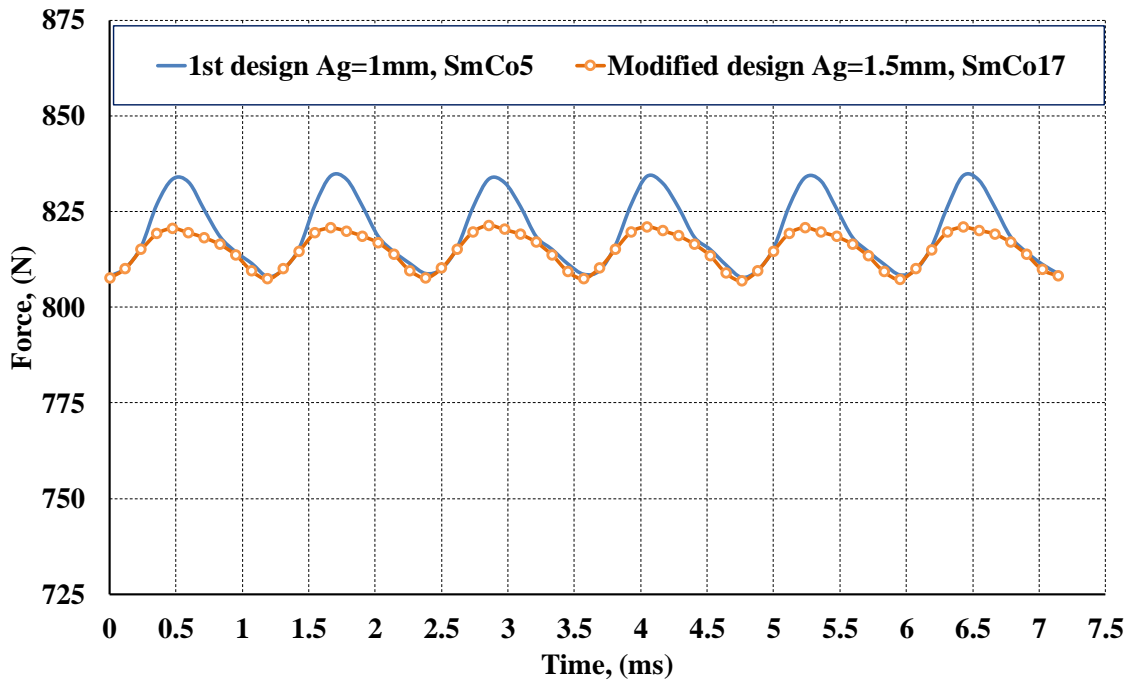


Figure 5-4: Variation of rated load force over electrical cycle with air gap and magnet grade changes

Table 5-1: Optimal machines dimensional, volume and mass parameters

Parameter, unit	1st design	Modified design
Stator diameter ($2R_{OS}$), mm	180	
Tooth width (T_w), mm	7.7	
Stator core back height (SCBH), mm	4	
Turns per coil	40	
Copper mass, Kg	9.34	
Stator mass, Kg	16.45	
Air-gap, mm	1	1.5
Translator diameter ($2R_{OT}$), mm	104	103
PM height – width (M_H, M_W), mm	9- 7.5	12 - 8
PM mass, Kg	1.17	1.59
Translator mass, Kg	3.56	4.19

Table 5-2: Optimal machines performance parameters

Parameter, unit	1st design	Modified design
P_{iron} , W	16	15.6
P_{cu} , W	76	75
P_{ECL} , W	113	136
J_{max} , A/mm ²		5.8
Rated load force ripple ($F_{r(pp)}$), N	27	14.5
$P_{\text{out(elect)}}$, kW	3.75	3.7
$P_{\text{in(mech)}}$, kW	3.93	3.91
% Efficiency	95.2	94.6
Power density, kW/m ³	1.23	1.21
Power mass ratio, W/Kg	190	179

To avoid the manufacturing complexity if segmented magnets are supplied, the larger air gap design is selected for further investigations despite the reduced power density and power mass ratios.

5.4 Pole number investigation

Another machine model of same stator structure but a 5 pole translator has been designed and compared with the modified 7 pole design, see Figure 5-5. Both designs were optimised assuming ignored end effects. Also, they have the same stator outer diameter, same stroke ratio, same air gap length of (1.5mm) and same magnets grade for comparison fairness.

The purpose of this comparison is to:

- 1- Describe the effect of lower pole number on the resultant machine performance parameters.
- 2- Analyse the cogging force at both no-load and loading conditions such that a formula describing these effect can be generalised.

Typical machine dimensional and mass parameters are listed in Table 5-3, where another parameter is added and termed as the effective PM mass per pole, (bolded in the table), in order to explain its importance on the resulting force ripple at both rated and no – load condition. Table 5-4 lists the performance parameters of the competing designs.

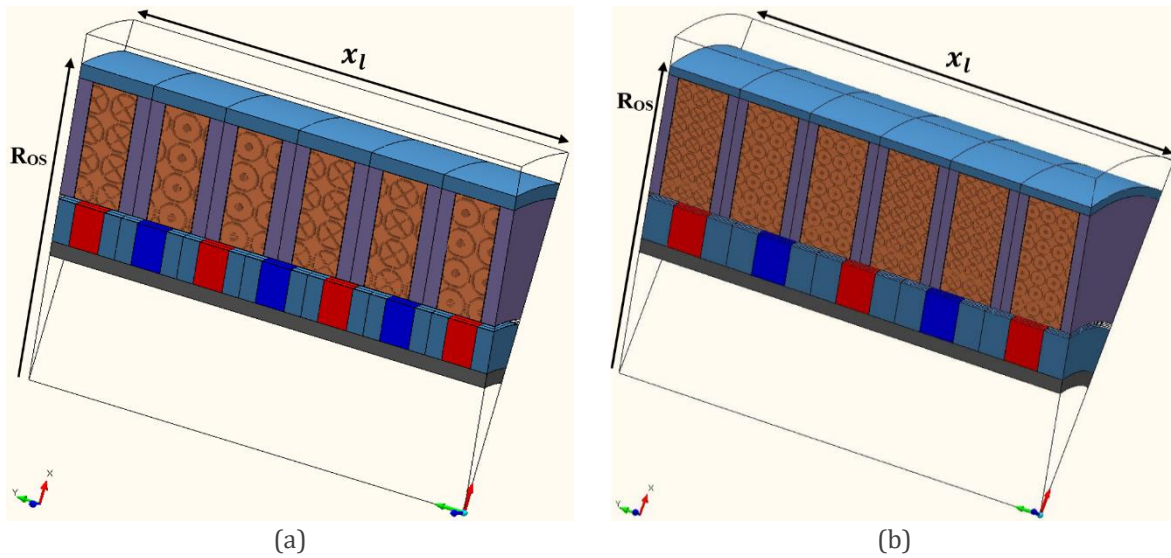


Figure 5-5: Configurations of the competing machines (a) 7 pole design; and (b) 5 pole design

Table 5-3: Typical machines dimensional and mass parameters

Parameter, unit	7 pole design	5 pole design
Stator diameter ($2R_{os}$), mm		180
Tooth width (T_w), mm	7.7	5.6
Stator core back height (SCBH), mm	4	2.5
Turns per coil	40	49
Copper mass, Kg	9.34	11.58
Stator mass, Kg	16.45	16.77
Air-gap, mm		1.5
Translator diameter ($2R_{ot}$), mm		103
PM height – width (M_H, M_W), mm	12 - 8	12 – 9.5
PM mass, Kg	1.59	1.35
PM mass/pole	0.227	0.27
Translator mass, Kg	4.19	4.17
Volume, mm ³		3.05×10^{-3}
Total mass, Kg	20.64	20.94

Table 5-4: Typical machines performance parameters

Parameter, unit	7 pole design	5 pole design
P_{iron} , W	15.6	15.7
P_{cu} , W	75	96
P_{ECL} , W	136	66
J_{max} , A/mm ²	5.8	5.88
Rated load force ripple ($F_{r(pp)}$), N	14.5	58.3
$P_{out(elect)}$, kW	3.7	3.83
$P_{in(mech)}$, kW	3.91	3.99
% Efficiency	94.6	96
Power density, kW/m ³	1.21	1.25
Power mass ratio, W/Kg	179	183

Compared to the 7 pole translator, the 5 poles design model has a better PM utilisation with a total saving of 15 % in material and a consequent lower eddy current loss in the magnets. There is an increase in copper loss resulting from the increased slot geometry and the increased electrical loading of the design. However, higher electrical loading means a higher electrical power output and hence a better overall machine efficiency.

The force capability of typical designs is shown in Figure 5-6 at rated load. The no-load cogging forces due to slotting effect over half electrical cycle is shown in Figure 5-7.

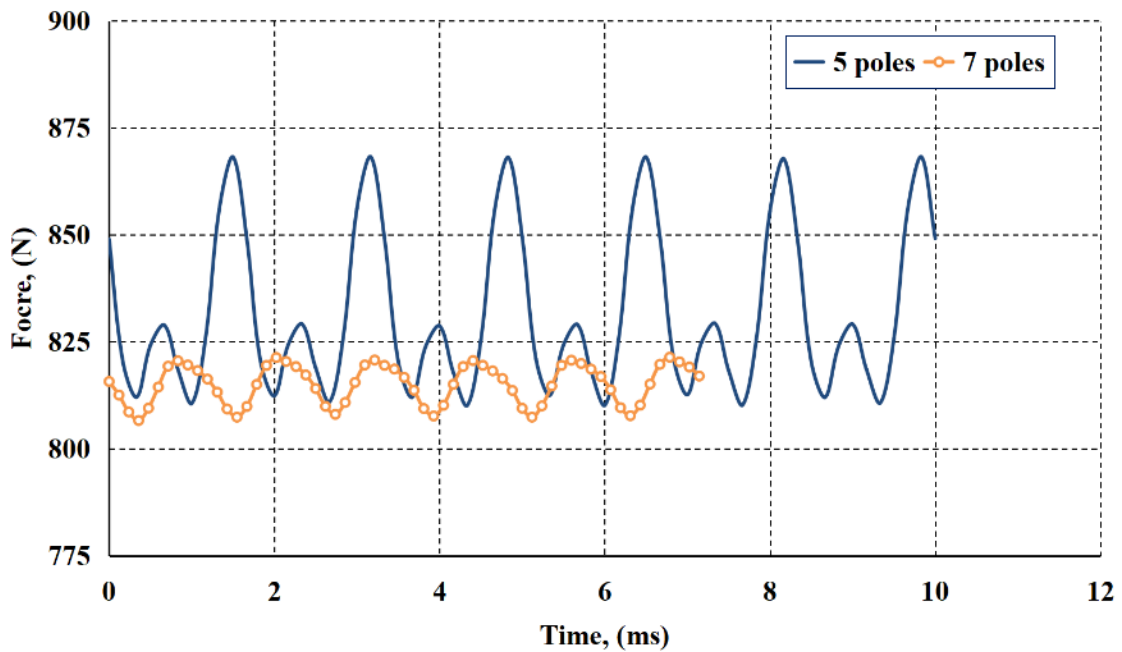


Figure 5-6: Variation of rated electromagnetic force over electrical cycle with 5 & 7 magnetic poles

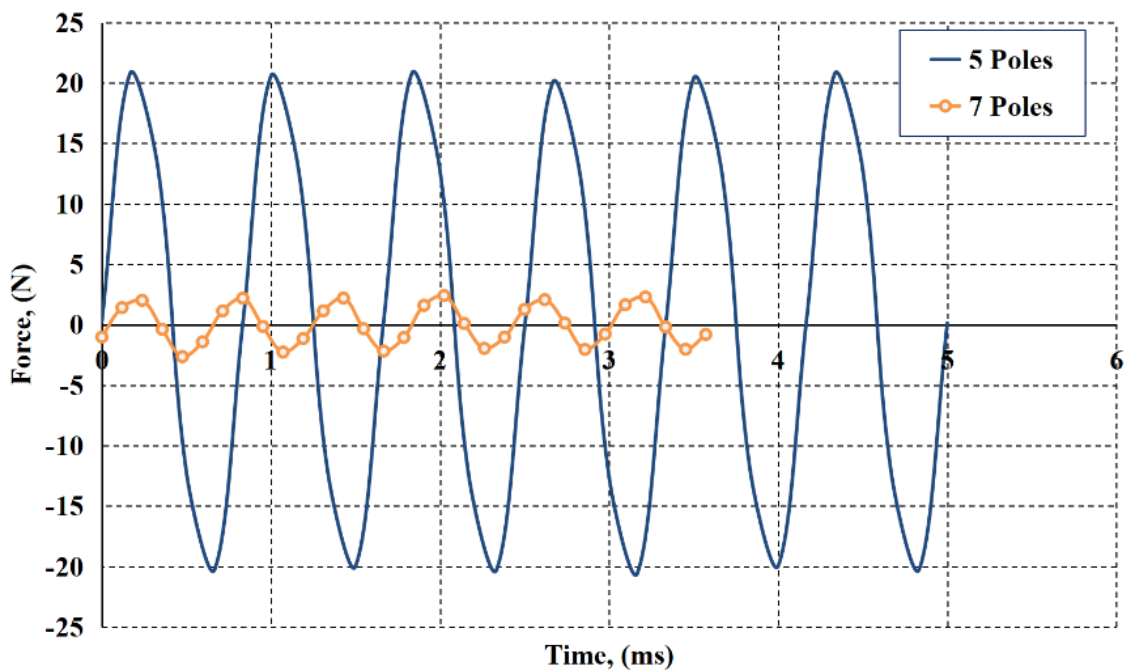


Figure 5-7: Variation of no-load cogging force over a half electrical with 5 & 7 magnetic poles

Figure 5-7 shows that the electrical frequency decreases as the pole number decreases in the machine topology under investigation. Further, it shows that the higher the PM mass per pole ratio, the higher force fluctuation at both loading conditions. From these two graphs, the variation of cogging cycle is periodic with periodicity (R_c) depending on the number of stator slots and translator poles, [75, 116], and is six in these typical design models over one pole pitch in both cases. Therefore, the variation of cogging force over one translator pole as a function of mover position (x) can be expressed as:

$$\bar{F}_{cog}(x) = \hat{F}_{cm} \cdot \sin\left(\frac{\pi}{\tau_p} R_c \cdot x \pm \vartheta_c\right) \quad 5-1$$

$$\text{with} \quad R_c = \frac{LCM(N_S, N_p)}{N_p} = N_S \quad 5-2$$

Where (\hat{F}_{cm}) is the peak of cogging force and the symbols (N_S , N_p , τ_p) are the number of slots, number of translator poles and translator pole pitch, respectively. The (\pm) sign in phase shift (ϑ_c) holds for oscillating motion of the translator, and the phase shift represents the shift from position corresponding to peak cogging force with respect to the stationary stator, where: $0^\circ \leq \vartheta_c \leq 180^\circ$. (LCM) stands for Least Common Multiple between stator slot number and translator pole number.

With regard to design selection, it is most favourable that when a LG is selected for FPE applications, its reacting force must be as smooth as possible to ensure stable system operation and accurate in-cylinder piston motion control. Since the 7 pole design model has the lower force fluctuation it is therefore more suitable for the application compared with the 5 pole machine model.

5.5 Power conversion technology investigation

All the machine designs described previously have considered an assumed balanced Resistive Loading (RL) to dump the power generated by the linear machine. In the literature [10, 61, 79, 100, 128], the load was undefined and its impacts on the machine design and the resulting performance parameters therefore has not previously been considered. In this section, two additional possible power conversion technologies are considered to investigate the electrical circuit influence on the resultant machine dimensional and performance parameters while extracting the rated power. The resultant electrical power output will be a function of machine losses and the operating power factor.

The two additional power conversion technologies considered are:

- (a) Grid Interface (GI): The Grid Interface scenario assumes power is injected into the referenced LV side of the UK power grid, see Figure 5-8. It assumes a 5 % voltage drop in each uncontrolled conversion unit representing internal losses, and an ideal DC link voltage.
- (b) Unity Power Factor Controlled Converter (UPFCC): The Unity Power Factor Controlled Converter shown in Figure 5-9, assumes a fully controlled current density equals that resulted from the previous (GI) loading method. The Controlled Converter forces the machine to operate at UPF, i.e. the current is controlled to be in phase with the induced EMF and the load absorbs all the real power generated by the alternator [128].

In fixed speed, rotary applications, Unity Power Factor could be achieved by using a tuning capacitor to offset the phase synchronous inductive reactance. In a linear machine, varying electrical frequency means varying reactance and advanced control techniques, with the associated cost and losses, are required. This can be thought of as the penalty of compensating phase inductance effects in variable speed direct driven machines in order to convert the variable frequency generated power to a constant frequency useful power [129, 130].

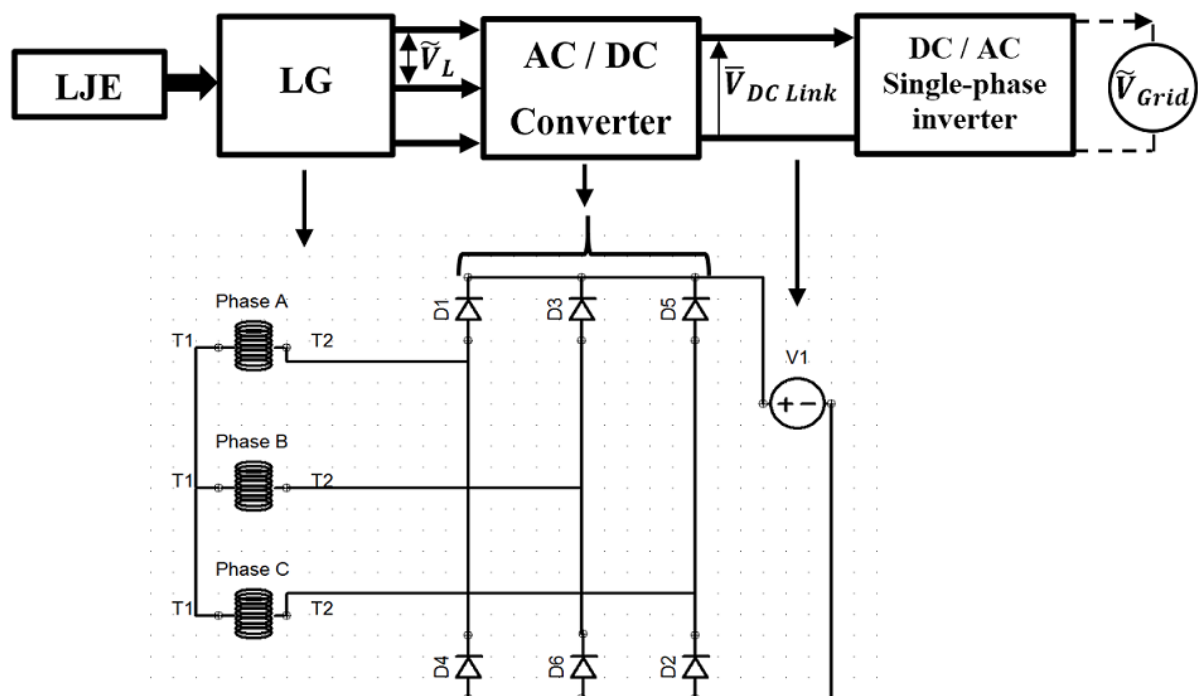


Figure 5-8: Power circuit for Grid Interface scenario and FEA software circuit implemented

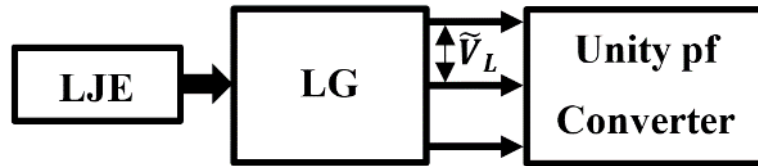


Figure 5-9: Power circuit for Unity power factor controlled converter scenario

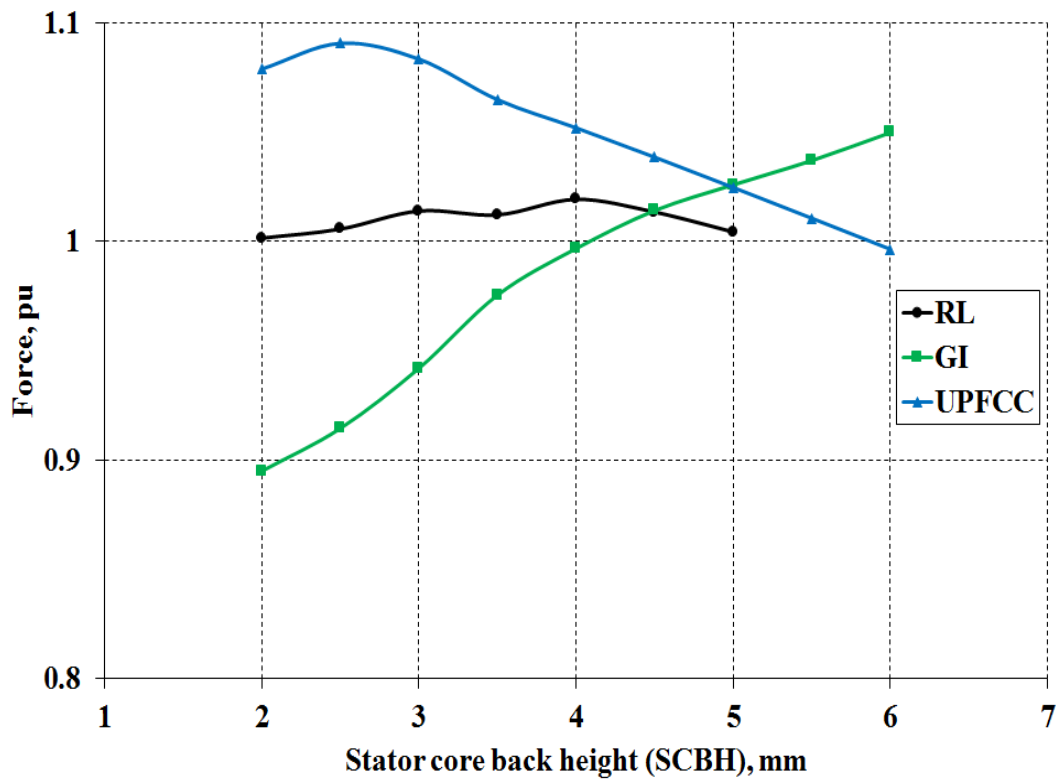
The effect of power convertor on machine dimensions like the stator yoke and tooth width appear not to have been considered with care elsewhere, e.g. [10, 79, 128]. Therefore, besides performing design study for single tooth width value in all design models, see Figure 5-10(a), these dimensions have been examined for the rated force capability against their combined variation as shown in Figure 5-10(b-d).

From these optimization results, it can be seen clearly that the trend of each surface change is different, highlighting the importance of considering the power conversion scenario at the design stage. Also, it clarifies that these machine dimensions having notable influence on the resulting force capability of the range 12 %, 20 % and 25 % in the RL, GI and UPFCC design models respectively. Lastly, the manual design methodology adopted can exactly give the optimal dimension for the design variable under consideration. For instance, the effect of changing tooth width for fixed slot and core-back height dimensions can be explained by examining this effect on the magnetic circuit reluctance (\mathcal{R}), knowing that the reluctance increases linearly with flux path length, and inversely with the cross-sectional area and permeability. Decreasing tooth width increases the electrical loading, due to the increased coil area. On the other hand, and for a fixed stator diameter, this will result in decreasing the machine magnetic loading. The hypothesis is reversed as tooth width is increased, and the optimal value is selected as a balance between the coupled electromagnetic loadings.

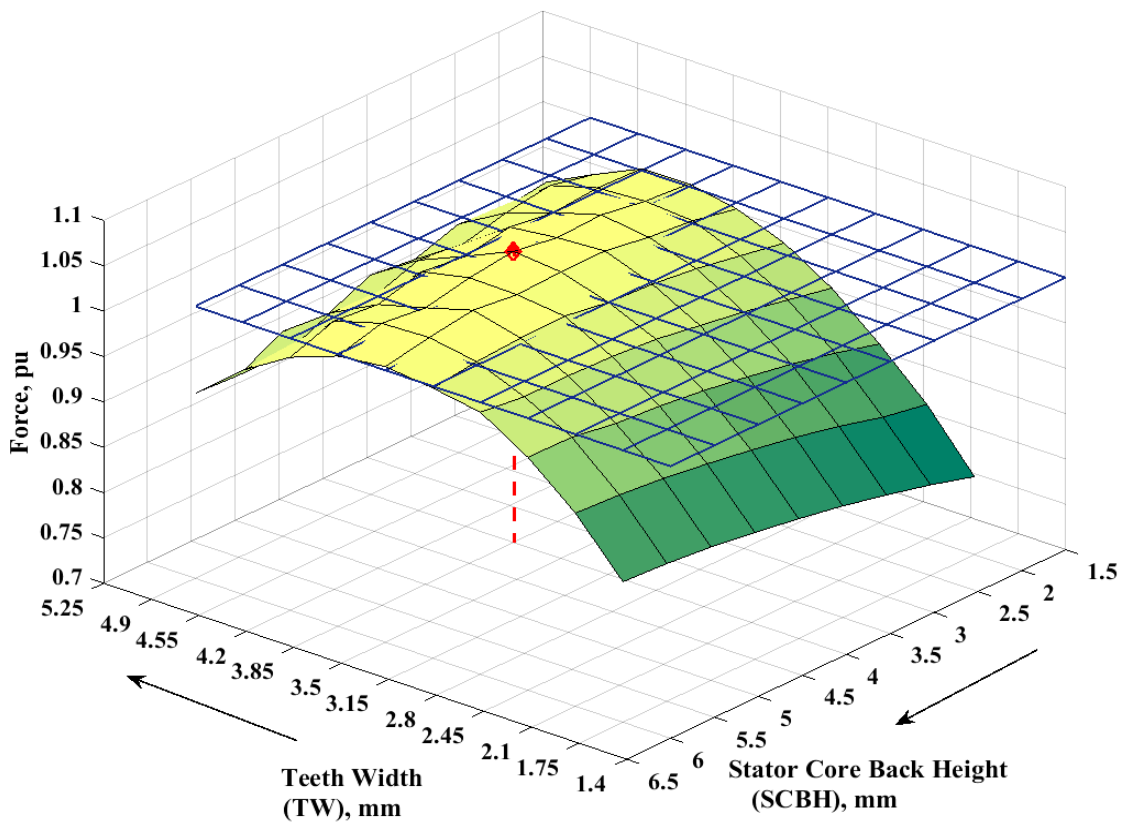
Final selected dimensions are highlighted in the graphs considering manufacturing feasibility, although other dimensions can be selected with attention to machine losses when thinner dimensions are considered. Dimensional and performance parameters for the three machine design models are compared as listed in Table 5-5 and Table 5-6 respectively.

In comparison with RL design model, the GI model has almost the same translator and overall machine mass, however, there is an extra cost of 12.6 % increase in magnet material, an 8.4 % increase in stator core mass and a 7.5 % reduction in copper mass.

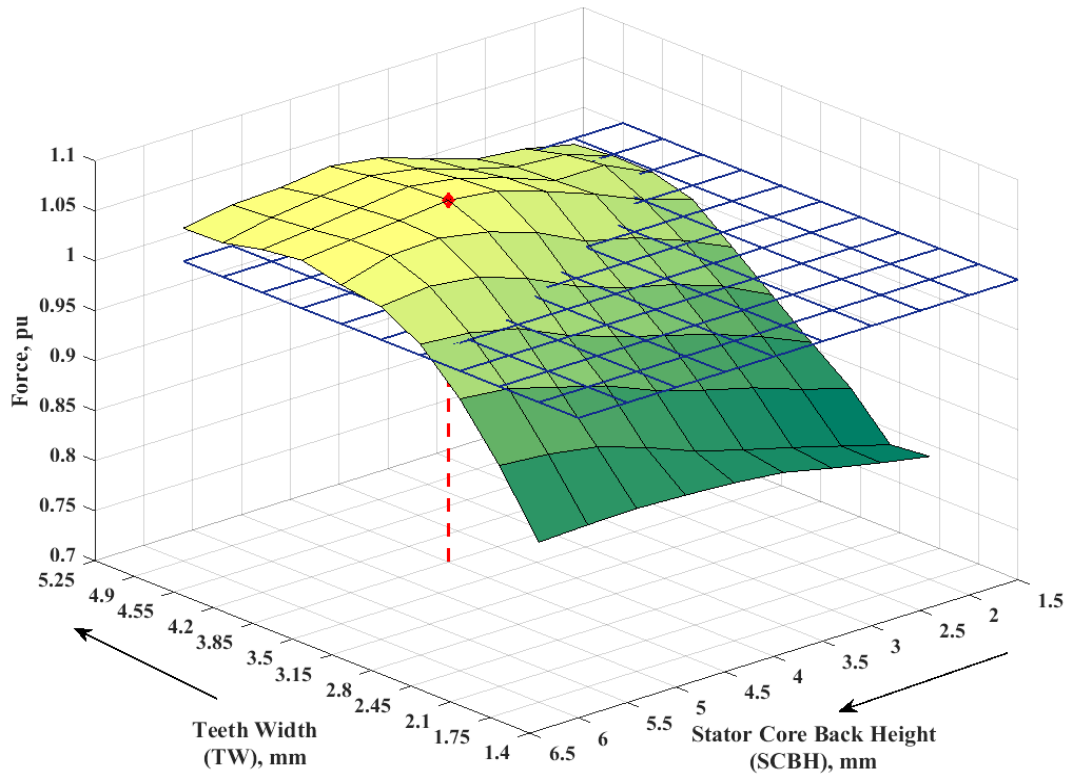
High current loading is responsible for a 220 % increase in copper loss, giving notable reductions in machine efficiency and power densities and requiring external cooling. Current density in the RL design version is such that the machine could be naturally-cooled.



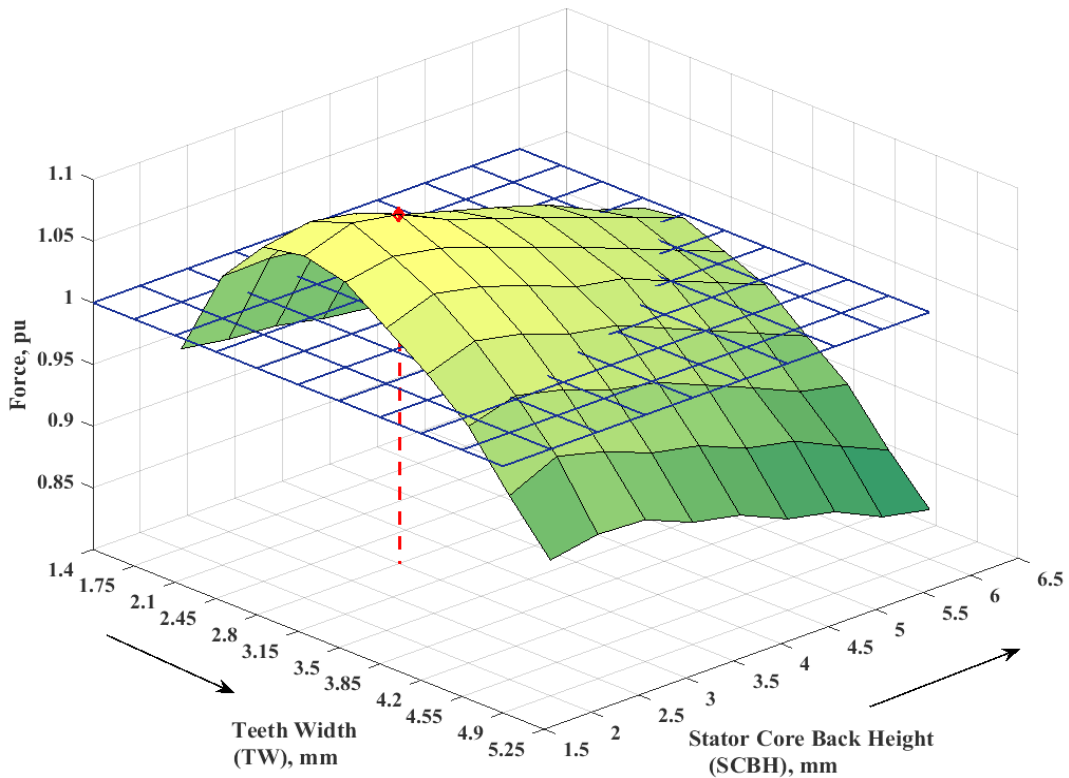
(a)



(b)



(c)



(d)

Figure 5-10: The effect of teeth width and stator core back height variation on the force capability (a) 2-D view for optimal tooth width; and in 3-D view for (b) Resistive Loading; (c) Grid Interface; and (d) Unity Power Factor Controlled Converter

Table 5-5: Typical machines dimensional and mass parameters based power conversion method

Parameter, unit	RL design	GI design	UPFCC design
Stator diameter ($2R_{os}$), mm		180	
Tooth width (T_w), mm	7.7		5.6
Stator core back height (SCBH), mm	4	4.5	3
Turns per coil	40	112	146
Copper mass, Kg	9.34	8.64	11.38
Stator mass, Kg	16.45	16.35	16.74
Air-gap, mm		1.5	
Translator diameter ($2R_{OT}$), mm		103	
PM height – width (M_H, M_w), mm	12 – 8	12 – 9	5 – 5.5
PM mass, Kg	1.59	1.79	0.5
PM mass/pole	0.227	0.27	0.071
Translator mass, Kg	4.19	4.21	2.51
Volume, mm ³		3.05×10^{-3}	
Total mass, Kg	20.64	20.56	19.25

Table 5-6: Typical machines performance parameters based power conversion method

Parameter, unit	RL design	GI design	UPFCC design
Hysteresis and eddy current iron loss, W	13, 2.6	9.5, 2.0	23, 12
P_{iron} , W	15.6	11.5	35
P_{cu} , W	75	165	231
P_{ECL} , W	136	108	159
J_{max} , A/mm ²	5.8		9.15
Rated force ripple as a percentage to rated force ($\%F_{r(pp)}$)	1.77%	15.17%	3.1%
$P_{out(elect)}$, kW	3.7	3.33	3.73
$P_{in(mech)}$, kW	3.91	3.82	4.16
% Efficiency	94.6	86.5	89.8
Power density, kW/m ³	1.21	1.09	1.22
Power mass ratio, W/Kg	179	162	194

This GI design also shows the highest rated force ripple compared with other design models, and will be explained at the end of this section. The UPFCC design model offer savings of 65.5 % and 30.5 % with respect to PMs and stator core material versus an extra 22 % copper mass. Also, it has the highest power densities and the lightest translator mass compared with other designs. However, the significant increase in copper loss, of order three compared to that of RL design, resulted in a notable efficiency reduction.

The variation of the cogging force at no – load over half an electrical cycle shown in Figure 5-11 clarifies that the UPFCC design has the lowest cogging, due to the low PM material mass as well as the lowest PM mass/pole ratio in this design version.

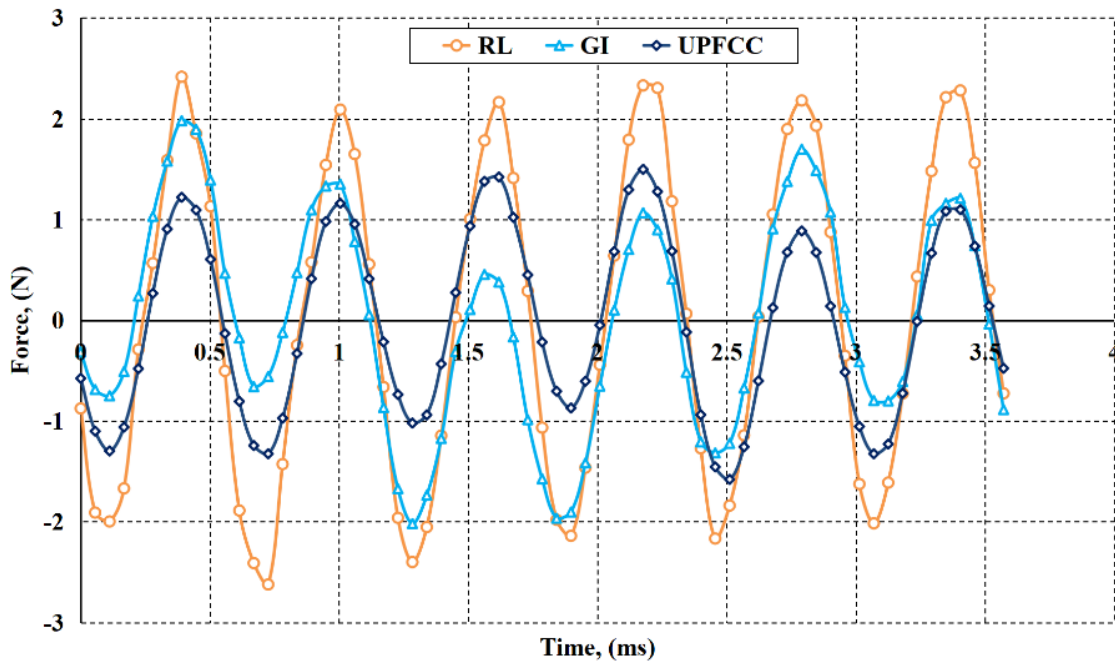


Figure 5-11: Cogging force variation based power conversion method

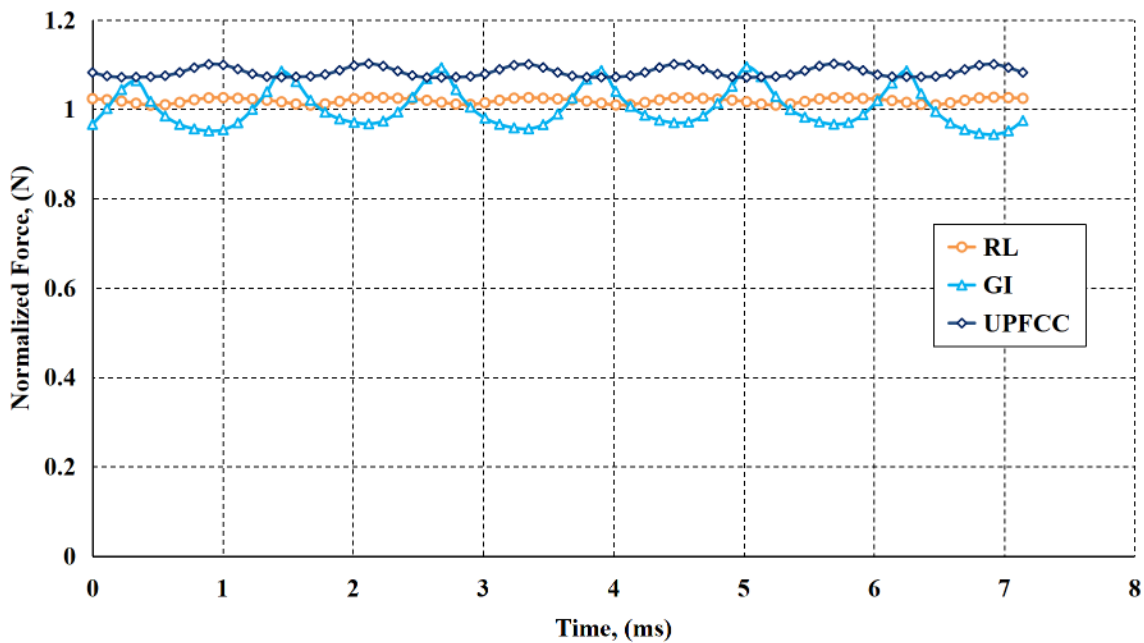


Figure 5-12: Rated load force fluctuation based power conversion method

However, the rated force variation over one electrical cycle shown in Figure 5-12 clearly shows that the force ripple is totally different from the case at no-load condition, and is significantly higher in the GI design version. One reason is the high PM mass/pole ratio compared with other design models.

The other reason can be explained with the aid of the circuit diagram shown in Figure 5-13. Assuming identical phase quantities and parameters, the instantaneous current (I) circulating in the assigned path of the circuit may be expressed as follows:

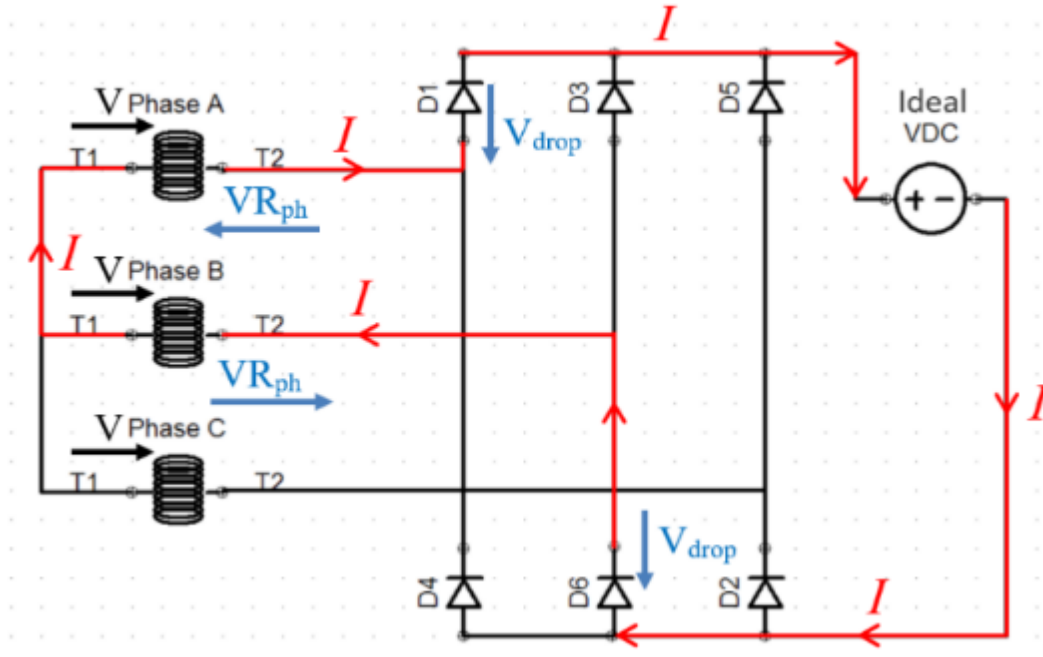


Figure 5-13: Grid Interface design circuit diagram clarifying current path at an instant of three phase system operation.

$$I = \frac{[V_a(\omega t) - V_b(\omega t - 2\pi/3) + 2L_{ph} \frac{dI}{dt}] - [V_{DC} + 2V_{drop}]}{2R_{ph}}, (A) \quad 5-3$$

Where

$V_a(\omega t)$: Phase (a) induced emf, V.

$V_b(\omega t - 2\pi/3)$: Phase (b) induced EMF, V.

L_{ph}, R_{ph} : Phase inductance and resistance, H, Ω .

And V_{drop} : diodes ON state voltage drop, V.

Equation (5-3) clarifies that the instantaneous circulating current (I) is a measure of the induced phase voltages difference, i.e. the line voltage (V_{ab}), supported by the energy stored (released) in the uncompensated phase inductance of both phases, and is limited by the DC link voltage and partly by converter and phase resistance volts drops. This can be noticed from the variation of phase voltages in all designs, and a line voltage in the GI design, as shown in Figure 5-14. Figure 5-15 shows the variation of phase and DC link current quantities in the GI design model. Therefore, in the GI design, the higher on load force ripple is due to the high instantaneous current flow which is also responsible of the high resulting current density in the design.

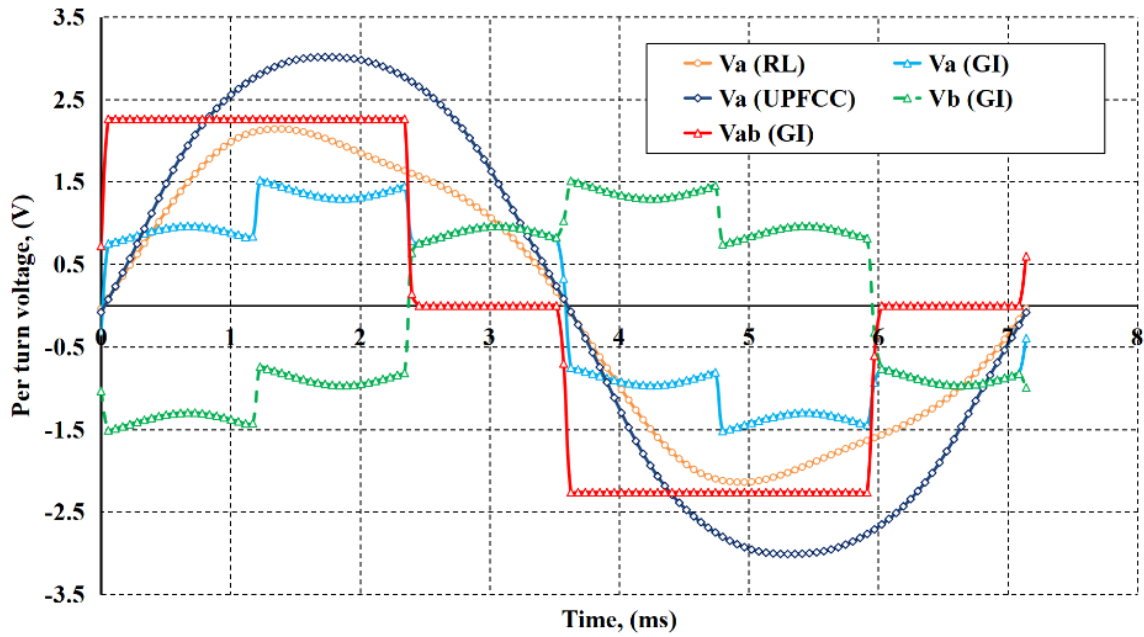


Figure 5-14: Variation of phase and line voltage quantities per turn over one electrical cycle for the three selected design models

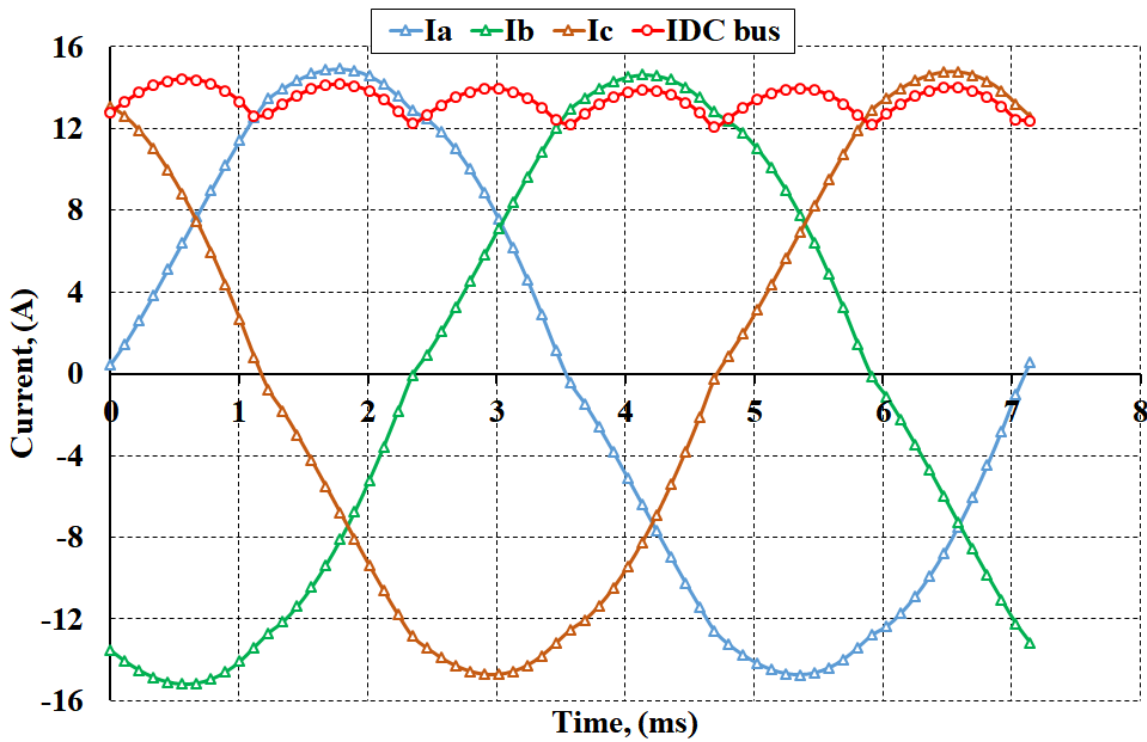


Figure 5-15: Variation of phase and DC link current quantities over one electrical cycle in the machine design model for Grid Interface application

It should be appreciated that although the same current density is used in the UPFCC design scenario, yet the compensation of phase inductance by the controlled converter has the advantage of reducing the force ripple to almost (1/5th) of that in the GI design.

Thus, controlling the current flowing from the alternator could help in minimizing the on load force ripple, but has negative impacts on the other performance parameters of the machine. Furthermore, if a cogging force reduction technique is applied [108, 109], it should be assessed not only at no – load conditions, but also and most importantly at rated loads with consideration to the power conversion method and the load variation margins.

5.6 Conclusion

This chapter presented further investigation with regard to machine performance against changes in material and three sets of load electrical circuit variation. These investigations are required to take a design model with load integrity and make it manufacturable.

Initially, the effect of changing parts of stator and translator core materials, the yoke and the moving pole iron segments have been considered in order to comply with the flux path nature within machine geometry. It is shown that, although having a lower permeability, using SMC material instead of laminated steel sheets has a negligible effect on force capability, but greatly simplifies the manufacturing process of these parts.

The first set considered the effect of air-gap length and magnet grade changes accounting for magnets coating should necessary. A penalty of 26 % PM mass increase for same performance in a larger air-gap even with the higher magnet grade. However, cogging forces have reduced to almost 46 % compared to the initial design which can be considered an improvement to this specific performance parameter.

The second set considered a comparison between the modified design versus a lower pole, 5 pole design, and it showed higher cogging force levels for low pole number, from which it is found that the cogging force amplitude increases as the PM mass/pole ratio increase, which is proved also in the third set.

Finally, the effect of power conversion scenarios on the machine design has been explained and it showed the effect of machine current loading in varying the force ripple which means that the variation of load margins must also be taken into consideration when investigating a cogging force reduction technique.

Amongst the three models, the machine designed for unity power factor operation showed the highest power densities, the lightest translator mass, the lowest requirement for PM material and gave the highest electrical power output. The GI version had the largest force ripple and the RL version gave the best efficiency.

Therefore, the RL design model is taken forward to the next chapter for mathematical modelling, prototyping and testing (Chapters 8 & 9).

Chapter 6 : Integrated System Model

6.1 Introduction

This chapter presents a novel dynamic realisation of the Linear Joule Engine (LJE) integrated with the Linear Generator (LG) model using Siemens LMS Imagine.Lab AMESim which aims to investigate the dynamic performance of the whole engine-generator system. A general mathematical Resistive Loading machine model designed in the previous chapter, incorporating all interacting electromagnetic forces, is presented. Then, model implementation in MATLAB/Simulink is used to predict the machine performance against the engine velocity profile, clarifying the effect of current loading on LG force profile. Finally, the model is transferred to AMESim software and overall system performance is investigated for stable operation, electrical load sensitivity and most importantly cogging force and its effect on system performance. The model also accounts for machine loading and total efficiency variation over a mechanical cycle. This enables the system designer to investigate the effect of the actual LG model reacting force on the engine performance, rather than assuming the electrical machine behaves simply as a damper. As a contribution to existing work, combined effects of electromagnetic forces and losses have never been considered before. Moreover, the effects of machine inductance and electrical loading on the LG reacting force have not been highlighted earlier, which is one of the merits in the operation of the integrated system.

6.2 System description

A simplified schematic diagram of the system is shown in Figure 6-1. Recalling the steady-state balanced force equation of the reversible (oscillating) system from Chapter three, repeated below:

$$\pm \overrightarrow{F_{E1,2}} + \overrightarrow{F_{LG1,2}} + \overrightarrow{F_{C1,2}} = a \cdot M_m \quad 6-1$$

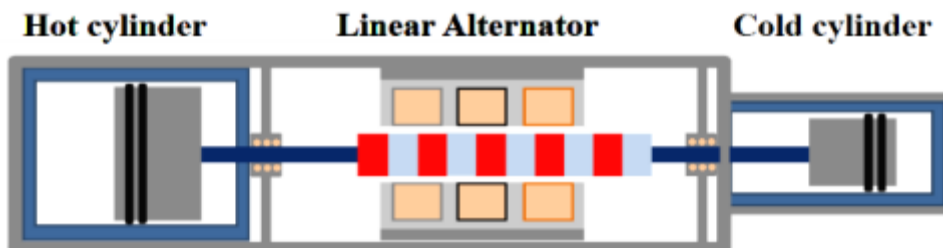


Figure 6-1: Simplified schematic diagram of the integrated system

The term $(a.M_m)$ represents the acceleration multiplied by total moving mass obeying Newton's second law of motion. The left hand term consists of three parts. The first part ($\overrightarrow{F_{E1,2}}$) is the driving force (s) which is generated in the expanding cylinder of double – acting pistons [107] shown on the left of the system in Figure 6-1.

A similar structure is found on the right side of the system, where this cylinder represents a compressor producing the reacting forces ($\overrightarrow{F_{C1,2}}$). The third term is the LG reacting force ($\overrightarrow{F_{LG}}$), bolded in (6-1), which is shown in the middle of the system. System frictional loss, in general, vary linearly with system speed. Friction loss is composed of system linear bearings loss and piston – cylinder loss, and due to the direct coupling of LG translator with pistons via the connecting rod, this loss has low values and in steady – state analysis it can be assumed constant [5, 105]. This loss is accounted for in the engine model.

As described before, the reacting force of the LG was approximated by a simple damper elsewhere [102, 104, 106], and therefore it was not accurately representing the actual behaviour of the machine. By using partitioning of this force into its components, a mathematical model is derived taking into consideration all machine performance parameters and forces which are determined using empirical equations and based on slot/pole number combination [116].

6.3 Linear Generator reacting force components

The machine model designed for resistive loading in Chapter 5 was shown to have the highest efficiency. Also, it offers flexibility in applying different loading conditions by varying the load resistance. The LG reacting force in (6-1) can be subdivided as follows:

$$\overrightarrow{F_{LG1,2}} = \overrightarrow{F_{cog}} + \overrightarrow{F_{AR}} + \overrightarrow{F_{cu\ loss}} + \overrightarrow{F_{iron\ loss}} + \overrightarrow{F_{PMec}} + \overrightarrow{F_{ele}} \quad 6-2$$

6.3.1 Cogging force

The first right hand term in (6-2) represents the inherent cogging force ($\overrightarrow{F_{cog}}$) which was defined earlier and is due to the variation in the reluctance seen by magnets due to stator teeth, with periodicity (R_c) depending on the number of stator slots and translator poles. It can be approximated to sinusoidal variation along translator motion and its expression given in (5-1) may be written as:

$$\overrightarrow{F_{cog}}(x) = \hat{F}_{cm} \cdot \sin\left(\frac{x \cdot \pi \cdot R_c}{\tau_p} \pm \vartheta_c\right) \quad 6-3$$

The amplitude of cogging force (\hat{F}_{cm}) is found from FEA results at no-load condition. In previous machine FEA modelling procedures, the use of boundary condition assume the model represents 7 pole pitches of an infinitely long machine. Therefore, the cogging force retrieved was only due to stator slotting. In the adopted machine topology with a long translator - short stator, both the slot and the stator ends contribute to the cogging force, as both are active during system operation. For example, if the translator is set at the far left end of the motion path, the right end cogging force is active in addition to that due to slotting, see Figure 6-2 (a). At an arbitrary position of motion path apart from motion ends, see Figure 6-2(b) both ends and slot cogging forces are active and so on.

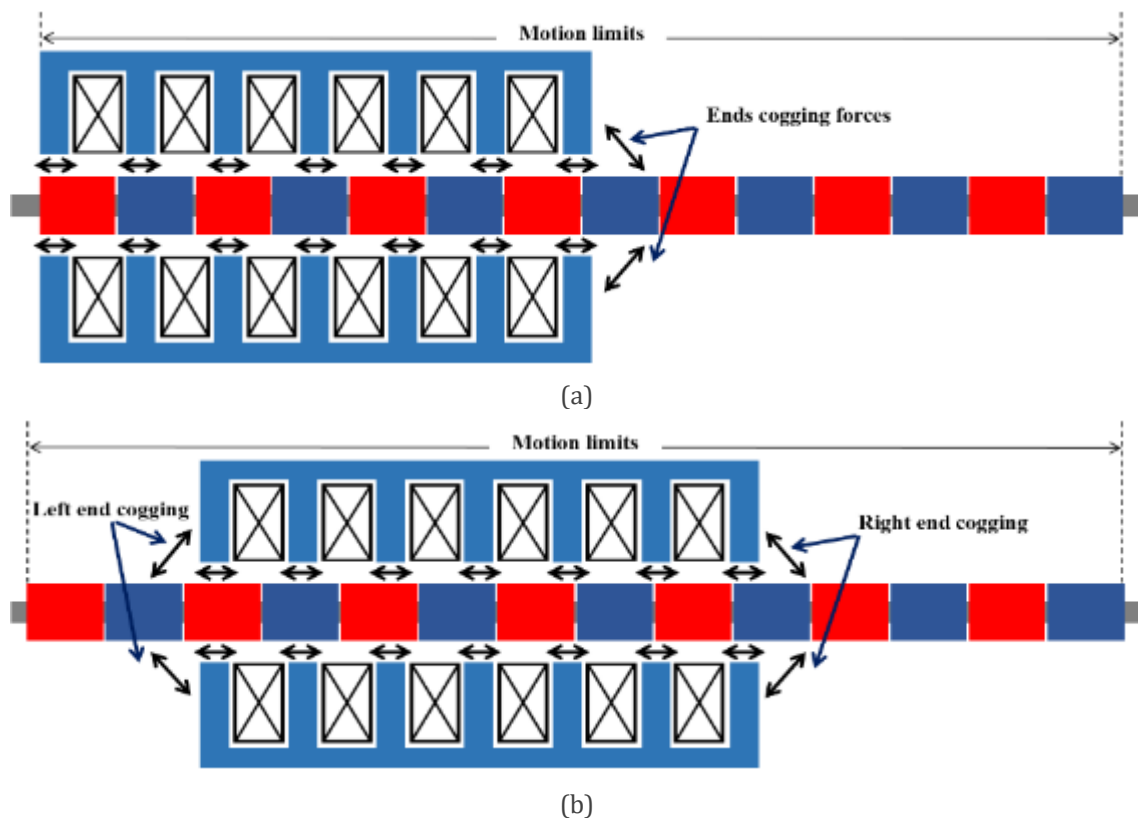


Figure 6-2: Short Stator-Long Translator machine topology showing slot and end cogging at (a) Left motion limit; and (b) Arbitrary position between motion limits

In the machine mathematical model to be analysed, both forces are investigated and therefore two cases emerge. The first case (Case I) considers cogging force due to the stator slotting only, while the second case (Case II) considers the resultant combined forces, see Figure 6-3.

As can be seen, the cogging force amplitude and the periodicity cycles are case sensitive, appreciating that end cogging forces are much higher compared to that due to slot cogging [109, 131], the effect of this will be explained in more detail in the next chapter.

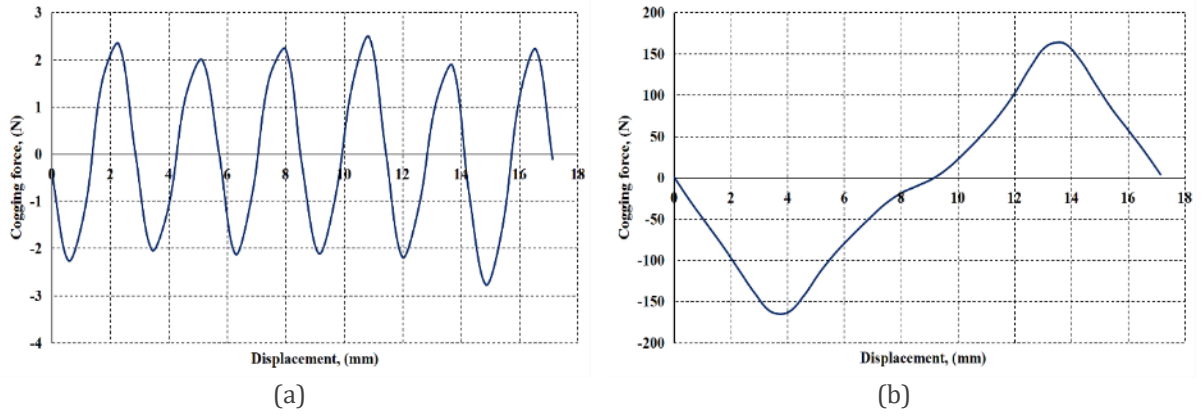


Figure 6-3: Cogging force variation over one pole pitch due to (a) Stator slotting – case I; and (b) Stator slotting and ends – case II (FEA)

Also, it is obvious that cogging cycles in case II is reduced to be one over half an electrical cycle, two for the whole cycle as there is only two stator ends, and therefore R_c in (6-3) is reduced to be (2) and hence:

$$\bar{F}_{cog}(x) = \hat{F}_{cm} \cdot \sin\left(\frac{2 \cdot x \cdot \pi}{\tau_p} \pm \vartheta_c\right) \quad 6-4$$

6.3.2 Armature reaction (reluctance) force

The second term in (6-2), \bar{F}_{AR} represents the armature reaction force of amplitude (\hat{F}_r) and is due to coil current driven flux. It varies with the electrical current loading and the mover position with repetition cycles equal to the number of machine phases (m) over one translator pole pitch as shown in Figure 6-4. In general, the armature reaction force is in phase with stator travelling MMF, and is given as:

$$\bar{F}_{AR}(x) = \hat{F}_r \cdot \sin\left(\frac{m \cdot \pi \cdot x}{\tau_p}\right) \quad 6-5$$

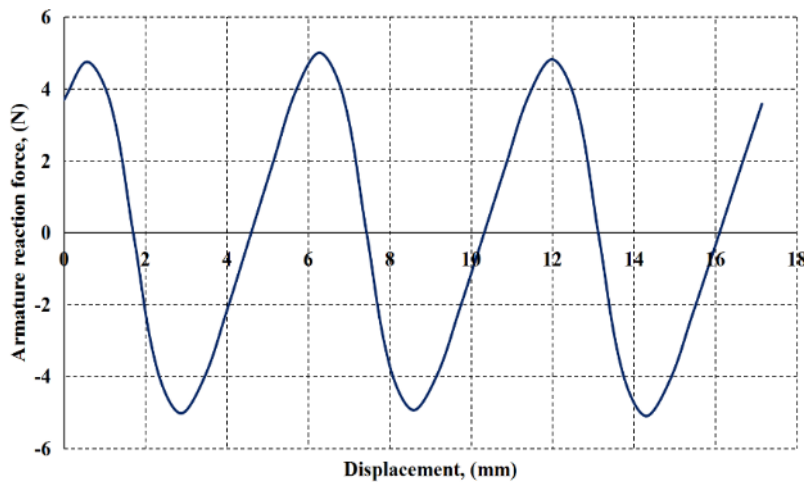


Figure 6-4: Armature reaction force variation over one pole pitch due to rated current, FEA

6.3.3 Back EMF and phase inductance

There is a sinusoidal variation of useful air-gap flux with position, peaking at ($\hat{\phi}$), shown in Figure 6-5, for a constant velocity of (v , m/s). Hence for a coil of (N) turns per phase, the phase induced EMF (\bar{E}_{ph}) can be calculated using the expression in (3-8) Chapter three, expressed as follows:

$$\bar{E}_{ph} = -N \frac{d\phi}{dx} = -N \cdot \omega \cdot \hat{\phi}_{ph} \cdot \cos(\omega x) \cdot v, \text{ (V)} \quad 6-6$$

With $\omega = 2\pi f_e$; and f_e is the electrical frequency.

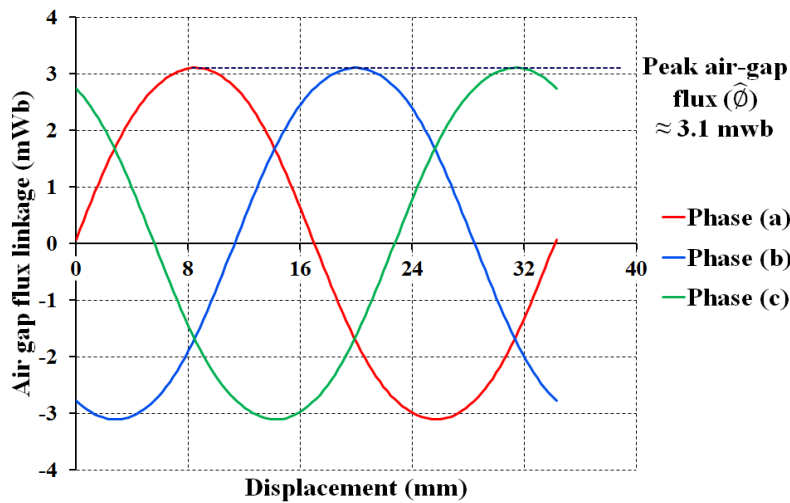


Figure 6-5: Variation of air gap flux with translator position over one electrical cycle (FEA)

Per phase machine inductance (L_{ph}) is obtained using FEA results as shown in Figure 6-6, where the variation of phase inductance over position is clarified for all phase. Although the variation of inductance may be considered negligible ($<1\%$), the effective value is taken to be the average of this variation, which is almost the same for all phases.

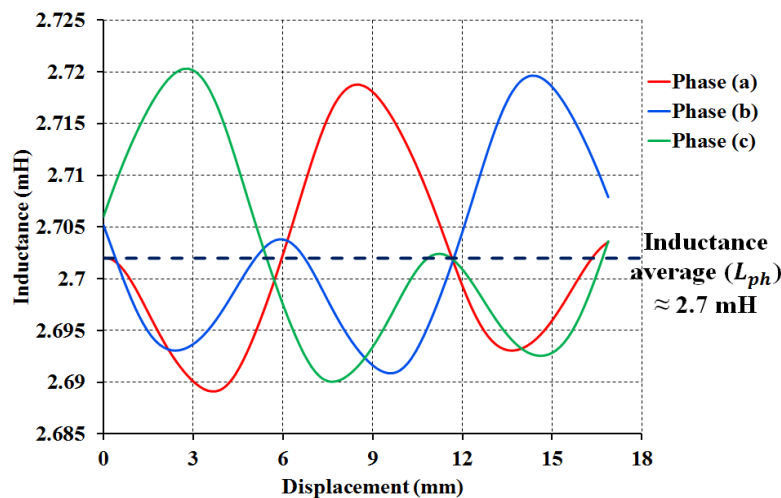


Figure 6-6: Variation of phase inductance with translator position over half an electrical cycle (FEA)

6.3.4 Equivalent circuit and phase resistance

Equation (6-7) was used to calculate the per phase effective resistance in the FEA model by knowing the copper loss at any loading condition, where:

$$R_{ph} = \frac{P_{cu(ph)}}{\bar{I}_{ph}^2}, \quad (\text{Ohm}) \quad 6-7$$

Using the per phase equivalent circuit diagram shown in Figure 6-7, assuming balanced variable resistive load, phase currents can be obtained from:

$$\begin{aligned} \bar{I}_a &= \frac{1}{L_a} \int [\bar{E}_a - \bar{I}_a(R_L + R_a)] dt \\ \bar{I}_b &= \frac{1}{L_b} \int [\bar{E}_b - \bar{I}_b(R_L + R_b)] dt, \quad (\text{A}) \\ \bar{I}_c &= \frac{1}{L_c} \int [\bar{E}_c - \bar{I}_c(R_L + R_c)] dt \end{aligned} \quad 6-8$$

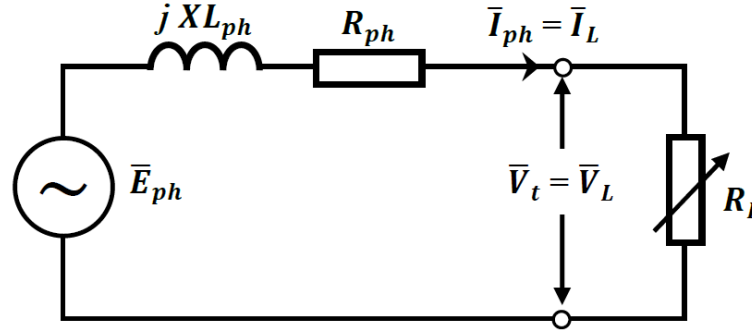


Figure 6-7: Per phase equivalent circuit of a Linear Generator supplying variable resistive load

6.3.5 Losses

By knowing the phase currents and resistances, the force representing the copper loss is determined in (6-9):

$$\bar{F}_{cu\ loss} = (I_a^2 \cdot R_a + I_b^2 \cdot R_b + I_c^2 \cdot R_c) / v, \quad (\text{N}) \quad 6-9$$

Machine iron loss (P_{iron}) components are the hysteresis (P_h) and eddy currents (P_e) losses of magnetic circuit material. Additionally, eddy current losses are present in the magnets and the supporting tube (P_{Pmec}) due to translator motion in the combined interacting magnetic fields of magnets and that of stator winding travelling MMF field. These losses also obtainable from FEA results are shown in Figure 6-8.

These losses are responsible for producing the combined force (\bar{F}_{loss}) that varies with system velocity, being maximum at the motion center and minimum or zero at both ends. With a constant (C_{loss}) representing these velocity dependant losses that can be found from the curve, this force is determined in (6-10) as:

$$\bar{F}_{loss} = C_{loss} \cdot v, \quad (\text{N}) \quad 6-10$$

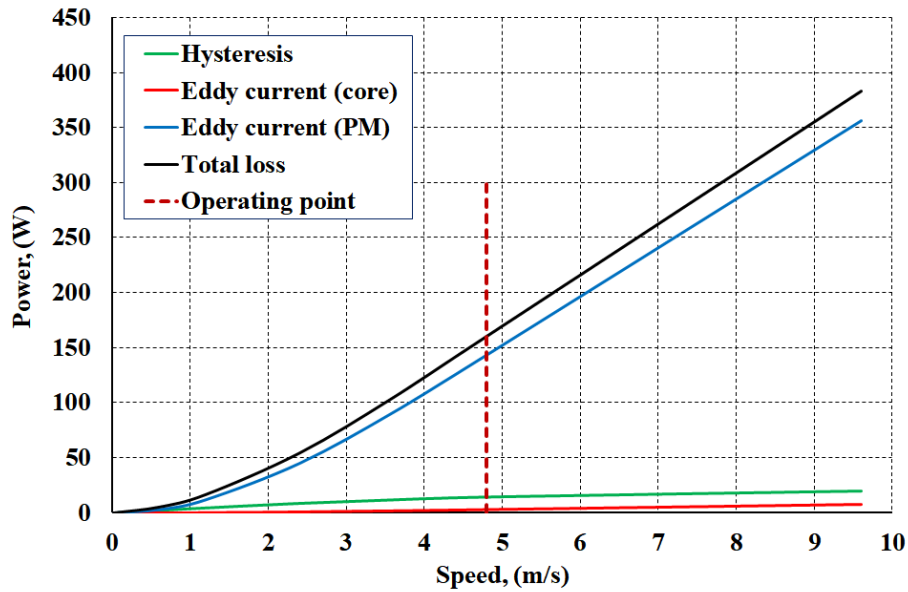


Figure 6-8: Core loss and magnets eddy currents loss variation with speed at rated load (FEA)

6.3.6 Electrical power generated and efficiency

Machine electrical power output and the corresponding force (\bar{F}_{ele}) can be explained as given in (6-11) with the machine efficiency obtained using (6-12).

$$\bar{F}_{ele} = (I_a^2 \cdot R_L + I_b^2 \cdot R_L + I_c^2 \cdot R_L) / v, \quad (\text{N}) \quad 6-11$$

And

$$\% \eta = \frac{\text{output}}{\text{input}} = \frac{\bar{F}_{ele}}{\bar{F}_{LG}} \times 100\% \quad 6-12$$

6.4 Analytic model validation

A general machine analytic model has been built in MATLAB/Simulink. Useful design model and optimal machine data used in the analytic model are listed in Table 6-1 for the resistive loading power conversion scenario design. The table also includes useful data obtained from analysing the optimal design model using FEA with maximum engine speed. These data include per phase equivalent circuit parameters, peaks of cogging and armature reaction forces (\hat{F}_{cm} and \hat{F}_r), iron loss components and PM eddy currents loss.

The general MATLAB/Simulink model Framework is shown in Figure 6-9, while the detailed model is shown in Figure 6-10. At rated load, both the LG analytic and FEA models are investigated against the engine's velocity profile when driving a simplified damper, Chapter Three - Figure 3-4(a), in a feedforward manner as shown in Figure 6-11.

Table 6-1: Useful dimensions and machine performance parameters for the resistive loading design model

Parameter, symbol (unit)	Value
Stroke amplitude, (mm)	120
Rated power output, (kW)	3.35
Phases, m	3
Slots, N_S	6
Turns per phase, N	40
Poles, N_p	7
Translator pole pitch, τ_{pp} (mm)	17.1428
Per phase resistance, R_{ph} (Ω)	0.227
Per phase inductance, L_{ph} (mH)	2.7
Resistive loading, R_L (Ω)	$2 \leq R_L \leq 12$
Peak air-gap flux, $\hat{\Phi}$ (mWb)	3.1
Peak cogging force due to slotting only, \hat{F}_{cm} (N)	2.5
Peak cogging force due to slotting and ends, \hat{F}_{cm} (N)	170
Peak armature reaction force, \hat{F}_r (N)	5
Core hysteresis and eddy currents losses, P_{iron} (W)	15.6
Magnets eddy currents loss, P_{Mec} (W)	136

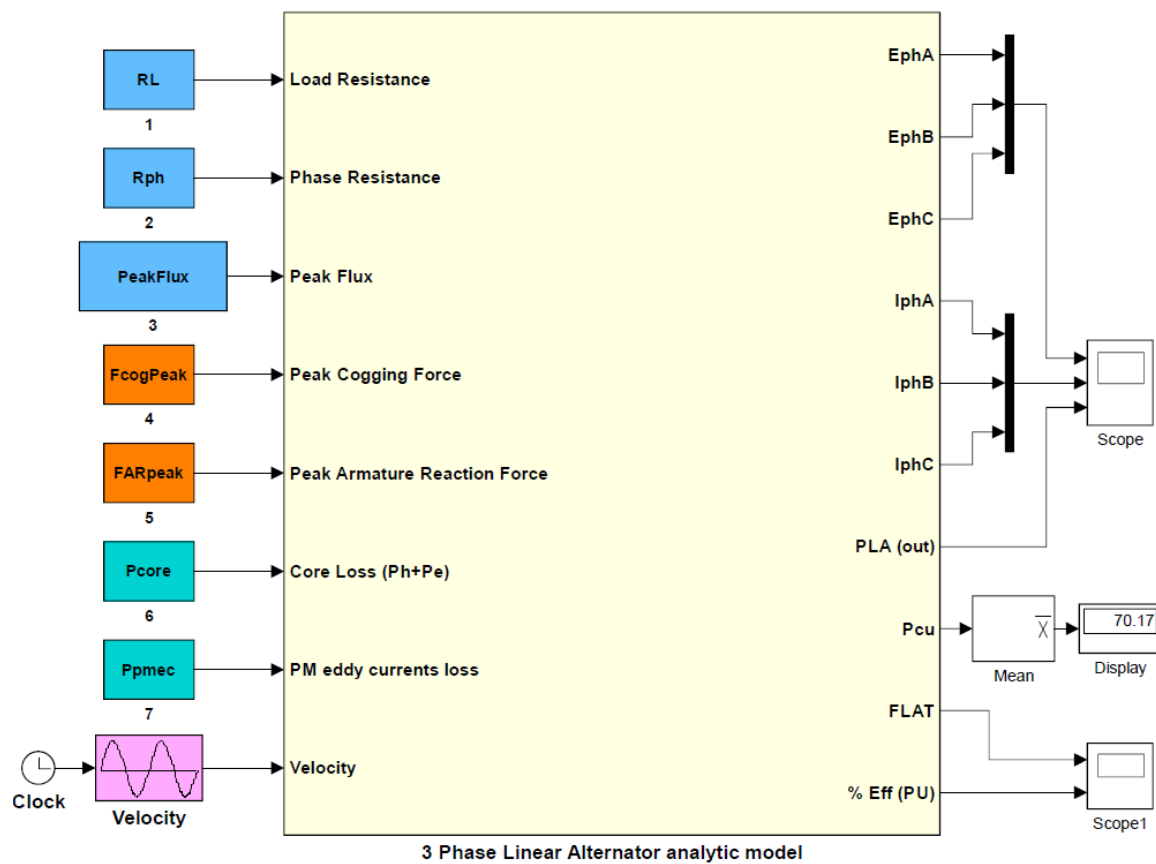


Figure 6-9: General Linear Generator analytic model implementation in MATLAB/SIMULINK

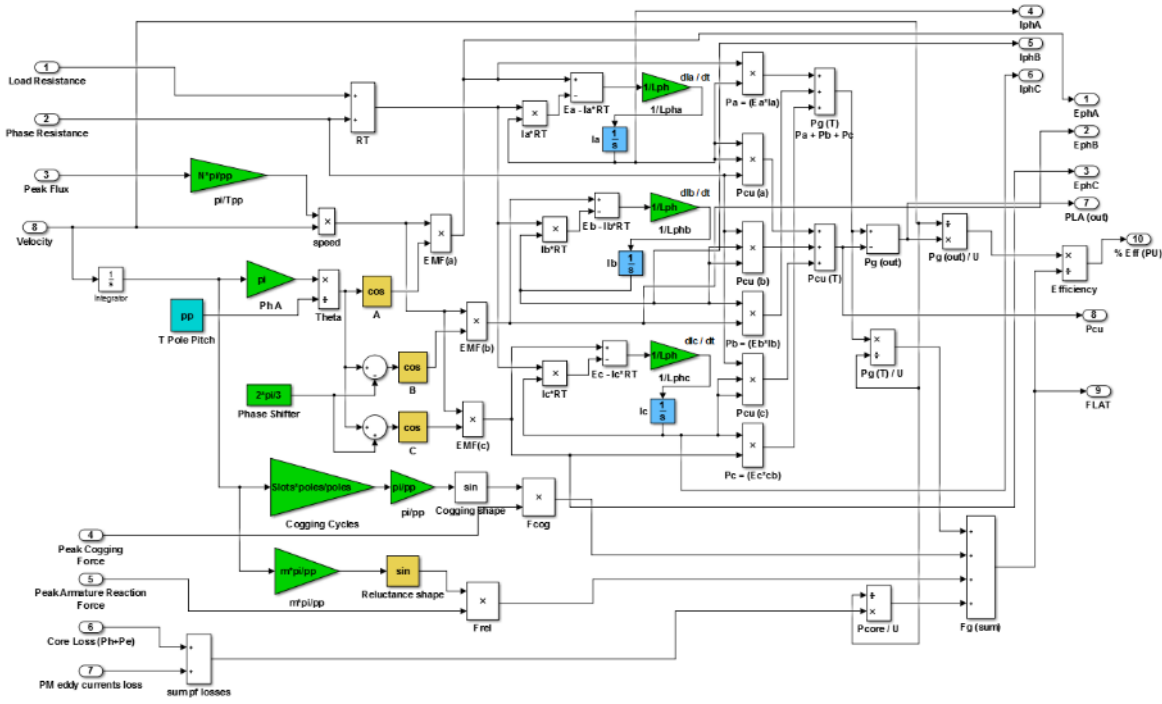


Figure 6-10: Detailed Linear Generator analytic model implemented in MATLAB/SIMULINK

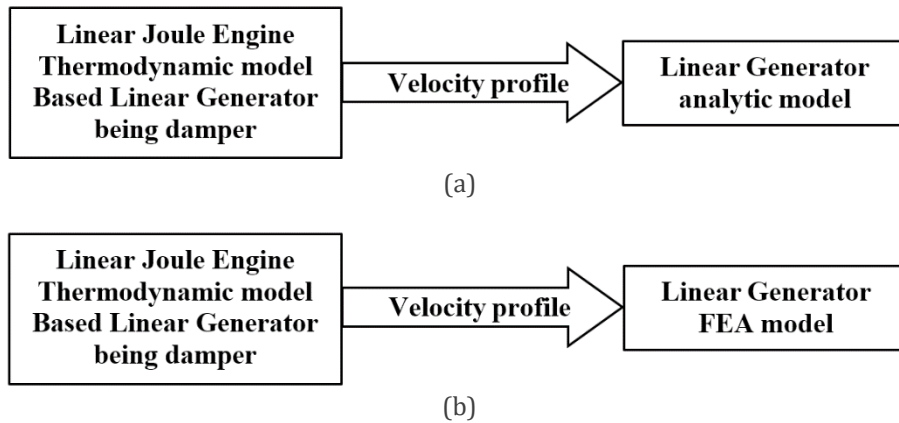


Figure 6-11: Feedforward investigation against engine's velocity profile (a) Analytic model; (b) FEA model

Using the analytic model, the variation of phase induced EMF, phase currents and power dumped in the load resistance, at peak load condition, are shown in Figure 6-12(a-c). Phase EMFs and currents show amplitudes imbalance over the entire mechanical cycle with variable electrical frequency (f_e) operation. The variation of the output power over the entire mechanical cycle shows a smooth profile, similar to the velocity profile.

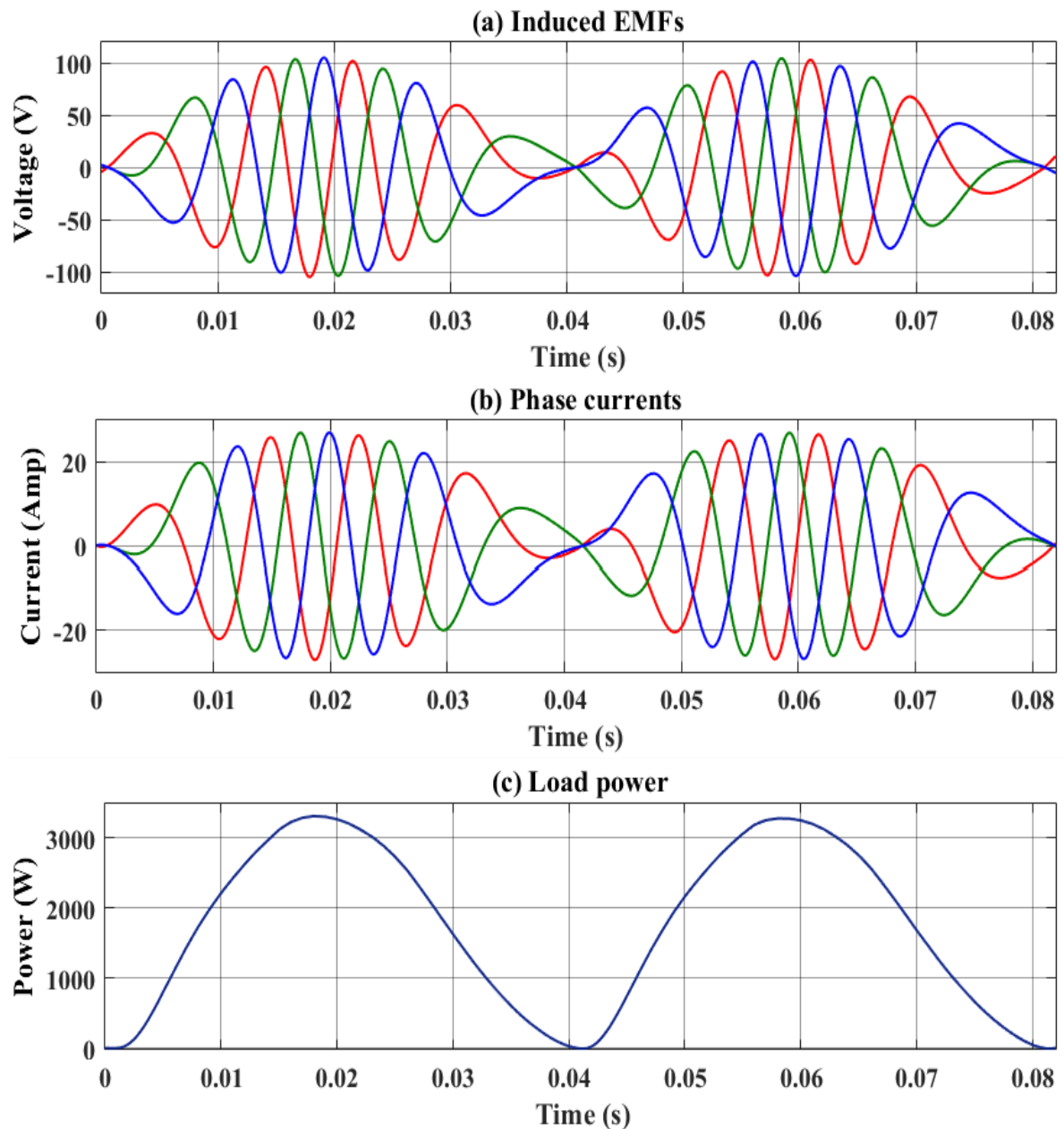


Figure 6-12: One mechanical cycle variation of (a) EMF induced per phase; (b) Phase currents; and (c) Electrical power dumped by the load

6.5 Electromagnetic force comparison

The LG electromagnetic force results obtained from both the analytic and the FEA models are compared with that obtained from engine model when driving the simplified damper approximating the linear machine, Chapter Three - Figure 3-4(b). The force comparison is shown in Figure 6-13. First of all, it is clear that the force predicted analytically is considered in a good agreement with that obtained from FEA model. The force fluctuation, identified with both simulation tools, is obvious and its origins are from the combined effect of the interacting cogging and armature reaction forces superimposed on the electrical power force profile.

Secondly, when comparing the LG force from a damper, as normally used to represent the LG force [103-105], with the force results using both simulation tools a difference is clearly seen. The effect of machine inductance works in adding forces reflecting the stored/released energy in phase inductance due to the variable speed operation over the entire mechanical cycle. The resultant total LG force is a flat profile, with fluctuation, and this may have an impact on the thermodynamic performance of the engine.

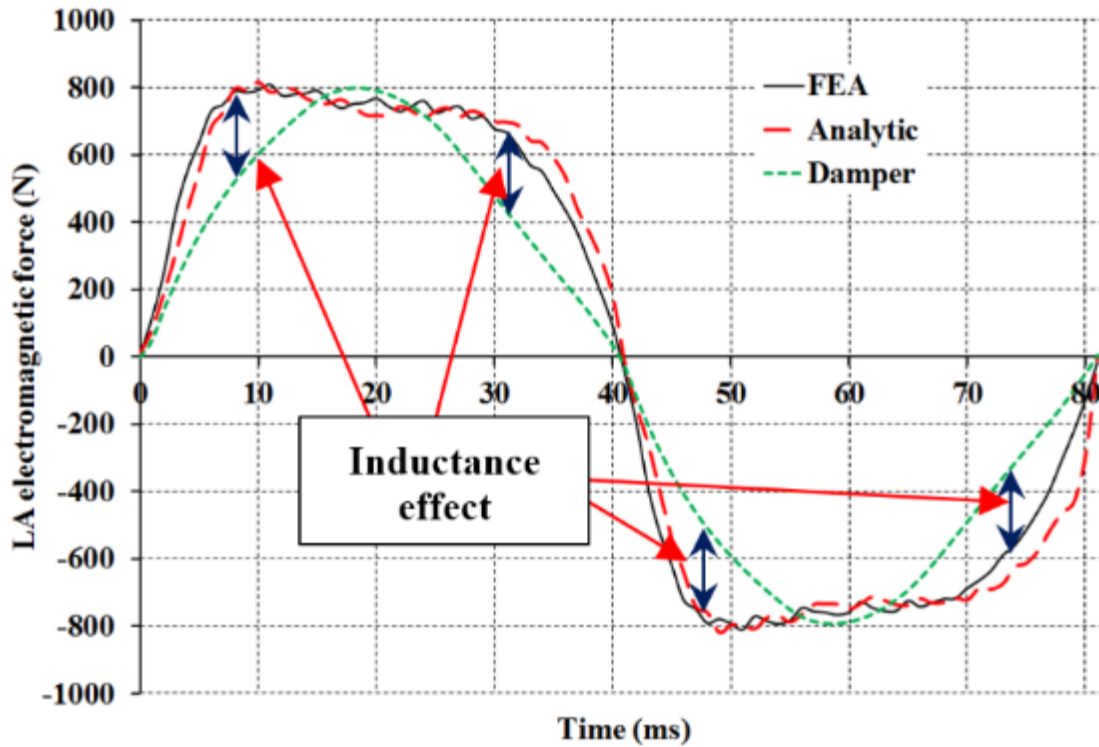


Figure 6-13: Linear Generator reacting force profile comparison and inductance effect

However, results show that LG force profile follows the velocity profile at loads lower than the peak (rated) load, see Figure 6-14. This linear variation changes as the load exceeds 76 % of the machine rating and results in a flattening of the force profile. Above that point of loading, the effective load resistance increases the time constant of the series phase circuit and causes a fast decay of inductance voltage across phase resistors, accompanied by a rise in the rate of change of phase current with time (dI_{ph}/dt). As a consequence, higher energy will be stored (released) in phase inductance which must be supplied by the driving engine to the machine as an extra force, as clarified by arrows in Figure 6-13. Such a force profile shape will have an effect on engine behaviour when compared with a damper force, and the result will be unpredictable on the interconnected processes.

The most important parameter for consistency between the electric machine and engine models is the engine compression ratio, as any change in this parameter would affect the stroke amplitude and the total system dynamic stability.

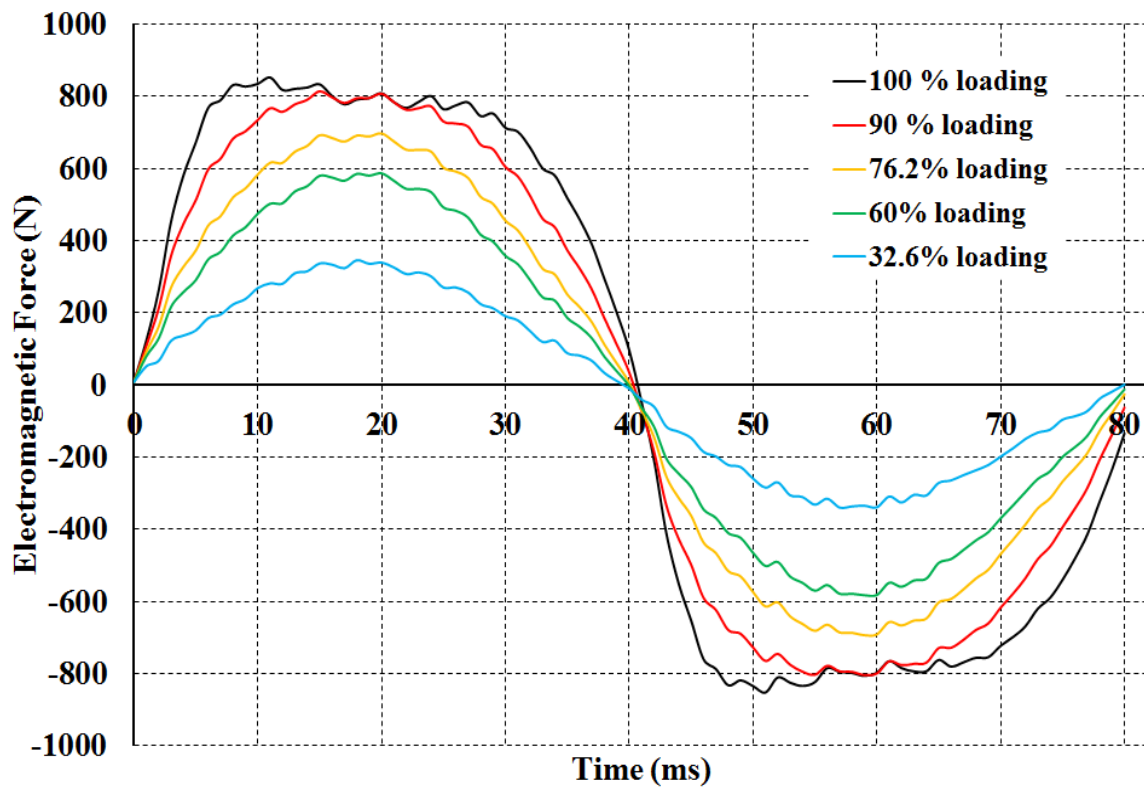


Figure 6-14: Linear Generator reacting force profile variation with load over one mechanical cycle

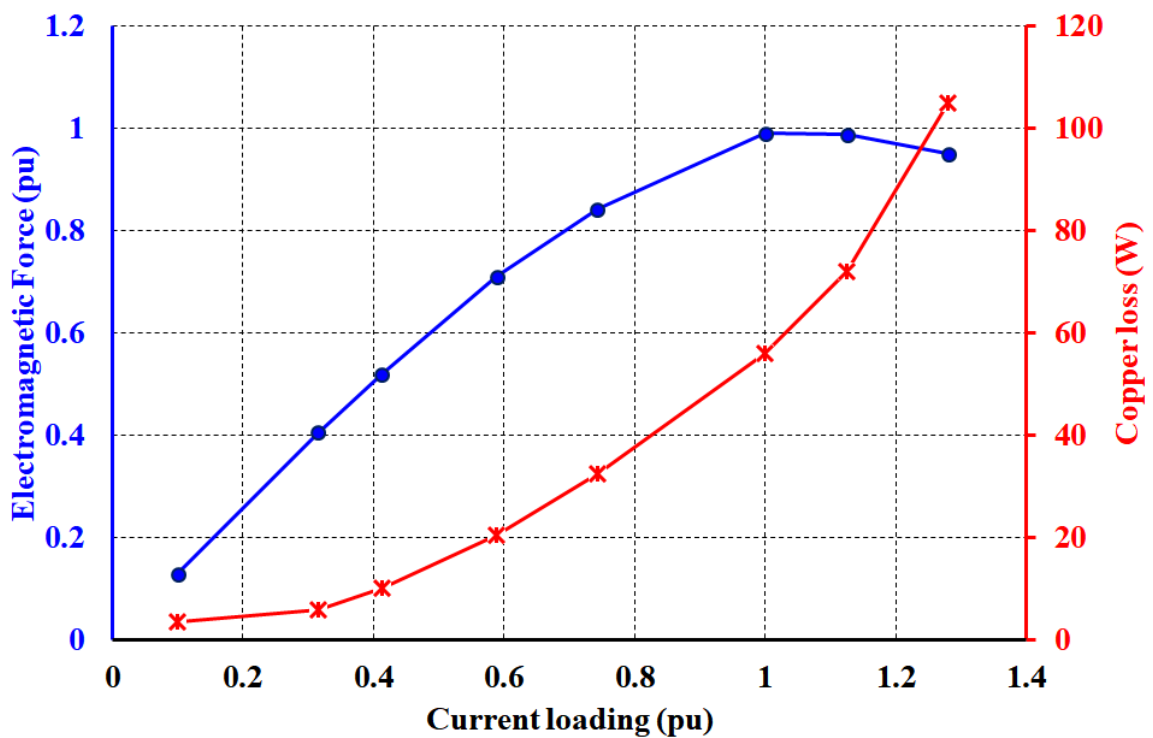


Figure 6-15: Variation of electromagnetic force and copper loss with current loading (FEA)

The FEA model is used for further investigation on machine performance prediction at different loading conditions. The effect of current loading on the resultant electromagnetic force and copper loss, both averaged over one electrical cycle, is shown in Figure 6-15. It is obvious that the force capability increases with current loading until reaching the design force. Any further current increase would result in increasing the copper losses of the machine and the consequent reduction of the resulting force. This relationship has been described by other research groups [101, 105, 106] to be linear, and the fact is linearity starts to decline at current loading of almost 60 % of rated current till reaching peak loading and then further slow declination that starts due to the increased machine losses.

6.5.1 Effect of cogging force on machine performance

Analytic prediction of the effect of cogging forces on machine efficiency has been investigated. Figure 6-16 shows the variation of instantaneous LG dynamic efficiency over an entire mechanical cycle, with ignored ends effect (Case I). One important conclusion from this graph needs to be discussed here. It can be noticed that the efficiency is high over a wide span of the mechanical cycle. This indicates that the LG works at high efficiency value from a mechanical point of view. On the other hand, and from the electrical machine design point of view, the machine is working at an electrical efficiency according to its current loading, i.e. in this case it works with an electrical efficiency of only 0.76 pu.

When the cogging force with end effect is considered, (Case II), a larger effect on efficiency is noticed, with instants showing efficiency higher than unity as can be seen in Figure 6-17. The combined effect of these electromechanical forces, cogging and armature reaction, is therefore assisting or hindering the engine action while driving the LG translator. This bidirectional action increases with the amplitude of the cogging force which is in turn based on the size and topology of the machine.

A further view on the effect of cogging force on the machine efficiency, averaged over an entire mechanical cycle, against current loading is demonstrated in Figure 6-18 for the both cases. It can be seen that the efficiency increases with increasing current loading in Case I machine, i.e. when machine end effects are ignored. Case II machine model shows an efficiency experiencing decrease while current loading is increasing. On the other hand, accounting for end effects, higher efficiency value at peak electrical loading can be noticed with the fact that the resulting electromagnetic force has large force fluctuations. In practice, for both cases, as mentioned earlier, an unpredictable impact on engine compression ratio and the consequent variation in stroke amplitude and on the overall interconnected system dynamics would be a result.

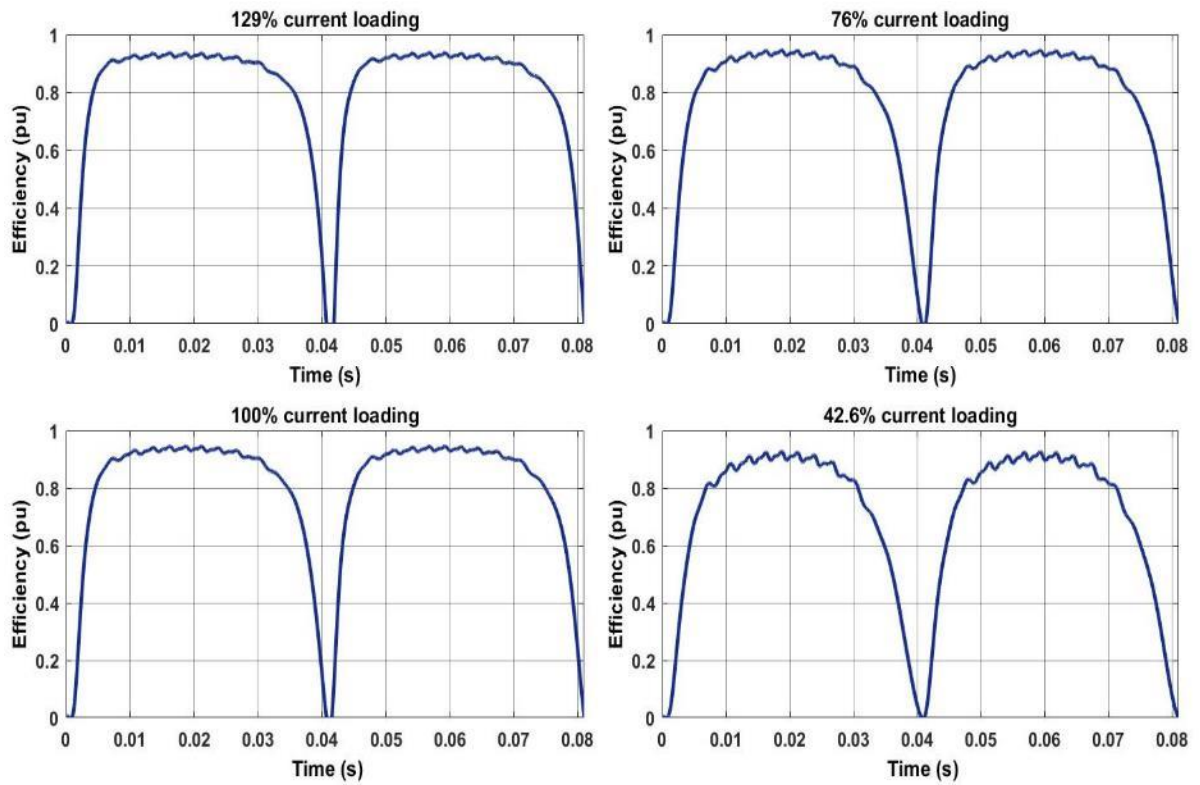


Figure 6-16: Effect of cogging force due to slot cogging and ignored end effects on the LG efficiency over entire mechanical cycle at different current loading (Case I)

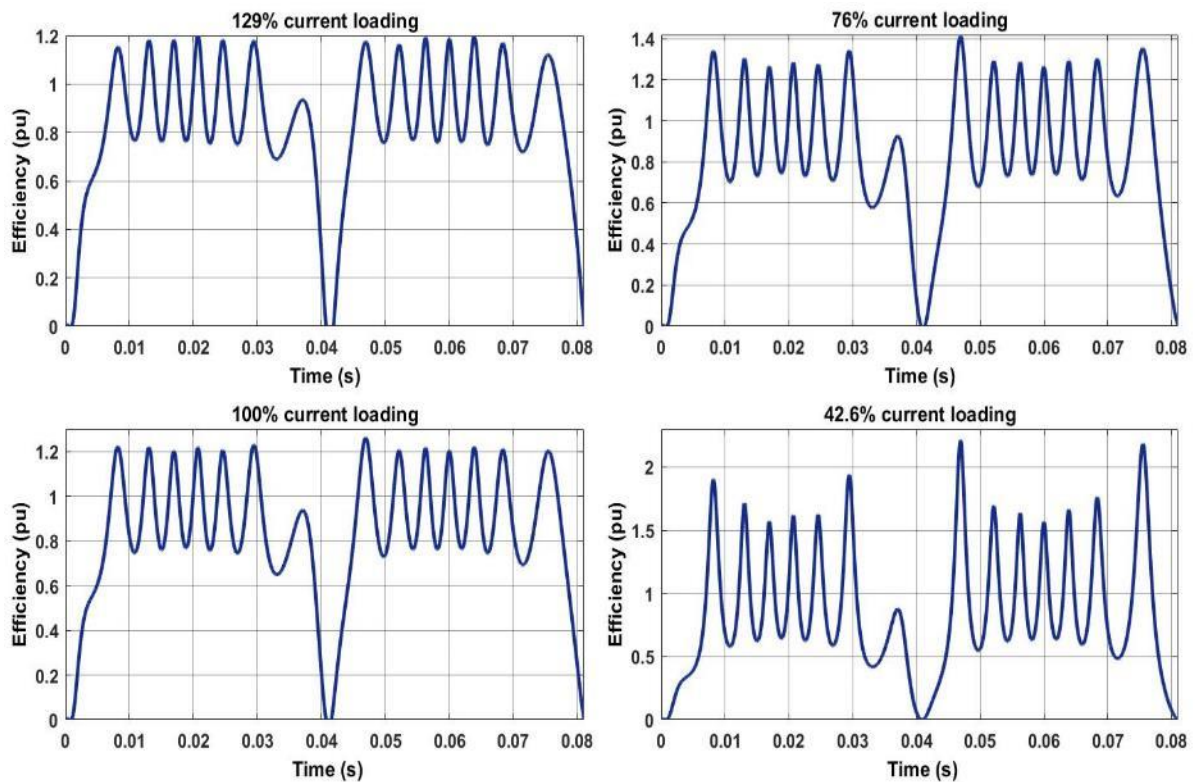


Figure 6-17: End effects on cogging force amplitude and LG efficiency over an entire mechanical cycle at different current loading (Case II)

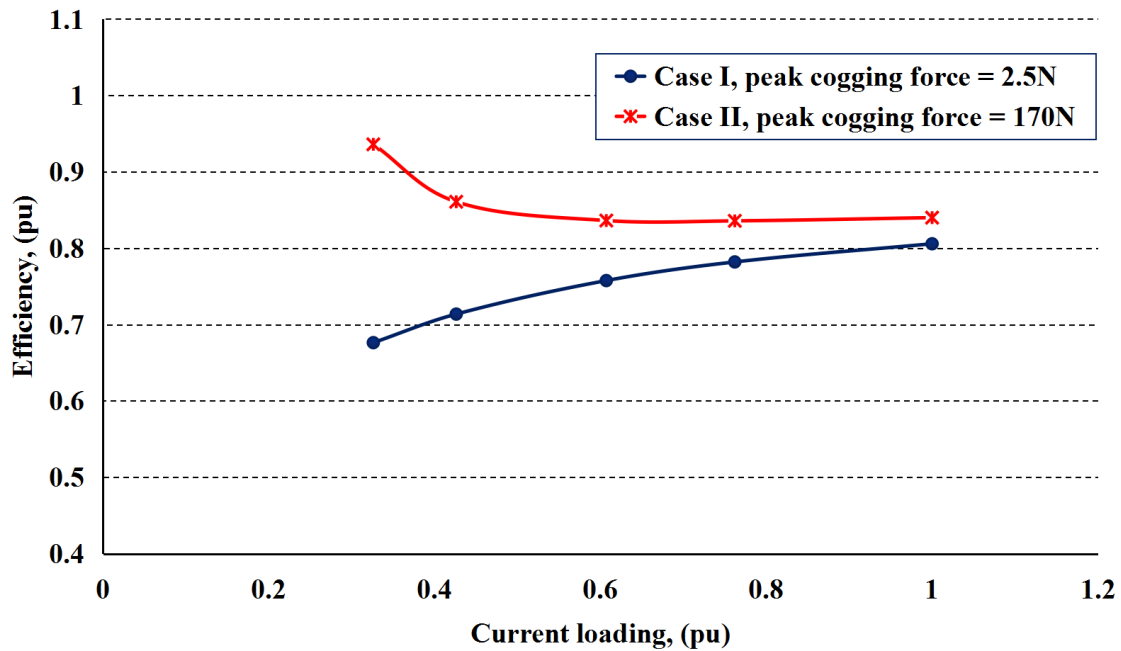
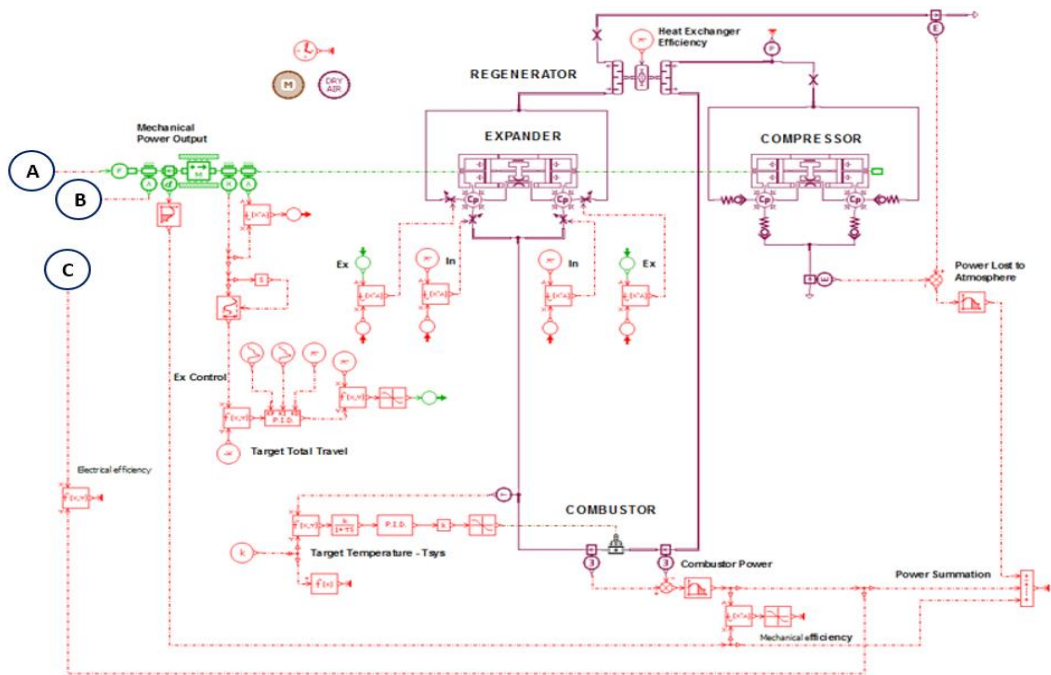


Figure 6-18: Effect of cogging force amplitude on LG efficiency averaged over the entire mechanical cycle at different current loading

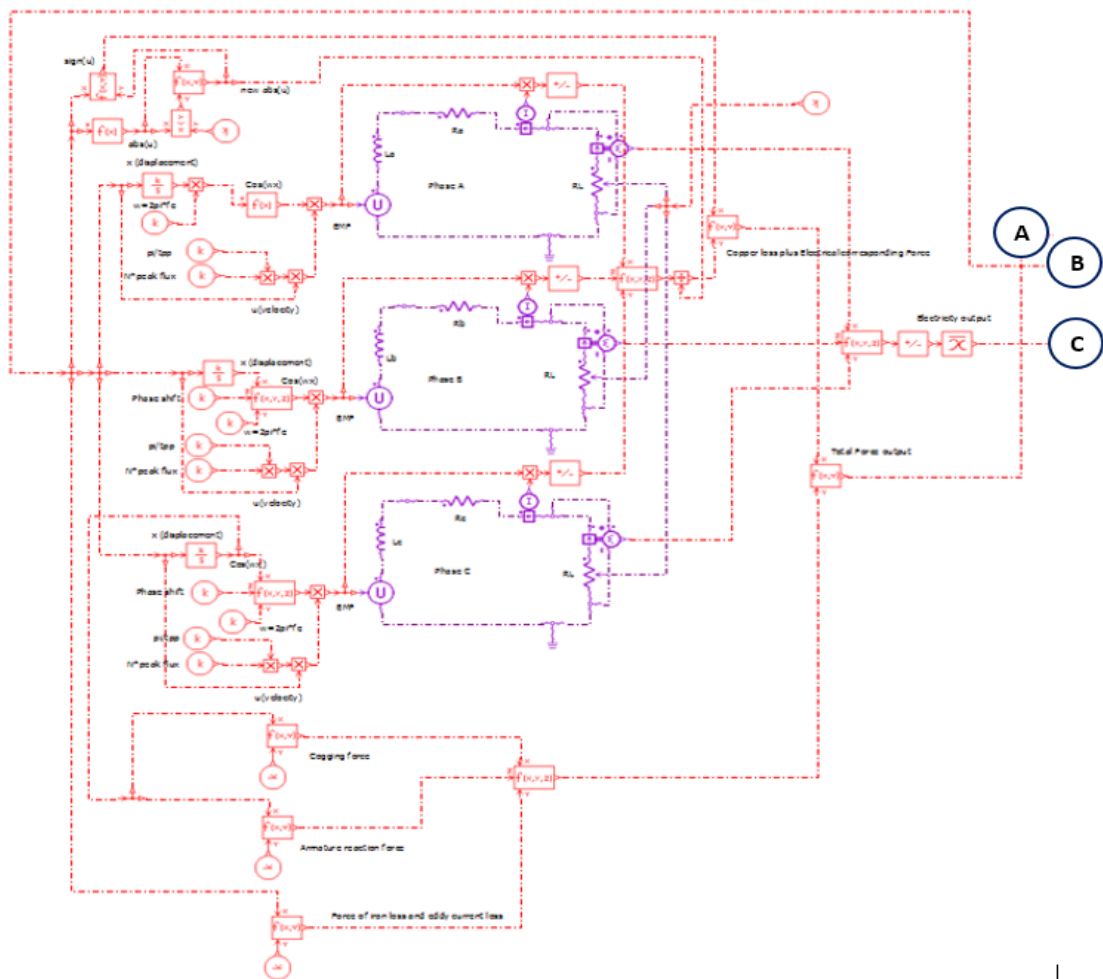
Therefore, the cogging force amplitude and its effect cannot be assessed or predicted unless a dynamic model incorporating both the engine and generator coupled dynamically is run. This is explained in the next section.

6.6 Coupled system model

In this section, a novel coupled dynamic model incorporating both the Linear Joule Engine model, described in Chapter 3, and the LG analytical model described in previous section replacing the damper is realized. The model using Siemens LMS Imagine.Lab AMESim is shown in Figure 6-19 overleaf. The system model is unique and works in a closed loop form as shown in Figure 6-20. Furthermore, the coupled model links the mechanical and electrical systems of the novel engine-alternator, and provides a solid dynamic performance prediction of the entire system. Investigating the dynamic operation of the overall system incorporating an accurate LG model gives increased accuracy for the system performance estimation, rather than predicting the performance of the coupled systems individually, as has been done previously. Two LG analytic model variable parameters have been selected to investigate their effects on system stability, LG efficiency, overall system efficiency and electrical power delivery. The variable parameters are the cogging force amplitude that varies according to machine topological variation (labelled as case I and case II), and the electrical loading of the LG by altering the resistive load.



(a)



(b)

Figure 6-19: Coupled System model in LMS (a) Linear Joule Engine model; (b) Linear Generator model

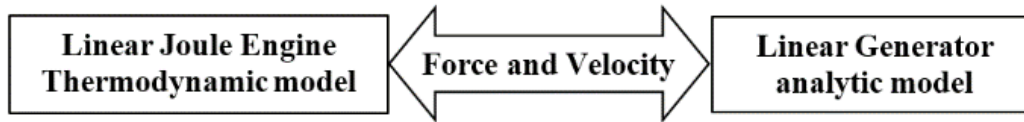


Figure 6-20: System integral model development

6.6.1 Operational performance

The system model is run for 36 seconds using the LG machine model (Case I), while the engine is powered by an 800 °C heat source. At steady-state operation, the achieved thermal and electrical efficiencies are 34 % and 30 % respectively, with a 1.88 kW electrical power generation. This makes the system desirable in micro-scale compared to its rival technologies [2, 121].

Table 6-2: Total electrical efficiency of the integrated system

Current loading, %	Total electrical efficiency, %		LG efficiency, %	
	Case I	Case II	Case I	Case II
1	29.83	---	93.92	---
97.16	29.71	---	93.81	---
96.99	---	30.04	---	93.8
95.68	---	30.22	---	93.92
95.67	---	29.3	---	93.54
94.31	29.56	---	93.68	---
94.15	---	29.28	---	93.67
91.56	29.39	---	93.52	---
88.97	28.05	---	93.4	---
88.84	---	29.05	---	93.4
84.01	---	27.78	---	93.12
84.00	27.76	---	93.11	---
78.96	---	26.67	---	92.82
78.91	27.43	---	92.82	---
71.45	---	25	---	92.12
71.4	25.2	---	92.19	---
65.25	---	23.88	---	91.52
65.21	24.04	---	91.52	---
59.95	---	22.03	---	90.84
59.91	22.59	---	90.85	---
55.32	---	20.84	---	90.15
55.28	21.05	---	90.15	---
51.46	---	20	---	89.49
51.42	19.32	---	89.45	---
47.98	---	18.4	---	88.76
47.94	19.09	---	88.76	---
31.18	13	12.67	83.39	83.56

For the same running time period, the system model is run under different load conditions upon reaching the stalling point of the engine. The system starts to approach a stable operation after eight (8) seconds. Hence, data is collected and analysed over one complete mechanical cycle at the end of the running period to ensure stable operation. Total system electrical efficiency is obtained using the formula in (6-13).

$$\% \text{ Total electrical efficiency} = \eta_{engine} \times \eta_{LG} \times 100\% \quad 6-13$$

By varying load resistance in the LG machine model (Cases I and II), the system electrical efficiency and the LG efficiency corresponds to each loading condition results listed in Table 6-2, and shown in Figure 6-21 and Figure 6-22.

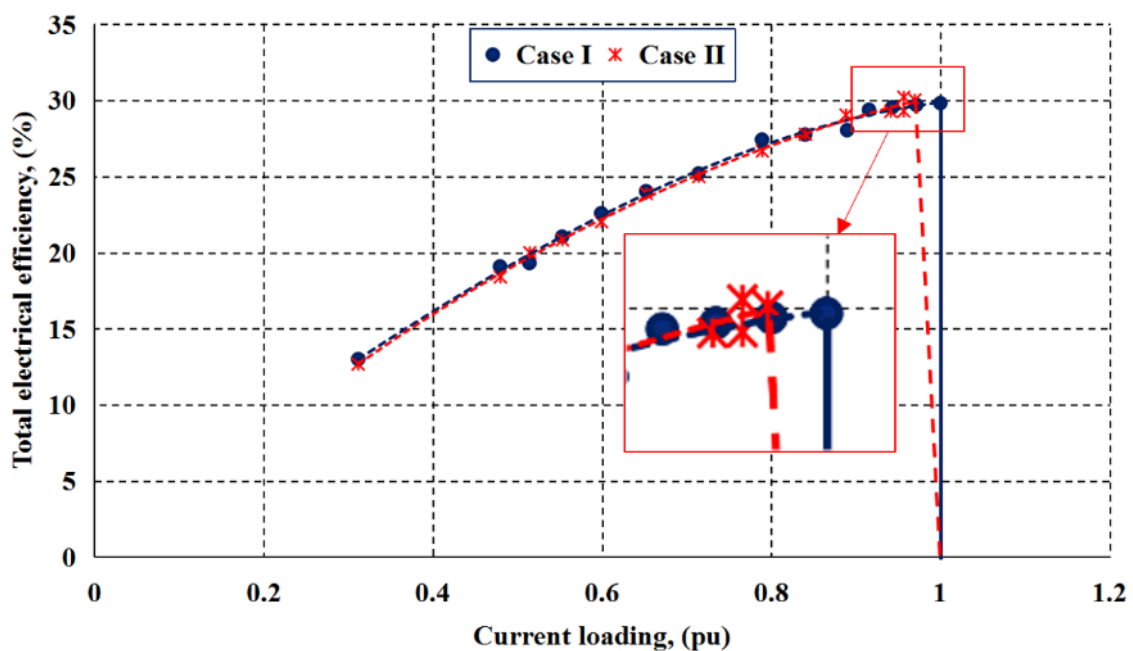


Figure 6-21: Total system electrical efficiency graph

The effect of high cogging force amplitude (Case II) is clearly seen in the tabulated efficiency results and graphs. Additionally, higher electrical loadings can be achieved at lower cogging force amplitudes (Case I).

A current value of only 97 % can only be achieved when the LG machine model exhibits a high cogging amplitude. Nevertheless, a higher system efficiency is achieved in machine model Case II, which implies that a high cogging force amplitude acts to assist the engine to drive the loaded LG machine model. An overall system electrical efficiency of 30 % is shown to be achievable by the system, while the LG can achieve an efficiency of ($\leq 94\%$) for both cases even with the lower current loading in Case II compared to Case I.

The converged overall system electrical efficiency for both LG models imply that the engine supplies all the reflected LG force components. Hence, as the cogging force amplitude is high, the engine force transduced into electrical power becomes lower resulting in a lower electrical power generated over an entire mechanical cycle which explains the reduction in the LG current rating for the same applied load in Case II system model.

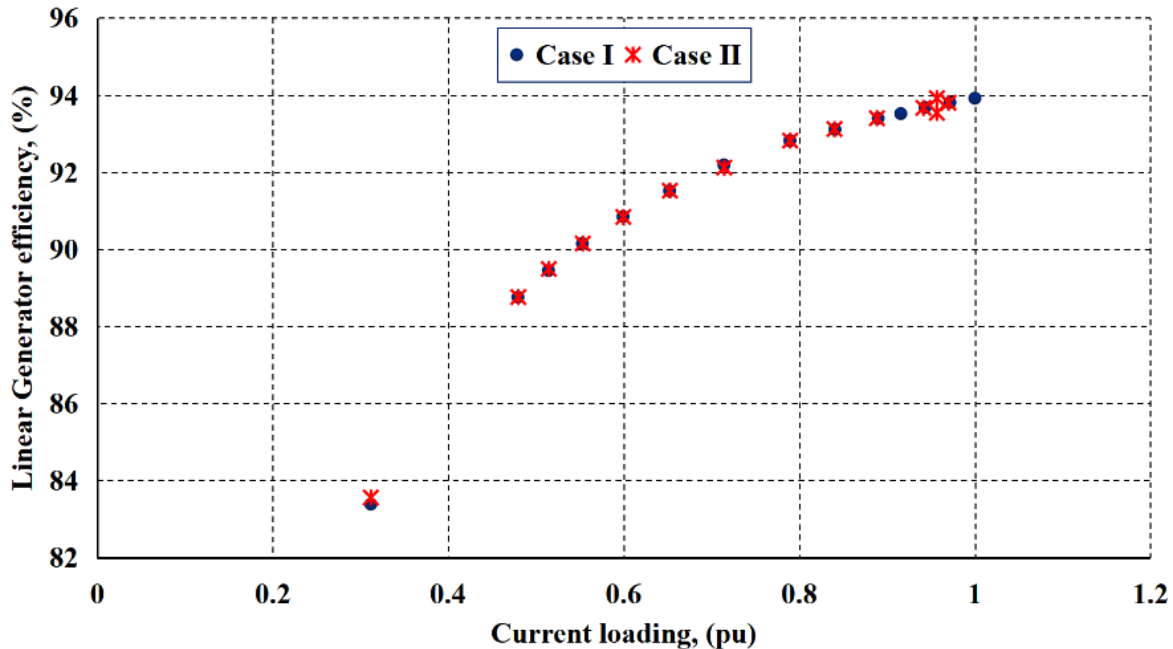


Figure 6-22: Linear Generator efficiency graph

6.6.2 System frequency and electrical power generated

At the rated load of each LG models, the variation with time of the electrical power generated in the first second for both cases is shown in Figure 6-23, where it can be seen clearly that the system with LG model of high cogging force (Case II) responds in a slower manner to the driving engine during first ($t = 0.4$ seconds) of operation, where divergence between the two curves can be seen.

This divergence continues until both systems reach stable operational margins, as observed by monitoring the system mechanical frequency (f_m), as shown in Figure 6-24. Focusing on the time after ($t = 4$ seconds) just for clarity. The system with LG model Case I runs faster, i.e. the high cogging force in the system with LG model Case II causes a slower system operation, or the existence of high cogging force in the LG has a decelerating effect on the overall operating system.

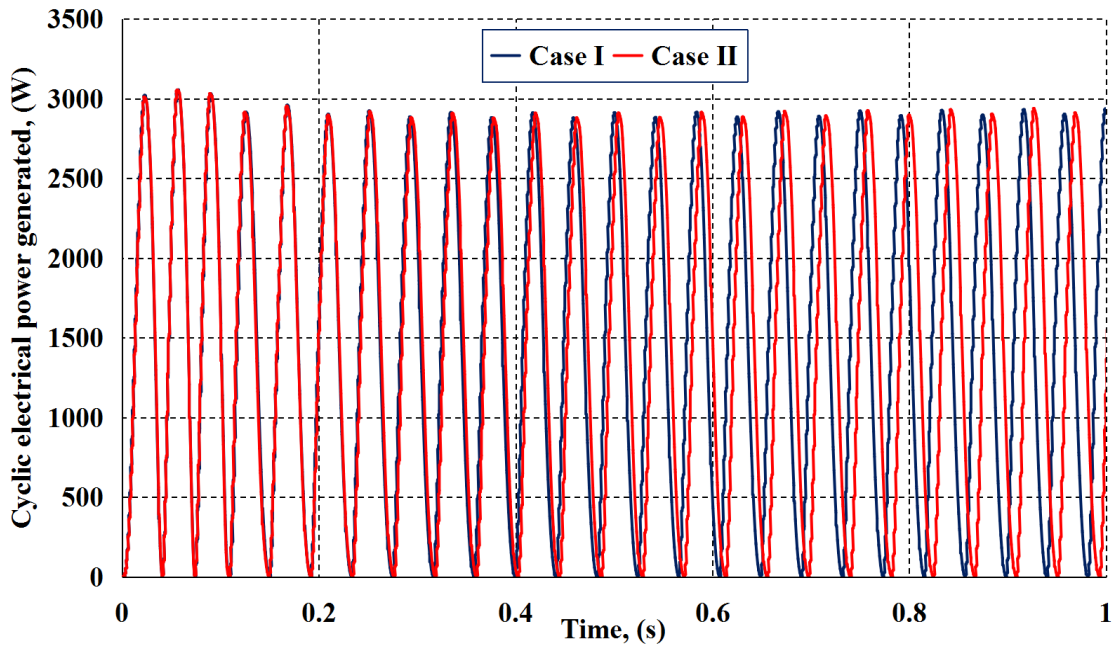
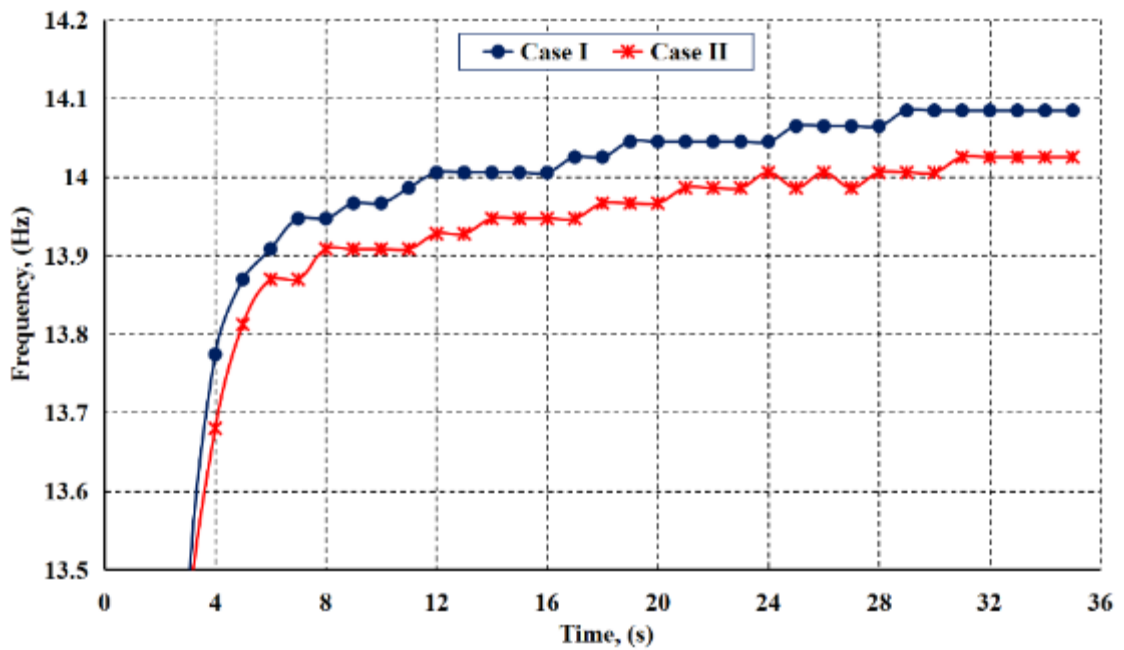


Figure 6-23: Linear Generator cyclic electrical power generated variation with time

Figure 6-24: System cyclic mechanical frequency (f_m)

This decelerating effect has the impact of reducing the total electrical power generated, over the mechanical cycle, as can be seen in Figure 6-25, which is decreased by (0.56%) at rated load. This electrical power decrease is a combined effect of the reduced current loading, in addition to the reduced EMF generated per phase influenced by a decrease of (0.21%) in peak system velocity, see Figure 6-26.

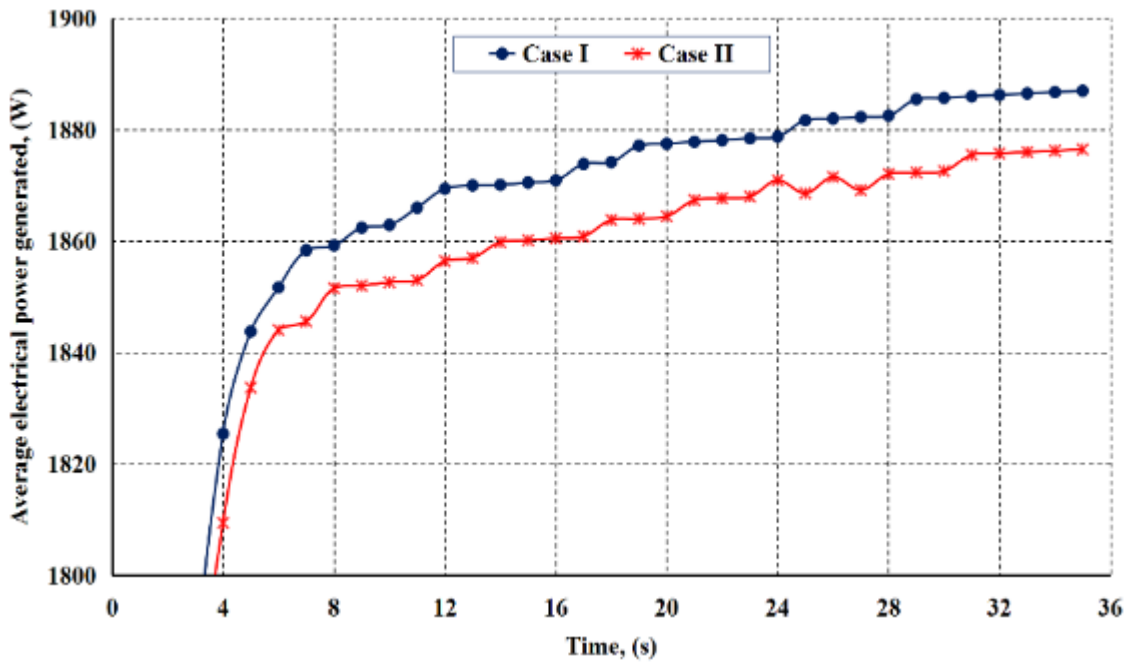


Figure 6-25: Averaged electrical power generated versus time

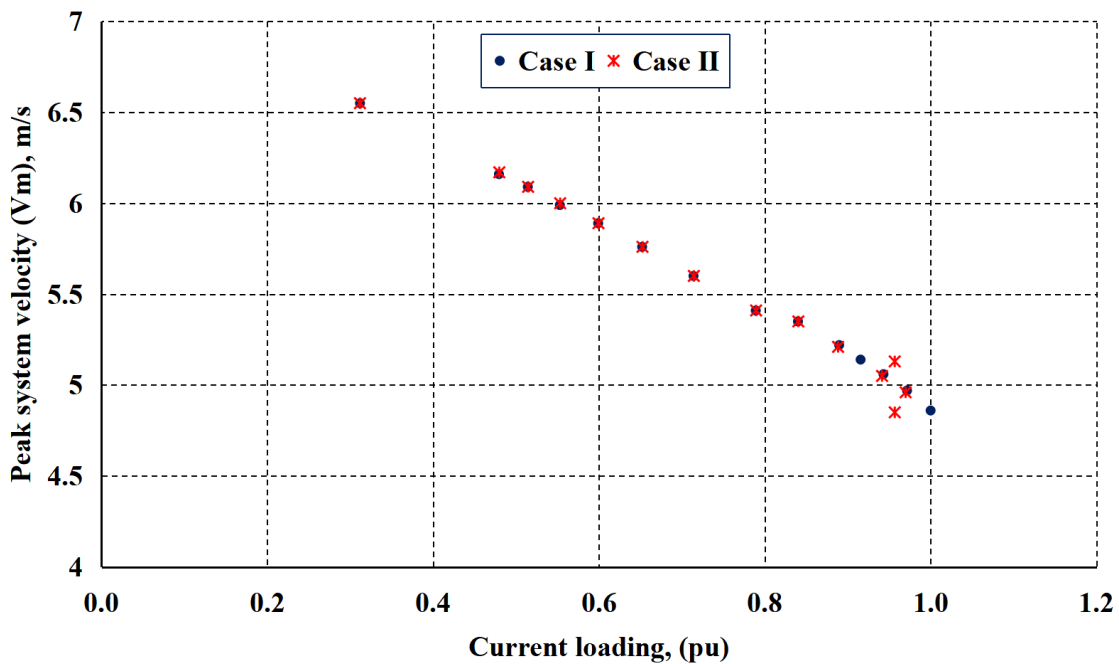


Figure 6-26: Peak system velocity versus current loading

6.7 Energy conversion system

As stated at the beginning of this research, the intended use of the overall system is for electrical power generation. Therefore, as an energy conversion system, the electrical energy loss due to high cogging force amplitude of the LG is a good way to estimate the loss in the electrical power delivered to the load by the system for any period of operating time.

By making use of the electrical power generated data shown in Figure 6-25 and the corresponding operational time in seconds, the electrical energy curves of both system models are shown in Figure 6-27. The negative impact of high cogging force amplitude on the total energy converted into an electrical energy is clear. The energy curve also clarifies that both systems reach their stable operation after (15 seconds) with a total energy difference rounding about (0.14 %) which is (0.2J) difference. Therefore, if both systems are continuously operated at rated loads for an hour period of time, there will be a loss in the power generated of $(0.2\text{J} * 3600\text{s} = 720\text{ J})$, assuming all the working time is continuously stable.

In practice, if this power loss is enumerated for a number of similar working units, as well as for the number of working hours, the total power loss sum will be effectively large, depending on the number of units and the working hours.

Thus, if a LG of high cogging force amplitude is to be integrated with this engine, or with any similar direct driven linear system, cogging force reduction technique employment become compulsory in order to reduce the effect of cogging force on the electrical generated power.

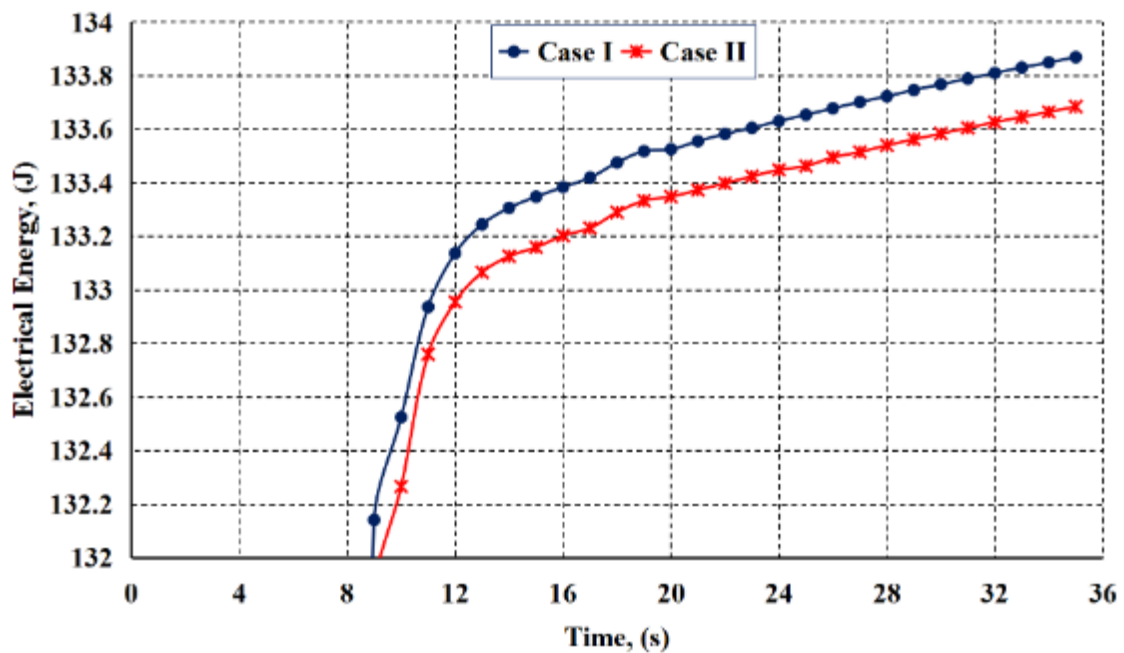


Figure 6-27: Electrical Energy versus time

6.8 Conclusion

This chapter presented a novel analytical model of the Linear Generator under investigation for use with the Linear Joule Engine. The analytic model accounts for all machine interacting electromagnetic force components. It was shown that the assumption of approximating the electric machine by a damper is an oversimplification.

The critical impacts of high cogging force amplitudes on the electrical power generated was also investigated for the engine-generator system by a novel dynamic system incorporating both the LJE and the LG models. The model is unique and its realisation is considered a new step in this research area. The LG analytical model is flexible and few straight forward modifications can be performed in which other electric machine topologies can be implemented.

The critical impacts of a machine topology exhibiting high cogging force amplitude on shaping the LG force profile was highlighted, at first by using the analytic model driven by the engine velocity in a feedforward manner. Then, using the novel dynamic system model which was developed and investigated in a closed loop form to highlight the various effects of high cogging force on various system performance parameters.

Current loading degradation was primarily identified, although overall system efficiency has negligibly affected. By monitoring the cyclic mechanical frequency and the electrical power generated by the system, the deceleration effect of high cogging force amplitudes was identified and its effect on electrical power generated, energy and power loss has been explained for the first time in this research area.

The following are some concluding remarks and recommendations:

- 1- The engine is able to drive a loaded electric machine exhibiting high cogging force amplitude.
- 2- The lower cogging force amplitude in a linear machine topology, the faster working system and the more electrical power generated per a working period of time.
- 3- In the intended application, selection of a linear machine of high cogging force amplitudes must be accompanied by applying a cogging force reduction technique, in order to gain more generated power.

Chapter 7 : Novel Cogging Force Reduction Technique

7.1 Introduction

As discussed in the Chapter 2 – section 2.8, most PM Linear Machines (PMLMs) used in actuating, servo and automated industrial systems require applying a reduction technique to reduce this force effects. Such force affects the positional accuracy which is to be maintained within the accepted error ranges, or to cope with the application safety standards. In the previous chapter, the effect of this force on the generated power by the Linear Generator (LG) has been identified and power loss was assessed. It works in reducing the amount of energy transformed into an electrical energy, and mostly is due to the ends effect of the machine topology. Therefore, a reduction technique must be applied to eliminate, or reduce this effect. Since, the application is spatially constrained, the reported structural techniques would result in a reduced power density because most, if applied, would lead to the increase of inactive machine volume (length). On the other hand, and since the control theory and techniques are out of the scope of current research, a new structural technique is investigated.

In the following sections, a novel technique is proposed to minimise cogging force effect due to stator ends. At first, an analytical expression based flux distribution at both machine ends is presented to describe this the cogging force analytically. Then the technique is applied and optimised looking at specific machine performance parameters. Finally, the final optimal solution is concluded and a selected design is compared with the initial design to quantify the effectiveness of the proposed technique and the resultant machine performance.

7.2 Ends cogging force analysis

The flux distribution within the selected machine geometry has the nature shown in Figure 7-1. It can be seen that flux lines spread across both stator ends' faces due to the flux leaking from the inactive magnetic poles, those very close, ungoverned by stator structure. At both ends, these flux lines spread over the side face of the end tooth starting from its bottom (tip) with density decreases gradually up to the top of the same tooth. Both sides' forces are attractive, and its (n_{th}) harmonic vary with pole position (x) due to stationary stator ends and therefore can be expressed in phasor notation as follows:

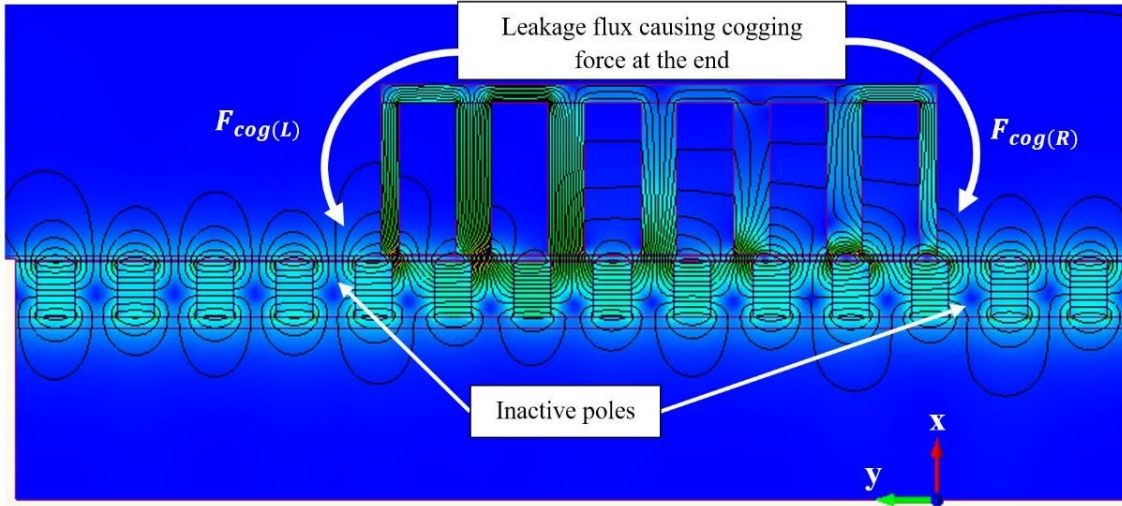


Figure 7-1: Flux distribution within the selected machine initial design topology (FEA)

$$\begin{aligned} \bar{F}_{cog(x)_{L,R}} &= \sum_{n=1}^{\infty} (\hat{F}_{cm,n} \cdot e^{j(\phi_n + \vartheta_{sh,n})}) \\ &= \sum_{n=1}^{\infty} \hat{F}_{cm,n} (\cos(\phi_n + \vartheta_{sh,n}) + j\sin(\phi_n + \vartheta_{sh,n})) \end{aligned} \quad , (N) \quad 7-1$$

Where: $\phi_n = n \frac{2\pi \cdot x}{\tau_p}$; $\hat{F}_{cm,n}$ is the (n_{th}) harmonic cogging amplitude; and $\vartheta_{sh,n}$ is the angle corresponds to zero cogging force position reference.

Equation (7-1) clarifies that both ends forces have instantaneous radial as well as axial force components, with the radial component $j \sum_{n=1}^{\infty} \hat{F}_{cm,n} (\sin(\phi_n + \vartheta_{sh,n}))$, being cancelled out totally due to tubular geometry symmetry during the whole operating stroke. The remaining axial component is the active, major contributor in forming cogging forces at both ends and is therefore needs minimisation, or cancellation if possible.

It should be noted that both forces are opposed to each other and displaced geometrically by a factor of (N_p), the instantaneous active poles, plus a shift of ($\frac{N_s}{N_p}$) between ends faces due to the fractional pole/slot machine combination. This is also depicted by the spatial magnetic nature of each pole at opposite stator ends of Figure 7-1. Thus, the variation of the left and the right axial force components may be expressed as given in (7-2):

$$\begin{aligned} \bar{F}_{cog(x)_L} &= \sum_{n=1}^{\infty} \hat{F}_{cm,n} \left(\cos \left(n \frac{2\pi \cdot x}{\tau_p} + \vartheta_{sh,n} \right) \right) \\ \text{And} & \\ \bar{F}_{cog(x)_R} &= \sum_{n=1}^{\infty} \hat{F}_{cm,n} \left(\cos \left(n \frac{2\pi \cdot (x + N_p)}{\tau_p} + \left(n \frac{N_s}{N_p} + \vartheta_{sh,n} \right) \right) \right) \end{aligned} \quad , (N) \quad 7-2$$

For a shift angle ($0 \leq \vartheta_{sh,n} \leq \frac{\pi}{2}$), the total cogging force sum ($\bar{F}_{cog(x)_T}$) would be as in (7-3),

$$\bar{F}_{cog(x)_T} = \begin{cases} \sum_{n=1}^{\infty} \hat{F}_{cm,n} \left(\cos \left(n \frac{2\pi x}{\tau_p} \right) \left(1 + \cos \left(n \frac{N_S}{N_P} \right) \right) - \sin \left(n \frac{2\pi x}{\tau_p} \right) \sin \left(n \frac{N_S}{N_P} \right) \right), \vartheta_{sh,n} = 0 \\ \sum_{n=1}^{\infty} \hat{F}_{cm,n} \left(\sin \left(n \frac{2\pi x}{\tau_p} \right) \left(1 + \cos \left(n \frac{N_S}{N_P} \right) \right) + \cos \left(n \frac{2\pi x}{\tau_p} \right) \sin \left(n \frac{N_S}{N_P} \right) \right), \vartheta_{sh,n} = \frac{\pi}{2} \end{cases} \quad 7-3$$

Therefore, for any shift angle $\vartheta_{sh,n}$, (7-3) clarifies that the slot/pole combination shift influencing the effective ends forces amplitudes. This analysis has been validated at no-load using FEA by considering one electrical cycle and the cogging force due to one pole at each side of the stator core shifted by full active poles showing peak-to-peak variation of (460 N)/pole. The separate forces are summed together and compared to their combined effect using FEA as shown in Figure 7-2.

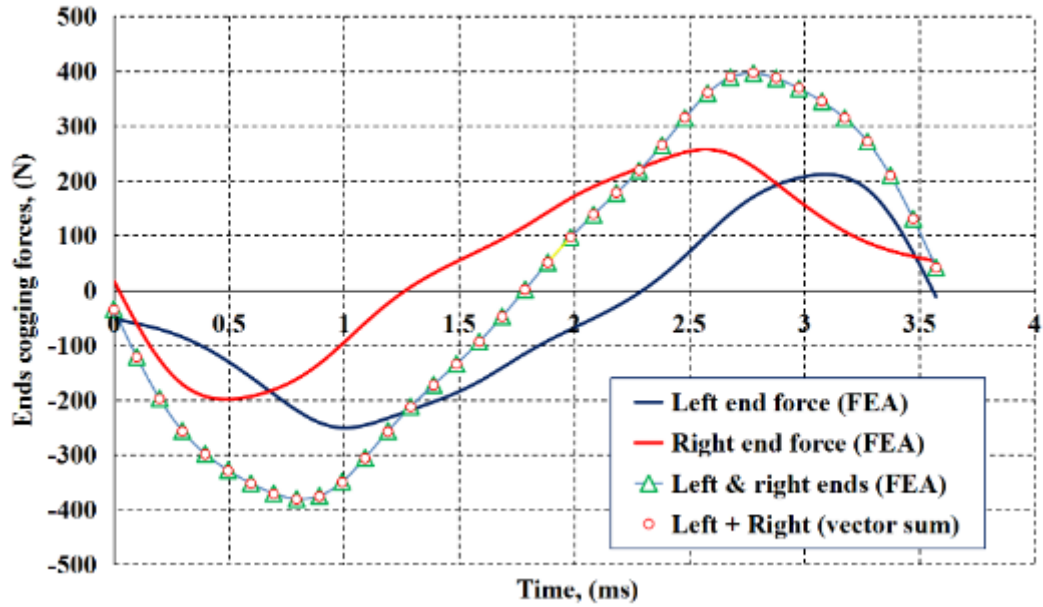


Figure 7-2: No – load cogging force variation due to one pole and stator ends

7.2.1 Novel technique description

In order to make the ends forces compensate each other, totally or partially, the use of magnetic Flux Gathering Rings (FGR) is proposed in order to add an axial physical shift of (ΔD_{axial}) between these ends forces, i.e. between stator ends faces. These FGRs can be attached to the outside face of both end teeth close to the tooth tip, see Figure 7-3, and it would work to gather the flux and imply a magnetic shift between the ends forces to compensate each other. As the flux is gathered at these two rings of optimal dimensions, both end cogging forces are minimised, or cancelled.

This technique would be sufficient instead of using auxiliary poles at the ends [111, 113] or extending the whole end tooth [110, 114] which would lead to a reduced resultant force (power) density, or introduce an imbalance to the magnetic circuit parameters when ends teeth are shortened [79, 115].

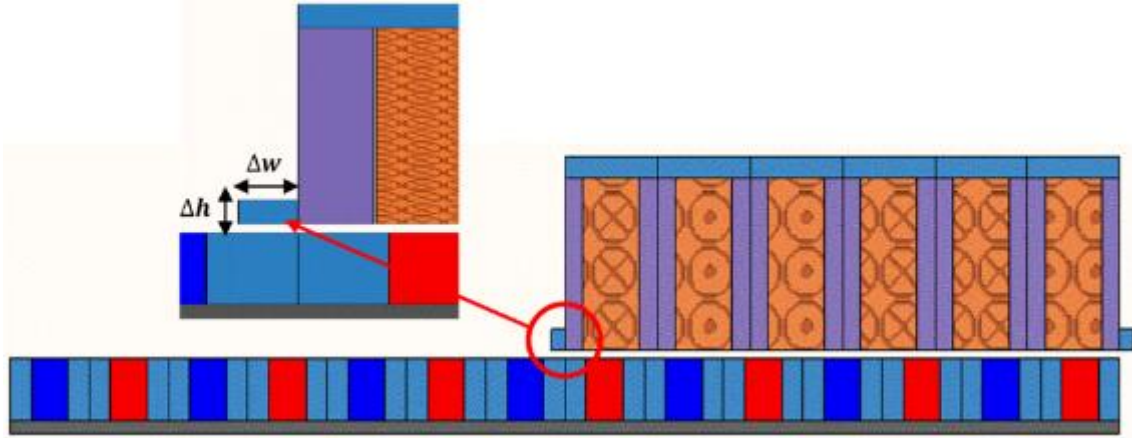


Figure 7-3: Flux Gathering Rings positioning in stator geometry

7.2.2 Flux Gathering Ring optimisation procedure

The optimisation objective is to minimise the total force ripple without affecting the rated force capability of the machine. In order to accomplish this, FGR height and width were varied incrementally in the range of $(\Delta\{h, w\} \in \{0.5: 6\})$ with a step of (0.5 mm) in FEA modelling. Effect on the normalised total force ripple is shown in Figure 7-4(a), with an added grid at $(Grid = 0.35 F_{r(pp)-initial\ design})$ to make initial assessment to the technique. Results show that for different FGR heights, the total force ripple starts to decline with each increment of FGR width until approaching a specific margin where afterwards force ripple starts to increase again. The effect of FGR height in the range $(0 < \Delta h < 2mm)$ may be considered satisfactory to reduce the force fluctuation, yet it requires wider FGR which, in practice, adds complexity to manufacture such critical dimensions and depends directly on machining accuracy and the rigidity of the chosen magnetic material the rings should be made off.

On the other hand, it can be seen that lower force ripple can be achieved at $(\Delta w = 3.5mm)$ irrespective of FGR height after $(\Delta h > 2mm)$. At this width dimension, a total axial shift between the two ends cogging forces faces accomplished is $(\Delta D_{axial} = 7mm = 0.4\tau_p)$ and its effectiveness is obvious in bringing the total force ripple down to round about only $(F_{r(pp)} = 0.275 F_{r(pp)-initial\ design})$.

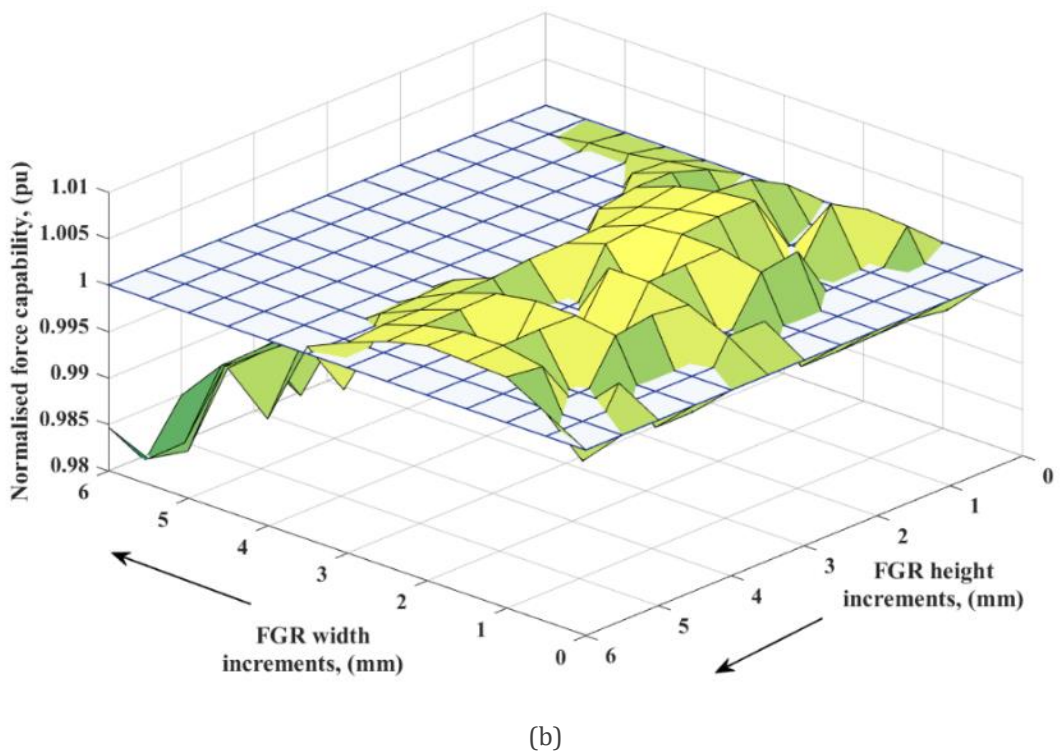
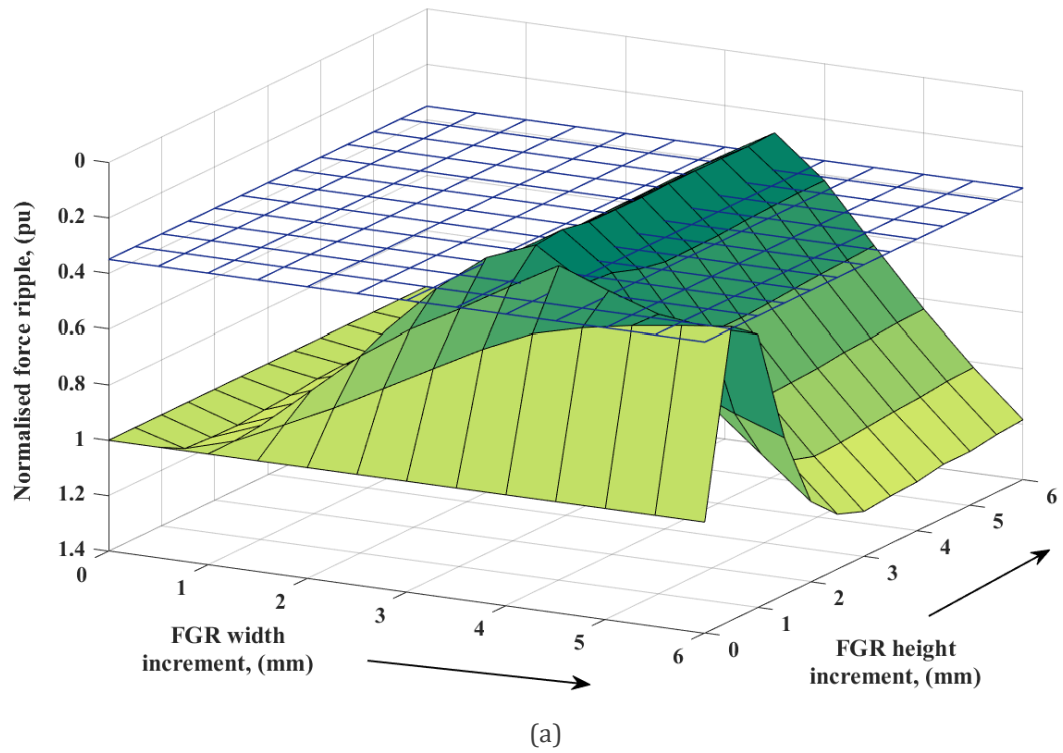


Figure 7-4: Flux Gathering Rings dimensional changes and effects on (a) Normalised force ripple; and (b) Normalised rated force capability (FEA)

The effect of FGR dimensional changes on the resultant normalised force capability is shown in Figure 7-4(b), where it can be seen that there is more than a single optimum, making geometry selection challenging. Although there is a slight increase in the force capability, the effective dimensions of the added FGR is still unclear, since most design points above unity have higher force capability compared to that of initial design model, and in such a case, a selection criterion should be used.

7.2.3 Optimal dimensions selection criteria

Singular solution (s), however, are still attainable with mathematical analysis that makes the decision in such cases more logical. If the ratio of the resultant force capability divided by the resultant force ripple ($F_{rated}/F_{r(pp)}$) is judged, see Figure 7-5, its resulting value would reflect the relationship between these interconnected performance parameters, “the highest means the best design.”

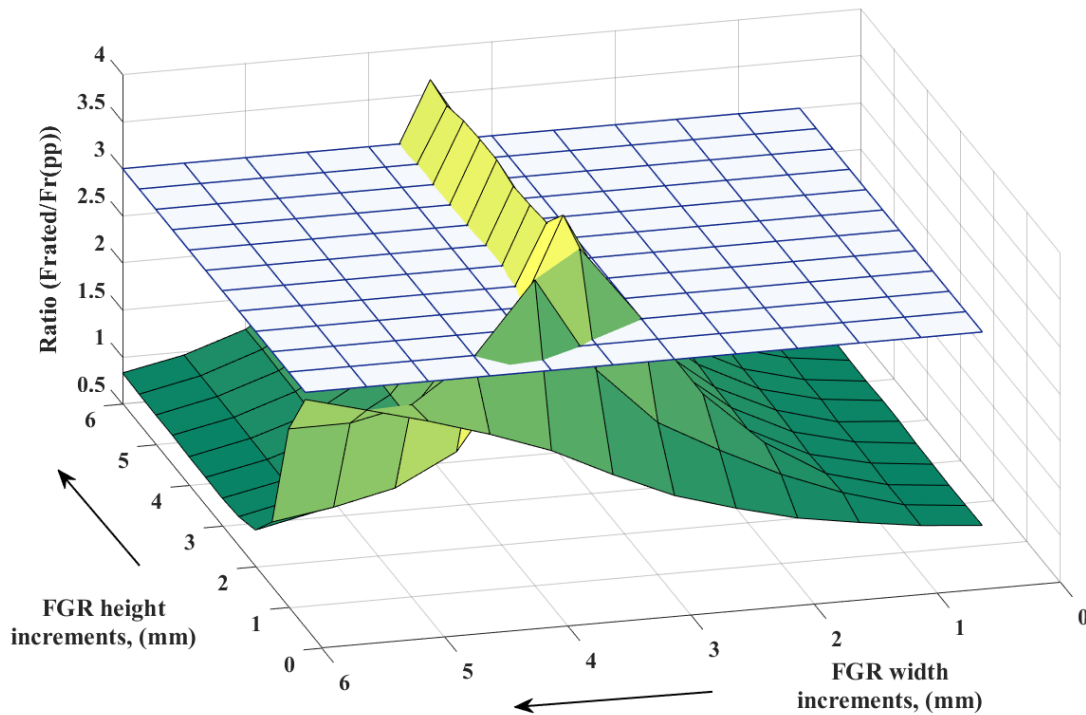


Figure 7-5: Proposed rational criterion to identify the effects of changing the dimensions of Flux Gathering Rings on both resultant force capability and consequent force ripple (FEA)

Using the proposed criterion in this specific case, any design model with a number higher than (3), implies a force capability higher than that of initial design model and a corresponding force ripple rounding below ($< 0.3 F_{r(pp)-initial\ design}$). The criterion results show again that FGR with width about ($\Delta w = 3.5\text{mm}$) is the best dimension to eliminate almost 72.5 % of cogging due to end effects.

Ignoring the designs of ($\Delta h \leq 3mm$) to eliminate manufacturing complications, the set of FGR dimensions and the corresponding FEA design model performance parameters are listed in Table 7-1. From the listed results, it is obvious that the difference is negligible for different FGR heights. This is also confirmed by comparing the resulting force capabilities of these models, as compared to that of initial design model as shown in Figure 7-6.

Table 7-1: Flux Gathering rings dimensions and effects on force capability and consequent force ripple of selected design models at $\Delta w = 3.5mm$

Parameter, (unit)	Initial design	FGR height (Δh), (mm)					
		3.5	4.0	4.5	5.0	5.5	6.0
$F_{rated (average)}$, (N)	843.2	839.1	844.5	844.2	844.1	838.6	843.9
$F_{r(pp)}$, (N)	326.5	90.2	89.2	89.2	89.6	90.4	89.4

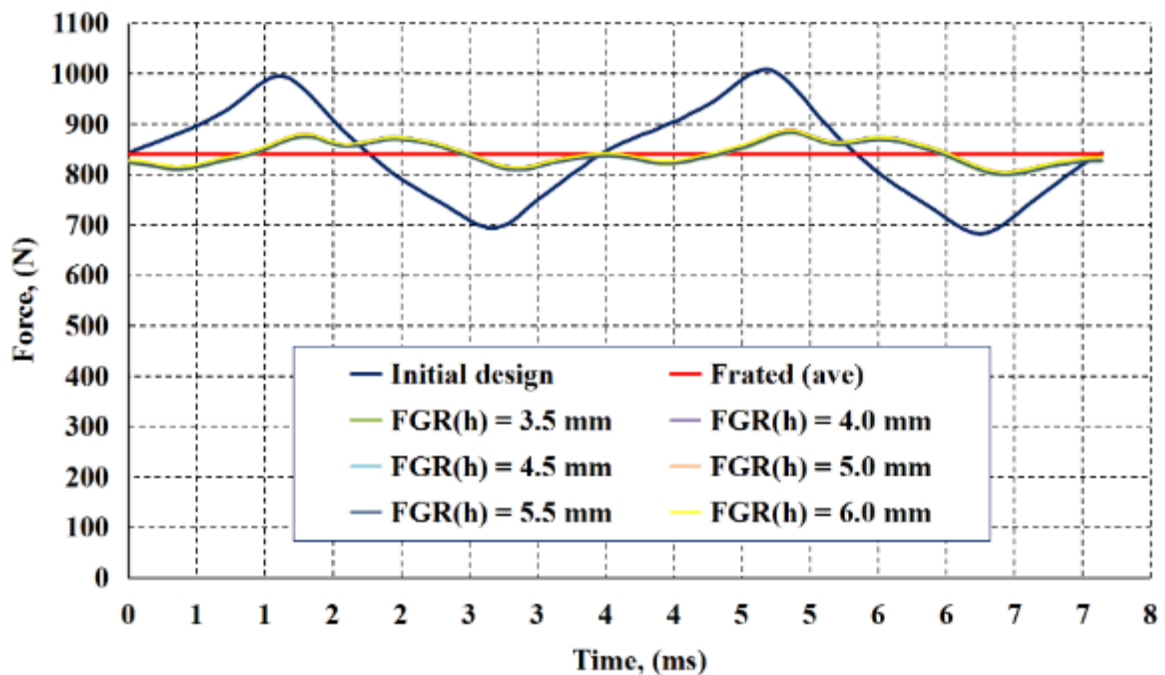
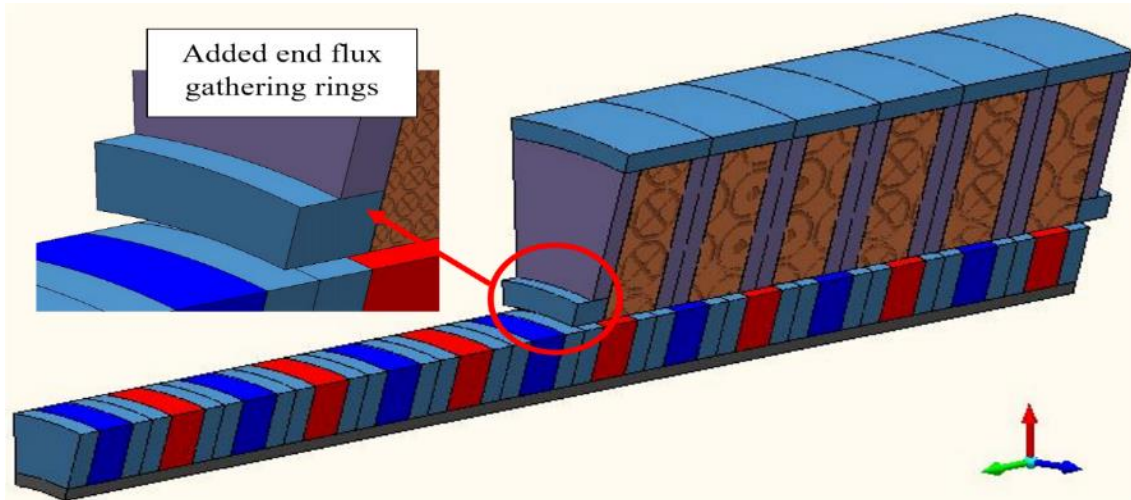


Figure 7-6: Variation of rated force over one electrical cycle of initial design, rated averaged force and those of selected FGR designs models (FEA)

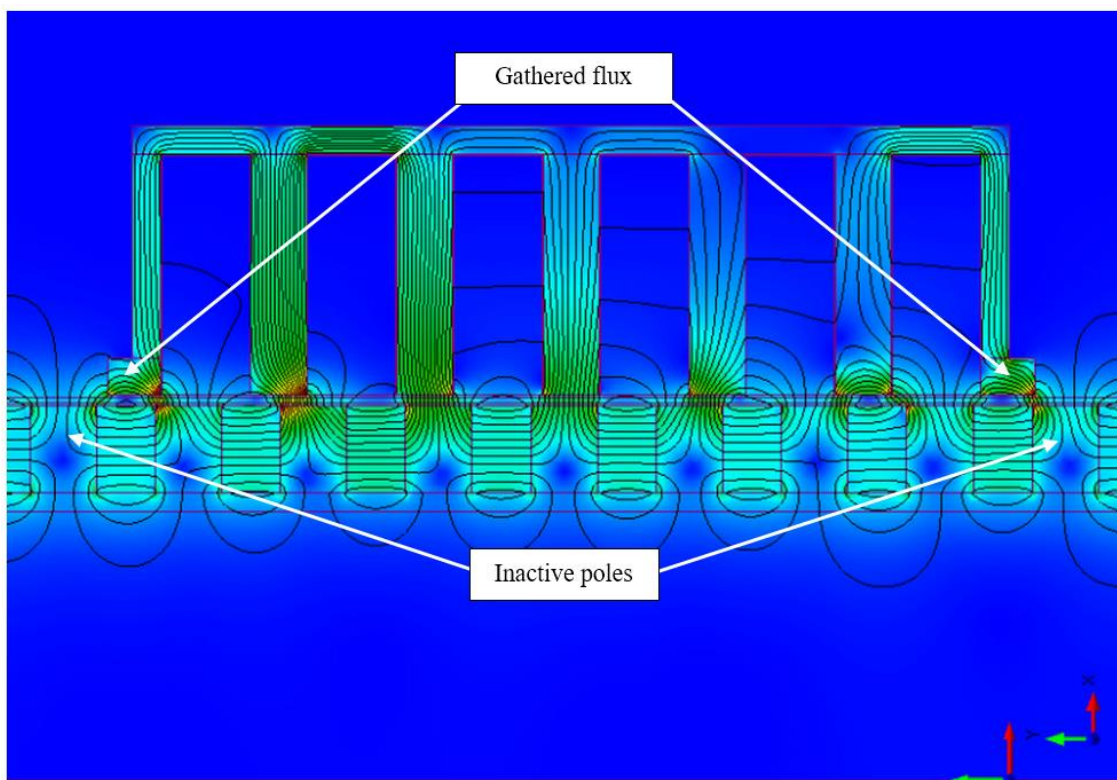
Scanning the results of Table 7-1 and those in Figure 7-6, picking any FGR of width ($\Delta w = 3.5mm$) and height in the range ($4.0mm \leq \Delta h \leq 5.0mm$) would guarantee a reduction in force ripple to be only (89.6N) and an average rated force of (844.1 N).

7.3 Selected Model performance

One model is selected to quantify the overall effect of the proposed method on the machine performance. The selected model for this purpose is with FGR dimensions of ($\Delta w = 3.5mm$, and $\Delta h = 5.0mm$). A 3D view of the model is shown in Figure 7-7(a), clarifying how these rings can be added by shortening the lateral teeth of the machine.



(a)



(b)

Figure 7-7: (a) Modified design model with added Flux Gathering Rings at both ends; (b) Flux distribution in the model after adding Flux Gathering Rings at both ends (FEA)

Soft magnetic Composite (SMC) material can be used in forming these rings to provide the necessary low reluctance, two-degree of freedom path to gather the flux at the ends, as shown in Figure 7-7(b).

The effect of adding FGRs and separate poles on the ends forces is shown in Figure 7-8, where the added magnetic rings helped in reducing the cogging force by 19.5 % per pole. However, the cumulative effect on the machine total cogging force at no-load is almost 75 % reduction in peak-to-peak force ripple as can be seen in Figure 7-9.

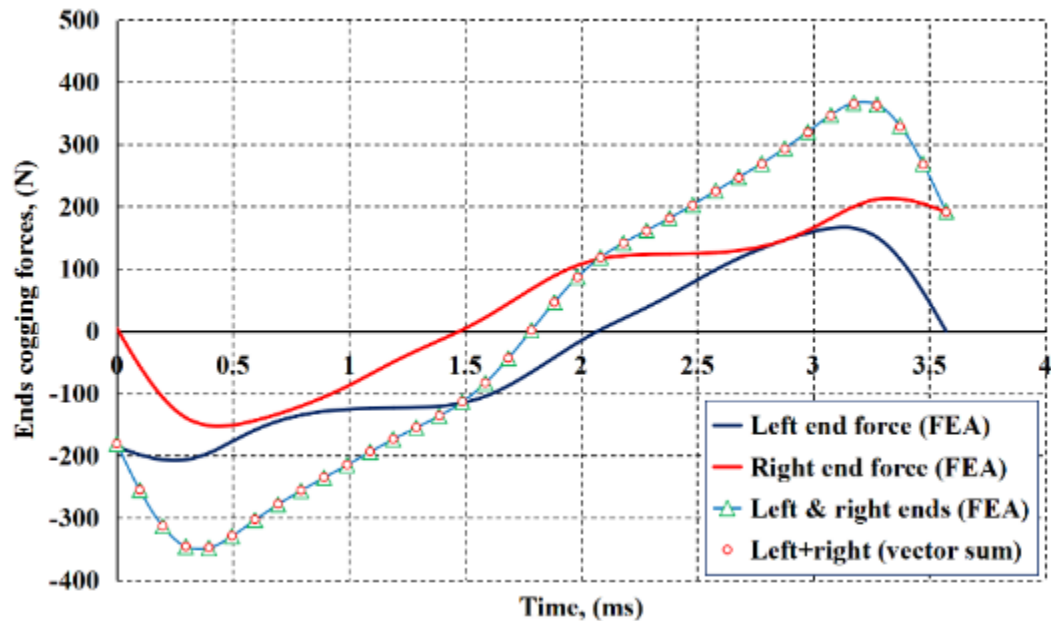


Figure 7-8: No – load cogging force variation due to inactive poles and stator ends with added FGR

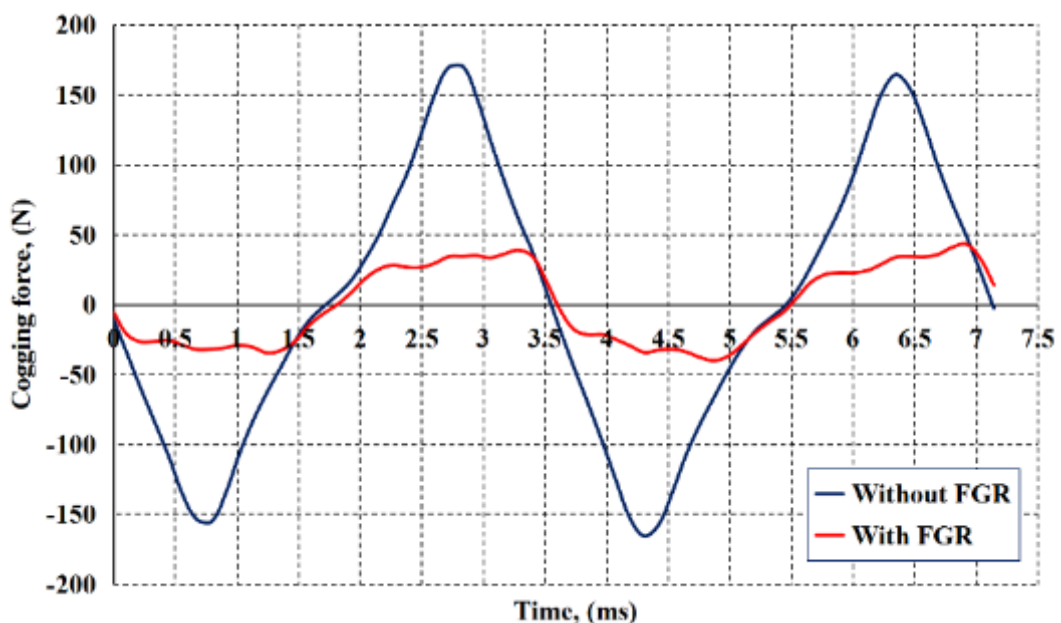
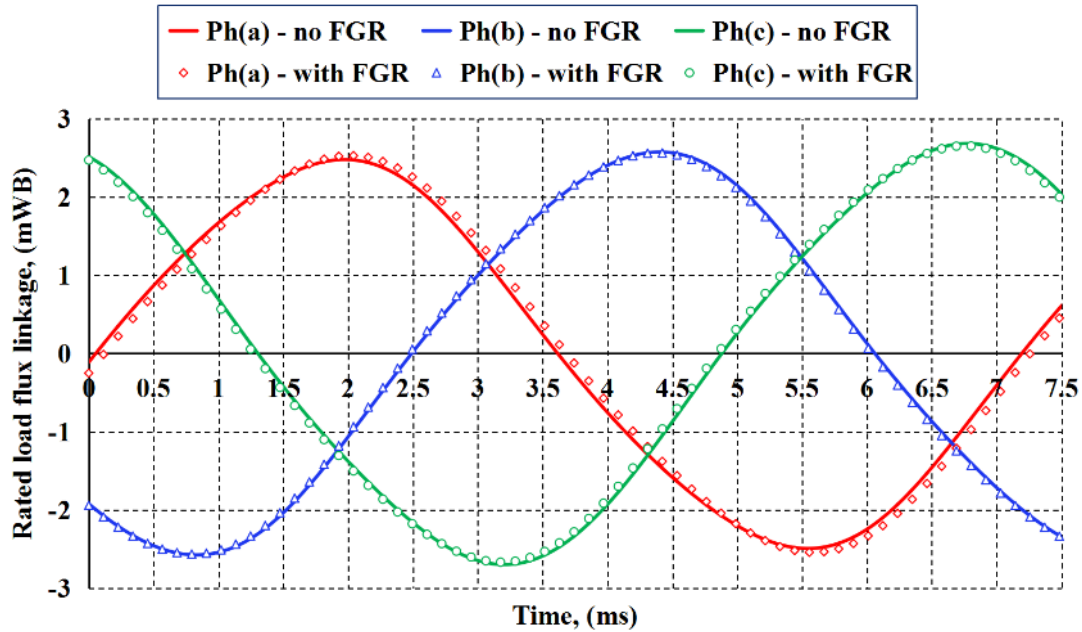
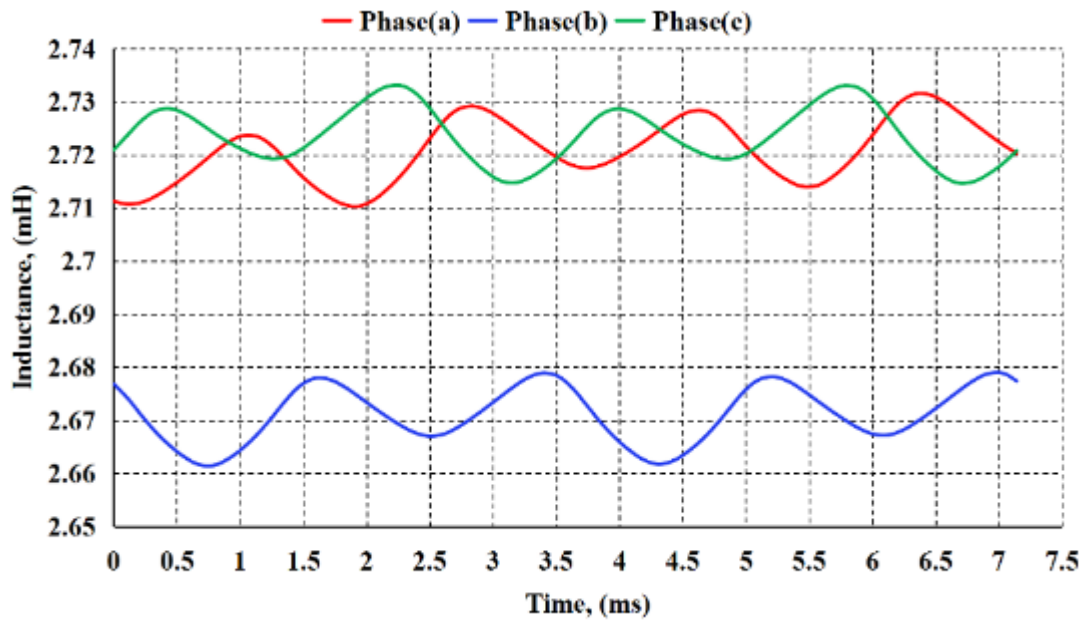


Figure 7-9: Effect of adding Flux Gathering Rings on total no-load cogging force over an electrical cycle (FEA)

The rated load flux linkage variation over one electrical cycle is shown in Figure 7-10(a), where it can be seen there is a slight difference in both phase (a) and (c) flux linkage. Consequently, this introduced an imbalance of ($\pm 0.95\%$) to phase inductances as can be seen in Figure 7-10(b). The phases with coils occupying stator lateral slots are more influenced compared to the centred coils those belonging to phase (b).



(a)



(b)

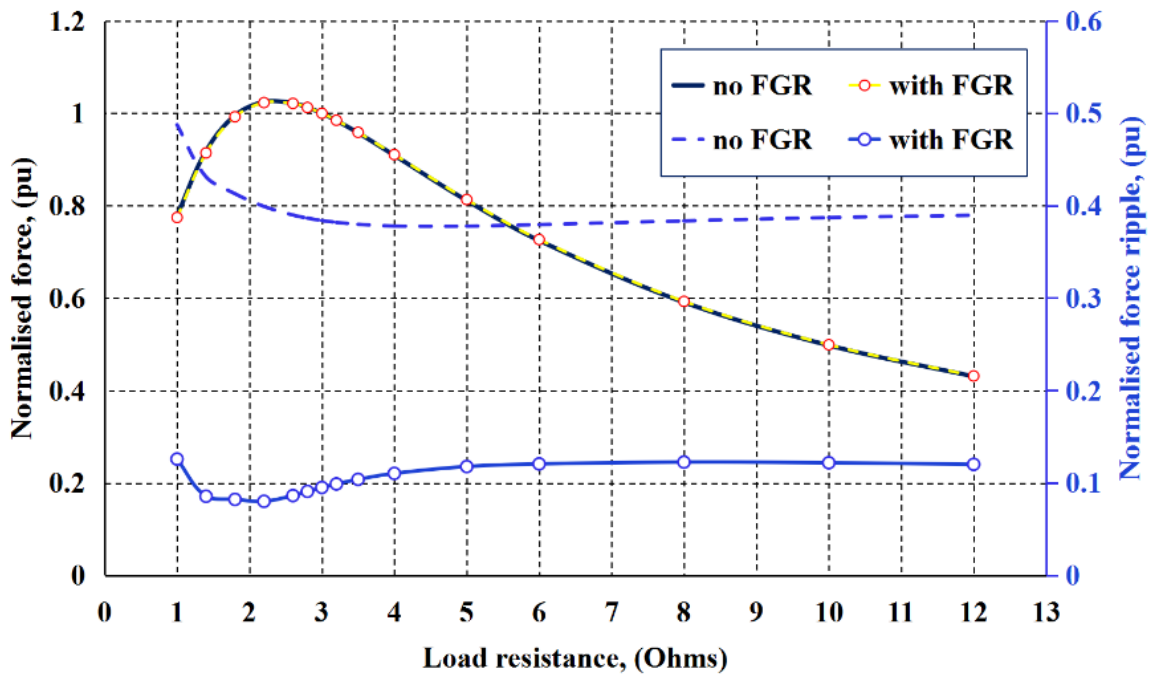
Figure 7-10: Effect of adding Flux Gathering Rings on (a) Flux linkage, and (b) Inductance (FEA)

A comparison including all affected geometrical and performance parameters of a typical design without FGR and the selected design with added FGR, both operating at a constant speed of (4.8 m/s), is listed in Table 7-2. All physical parameters are slightly increased so as most of the performance parameters, except the rated force ripple which its reduction was the goal, and the total machine efficiency. Under the same loading condition, efficiency reduction is due to the increased losses, mostly in the magnets and the supporting sleeve as eddy currents loss, as a consequence of the increased current density for same resistive loading, and hence the increased space harmonics of stator MMF traveling field. The increased current density also results in increasing the rated power, and hence the higher power densities, even with the reduced efficiency.

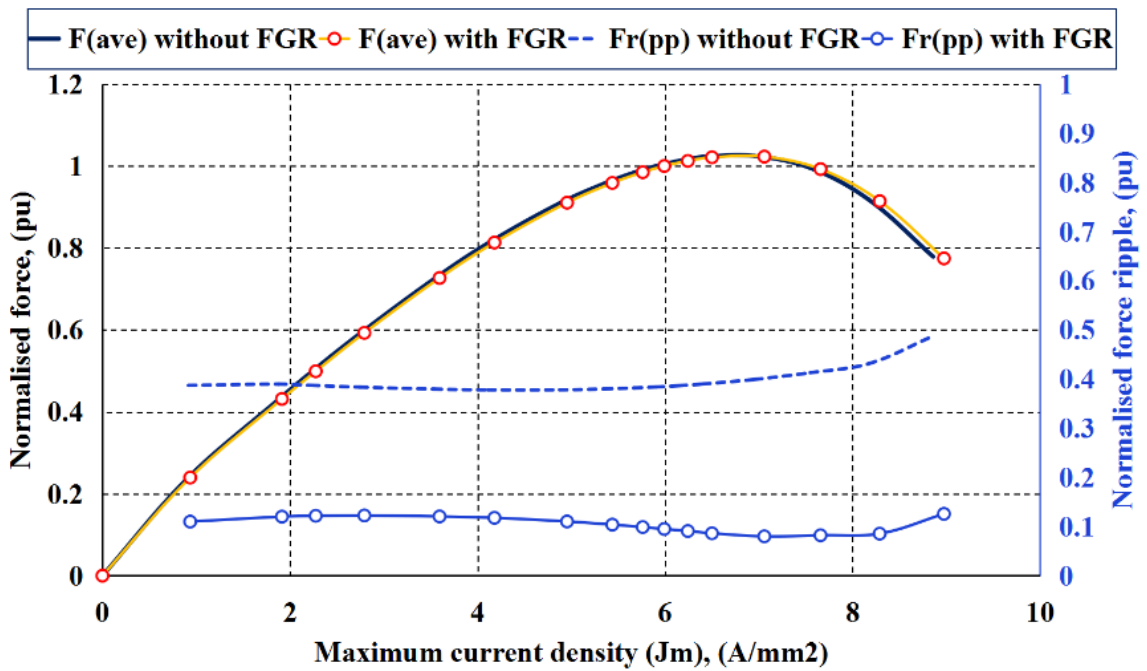
Table 7-2: Comparative table of machine design models

Parameter, unit	Without FGR	With FGR
Total mass, Kg	20.64	20.65
Volume, mm ³	3.05×10^{-3}	3.053×10^{-3}
P_{iron} , W	15.6	16.15
P_{cu} , W	75	78
P_{ECL} , W	136	155
J_{max} , A/mm ²	5.8	5.99
Peak total cogging force, \hat{F}_{cm} (N)	170	45
Rated force ripple, % $F_{r(pp)}$	38.7	10.6
$P_{\text{out(elect)}}$, kW	3.7	3.83
$P_{\text{in(mech)}}$, kW	3.91	4.08
% Efficiency	94.6	93.9
Power density, kW/m ³	1.21	1.25
Power mass ratio, W/Kg	179	185

The variation of rated force and corresponding peak-to-peak force ripple against resistive loading for both models is shown in Figure 7-11(a). It clarifies that rated force achieving design force is in the range ($1.8\Omega \leq R_L \leq 3\Omega$) for both designs with negligible difference, while the force ripple reduced to be less than 20% at ($R_L = 2.2\Omega$) by using FGR. Further, the proposed technique proves its effectiveness in reducing the total force fluctuation at different loading conditions. Thus, it is very useful for the variable speed drive system under consideration, since the back EMF is speed dependent as clarified, and so is the load current as illustrated in the previous chapter. This is also depicted in Figure 7-11(a) showing the effect of increased current density (J_{max} , A/mm²) on both the rated force and the accompanying force ripple.



(a)



(b)

Figure 7-11: Variation of normalised force and force ripple in both design models due to changes in (a) Resistive loading; (b) Current density (FEA)

7.4 Effect on total power generated

The amplitude of cogging force after applying the FGR technique is used in the system model presented in the previous chapter, and the model is termed Case III. At rated load, the electrical power generated, power loss, frequency and peak velocity at the stable operational region of the system for the three cogging force cases are listed in Table 7-3. The effect of minimising cogging force effect is clear in saving 7.1J per mechanical cycle. This corresponds to saving almost 486J per working hour instead of 720J if the cogging forces are not reduced.

Table 7-3: Flux Gathering rings effect on integrated system performance

Parameter, (unit)	System model		
	Case I	Case II	Case III
Electrical power generated, (W)	1887	1876.5	1883.6
Power loss, (W)	---	10.5	3.4
Frequency, (Hz)	13.97	13.93	13.95
Velocity, (m/s)	4.86	4.85	4.86

7.5 Conclusion

This chapter presented formulation of the cogging forces due to the ends in the adopted long translator-short stator machine topology. The analytical solution is verified by the FEA model results, in which the machine flux distribution clearly show how the flux is spread on the side faces of stator ends giving raise to ends cogging forces.

A new proposed method by adding Flux Gathering Rings at both ends to minimise cogging forces has been illustrated, applied and the optimal dimension have been obtained using a proposed selection criterion. Comparison results proved the effectiveness of the proposed method at different loading conditions, which is very important for the technology under investigation. The new resultant cogging force amplitude effect on the performance of the integrated system has been investigated using the system model described in previous chapter, and the employment of the proposed technique had showed its effectiveness in saving almost 486J per a working hour.

Chapter 8 : Construction of Prototype Machine and System Test Rig

8.1 Introduction

This chapter outlines the construction of the selected linear machine designed to operate under resistive loading, and the test rig for experimental testing. The machine has the dimensions listed in Table 8-1. The stator has an active length of (1:1) ratio to drive engine stroke divided into 6 slots. The translator has, however, twice the stator length divided into 14 magnetic poles. This construction is a long translator – short stator machine to facilitate measuring cogging force due to stator ends and quantify the effect of translator mass during the assembly of the machine. The challenges encountered while constructing and assembly will be discussed, perhaps to offer a good base for constructing similar machine topology with a different power rating. All machine parts were assembled by the technicians in the school of Electrical Engineering of Newcastle University.

Table 8-1: Dimensions of the machine design model under construction

Parameter, unit	RL design model
Phases	3
Slots (N_S), poles (N_P)	6, 14
Active length, mm	120
Slot width, mm	20
Stator outer diameter ($2R_{OS}$), mm	180
Stator core back (yoke) height, mm	4
Tooth width (T_W), mm	3.85
Turns per coil	40
Air gap, mm	1.5
Translator outer diameter ($2R_{OT}$), mm	103
PM height – width (M_H, M_W), mm	12 – 8

8.2 Stator construction

The stator parts are shown in Figure 8-1. Stator magnetic circuit is composed of two parts; each with a different magnetic material and properties. The prototype stator core back (yoke) is made of Somaloy 3P Soft Magnetic Composite (SMC) material. SMC is a pressed powdered material suitable for carrying 3D flux patterns. For industrial applications it may be directly pressed into component form.

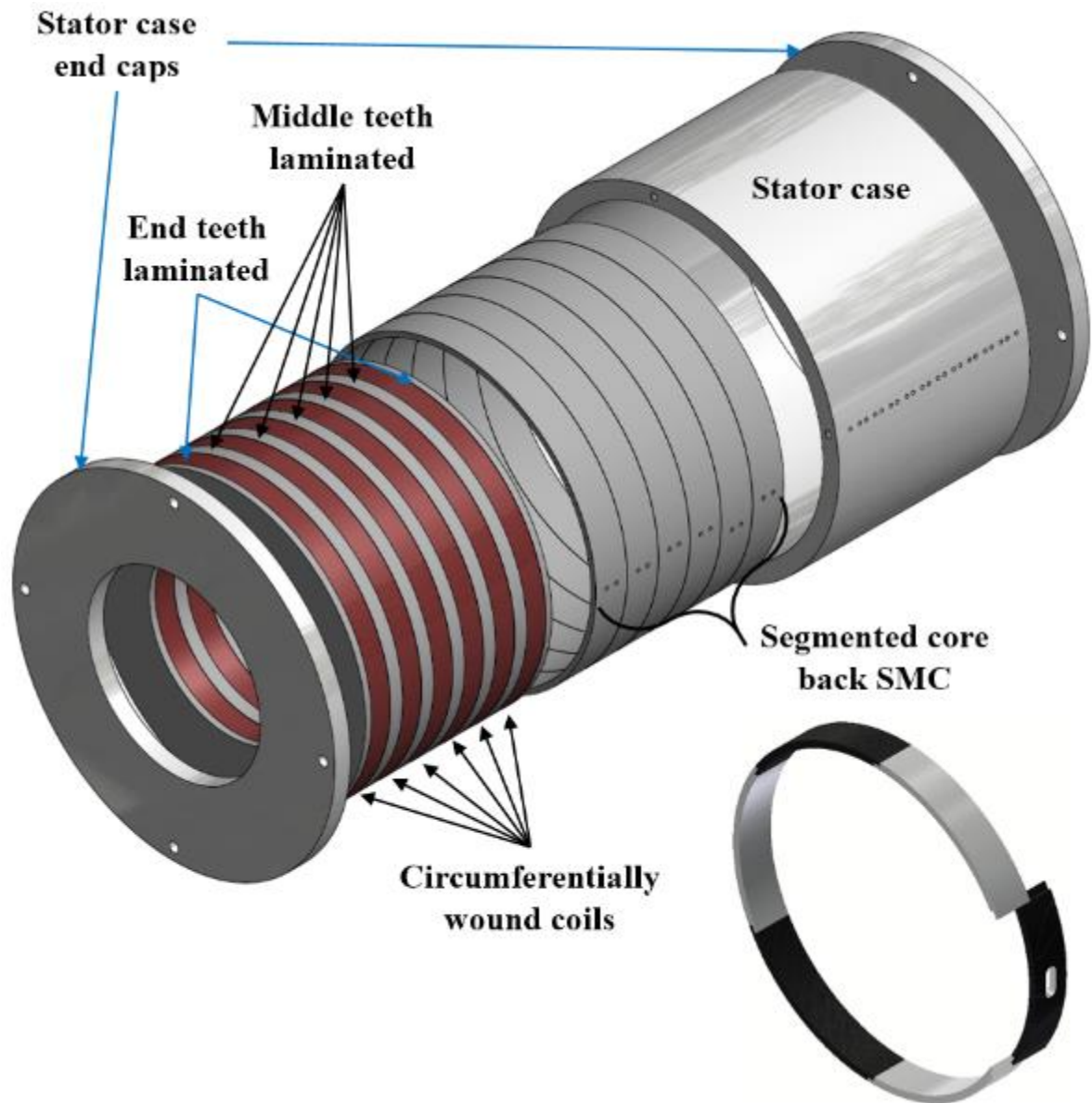


Figure 8-1: Stator parts

For “one off” and prototype machines, it is supplied in pre-pressed blocks which can be machined to the required shape prototype. SMC is supplied in discs of 120mm diameter and 20mm thickness. Because a single slot yoke component cannot be extracted from the available disc dimensions, the yoke was made from 6 circumferential segments, each has two sided oppositely stepped key guides as shown in Figure 8-1. One of the 6 segments has a punch to pass coil leads out through. 6 segmented yokes were made as there are 6 slots in the stator. A CNC wire cut machine (ROBOCUT) was used to machine out these segments from the SMC discs, while a mould was used to make desired punches in six segments. Figure 8-2 clarifies the tools and the SMC discs used in forming these segments.



(a) Wire cut machine



(b) Used and unused SMC discs



(c) Punching mould



(d) Segment with a punch

Figure 8-2: Tools and materials used in constructing stator slots core back

The laminated ring teeth are constructed from N020 lamination sheets of (0.35 mm) thickness bonded by Ultimeg 2002L epoxy. All middle teeth shared by two adjacent slots have a thickness of (7.7 mm), while the end teeth have half that width. Each middle tooth was made by stacking 22 laminations in sets, while 11 were used for the end teeth shown in Figure 8-3(a), all compressed and heated for 3 hours at 160°C to cure the epoxy to its highest strength. By using the cutting machine, all teeth were cut to the required dimensions from the bonded stacked laminations' sets. The mould shown in Figure 8-3(b) was used to assemble a middle tooth-coil-into 6 yoke segments as depicted in Figure 8-3(c) to prepare a full slot with one middle tooth, a total of 6 slot sets for the whole machine.

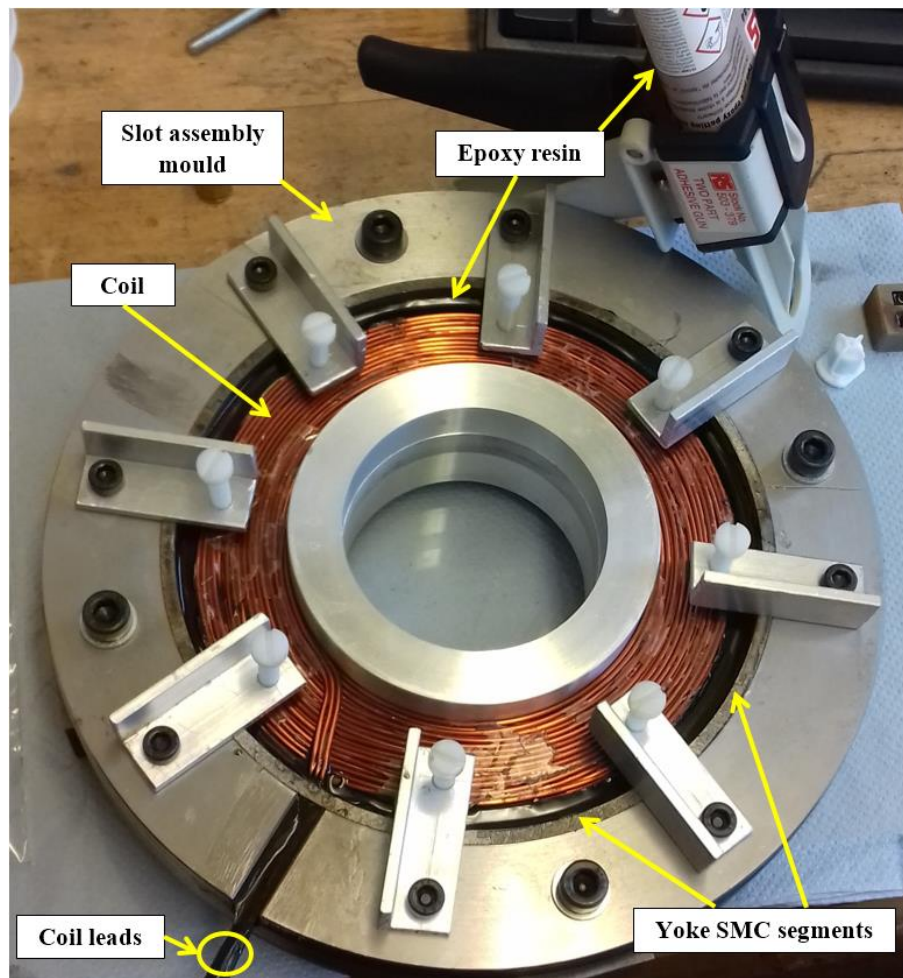
The end teeth were fixed after stacking assembled slots before inserting the whole machine into its housing (case).



(a) One stator end tooth



(b) Slot components assembly mould



(c) Stator slot assembly

Figure 8-3: Teeth and mould used in constructing and assembly of stator slots

Phase coils were made from Magnetemp CA-200 wire of 1.6mm diameter and in a bundle of 3 wires to form a strand wound in an outer wooden mould of inner stator bore diameter, see Appendix C - Figure C-11. This method achieved a fill factor of (0.62) although higher fill factor could be achieved with appreciation to coil leads exit from yoke structure. Each coil was glued using ultra strong standard epoxy (Araldite) that achieves full strength after 14 hours working time.

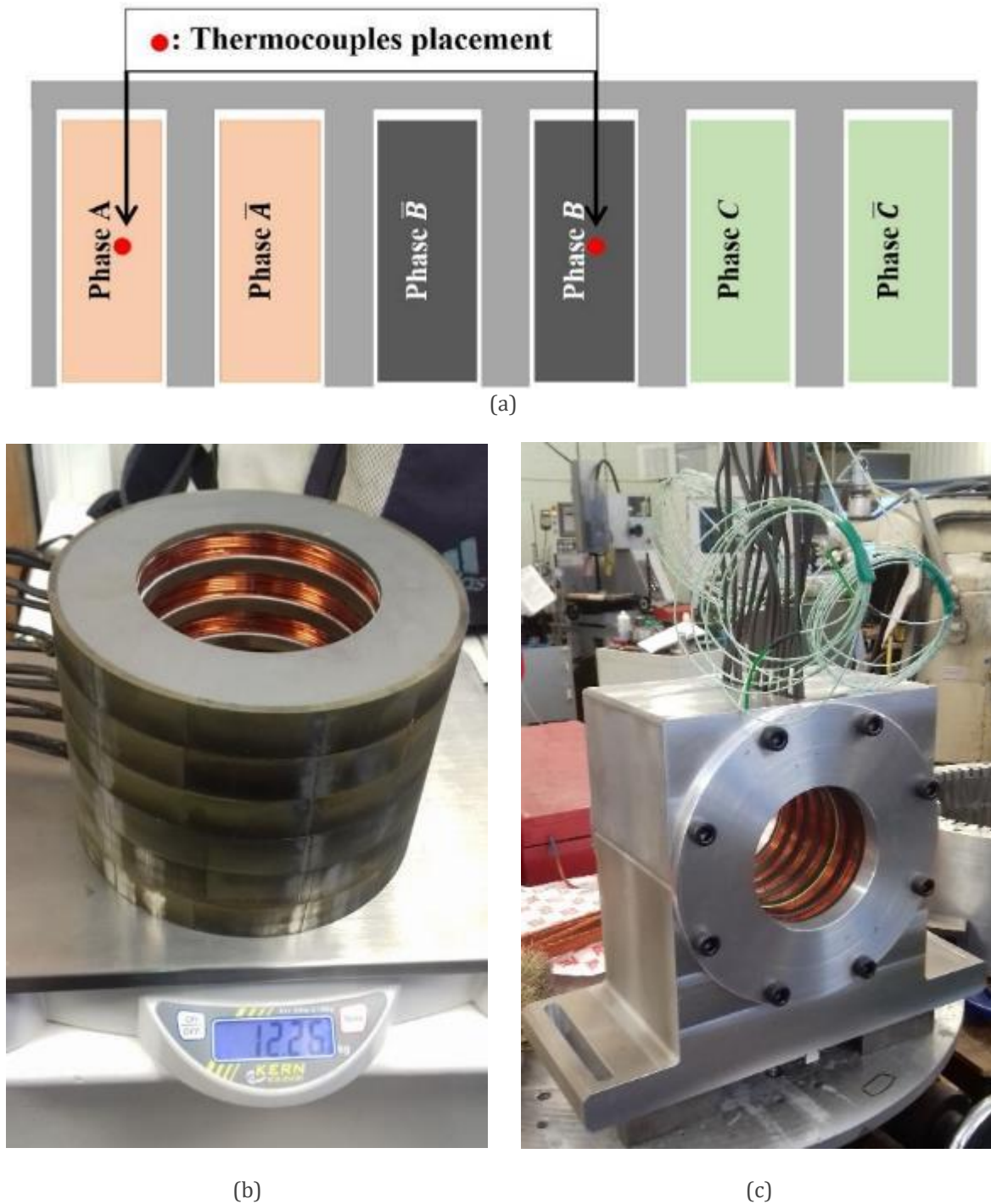


Figure 8-4: (a) Thermocouples placement; (b) Stator mass; and (c) Stator in housing

Nomex paper of 0.17mm thickness and maximum temperature resistance of 205°C was used as liners between the coil and the teeth. The remaining gap region between the coil and the yoke was filled with an epoxy resin that cures after 12 hours at room temperature. Type K thermocouples were placed at the centre of two coils belonging to two different phases, the centred phase and a lateral phase, in order to measure the temperature in machine coils (phases), see Figure 8-4(a). After stacking the slots together, the final stator assembly has a total mass of 12.26 kg before it was inserted into its housing, see Figure 8-4(b, c).

8.3 Translator construction

The translator is composed of two major components that form the magnetic poles, the axially magnetised Permanent Magnets (PMs) of alternate polarity which are sandwiched between SMC pole-pieces. The 14 magnetic poles were mounted on an aluminium supporting tube of 5mm thickness shown in Figure 8-5(a). The magnets used are the sintered Samarium Cobalt (Recomma 26) which were produced by Arnold Magnetic Technologies, and offer excellent magnetic properties at elevated temperature.

The assembly procedure started by mounting an end pole-piece of half the width of any middle pole-piece and a magnet on the supporting tube. This set worked as a magnetic pole polarity direction reference for the next assembled pole set, and the same manner was followed in stacking the other magnetic pole sets one after the other, see Figure 8-5(b).

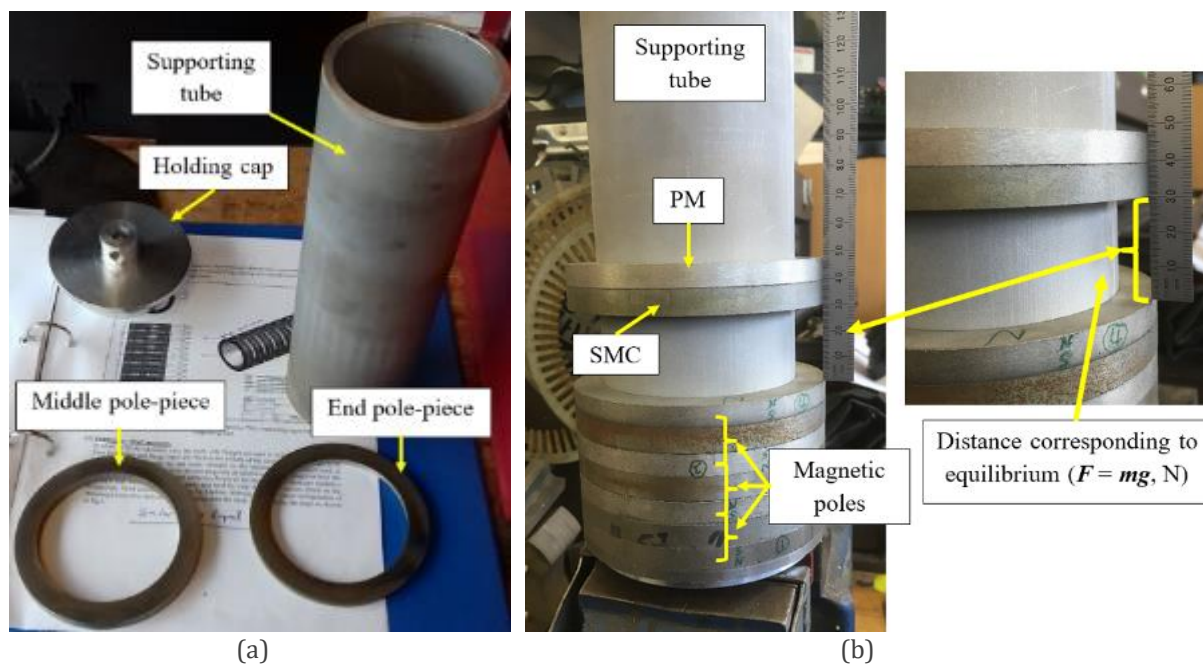


Figure 8-5: (a) Supporting tube, holding caps and SMC iron-piece; (b) Equilibrium point during assembly

During this procedure, it was noted that there is a distance between two consecutive poles at which when reached, the inserted pole set is attracted speedily to settle side by side with the stationary pole set(s). The same magnetic force nature is noted by using FEA modelling of pole assembly as shown in Figure 8-6. A repellent force starts to build up between poles as the distance between them is decreased until equilibrium point is reached. At equilibrium point, the repulsive force is equal in magnitude, and opposite in direction, to that of the moving weight of magnet-SMC pole segment set. Then, it starts to increase in an exponential manner until reaching its maximum at a distance (6.5mm) after which the repulsive force decays rapidly and becomes attractive with the stationary pole set. Some difference is noted between the experimental (30mm) and the predicted equilibrium point (32mm), which is attributed to the fact that during the manual pole set push onto the mounting tube there exist a frictional force acting in addition to moving weight, which is (0.8N) in this case.

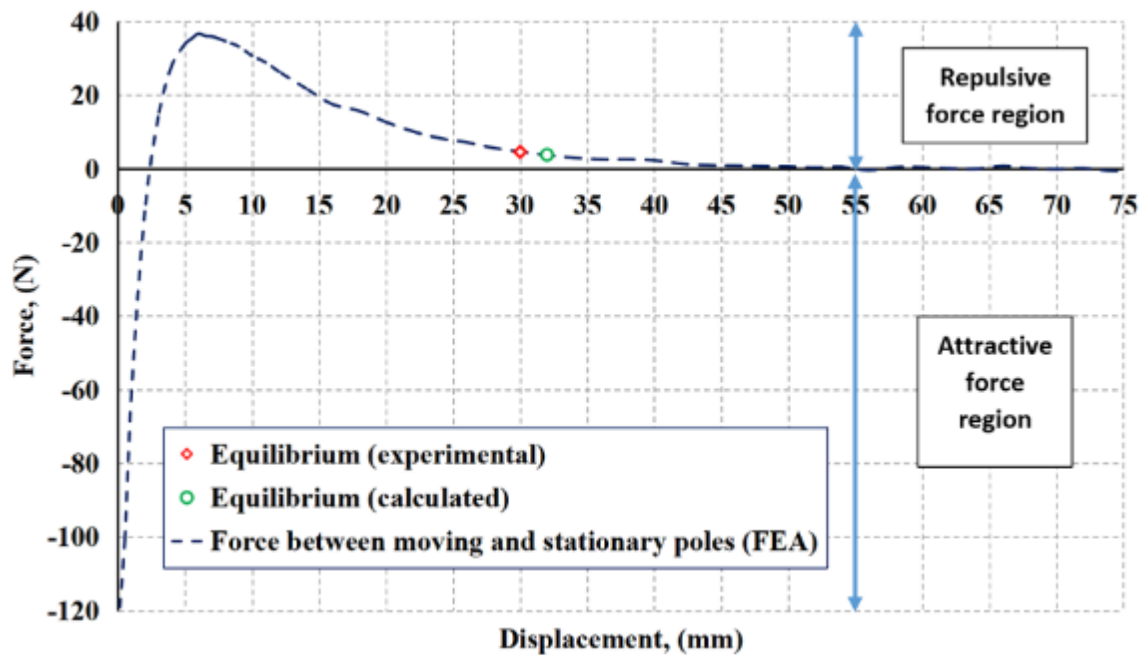
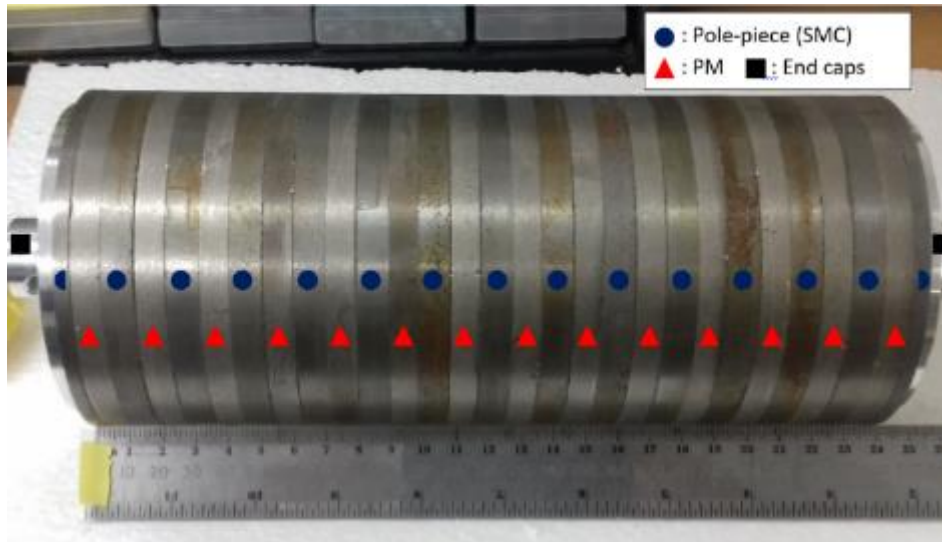


Figure 8-6: Force nature between moving and stationary magnetic pole sets

As the manual assembly was the available option to assemble the translator poles, this force behaviour was unavoidable to prevent the moving pole set from hitting the stationary pole set. Such bumps would weaken PM and pole-piece mechanical structures and must be avoided by adopting suitable gripping technique to control the mounting of consequent poles and prevent any pole components structural harmful hits. Such force is proportional to PM grade and size, the position at which it starts and translator geometry where all are factors affecting it and should be considered carefully before starting the assembly procedure.

After the full assembly of translator poles, the overall translator length and mass were measured without the holding shaft as shown in Figure 8-7, where there is a difference of 11 % compared to the calculated value using the dimensions of the materials and mass density.



(a)



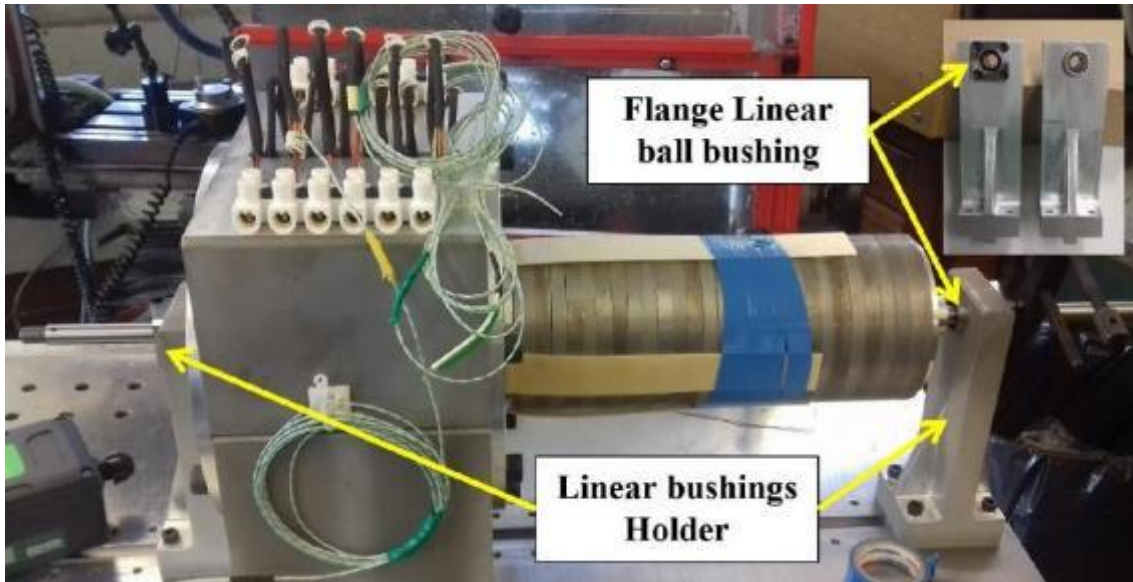
(b)

Figure 8-7: (a) Full translator; (b) Mass of full translator

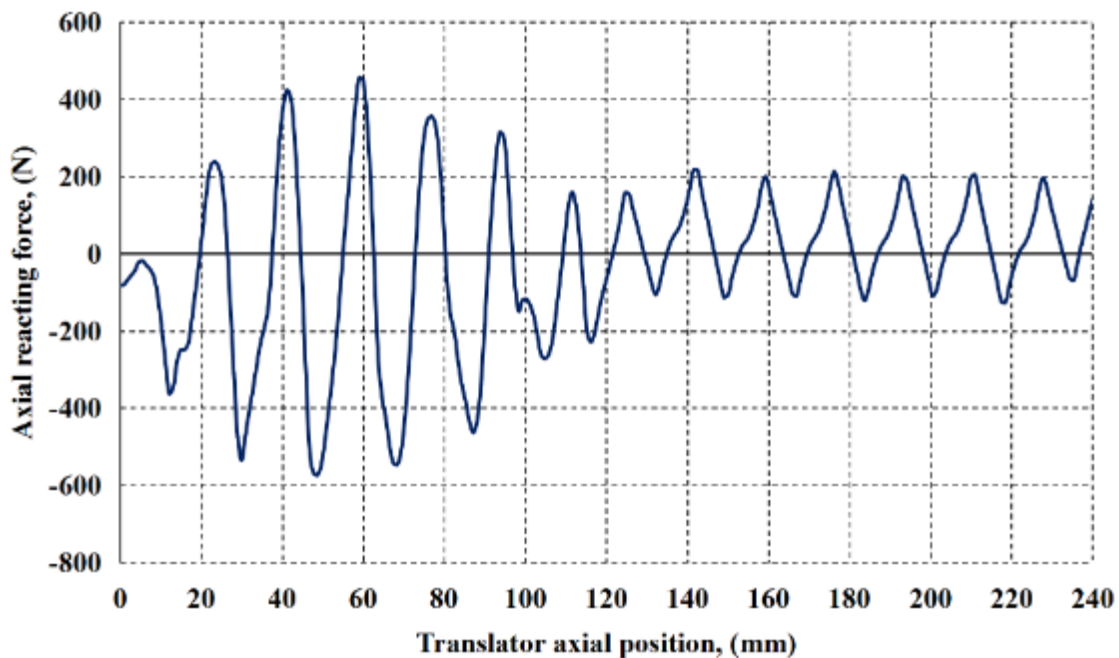
8.4 Machine assembly

Before approaching the final prototype assembly, some assembly issues have been encountered during gathering the members of the machine. This will be described in some details for referencing and the importance to protect the structural components from unwanted mechanical stresses, especially the magnets, in addition to the technicians' safety.

The stator unit was mounted rigidly on a 1m test bed plate with sliding ability. The translator structure was kept rigidly tightened by the end caps fitted on a shaft passing through it. Then, the translator-shaft unit was held in a centred position to stator geometry by using linear ball bushings as shown in Figure 8-8(a). Both the shaft and the linear ball bushings were supplied by Automation Components UK Company².



(a)



(b)

Figure 8-8: (a) Machine members' assembly; (b) Oscillating reacting force (FEA)

² <http://automationcomponents.co.uk>

Although the machine members were physically centred, during the manual insertion of translator into the stator, the reacting axial force due to machine cogging was oscillating between attractive/repulsive with an increased amplitude after each pole insertion. Figure 8-8(b) shows cogging force prediction assuming a uniform air gap. It shows that the reacting axial force settled to oscillate due to the combined slot and ends cogging force after achieving full stroke amplitude, i.e. 7 translator poles. This high oscillation in the axial reacting force introduced some shaft bending during the insertion of the translator. This, in addition to the translator mass, caused the shaft to bend as the translator is displaced away from the linear bushes towards the centre of the machine. The result was an air gap eccentricity, a high unbalanced radial attraction force between translator poles and stator teeth after inserting 2 poles and forced the assembly process to stop.

An estimation of the effective vertical radial force component ($F_y(t)$) acting on the translator, when exhibiting eccentricity with respect to stationary stator, is attempted with the aid of the cross sectional view of the machine model shown in Figure 8-9(a). For any eccentricity (U , mm) and an infinitesimally thin sector of ($d\theta$, mechanical degrees), the radial acting force in the vertical direction (F_y) in the air gap (g , mm), where: $Ag - U < g < Ag + U$, may be obtained as:

$$F_y = F_r \cdot \cos(\theta), \quad (\text{N}) \quad 8-1$$

and the total vertical acting force ($F_y(t)$) is then may be obtained as:

$$F_y(t) = \int_0^{2\pi} F_r \cdot \cos(\theta) d\theta, \quad (\text{N}) \quad 8-2$$

This force versus eccentricity in the range ($0 \leq U \leq Ag$, mm) is shown in Figure 8-9(b). Its amplitude is as much as (9.25:1) when compared to the maximum peak-to-peak axial oscillating force, and thus it starts to act in closing the air gap after a few inserted poles. Accurate prediction of the radial closing air gap force plays an important role in predicting the machine performance, in addition to the selection of the shaft supporting the translator structure and the corresponding safety and deformation factors [132, 133].

In order to overcome this problem, additional PTFE bearings acting on the external translator structure circumference have been added to stator structure from both sides, see Figure 8-10. The other option was to select a wider shaft that can withstand the high radial forces based on an allowable eccentricity. This would require new end caps, linear ball bushings and corresponding holders, in addition to ordering and manufacturing time requirements. Therefore, this option was not proceeded due to time constraints.

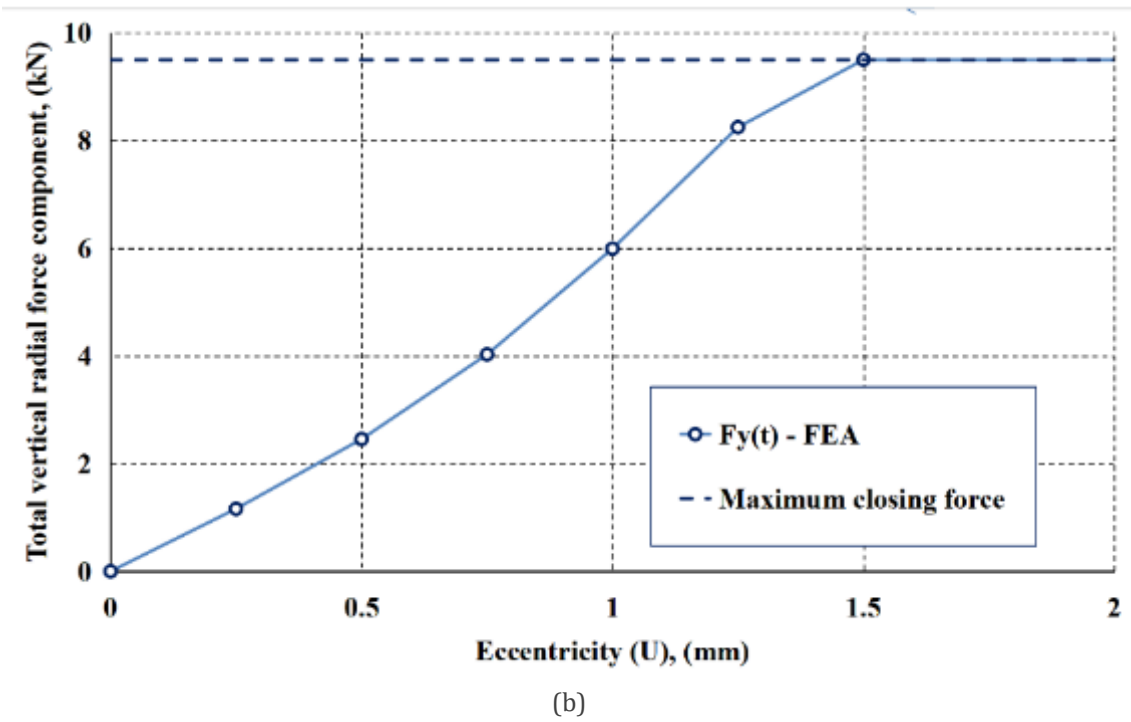
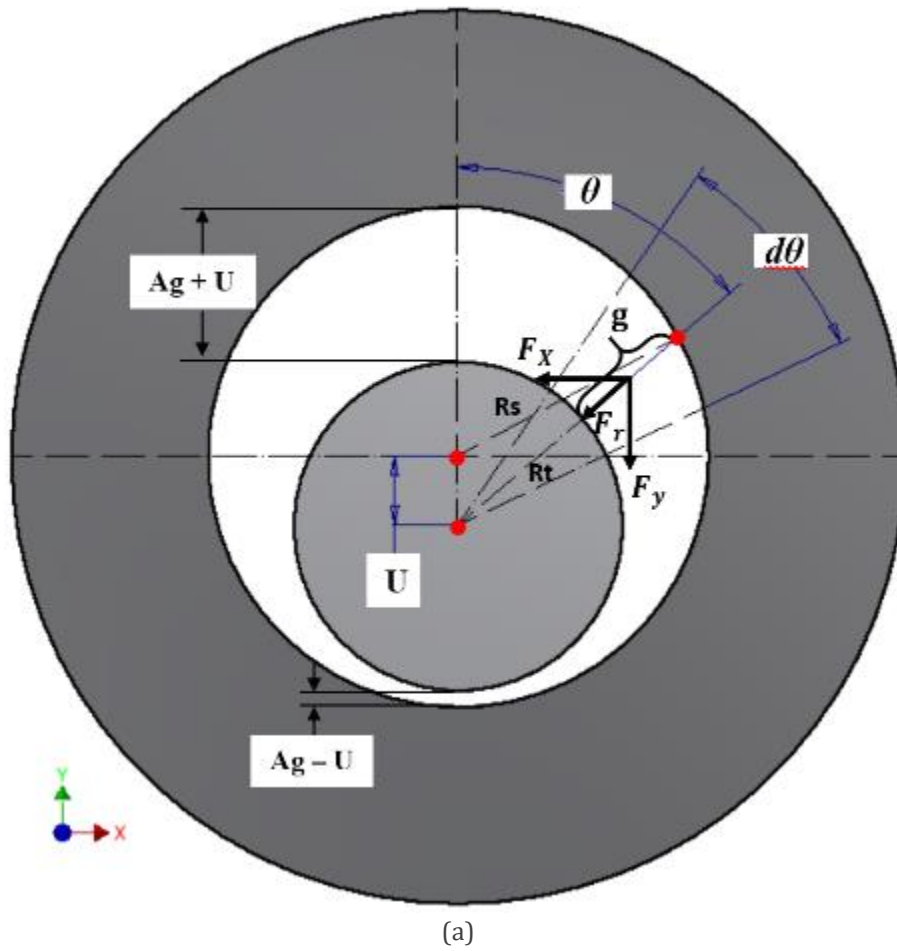


Figure 8-9: (a) Cross section view in machine model describing general translator eccentricity; (b) Effect of eccentricity on airgap total closer force (FEA)

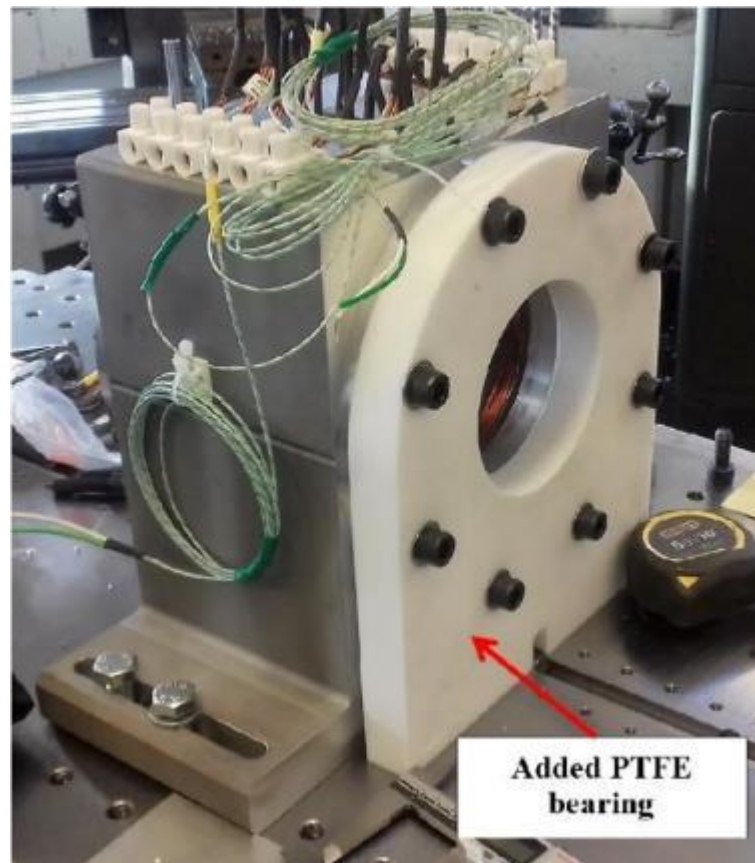


Figure 8-10: Added PTFE bearing to stator structure

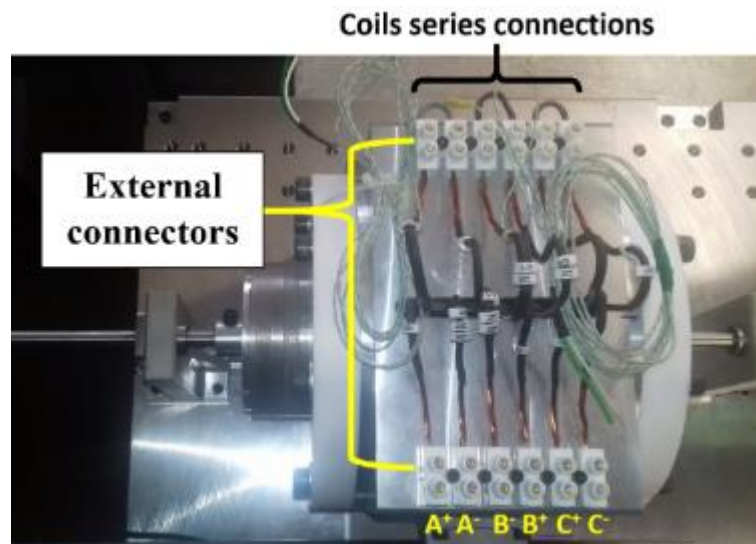


Figure 8-11: Added PTFE bearing to stator structure

8.4.1 Electrical Circuit and power connection

The terminals of each coil are connected to external connectors of appropriate current rating. Connectors were fixed on the machine case as shown in Figure 8-11, and served in achieving the following:

- Each coil can be tested separately for faults.
- Phase connection arrangements can be easily switched between star and delta connection. Parallel and Series coil combination can also be achieved easily.
- Current and voltage can easily be monitored for each individual coil.

8.5 Experimental test rig

The test rig shown in Figure 8-12 (a) was used to test the machine statically, and dynamically. The translator position was controlled by a commercial linear actuator which was mechanically secured to the bed plate. In this manner, the fixed actuator acts as the shaft locker in a rotating machine. The moving actuator part was secured mechanically to the translator shaft via two axial coupling units securing a force transducer (load cell)³ which was used to measure accurately the force on the translator over its possible range of axial displacement. Precise translator position measurement was accomplished via using the Linear Variable Differential Transformer (LVDT)³ shown in the Figure 8-12(a), coupled mechanically with the translator shaft for accurate position sensing. The LVDT outputs 49.98mV/mm with an accuracy of ($\pm 0.25\%$). The error in the load cell measurements is rounding about ($\pm 0.29\%$) over the full measuring scale.

Important machine parts drawings, manufacturer calibration certificate of both the load cell and the LVDT are included in Appendix D. Explanation of how the different measuring units' data were converted into a force and a position is also included.

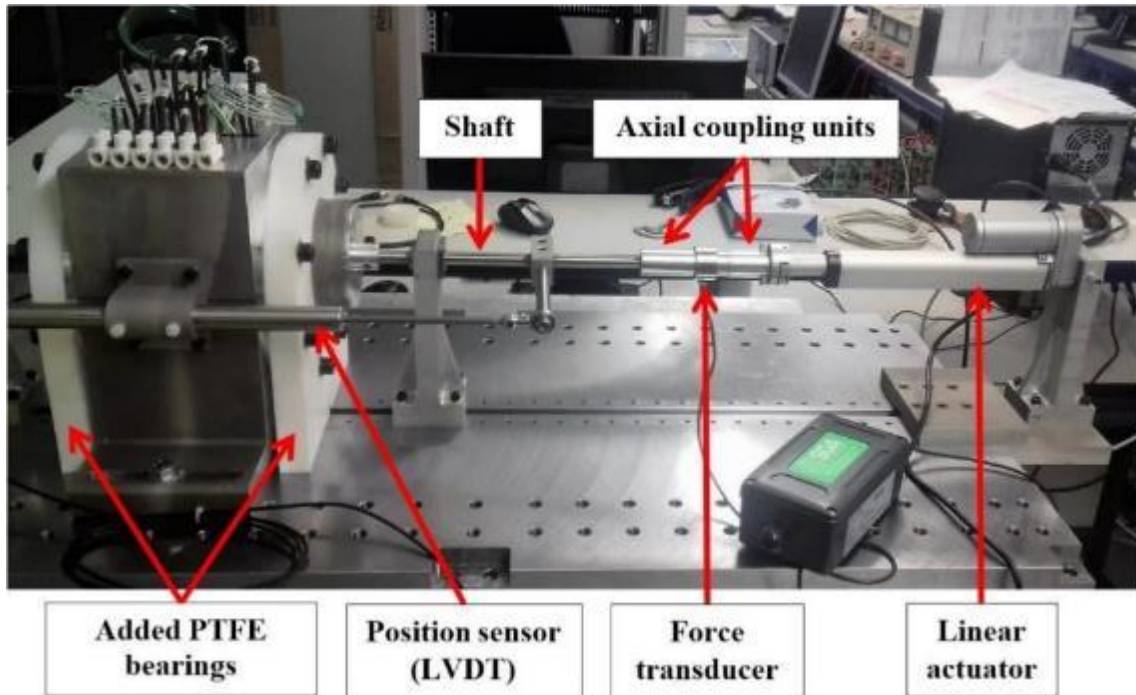
8.5.1 Limitation of available test rig

The test rig described above has the following limitation:

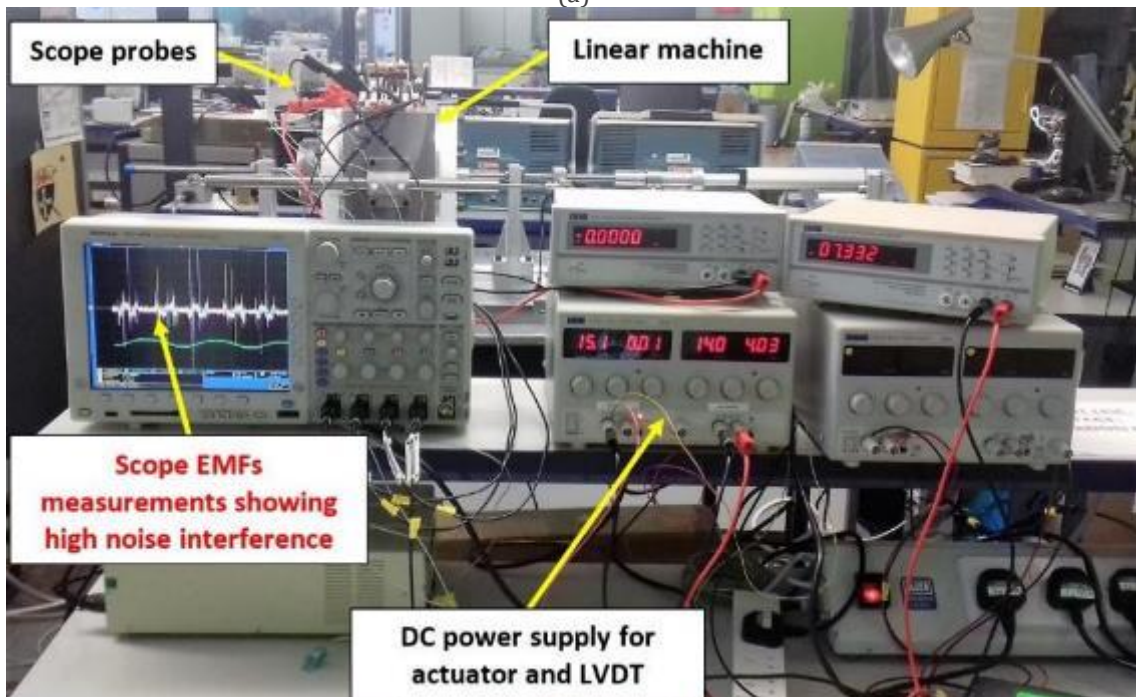
1. Although the linear actuator has a maximum stroke of (150mm), the axial displacement of the translator was not permitted to exceed the PTFE bearings; otherwise, translator eccentricity would be a result and lead to the structural fatigue or damage of different machine parts.
2. The limited maximum speed of the linear actuator was 5.7mm/s. Such a speed would be enough to move the translator linearly and at different excitation conditions and evaluate the machine behaviour statically. Yet, actuator speed rating is too low to be able to excite the rig with an appropriate transient speed.

³ www.appmeas.co.uk

At very low travelling speed, monitoring the EMF induced in machine phases is totally distorted due to the interference of the low level noise frequencies as clearly shown in Figure 8-12(b). Additionally, the iron and the PM losses are too low to measure. Segregation of machine losses requires driving the machine at higher speed level to be measured correctly. Running the machine under the speed of the available drive would give false prediction of these losses as they would be in the error percentages ranges of the used load cell.



(a)



(b)

Figure 8-12: (a) Experimental test rig; (b) Low speed measurements showing noise interference

8.6 Conclusion

The linear machine with moving magnet translator has been designed and its construction was demonstrated. During the construction process, valuable experience has been gained in dealing with SMC and PM materials. The design was accurate with regard to machine parts mechanical dimensions, and the use of the brittle SMC material in constructing the stepped ends stator yoke segments was successful without facing any issues during slot or final stator assembly.

During the translator components assembly, the repulsive/attractive force between moving-stationary magnetic poles was noticed and analysed. In designs requiring larger magnet material mass, such force behaviour would have damaging consequences if not properly managed, and thus it should be considered carefully before starting the assembly process. One solution is to use a suitable gripping technique to protect PM structure from harmful assembly hits.

Air gap closing force and eccentricity were the major problem solved by using PTFE bearing acting on the outer translator circumference, which reduced eccentricity effects during the insertion process of the translator into the stator bore. An analytical prediction of the closing air gap force has been presented to evaluate the effect of the eccentricity between the stator and the translator which could be used in selecting the shaft and linear bushings size and material.

Test rig arrangement and measuring units used were both described, with discussions on the limitation of the test rig used.

Chapter 9 : Testing and Results

9.1 Introduction

This chapter presents the test results obtained to validate the machine prototype that was built as detailed in the previous chapter. Tests were carried out in the Electrical Power Research Group Laboratory at Newcastle University. The whole testing procedure can be divided into the following sections:

- 1- Validation of cogging force: Obtaining the variation of cogging force over two pole pitches of the machine at no-load condition and compare it with that predicted by FEA design model.
- 2- Validation of static force: Apply DC current excitation to machine phases and obtaining the force profile variation over two pole pitches. Different DC levels were applied, results were obtained and compared with the FEA model results.
- 3- Temperature monitoring: Temperature rise in machine coils equipped with thermocouples was monitored and graphed to give an initial assessment to the temperature rise due to machine current loading only. Measurements were recorded at the end of a specific period of time, i.e. when temperature of the coils settles at a constant level, and with different DC current excitation.
- 4- Validation of EMF: At no-load condition the translator was moved continuously as the drive motor speed permit to monitor the induced EMF per machine phases and compare it with that obtained from FEA machine model.

9.2 Resistance measurement

All the measurements and tests are performed on the machine prototype without the addition of the end Flux Gathering Rings designed in Chapter 7. Coil resistance measurement detects any open or short circuit in the coils and helps in identifying any unbalance in different phase windings. Each coil was initially tested after taking it out from the wooden mould, then tested within the machine casing for any short circuit faults at room temperature. Variable voltage DC power supply was used for the purpose of measuring the phase resistance by applying different voltage amplitudes at the terminal of each phase, composed of two coils connected in series, and measure the corresponding current for each applied voltage. Then, the resistance value was averaged over the number of tests.

Theoretical resistance calculation, assuming an average diameter of the coil at the slot centre, was performed using the formula given as:

$$R_{ph} = \frac{a_s \cdot N_C \cdot l}{\sigma \cdot S \cdot A_C} \quad , (\Omega) \quad 9-1$$

Where (a_s) represents the number of coils connected in series; (N_C) is the number of coil turns; (l , m) is the length of one turn at coil centre; (σ) is the electrical conductivity of the copper and equals to ($1/5.77 \times 10^7$ S/m) at room temperature. (S) is the strand number, and (A_C , m^2) is the cross sectional area of the copper wire used. Table 9-1 shows the calculated, FEA predicted and the measured phases resistances. Higher value resulted from calculations since coil diameter is averaged at slot centre.

Due to connecting cables, connectors and the use of a wire of 3 strands ($S = 3$) with the gaps between them (circle packing), the measured resistance for each phase differs from the predicted FEA one, which would cause an error in copper loss and inductances. In addition to that, there exists a difference rounding about (± 5.9 %) between machine phases implying that one or more coils may have incorrect number of turns. Therefore, it is advised to use a winding machine in future rather than wind coils manually to form symmetrical coils with same exact number of turns.

Table 9-1: Predicted and measured resistance in machine phases

Phase identity	Resistance value (Ω)	% error
R_{ph} , calculated	0.301	32.6%
R_{ph} , FEA	0.227	base
Phase A, measured	0.26	12.7 %
Phase B, measured	0.269	18.5 %
Phase C, measured	0.253	11.5 %

9.3 Inductance measurement

Inductance measurement was performed on the phases before the machine assembly, i.e. without the magnets. By connecting a 50 Hz variable AC power supply across each phase and measuring the current through the phase winding while varying the voltage, the impedance can be measured. Three tests per phase were performed with different applied voltages and the calculation are averaged.

Using the measured phase resistance per phase, the inductance is then calculated and compared with that obtained from FEA model as listed in Table 9-2. Results show almost similar deviation from the base predicted FEA value and a difference that does not exceed ($\pm 1.9\%$) between different phases, which is considered good in verifying the machine model.

Table 9-2: Predicted and measured inductance in machine phases

Phase identity	Inductance value (mH)	% error
L_{ph} , FEA	≈ 1.96	base
Phase A, measured	≈ 1.62	17.3 %
Phase B, measured	≈ 1.64	16.3 %
Phase C, measured	≈ 1.61	17.8 %

9.4 Cogging force measurement

No-load cogging force variation with the translator displaced over two pole pitches is shown in Figure 9-1. As can be seen clearly in the figure, the measured results of both translator motion directions has a positive offset. However, when this offset is cleared as shown in Figure 9-2, the correlation between the predicted FEA model and the measured results is considered good, for both directions, with some notable deviation that occurs at some measured points. These deviations have two possible explanations. The first is the unavoidable mechanical tolerance in the machining processes of both the magnets and the soft magnetic composite spacers that, when accumulated, would result in a slight width difference in the consequent magnetic poles. Secondly, there is some influence due to the effect of machining different components composing the stator and the translator parts and the accompanying effects on materials magnetic properties. This is specifically in machining the soft magnetic composite (SMC) material and the laminated teeth, which is hard to quantify throughout FEA modelling, yet may have some unpredictable impacts on the results.

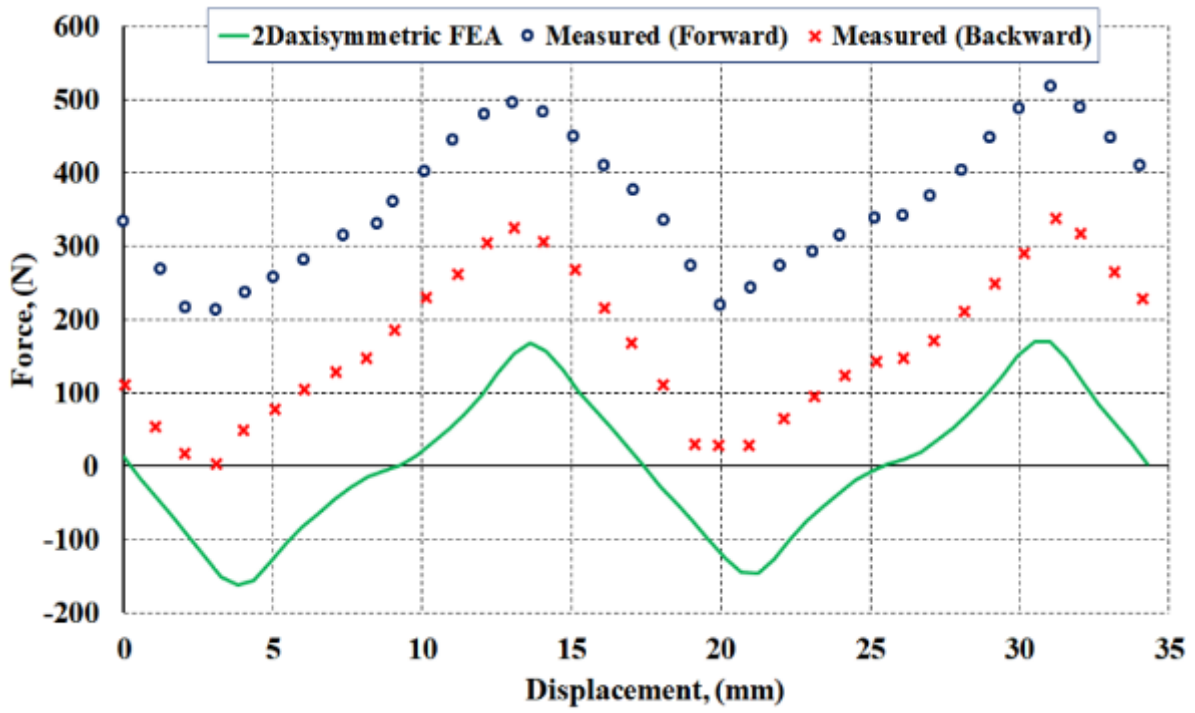


Figure 9-1: Measured cogging force variation with translator displaced over two pole pitches with offset

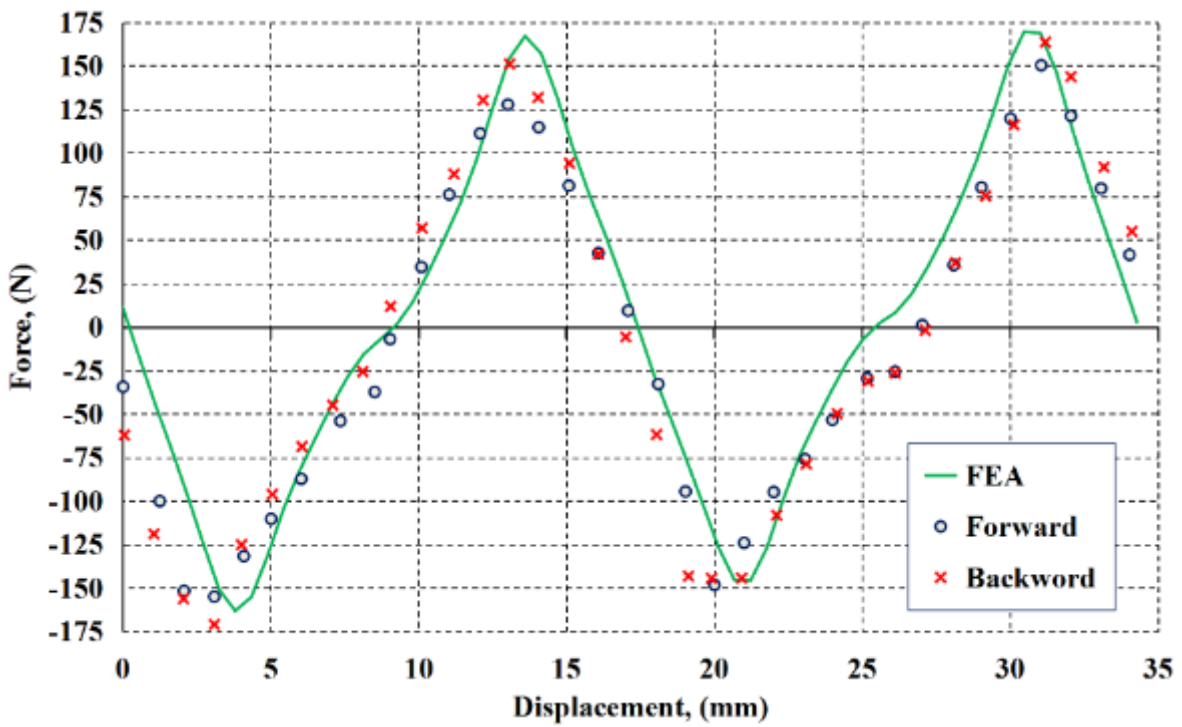


Figure 9-2: Measured cogging force variation with translator displaced over two pole pitches with removed offset

9.5 Force production

One of the methods to assess the capability of force productivity of a linear electrical machine is the DC static force testing. This test is applied to the machine prototype with its phases connected as shown in Figure 9-3. When applying a DC current at one phase and flows through the other parallel connected phases, this will correspond to an instant if three-phase sinusoidal currents were applied to machine phases. During performing the DC force test, the temperature of the coils assigned in Figure 9-3 was kept under monitoring and the measurements were recorded at the end of each applied DC current level. Each test lasted around 60 minutes and the steady temperature was recorded, see Figure 9-4.

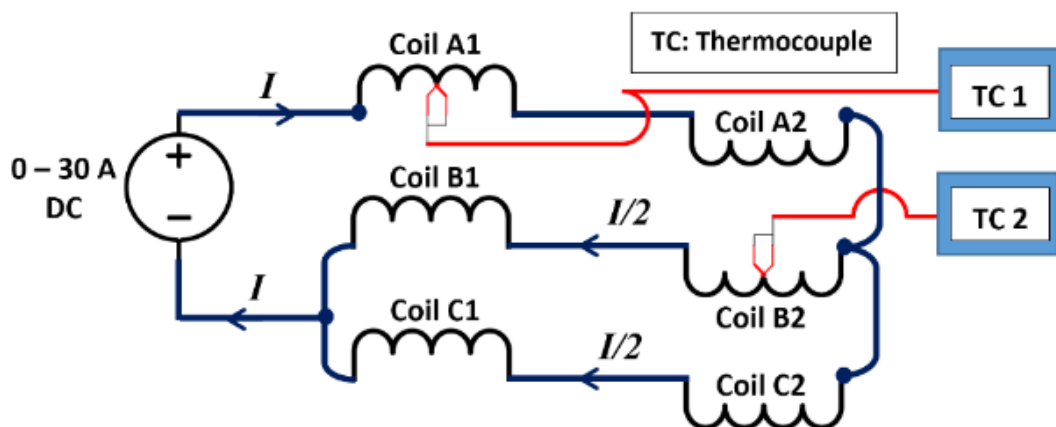


Figure 9-3: Electrical circuit phase connection during static force measurement test

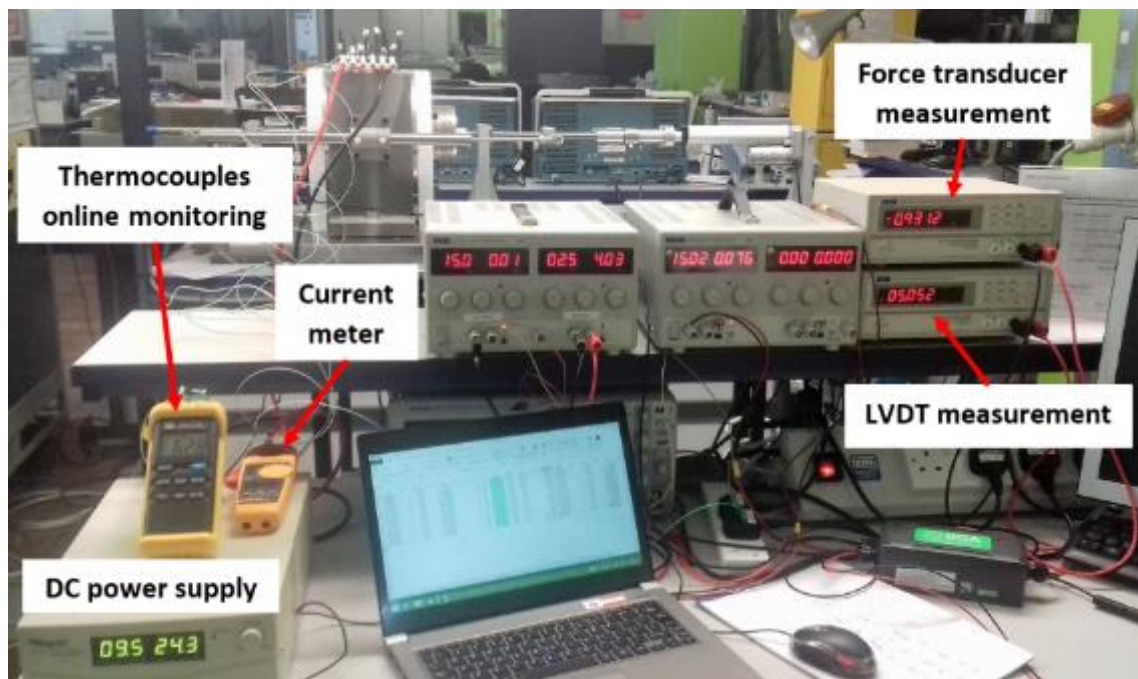


Figure 9-4: Online monitoring of machine coil temperature rise during static test

Comparison of typical test and FEA model results is performed for different current amplitudes. Each test measurements' offset was cleared and compared with the corresponding FEA model results as shown in Figure 9-5(a-d). It can be seen that the correlation between the two results is considered in a good agreement, with the cogging force pronounced at low current amplitudes and its effect tends to diminish as the current level is increased. Some notable divergence between results are also clear due to aforementioned explanations, however, the similar trend of both curves is obvious for different current levels with maximum deviation approaching 50% at start of some measured points.

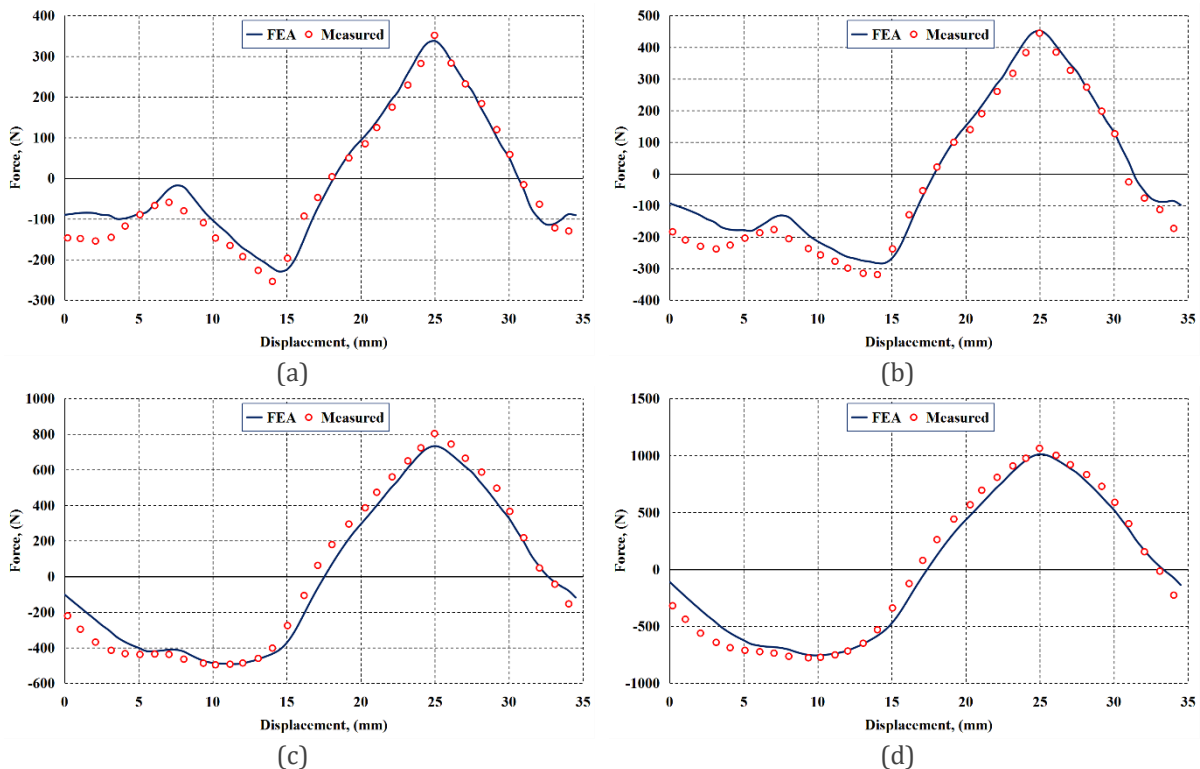


Figure 9-5: Static force test at different DC current amplitudes (a) $I = 4.8$ A; (b) $I = 8.0$ A; (c) $I = 16.0$ A; and (d) $I = 24.0$ A

9.6 Thermal analysis

The temperature increase in machine coils shown in Figure 9-3 was monitored and recorded during static DC force testing. The measurements were recorded after the temperature is settled for each DC current level and is shown in Figure 9-6. It is obvious that for current values below 8A, coil temperature remains unchanged showing ambient temperature. As the current increased above 8.0A, coils temperature starts to rise and settle at a higher value, with the centred coils showing higher temperature level compared to lateral coils. However, even with the highest current injected, the highest temperature does not lead the coils to overheat.

The heat generated in machine coils is due to machine electrical loading, the electrical power loss in machine winding. It does not embrace the space harmonics of armature winding mmf, as DC current produces only a stationary electromagnetic field.

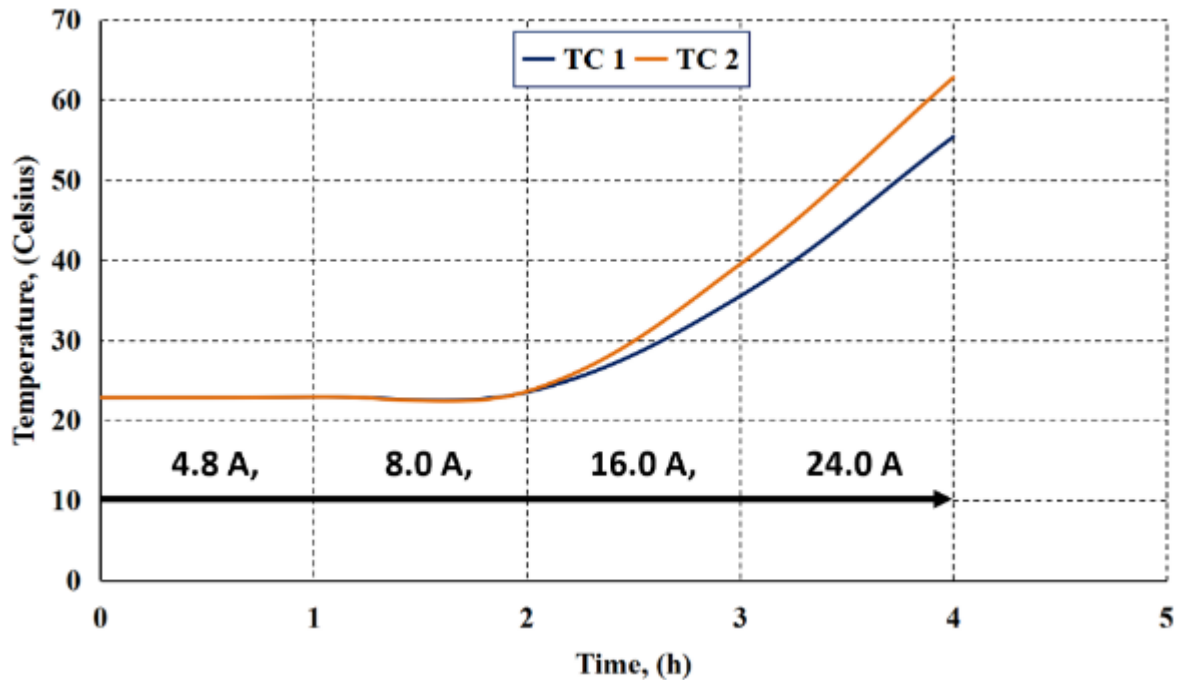


Figure 9-6: Temperature rise in machine coils over 4 working hours

The machine is designed for natural cooling and therefore future experimental work should consider exciting the machine windings with three phase variable voltage source with variable frequency to produce axially travelling field at different speeds. Additional thermocouples need to be fixed at specific positions in the machine housing to measure the temperature due to the combined effect of both current loading and the machine iron loss. This would give a more accurate prediction of stator magnetic circuit heat capacity and can be accomplished for both symmetrical and asymmetrical current waveforms, with and without the translator member. Suggested positions for thermocouple fixation are the centre of the machine housing and the centre of one machine case end caps.

9.7 No - Load EMF induced

An open circuit test was conducted by moving the translator at rated actuator speed (5.7 mm/s) to measure the EMF induced in the phases. Many experiments were carried out in order to measure the induced three phase EMFs, yet the waveform was highly distorted as can be seen in Figure 9-7, one of the best samples from the performed experiments measure.

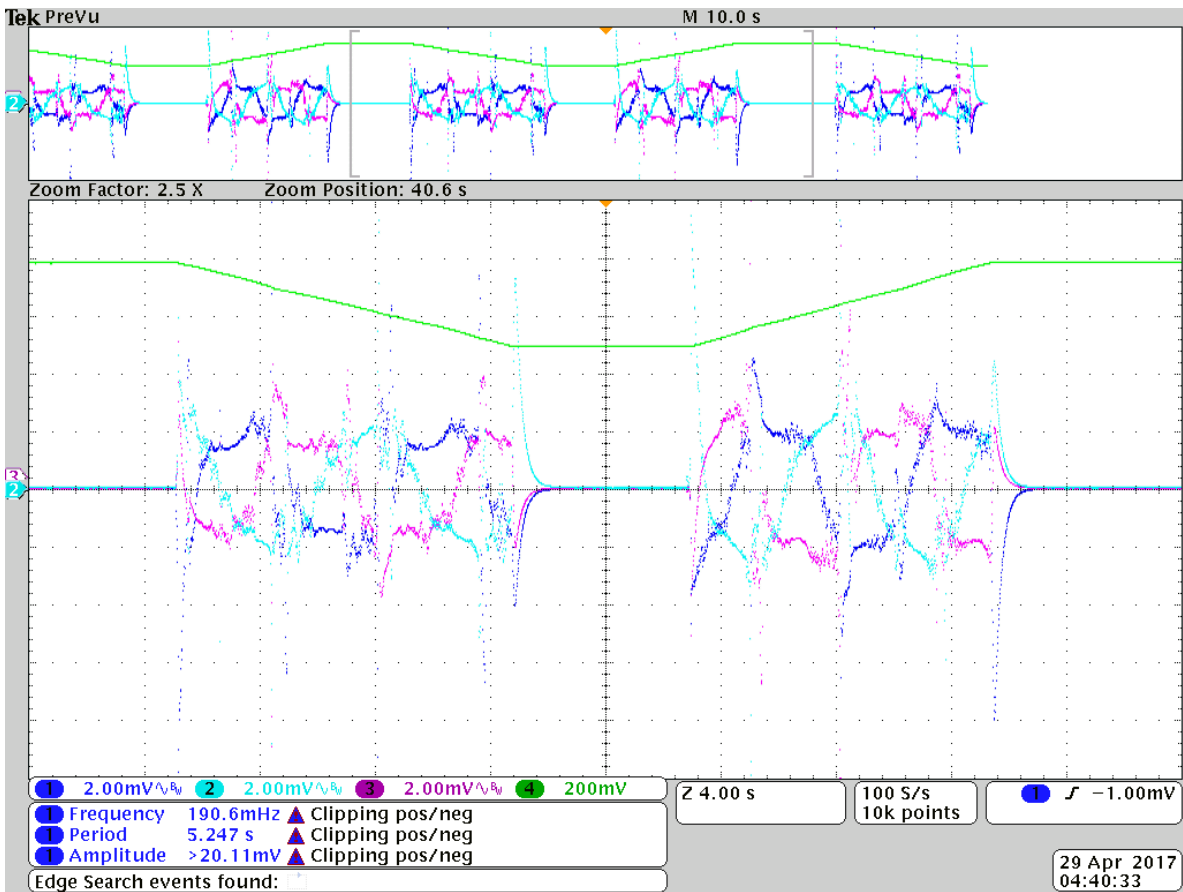


Figure 9-7: Measured EMF induced in machine phases

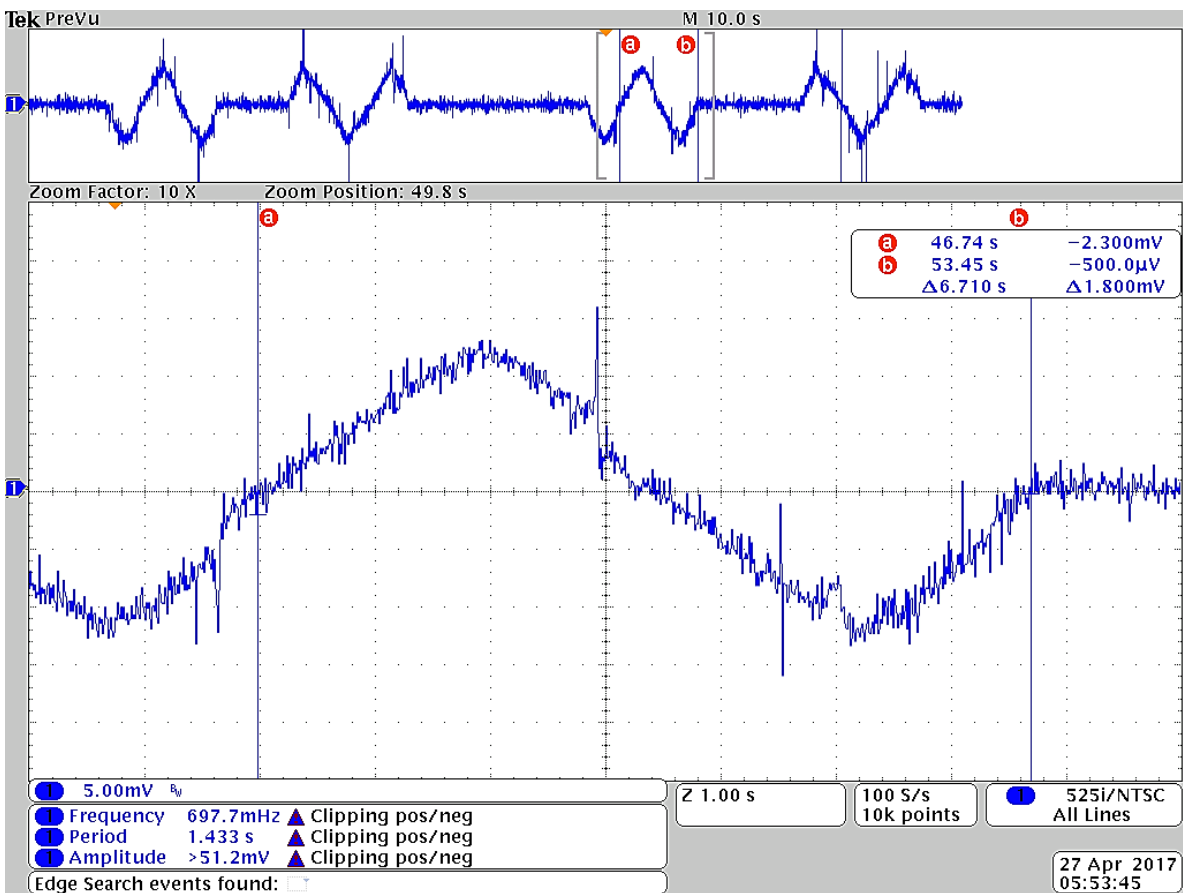


Figure 9-8: Measured EMF induced in one machine phase

In order to minimise the waveform distortion, one phase induced EMF was measured as shown in Figure 9-8, and compared with FEA model results as shown in Figure 9-9. A difference between the results is clearly seen with a maximum deviation of 9.5 % when comparing voltage waveform amplitudes. However, this may be considered fair with the existing noise in the measured signal at this low speed.

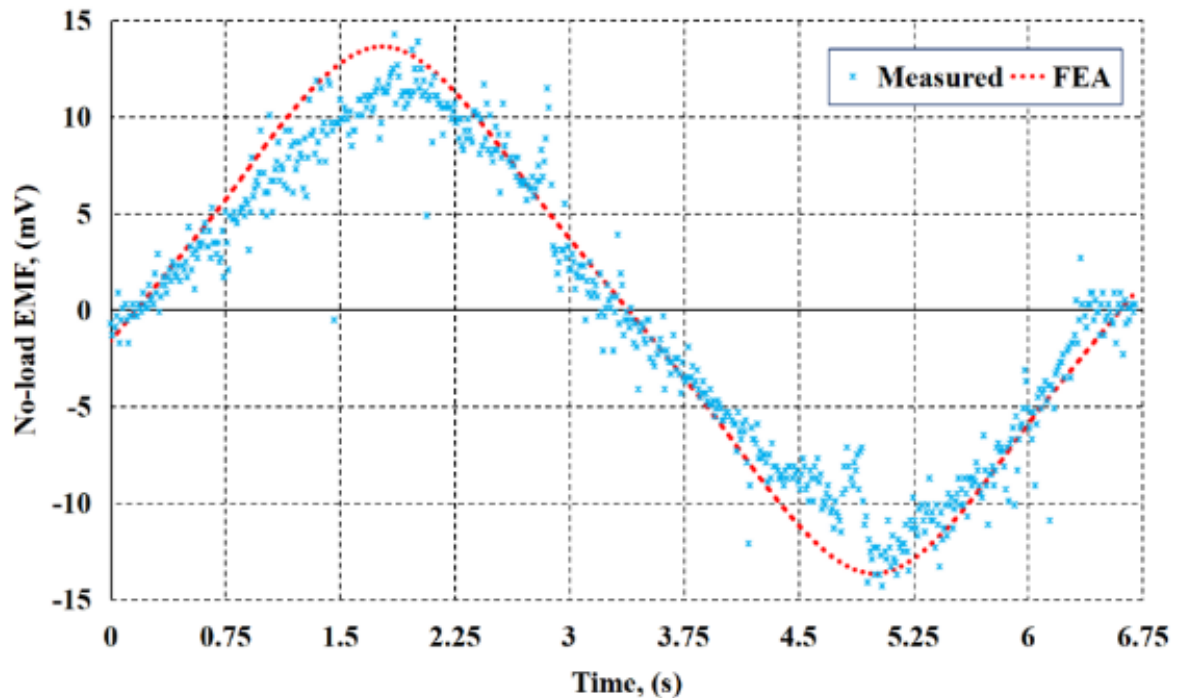


Figure 9-9: EMF induced in one phase measured comparison with FEA model result

9.8 Magnetic pole damage

All previous tests were performed on the prototype machine without the added ends Flux Gathering Rings designed in Chapter 7. Addition of these rings requires prototype disassembly. Therefore, the translator was removed from the stator in order to replace the end teeth with the newer teeth including the added Flux Gathering Rings, as shown in Figure 9-10. Unfortunately, during the second assembly of the machine some of the inserted poles were damaged inside the stator and prevented finishing the assembly, see Figure 9-11. This can be explained by the following reasons:

- 1- During translator pole set assembly and the noticed collisions, some pole components have weakened.
- 2- During the tests, the PTFE bearings were subjected to frictional force, especially during EMF testing, that acted to grind the bearings.

- 3- The grinded PTFE bearings lead to air-gap eccentricity to occur. The attracting force between stator teeth and the inserted magnetic pole components acted to bend the shaft and to fracture an SMC or a PM of the inserted poles, such that the inserted translator poles were stuck inside the stator.

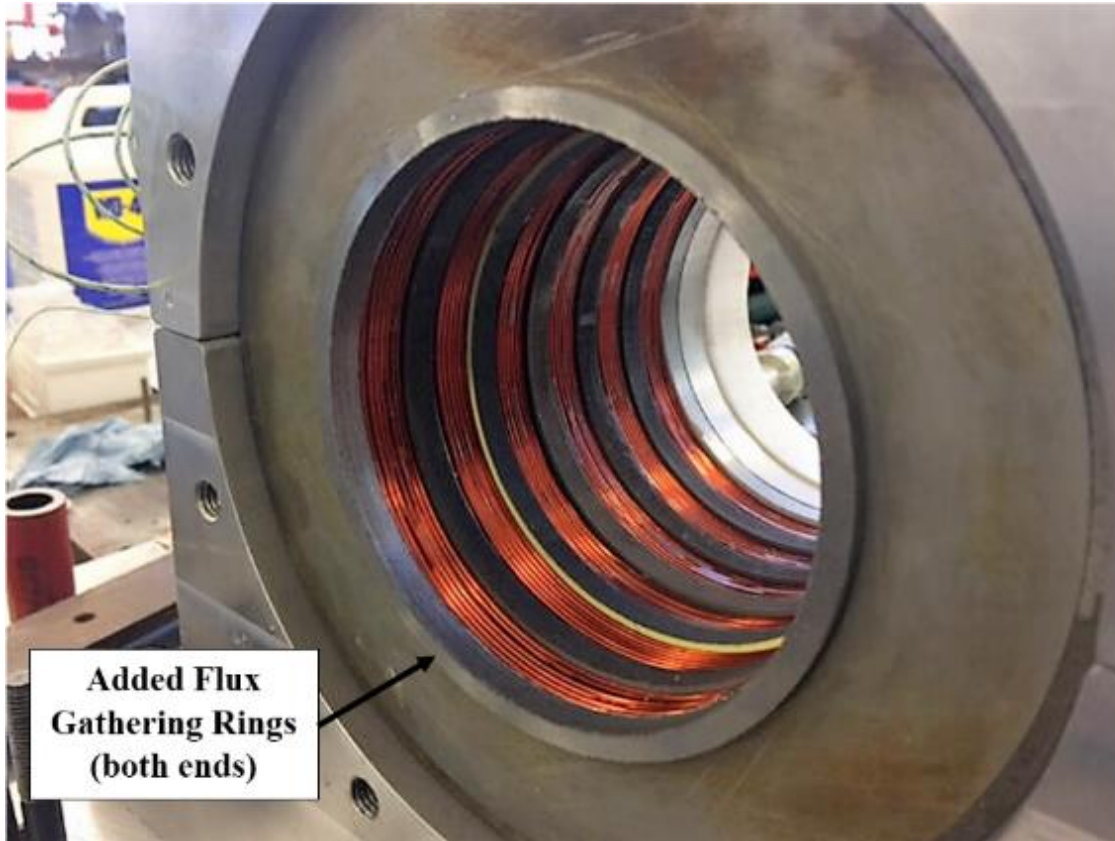


Figure 9-10: Stator end teeth with fitted Flux Gathering Rings

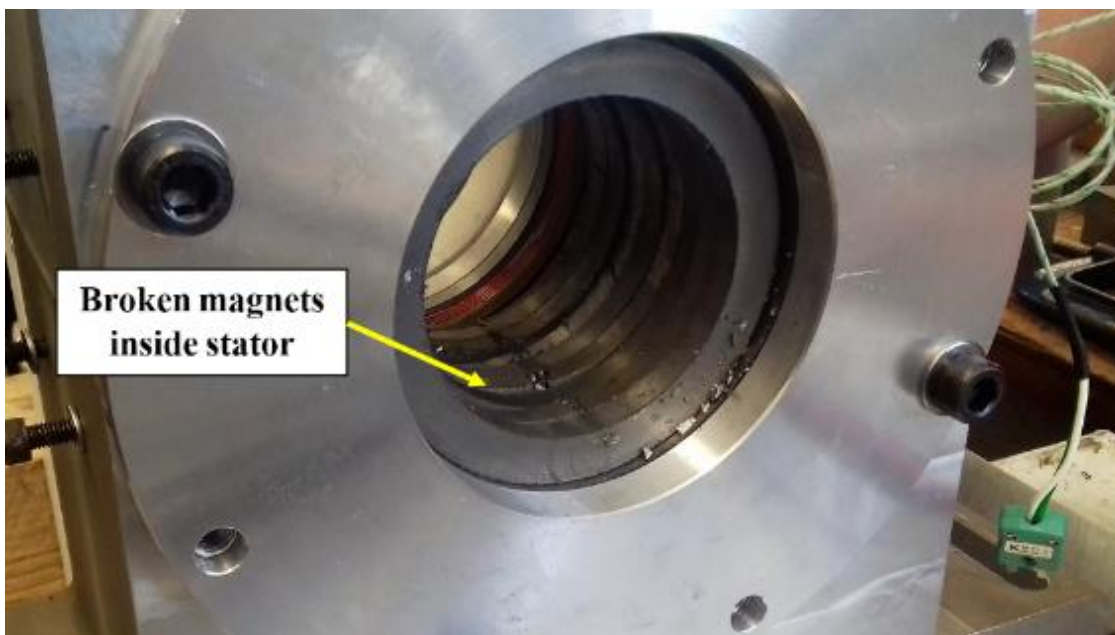


Figure 9-11: Stator end teeth with fitted Flux Gathering Rings

The efforts spent by the technician were highly appreciated to extract unbroken poles, yet the poles inside stator were totally damaged. The 7 remaining poles were not enough to perform any further testing. This will be considered as a future work to prove, experimentally, the effectiveness of novel cogging force reduction technique established in this research.

9.9 Conclusion

This chapter presented the tests of the machine which were conducted using a static and dynamic test rig. Cogging force variation over two full pole pitches was measured using the static test rig. The results showed a good agreement and verify the predicted values by FEA design model. DC static force capability test at different current amplitudes was performed, and also verify those predicted at each current level.

Temperature measurements were recorded. Centre coils of the machine during DC static force test were noted to heat more than end coils, which means that thermal conduction is poor at machine centre. However, although the highest temperature recorded is in the range for air cooling operation, yet source of heat was only due to a fixed current density of ($4\text{A}/\text{mm}^2$). Desired application operating condition will impose variable frequency, variable amplitude traveling field within the machine and thus other sources of heat would be added. Recommendation on further testing on the machine temperature rise are reported in order to account for all heat sources within the machine.

Also, without knowing the temperature of the ambient surrounding the machine in the desired application with the engine, thermal analysis of the system will still lack thermal constraints, and this a good subject for a future research.

Open circuit test was also conducted to measure the EMF induced in machine phases, however, due to the very low dynamic test speed, scope waveform readings were highly distorted. Nevertheless, single phase EMF was measured and compared with FEA model results and showed good agreement with an error percentage not exceeding 9.5 %.

From the discussed results, important assembly recommendations are reported on the current machine topology. As the experience has shown during the initial and later assembly of the machine, it is recommended that smaller machine rating is more appropriate to deal with, in order for this potential technology to succeed. Smaller power rating machines is easy to maintain and go through assembly.

Chapter 10 : Conclusion and Future Work

10.1 Introduction

The main goal of this thesis is focused on the electromagnetic design, modelling and performance study of a linear machine operating as a Linear Generator (LG) for integration with a Linear Joule Engine (LJE) for the purpose of electrical power generation. Several aspects have been explored during the course of this PhD which are summarised in this chapter to verify meeting the research objectives.

10.2 Design constraints and investigated topology

The direct coupling of the LG with the engine piston requires the development of a system for use in a limited volumetric envelope. This requires knowing the interlink between the electrical machine and the driving engine geometrical and operational parameters. This aspect was not described in details elsewhere and has therefore been illustrated by deriving a set of constraints from the operational and geometrical characteristics of the engine in this study. Compact integrated system considers knowing the engine dimensions to achieve a compact system in both axial and radial system coordinates. However, selection of these design parameters is not fixed, where different selected parameters would give different machine specification, different integrated system dimensions and variation in the associated performance. The (1:1) ratio of active machine-to-stroke amplitude lengths investigated in this study showed a compact vertical system with a total system length of 5 times the engine stroke. A ratio of (1/2:1) is worth to investigate in a future study in order to see the subsequent effect on the system dimensions using the current study as a base.

10.3 Optimisation method and investigated topology

The design of three possible machine topologies had been investigated sharing the same constructional features and design constraints. The results showed that the radially magnetised machine topology was below the design force by 25%. The other two machine alternatives have showed satisfactory and comparable performance. The machine equipped with the Flux-Concentrated magnet was selected over the Quasi Halbach arrangement, due to the better PM utilisation of the former, as explained in Chapter 4 - section 4.7. The optimisation method is clear and fast as it avoids solving the unwanted changes of various design variables. The method can be used in designing other machine topologies by setting the desired design objectives for a known set of design constraints.

10.4 Detailed machine design

The detailed design of the adopted machine topology had covered four aspects to select an efficient, manufacturable design with load integrity as described below.

- 1- **SMC material:** Using SMC material satisfies the multi directional flux paths within the machine core geometry, besides simplifying the manufacture process compared to laminated steel sheets. However, the low SMC permeability has the impact of degrading the machine performance in a fully SMC stator machine [73]. This study avoided the full SMC construction of the stator and limits the material use in parts of it, the core back, besides using it in the mover magnetic core as iron pole pieces. In both these parts the flux pattern has multi direction and using laminated steel sheets in practice is perhaps impossible. Throughout the detailed design investigated in Chapter 5, results had showed that using SMC this way has a negligible effect on the resultant force capability, 1.5%. Further investigation into the machine model with the teeth made of SMC material and the machine loading is variable would be an enlightening study by considering machine losses. In such a case, the stator core back can be made of radially stacked steel lamination sheets inserted between the adjacent teeth.
- 2- **Air-gap and PM grade:** During these changes it was shown that a penalty of 26% PM mass increase was the result of a machine model with a larger air-gap and a stronger magnet. However, the force fluctuation was reduced by increasing the air-gap length while utilising stronger magnet grade.
- 3- **Pole number:** The optimal 5 pole machine model was compared with the 7 pole design model. The comparison had showed remarkable design and performance parameters changes. Most importantly the effect of PM mass per pole ratio and the resultant force fluctuation. Results showed that higher efficiency can be obtained using a 5 pole design with a 15% saving in magnet mass, yet the resultant rated force fluctuation had increased up to 4 times than that in the 7 pole design.
- 4- **Power conversion technology:** The load electrical circuit change was investigated for the 7 pole machine model. It was shown that both the machine design and the performance were greatly influenced. This implies that knowing the exact use of the system is compulsory to design the machine according to the power extraction technology that will be used. The machine for unity power factor convertor application had offered the lightest mover mass and the highest electrical power generated.
The grid interface application offered comparable dimensional parameters with the pure resistive loading design model, yet with a higher rated force fluctuation.

The best efficiency was achieved by assuming the load is purely resistive. It is worth to mention that the selection of the topology according to power conversion scenario also subject to meeting the design constraints. For instance, a lighter moving mass machine design would result in a faster system operation irrespective of the electrical load variation. This means that the mechanical frequency of the system will subject to changes and hence one of the design constraints had changed.

10.5 System modelling

This thesis presented a new analytical model of the Linear Generator with the inclusion of all interacting mechanical and electromagnetic forces of different origins. Cogging force, armature reaction and losses were all not considered in the found literature. These forces were previously not taken into consideration and neglected in the existing literature by oversimplifying the linear machine to act as a simple damper.

Detailed model description with FEA validation were reported. Critical impact of cogging force amplitude on machine performance and efficiency were investigated in a feedforward manner. The effect of machine inductance on shaping the machine force profile was described with FEA validation. Then, a novel dynamic system incorporating both the engine – generator coupled directly and work in a closed form was described. The model presented is an important investigative tool in the current research area.

The impact of integrating a linear generator of high cogging force amplitude on the system performance and electrical power generated was introduced. Deceleration effect was the most important impact of the high cogging force with the consequences such as the reduced electrical power generated and the reduced rated current.

This dynamic model is unique in this field and can be modified to investigate other linear machine types for applicability in this innovative technology. Possible extension and modification to the model is the inclusion of the thermal effect on the effective phase resistance, and on the operating point of the PM.

10.6 Cogging force reduction technique

A new structural cogging force reduction technique was presented in Chapter 7 with analysis and FEA validation. The technique adopts modifying the machine structure by adding Flux Gathering Rings at both machine ends to reduce cogging force due to ends effect. The optimal dimensions of the added rings have not only a negligible effect on the machine volumetric dimensions, but also a positive impact on the resultant machine specific power density.

Applying the technique had showed its effectiveness in minimising the total cogging force at both no-load and rated load by 75 % and 72.5 % respectively. Moreover, it offers a saving of up to 67.5 % in electrical power generated by the system when investigated using the linear-generator dynamic model. However, some impacts are accompanying this saving such as the introduced (± 0.95 %) imbalance to phase inductances, which is worth to investigate deeply in a future work step. The technique should be further extended and applied to the 5 pole design which would be a good extension of the work.

10.7 Constructed model and test results

The selected machine design model was constructed and tested as illustrated in Chapters 8 and 9. The prototype construction challenges have been pointed out, mostly due to the high radial attraction forces during machine assembly. Assessment method of these forces was implemented using appropriate analysis. The method can be used in future to estimate these forces and to select the appropriate shaft diameter, which plays an important role in deciding the total moving mass of the integrated system. Intensive recommendations have also been reported regarding adjacent translator poles assembly to protect pole structure from magnetic field nature between the poles.

Machine phase parameters test were measured with the translator out of the stator. Results had showed a larger resistance and a lower inductance, and an imbalance in both compared with FEA results. However, this is considered to be acceptable by using the manual coil winding technique and with the existence of some errors in the test equipment.

Cogging force and DC static force tests results showed a good agreement with the FEA predicted values despite some deviations without losing the trend nature. EMF open circuit test was carried out, with the limited low speed ability and the unwanted distortion, and found to validate those predicted by FEA design model with maximum deviation not exceeding 9.5%. Therefore, the tests result presented in this thesis had verified that the linear generator design methodology adopted was successful with experimental validation.

Therefore, the adoption of moving magnet machine with Flux – Concentrated pole arrangement for integration with the driving engine is feasible and was confirmed by the reported dynamic model results with the extensive findings on system consistency and feasibility.

10.8 Importance of the technology

The dependency on fossil fuels in electrical power generation have attracted many researchers to investigate innovative technologies using various renewable energy resources. One of these technologies is investigated in this thesis which incorporates a LJE driving a LG for electrical power generation. Compared to rotary engines that suffer from efficiency reduction in small scale applications, small scale linear engines, on the other hand, overcoming the efficiency reduction irrespective of the load variation [107]. Successful implementation of the system offers a significant opportunity to reduce energy cost with the fewer components of the engine, in addition to the increased efficiency, the reduced unwanted emission and the wide range of applicability. However, the success of the technology is linked between the two major components of the system: the LJE and the connected LG, the design of which is highly depends on the engine operational and dimensional characteristics to satisfy an efficient, compact system.

10.9 Future work

There is much work in the area of this promising technology and is therefore split into two major parts due to the Multiphysics nature of the integrated system. The first part covers the possible future steps to further progress in investigating the electromagnetic design of the linear machine and the suitability for integration with the driving engine under the same constraints.

10.9.1 Future electromagnetic machine design

The following are some machine design suggestions for the same existing design constraints, i.e. same driving engine. These are:

- 1- Other feasible slot/pole combination, listed in Chapter 4 - Table 4-1, would form a good future extension to the work considered in this thesis for further study on the effect of slot/pole changing on machine design, performance and specifications.
- 2- Single – phase machine with 3 slots/pole/phase, i.e. $q = 3$ as shown in Figure 10-1. The machine must subject to the same design constraints and compared with the existing design. The stator core back should be modified to be able to carry the flux from three consecutive teeth without saturation, and thus a heavier stator with smaller slot geometry is a result. Both stator and translator key design parameters require optimisation to achieve the balancing between the magnetic and electric loadings.

Analytical model need to be modified for the newer optimal key design parameters of the single-phase machine. Inspection of model can then be accomplished using feed forward in Simulink, and dynamically in LMS using the modified models with respect to cogging and armature reaction forces and their combined effects on the resulting force profile, and overall system integral performance.

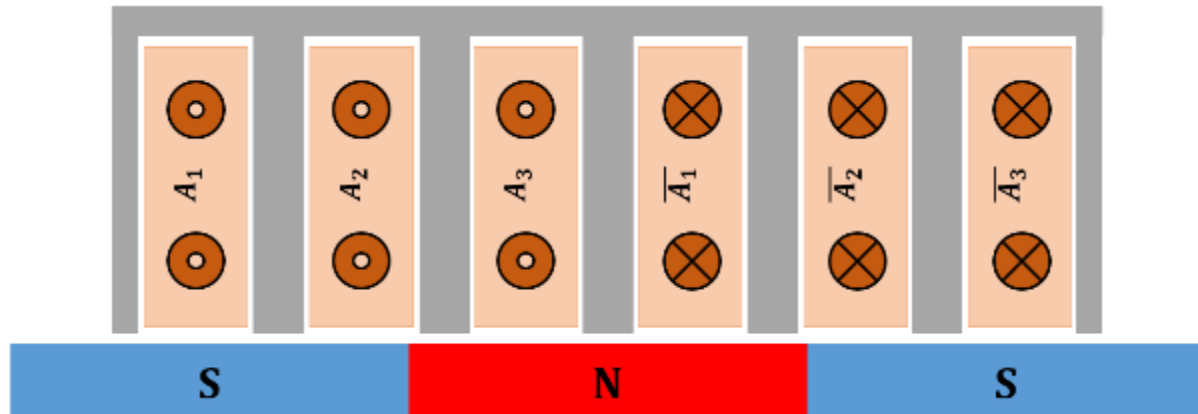


Figure 10-1: Single phase linear machine design proposal

- 3- Six - phase machine design, a newer linear machine design model in this field. The same stator key parameters can be fixed in this design. The translator pole pitch and pole number must be redesigned to achieve the required 60° electrical between phases. The same steps reported in the previous point can then be repeated with respect to investigating the design, design model validation and performance investigation using the various modelling tools. This machine model is new and its optimisation can include the power conversion scenarios proposed in Chapter 5 – section 5.5.
- 4- Another possible future work on the electromagnetic machine design is by splitting the driving force into two identical forces, where each force is used to drive a separate linear machine. Both machines are now mechanically driven in parallel. The electrical load can be shared offering for load sharing concept investigation. However, separate electrical loads can be supplied. This idea is novel by itself in this research area in which each machine must be optimised according to the desired electrical load. If same electrical load is assumed, identical machines would be a result. In such a case, a physical axial displacement can be introduced between the mounted stationary members of the identical machines to offset the resulting cogging force, or rated load force fluctuation. After designing the machine model, the parallel operation must be proved by FEA which requires modelling of the two machines with appropriate coupling in a single run, then machine modelling can be considered for performance prediction.

10.9.2 Future thermal analysis

The second part would cover the complete thermal analysis of the whole system. Since the engine is thermally driven, knowing the heat transferred to the electrical machine parts is compulsory. As thus, machine members cooling system and applicability in practice should be deeply investigated. However, in case of moving magnet machine design, cooling technique could be a real challenge from mechanical point of view. Therefore, focus should be on cooling the armature winding such that the heat generated by stator windings is distributed along the active stator volume uniformly upon reaching its minimum levels at stator housing surface.

In this thesis, natural cooling was assumed in the design, and it was shown via the experimentation performed in Chapter 9 - section 9.6, Figure 9-6 that electrical power loss and the heat generated in the machine coils are unevenly distributed. Therefore, its performance would be affected due to the expected machine phase impedance imbalance, mostly due to unbalanced effective phase resistance. Unless a cooling method is applied to the stator of the machine, efficient system operation will be lost. Possible cooling methods are:

- 1- Blown air: whereby air is blown over the outer surface of the machine housing by a fan, and the housing of the machine can be optimised to improve heat removal by designing the outer surface to have fins in order to increase the surface area over which air is blown.
- 2- Wet cooling: whereby the machine stator/housing is flooded by a coolant like water.

REFERENCES

- [1] W. Cawthorne, P. Famouri, and N. Clark, "Integrated design of linear alternator/engine system for HEV auxiliary power unit," in *Electric Machines and Drives Conference, (IEMDC 2001) IEEE International*, 2001, pp. 267-274.
- [2] R. W. Moss, A. P. Roskilly, and S. K. Nanda, "Reciprocating Joule-cycle engine for domestic CHP systems," *Applied Energy*, vol. 80, pp. 169-185, 2005.
- [3] W. R. Cawthorne, P. Famouri, C. Jingdong, N. N. Clark, T. I. McDaniel, R. J. Atkinson, *et al.*, "Development of a linear alternator-engine for hybrid electric vehicle applications," *IEEE Transactions on Vehicular Technology*, vol. 48, pp. 1797-1802, 1999.
- [4] M. R. Hanipah, R. Mikalsen, and A. P. Roskilly, "Recent commercial free-piston engine developments for automotive applications," *Applied Thermal Engineering*, vol. 75, pp. 493-503, 2015.
- [5] R. Mikalsen and A. P. Roskilly, "The design and simulation of a two-stroke free-piston compression ignition engine for electrical power generation," *Applied Thermal Engineering*, vol. 28, pp. 589-600, April 2008.
- [6] R. Mikalsen and A. P. Roskilly, "Performance simulation of a spark ignited free-piston engine generator," *Applied Thermal Engineering*, vol. 28, pp. 1726-1733, 10// 2008.
- [7] R. Mikalsen and A. P. Roskilly, "A computational study of free-piston diesel engine combustion," *Applied Energy*, vol. 86, pp. 1137-1143, 2009.
- [8] R. Mikalsen and A. P. Roskilly, "A review of free-piston engine history and applications," *Applied Thermal Engineering*, vol. 27, pp. 2339-2352, October 2007.
- [9] W. M. Arshad, P. Thelin, T. Backstrom, and C. Sadarangani, "Use of transverse-flux machines in a free-piston generator," *IEEE Transactions on Industry Applications*, vol. 40, pp. 1092-1100, 2004.
- [10] J. Wang, M. West, D. Howe, H. Z. D. La Parra, and W. M. Arshad, "Design and Experimental Verification of a Linear Permanent Magnet Generator for a Free-Piston Energy Converter," *Energy Conversion, IEEE Transactions on*, vol. 22, pp. 299-306, 2007.
- [11] F. Rinderknecht, "A highly efficient energy converter for a hybrid vehicle concept - focused on the linear generator of the next generation," in *Ecological Vehicles and Renewable Energies (EVER), 2013 8th International Conference and Exhibition on*, 2013, pp. 1-7.
- [12] Q.-f. LI, J. XIAO, and Z. HUANG, "Flat-type permanent magnet linear alternator: A suitable device for a free piston linear alternator," *Journal of Zhejiang University SCIENCE A*, vol. 10, pp. 345-352, 2009.
- [13] P. Zheng, A. Chen, P. Thelin, W. M. Arshad, and C. Sadarangani, "Research on a Tubular Longitudinal Flux PM Linear Generator Used for Free-Piston Energy Converter," *IEEE Transactions on Magnetics*, vol. 43, pp. 447-449, 2007.
- [14] P. Famouri, W. R. Cawthorne, N. Clark, S. Nandkumar, C. Atkinson, R. Atkinson, *et al.*, "Design and testing of a novel linear alternator and engine system for remote electrical power generation," in *Power Engineering Society 1999 Winter Meeting, IEEE*, 1999, pp. 108-112 vol.1.
- [15] W. P. Hew, J. Jamaludin, M. Tadjuddin, and K. M. Nor, "Fabrication and testing of linear electric generator for use with a free-piston engine," in *Power Engineering Conference, 2003. PECon 2003. Proceedings. National*, 2003, pp. 277-282.

- [16] T. T. Dang, M. Ruellan, H. B. Ahmed, L. Prevond, and B. Multon, "Sizing optimization of tubular linear induction generator for a new stirling micro-cogenerator system," in *Power Electronics, Electrical Drives, Automation and Motion (SPEEDAM), 2014 International Symposium on*, 2014, pp. 1362-1367.
- [17] T. T. Dang, M. Ruellan, L. Pr, x00E, vond, H. B. Ahmed, *et al.*, "Sizing Optimization of Tubular Linear Induction Generator and Its Possible Application in High Acceleration Free-Piston Stirling Microcogeneration," *IEEE Transactions on Industry Applications*, vol. 51, pp. 3716-3733, 2015.
- [18] P. A. J. Achten, "A review of free piston engine concepts," SAE Technical Paper 0148-7191, 1994.
- [19] M. Goertz and L. Peng, "Free piston engine its application and optimization," SAE Technical Paper 0148-7191, 2000.
- [20] R. S. Tikkanen and M. Vilenius, "Hydraulic free piston engine — Challenge for control," in *Control Conference (ECC), 1999 European*, 1999, pp. 2943-2948.
- [21] E. R. Laithwaite, "Linear induction motors," *Proceedings of the IEE - Part A: Power Engineering*, vol. 104, pp. 461-470, 1957.
- [22] E. R. Laithwaite and G. F. Nix, "Further developments of the self-oscillating induction motor," *Proceedings of the IEE - Part A: Power Engineering*, vol. 107, pp. 476-486, 1960.
- [23] E. R. Laithwaite, D. Tipping, and D. E. Hesmondhalgh, "The application of linear induction motors to conveyors," *Proceedings of the IEE - Part A: Power Engineering*, vol. 107, pp. 284-294, 1960.
- [24] J. C. West and B. V. Jayawant, "A new linear oscillating motor," *Proceedings of the IEE - Part A: Power Engineering*, vol. 109, pp. 292-300, 1962.
- [25] E. R. Laithwaite and F. T. Barwell, "Linear induction motors for high-speed railways," *Electronics and Power*, vol. 10, pp. 100-103, 1964.
- [26] G. F. Nix and E. R. Laithwaite, "Linear induction motors for low-speed and standstill application," *Electrical Engineers, Proceedings of the Institution of*, vol. 113, pp. 1044-1056, 1966.
- [27] E. R. Laithwaite and R. S. Mamak, "An oscillating synchronous linear machine," *Electrical Engineers, Journal of the Institution of*, vol. 8, pp. 159-160, 1962.
- [28] E. R. Laithwaite and R. S. Mamak, "An oscillating synchronous linear machine," *Proceedings of the IEE - Part A: Power Engineering*, vol. 109, pp. 415-426, 1962.
- [29] E. R. Laithwaite and S. A. Nasar, "Linear-motion electrical machines," *Proceedings of the IEEE*, vol. 58, pp. 531-542, 1970.
- [30] M. Poloujadoff, "Linear induction machines I. History and theory of operation," *IEEE Spectrum*, vol. 8, pp. 72-80, 1971.
- [31] M. Poloujadoff, "Linear induction machines II. Applications," *IEEE Spectrum*, vol. 8, pp. 79-86, 1971.
- [32] G. V. Sadler and A. W. Davey, "Applications of linear induction motors in industry," *Electrical Engineers, Proceedings of the Institution of*, vol. 118, pp. 765-776, 1971.
- [33] S. A. Nasar, "Electromagnetic fields and forces in a linear induction motor, taking into account edge effects," *Electrical Engineers, Proceedings of the Institution of*, vol. 116, pp. 605-608, 1969.
- [34] B. t. Ooi and D. C. White, "Traction and Normal Forces in the Linear Induction Motor," *IEEE Transactions on Power Apparatus and Systems*, vol. PAS-89, pp. 638-645, 1970.
- [35] M. W. Davis, "Development of Concentric Linear Induction Motor," *IEEE Transactions on Power Apparatus and Systems*, vol. PAS-91, pp. 1506-1513, 1972.

- [36] S. A. Nasar, L. d. Cid, and H. J. Holley, "Computations of Fields and Forces in a Two-Sided Linear Induction Motor," *IEEE Transactions on Power Apparatus and Systems*, vol. PAS-92, pp. 1310-1315, 1973.
- [37] V. Lemarquand, R. Ravaud, and G. Lemarquand, "A new linear voice-coil motor for ironless loudspeakers: Analytical study," in *The XIX International Conference on Electrical Machines - ICEM 2010*, 2010, pp. 1-5.
- [38] J. Wang, W. Wang, K. Atallah, and D. Howe, "Design of a linear permanent magnet motor for active vehicle suspension," in *2009 IEEE International Electric Machines and Drives Conference*, 2009, pp. 585-591.
- [39] L. Bertola, T. Cox, P. Wheeler, and S. Garvey, "Superconducting and conventional electromagnetic launch system for civil aircraft assisted take-off," in *2016 IEEE Energy Conversion Congress and Exposition (ECCE)*, 2016, pp. 1-6.
- [40] L. Bertola, T. Cox, P. Wheeler, S. Garvey, and H. Morvan, "Superconducting Electromagnetic Launch System for Civil Aircraft," *IEEE Transactions on Applied Superconductivity*, vol. 26, pp. 1-11, 2016.
- [41] J. M. D. Coey, "Hard Magnetic Materials: A Perspective," *IEEE Transactions on Magnetics*, vol. 47, pp. 4671-4681, 2011.
- [42] <http://www.magnetnrg.com/pm-history.html>.
- [43] J. Wang and N. J. Baker, "Comparison of flux switching and modulated pole linear machines for use with a free piston," in *2015 IEEE International Electric Machines & Drives Conference (IEMDC)*, 2015, pp. 642-648.
- [44] I. Boldea and S. A. Nasar, *Linear electric actuators and generators*: Cambridge University press, 1997.
- [45] I. Boldea and S. A. Nasar, "Linear electric actuators and generators," *IEEE Transactions on Energy Conversion*, vol. 14, pp. 712-717, 1999.
- [46] Z. Xu and S. Chang, "Improved Moving Coil Electric Machine for Internal Combustion Linear Generator," *IEEE Transactions on Energy Conversion*, vol. 25, pp. 281-286, 2010.
- [47] I. Fazal, K. Mohd Noh, S. A. Zulkifli, T. Ibrahim, and K. S. R. Rao, "Modeling and simulation of a moving-coil linear generator," in *2010 International Conference on Intelligent and Advanced Systems*, 2010, pp. 1-5.
- [48] R. Cao, M. Cheng, C. Mi, W. Hua, and W. Zhao, "Comparison of Complementary and Modular Linear Flux-Switching Motors With Different Mover and Stator Pole Pitch," *IEEE Transactions on Magnetics*, vol. 49, pp. 1493-1504, 2013.
- [49] R. Cao, Y. Jin, Y. Zhang, and M. Cheng, "A New Double-Sided HTS Flux-Switching Linear Motor With Series Magnet Circuit," *IEEE Transactions on Applied Superconductivity*, vol. 26, pp. 1-5, 2016.
- [50] L. Huang, H. Yu, M. Hu, J. Zhao, and Z. Cheng, "A Novel Flux-Switching Permanent-Magnet Linear Generator for Wave Energy Extraction Application," *IEEE Transactions on Magnetics*, vol. 47, pp. 1034-1037, 2011.
- [51] J. Yang, L. Huang, M. Hu, H. Yu, C. Jiu, and D. Zhao, "Research on a control strategy of the flux-switching permanent magnet linear generator for wave energy extraction," in *2015 18th International Conference on Electrical Machines and Systems (ICEMS)*, 2015, pp. 1666-1670.
- [52] R. Cao, M. Cheng, and B. Zhang, "Speed Control of Complementary and Modular Linear Flux-Switching Permanent-Magnet Motor," *IEEE Transactions on Industrial Electronics*, vol. 62, pp. 4056-4064, 2015.
- [53] J. Wang, W. Wang, R. Clark, K. Atallah, and D. Howe, "A tubular flux-switching permanent magnet machine," *Journal of Applied Physics*, vol. 103, p. 07F105, 2008.

-
- [54] J. Wang, W. Wang, K. Atallah, and D. Howe, "Comparative studies of linear permanent magnet motor topologies for active vehicle suspension," in *2008 IEEE Vehicle Power and Propulsion Conference*, 2008, pp. 1-6.
- [55] P. Zheng, Y. Sui, C. D. Tong, J. G. Bai, B. Yu, and F. Lin, "A novel single-phase flux-switching permanent magnet linear generator used for free-piston Stirling engine," *Journal of Applied Physics*, vol. 115, p. 17E711, 2014.
- [56] P. Zheng, Y. Sui, B. Yu, L. Cheng, and W. Wang, "A tubular single-phase dual-stator flux-switching PM oscillating generator with series magnetic circuit," in *2015 IEEE Magnetics Conference (INTERMAG)*, 2015, pp. 1-1.
- [57] W. Cawthorne, P. Famouri, and N. Clark, "Integrated design of linear alternator/engine system for HEV auxiliary power unit," in *Electric Machines and Drives Conference (IEMDC), IEEE International*, 2001, pp. 267-274.
- [58] J. Wang, G. W. Jewell, and D. Howe, "A general framework for the analysis and design of tubular linear permanent magnet machines," *Magnetics, IEEE Transactions on*, vol. 35, pp. 1986-2000, 1999.
- [59] J. Wang, G. W. Jewell, and D. Howe, "Design optimisation and comparison of tubular permanent magnet machine topologies," *IEE Proceedings - Electric Power Applications*, vol. 148, pp. 456-464, 2001.
- [60] J. Wang, D. Howe, and G. W. Jewell, "An improved axially magnetised tubular permanent magnet machine topology," in *2002 International Conference on Power Electronics, Machines and Drives (Conf. Publ. No. 487)*, 2002, pp. 303-308.
- [61] J. Wang, D. Howe, and G. W. Jewell, "Analysis and design optimization of an improved axially magnetized tubular permanent-magnet machine," *IEEE Transactions on Energy Conversion*, vol. 19, pp. 289-295, 2004.
- [62] J. Wang and D. Howe, "Analysis of axially magnetised, iron-cored, tubular permanent magnet machines," *IEE Proceedings - Electric Power Applications*, vol. 151, pp. 144-150, 2004.
- [63] J. Wang, D. Howe, and G. W. Jewell, "Fringing in tubular permanent-magnet Machines: part II. Cogging force and its minimization," *IEEE Transactions on Magnetics*, vol. 39, pp. 3517-3522, 2003.
- [64] J. Wang, D. Howe, and G. W. Jewell, "Fringing in tubular permanent-magnet machines: Part I. Magnetic field distribution, flux linkage, and thrust force," *IEEE Transactions on Magnetics*, vol. 39, pp. 3507-3516, 2003.
- [65] J. Wang and D. Howe, "Design optimization of radially magnetized, iron-cored, tubular permanent-magnet machines and drive systems," *IEEE Transactions on Magnetics*, vol. 40, pp. 3262-3277, 2004.
- [66] Y. Amara, J. Wang, and D. Howe, "Stator iron loss of tubular permanent magnet machines," in *Conference Record of the 2004 IEEE Industry Applications Conference, 2004. 39th IAS Annual Meeting.*, 2004, pp. 2119-2124 vol.3.
- [67] Y. Amara, J. Wang, and D. Howe, "Stator iron loss of tubular permanent-magnet Machines," *IEEE Transactions on Industry Applications*, vol. 41, pp. 989-995, 2005.
- [68] Y. Amara, W. Jiabin, and D. Howe, "Analytical prediction of eddy-current loss in modular tubular permanent-magnet machines," *IEEE Transactions on Energy Conversion*, vol. 20, pp. 761-770, 2005.
- [69] J. Wang and D. Howe, "A Linear Permanent Magnet Generator for a Free-Piston Energy Converter," in *IEEE International Conference on Electric Machines and Drives, 2005.*, 2005, pp. 1521-1528.

- [70] J. Chai, J. Wang, and D. Howe, "Evaluation of stator iron loss in tubular permanent magnet machines by three-dimensional finite element analysis," in *2006 3rd IET International Conference on Power Electronics, Machines and Drives - PEMD 2006*, 2006, pp. 197-201.
- [71] J. Wang and D. Howe, "Tubular modular permanent-magnet machines equipped with quasi-Halbach magnetized magnets-part I: magnetic field distribution, EMF, and thrust force," *IEEE Transactions on Magnetics*, vol. 41, pp. 2470-2478, 2005.
- [72] J. Wang and D. Howe, "Tubular modular permanent-magnet machines equipped with quasi-Halbach magnetized magnets-part II: armature reaction and design optimization," *IEEE Transactions on Magnetics*, vol. 41, pp. 2479-2489, 2005.
- [73] J. Wang and D. Howe, "Influence of soft magnetic materials on the design and performance of tubular permanent magnet machines," *IEEE Transactions on Magnetics*, vol. 41, pp. 4057-4059, 2005.
- [74] J. Wang, W. Wang, K. Atallah, and D. Howe, "Demagnetization Assessment for Three-Phase Tubular Brushless Permanent-Magnet Machines," *IEEE Transactions on Magnetics*, vol. 44, pp. 2195-2203, 2008.
- [75] N. Bianchi, S. Bolognani, and A. D. F. Cappello, "Reduction of cogging force in PM linear motors by pole-shifting," *IEE Proceedings - Electric Power Applications*, vol. 152, pp. 703-709, 2005.
- [76] J. Wang, M. Inoue, Y. Amara, and D. Howe, "Cogging-force-reduction techniques for linear permanent-magnet machines," *IEE Proceedings - Electric Power Applications*, vol. 152, pp. 731-738, 2005.
- [77] S. T. Boroujeni, J. Milimonfared, and M. Ashabani, "Design, Prototyping, and Analysis of a Novel Tubular Permanent-Magnet Linear Machine," *Magnetics, IEEE Transactions on*, vol. 45, pp. 5405-5413, 2009.
- [78] Y. Sui, P. Zheng, B. Yu, L. Cheng, and Z. Liu, "Research on a Tubular Yokeless Linear PM Machine," *IEEE Transactions on Magnetics*, vol. 51, pp. 1-4, 2015.
- [79] Z. Ping, T. Chengde, B. Jingang, Y. Bin, S. Yi, and S. Wei, "Electromagnetic Design and Control Strategy of an Axially Magnetized Permanent-Magnet Linear Alternator for Free-Piston Stirling Engines," *Industry Applications, IEEE Transactions on*, vol. 48, pp. 2230-2239, 2012.
- [80] W. Li, G. Shuang, W. Diyun, and X. Zhang, "Design of a linear magnetic-gear free-piston generator for series hybrid electric vehicles," in *2010 IEEE Vehicle Power and Propulsion Conference*, 2010, pp. 1-6.
- [81] W. M. Arshad, T. Backstrom, and C. Sadarangani, "Analytical design and analysis procedure for a transverse flux machine," in *Electric Machines and Drives Conference, 2001. IEMDC 2001. IEEE International*, 2001, pp. 115-121.
- [82] A. COSIC, "Analysis of a Novel Transverse Flux Machine with a Tubular Cross-section for Free Piston Energy Converter Application," Doctoral Thesis, KTH School of Electrical Engineering, KTH, Stockholm, Sweden, 2010.
- [83] M. R. Harris, G. H. Pajooman, and S. M. A. Sharkh, "The problem of power factor in VRPM (transverse-flux) machines," in *1997 Eighth International Conference on Electrical Machines and Drives (Conf. Publ. No. 444)*, 1997, pp. 386-390.
- [84] W. M. Arshad, T. Backstrom, and C. Sadarangani, "Investigating a transverse flux machine with intermediate poles," in *2002 International Conference on Power Electronics, Machines and Drives (Conf. Publ. No. 487)*, 2002, pp. 325-328.
- [85] W. M. Arshad, P. Thelin, C. Sadarangani, and T. Blickstrom, "Analytical analysis and dimensioning of a low-leakage linear transverse-flux machine," in *Second International Conference on Power Electronics, Machines and Drives (PEMD 2004)*. 2004, pp. 414-419 Vol.1.

- [86] A. Cosic, C. Sadarangani, and M. Leksell, "3D analyses of a novel Transverse Flux machine for a free piston energy converter," in *2008 18th International Conference on Electrical Machines*, 2008, pp. 1-6.
- [87] Z. Ping, T. Chengde, C. Gang, Z. Jing, and S. Wei, "Research on the electromagnetic structure and performance of a novel transverse-flux PM linear machine used for free-piston energy converter," in *Digests of the 2010 14th Biennial IEEE Conference on Electromagnetic Field Computation*, 2010, pp. 1-1.
- [88] P. Zheng, C. Tong, G. Chen, R. Liu, Y. Sui, W. Shi, *et al.*, "Research on the Magnetic Characteristic of a Novel Transverse-Flux PM Linear Machine Used for Free-Piston Energy Converter," *IEEE Transactions on Magnetics*, vol. 47, pp. 1082-1085, 2011.
- [89] H. Yan, B. Yu, C. Xiao, Z. Song, J. Lin, and P. Zheng, "Research on a novel tubular transverse-flux permanent-magnet linear machine for free-piston energy converter," in *2011 International Conference on Electrical Machines and Systems*, 2011, pp. 1-5.
- [90] P. Zheng, S. Zhu, B. Yu, L. Cheng, and Y. Fan, "Analysis and Optimization of a Novel Tubular Staggered-Tooth Transverse-Flux PM Linear Machine," *IEEE Transactions on Magnetics*, vol. 51, pp. 1-4, 2015.
- [91] B. Yu, P. Zheng, B. Xu, J. Zhang, and L. Han, "Flux leakage analysis of transverse-flux PM linear machine," in *2014 17th International Conference on Electrical Machines and Systems (ICEMS)*, 2014, pp. 2284-2288.
- [92] I. Boldea, W. Congxiao, Y. Bin, and S. A. Nasar, "Analysis and design of flux-reversal linear permanent magnet oscillating machine," in *Conference Record of 1998 IEEE Industry Applications Conference. Thirty-Third IAS Annual Meeting (Cat. No.98CH36242)*, 1998, pp. 136-143 vol.1.
- [93] J. Schutte and J. M. Strauss, "Optimisation of a transverse flux linear PM generator using 3D finite element analysis," in *Electrical Machines (ICEM), 2010 XIX International Conference on*, 2010, pp. 1-6.
- [94] J. Schutte, L. H. Joubert, and J. M. Strauss, "Constrained optimisation of a transverse flux PM linear generator," in *2012 XXth International Conference on Electrical Machines*, 2012, pp. 595-599.
- [95] L. H. Joubert, J. Schutte, J. M. Strauss, and R. T. Dobson, "Design optimisation of a transverse flux, short stroke, linear generator," in *2012 XXth International Conference on Electrical Machines*, 2012, pp. 640-646.
- [96] L. H. Joubert and J. M. Strauss, "Optimisation of a transverse flux linear oscillating generator by transient 3D finite element analysis," in *Electrical Machines (ICEM), 2014 International Conference on*, 2014, pp. 602-608.
- [97] J. Wang and N. J. Baker, "A comparison of alternative linear machines for use with a direct drive free piston engine," in *8th IET International Conference on Power Electronics, Machines and Drives (PEMD 2016)*, 2016, pp. 1-6.
- [98] N. Ahmed, G. J. Atkinson, N. J. Baker, L. Sjöberg, and N. Stannard, "Flux Switching Modulated Pole Machine topologies which offer greater mechanical simplicity," in *2013 International Electric Machines & Drives Conference*, 2013, pp. 354-358.
- [99] N. J. Baker, J. Wang, and G. J. Atkinson, "Optimization and comparison of linear transverse flux and flux switching machines," in *2016 XXII International Conference on Electrical Machines (ICEM)*, 2016, pp. 2471-2477.
- [100] W. Jiabin, W. Weiya, K. Atallah, and D. Howe, "Design Considerations for Tubular Flux-Switching Permanent Magnet Machines," *Magnetics, IEEE Transactions on*, vol. 44, pp. 4026-4032, 2008.
- [101] R. Mikalsen and A. P. Roskilly, "The fuel efficiency and exhaust gas emissions of a low heat rejection free-piston diesel engine," *Proceedings of the Institution of Mechanical Engineers, Part A: Journal of Power and Energy*, vol. 223, pp. 379-386, 2009.

- [102]S. E. Pohl and M. Gräf, "Dynamic Simulation of a Free-Piston Linear Alternator in Modelica," presented at the 4th International Modelica Conference, Hamburg, Germany, 2005.
- [103]Q. Li, J. Xiao, and Z. Huang, "Simulation of a two-stroke free-piston engine for electrical power generation," *Energy & fuels*, vol. 22, pp. 3443-3449, 2008.
- [104]N. B. Hung and O. T. Lim, "A study of a two-stroke free piston linear engine using numerical analysis," *Journal of Mechanical Science and Technology*, vol. 28, pp. 1545-1557, 2014.
- [105]Huihua Feng, Yu Song, Zhengxing Zuo, Jiao Shang, Yaodong Wang and Anthony Paul Roskilly, "Stable Operation and Electricity Generating Characteristics of a Single-Cylinder Free Piston Engine Linear Generator: Simulation and Experiments," *Energies*, vol. 8, pp. 765-785, 2015.
- [106]B. Jia, Z. Zuo, G. Tian, H. Feng, and A. P. Roskilly, "Development and validation of a free-piston engine generator numerical model," *Energy Conversion and Management*, vol. 91, pp. 333-341, 2// 2015.
- [107]D. Wu and A. P. Roskilly, "Design and Parametric Analysis of Linear Joule-cycle Engine with Out-of-cylinder Combustion," *Energy Procedia*, vol. 61, pp. 1111-1114, 2014.
- [108]A. Souissi, I. Abdennadher, and A. Masmoudi, "An approach to reduce the cogging force in tubular linear PM synchronous machines," in *2015 Tenth International Conference on Ecological Vehicles and Renewable Energies (EVER)*, 2015, pp. 1-7, Tenth International Conference on Ecological Vehicles and Renewable Energies (EVER).
- [109]Q. Wang and J. Wang, "Assessment of cogging-force-reduction techniques applied to fractional-slot linear permanent magnet motors equipped with non-overlapping windings," *IET Electric Power Applications*, vol. 10, pp. 697-705, 2016.
- [110]J. P. Jastrzembski and B. Ponick, "Different methods for reducing detent force in a permanent magnet linear synchronous motor," in *IECON 2010 - 36th Annual Conference on IEEE Industrial Electronics Society*, 2010, pp. 823-828.
- [111]S. Gruber, R. Wegener, and S. Soter, "Detent force reduction of a tubular linear drive by using a genetic algorithm and FEM - verification of simulation results," in *IECON 2012 - 38th Annual Conference on IEEE Industrial Electronics Society*, 2012, pp. 1731-1736.
- [112]Y. W. Zhu, D. H. Koo, and Y. H. Cho, "Detent Force Minimization of Permanent Magnet Linear Synchronous Motor by Means of Two Different Methods," *IEEE Transactions on Magnetics*, vol. 44, pp. 4345-4348, 2008.
- [113]Y. w. Zhu, S. G. Lee, K. S. Chung, and Y. H. Cho, "Investigation of Auxiliary Poles Design Criteria on Reduction of End Effect of Detent Force for PMLSM," *IEEE Transactions on Magnetics*, vol. 45, pp. 2863-2866, 2009.
- [114]J. Zhang, C. Wu, X. Lianggen, M. Cheng, and J. Xinmiao, "Optimal design of a tubular linear surface-mounted permanent magnet actuator for high voltage breaker," in *2013 International Conference on Electrical Machines and Systems (ICEMS)*, 2013, pp. 1895-1900.
- [115]W. Shi, C. Xiao, Y. Lei, B. Yu, F. Wu, and P. Zheng, "Optimization on thrust ripple of an axial-flux permanent-magnet linear synchronous machine," in *Electrical Machines and Systems (ICEMS), 2011 International Conference on*, 2011, pp. 1-6.
- [116]M. Ashabani, J. Milimonfared, J. Shokrollahi-Moghani, S. Taghipour, and M. Aghashabani, "Mitigation of Cogging Force in Axially Magnetized Tubular Permanent-Magnet Machines Using Iron Pole-Piece Slotting," *IEEE Transactions on Magnetics*, vol. 44, pp. 2158-2162, 2008.

- [117]Y. w. Zhu, K. s. Jung, and Y. h. Cho, "The Reduction of Force Ripples of PMLSM Using Field Oriented Control Method," in *2006 CES/IEEE 5th International Power Electronics and Motion Control Conference*, 2006, pp. 1-5.
- [118]Y. w. Zhu and Y. H. Cho, "Thrust Ripples Suppression of Permanent Magnet Linear Synchronous Motor," *IEEE Transactions on Magnetics*, vol. 43, pp. 2537-2539, 2007.
- [119]S. W. Youn, J. J. Lee, H. S. Yoon, and C. S. Koh, "A New Cogging-Free Permanent-Magnet Linear Motor," *IEEE Transactions on Magnetics*, vol. 44, pp. 1785-1790, 2008.
- [120]H. J. Ahn, S. H. Lee, D. Y. Lee, K. B. Jang, and G. T. Kim, "A Study on the Characteristics of PMLSM According to Permanent Magnet Arrangement," in *2008 IEEE Industry Applications Society Annual Meeting*, 2008, pp. 1-6.
- [121]R. Mikalsen and A. P. Roskilly, "The free-piston reciprocating Joule Cycle engine: A new approach to efficient domestic CHP generation," in *International Conference on Applied Energy (ICAE2012)*, 2012.
- [122]S. M. A. Sufian, K. A. Sagar, M. A. Ullah, and D. Baidya, "Harvesting electrical power from waste heat using stirling engine," in *Strategic Technology (IFOST), 2014 9th International Forum on*, 2014, pp. 343-346.
- [123]L. Kutt and M. Lehtonen, "Automotive waste heat harvesting for electricity generation using thermoelectric systems - An overview," in *2015 IEEE 5th International Conference on Power Engineering, Energy and Electrical Drives (POWERENG)*, 2015, pp. 55-62.
- [124]I. Boldea and S. A. Nasar, "Permanent-Magnet Linear Alternators Part II: Design Guidelines," *IEEE Transactions on Aerospace and Electronic Systems*, vol. AES-23, pp. 79-82, 1987.
- [125]I. Boldea, *Variable Speed Generators*: CRC press, 2006.
- [126].....J. F. Gieras, Z. J. Piech, and B. Z. Tomczuk, *Linear Synchronous Motors*, 2nd ed.: CRC Press, 2011.
- [127]C. Jinhua, L. Youyong, Z. Chi, and J. Zhe, "Design and analysis of a permanent magnet linear generator for a free-piston energy converter," in *Industrial Electronics and Applications (ICIEA), 2014 IEEE 9th Conference on*, 2014, pp. 1719-1723.
- [128]Z. Ping, T. Chengde, Z. Jing, Y. Bin, L. Lin, B. Jingang, *et al.*, "Investigation of a 7-pole/6-slot Halbach-magnetized permanent-magnet linear alternator used for free-piston stirling engines," *Journal of Applied Physics*, vol. 111, p. 07E711, 2012.
- [129]A. H. Rajaei, M. Mohamadian, and A. Yazdian, "Carrier-based PWM and space vector modulation of three single phase PFC rectifier as generator-side converter of PM WECS," in *2012 IEEE Industry Applications Society Annual Meeting*, 2012, pp. 1-8.
- [130]E. Sunan, F. Kucuk, H. Goto, H. J. Guo, and O. Ichinokura, "Three-Phase Full-Bridge Converter Controlled Permanent Magnet Reluctance Generator for Small-Scale Wind Energy Conversion Systems," *IEEE Transactions on Energy Conversion*, vol. 29, pp. 585-593, 2014.
- [131]A. Souissi, I. Abdennadher, and A. Masmoudi, "An approach to reduce the cogging force in tubular linear PM synchronous machines," in *Ecological Vehicles and Renewable Energies (EVER), 2015 Tenth International Conference on*, 2015, pp. 1-7.
- [132]Q. Wang, H. Chen, T. Xu, J. Yuan, J. Wang, and S. Abbas, "Influence of mover yoke and winding connections on unbalanced normal force for double-sided linear switched reluctance machine," *IET Electric Power Applications*, vol. 10, pp. 91-100, 2016.

- [133]Q. Wang, H. Chen, and R. Nie, "Unbalanced normal force reduction in the eccentric double-sided linear switched reluctance machine," *IET Electric Power Applications*, vol. 10, pp. 384-393, 2016.

Appendix A: Tubular Machines FEA Modelling Techniques

This appendix describes the FEA modelling techniques conducted on the machine investigated in this research. The purpose is to explain the main differences between the accuracy of the results when a model is solved using the transient solver. The full machine model active length using the same dimensional parameters was built using the possible modelling methods, the 2D modelling, the 2D Axisymmetric (2DA) modelling and the 3D modelling, as shown in Figure A-1 respectively.

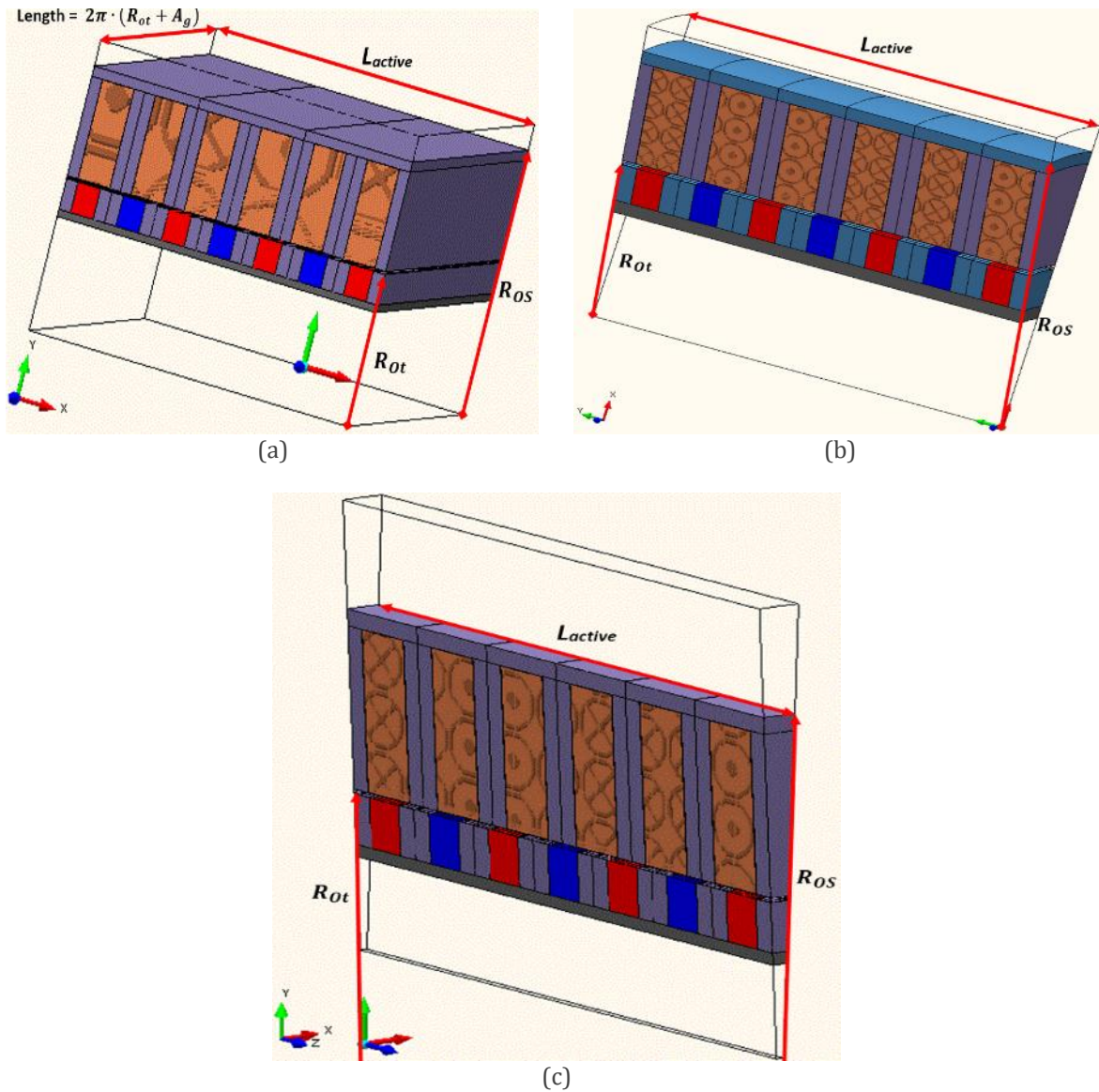


Figure A-1: FEA machine model using (a) 2D, (b) 2D axisymmetric, and (c) 3D

Using 2D FEA modelling requires that machine tubular model to cut axially and be unrolled (flattened), as described in Chapter 4 – section 4.5.1. The flattened length equals to the active machine bore circumference length. This results in longer length representation of the machine air gap and translator regions, and the vice versa occurs for the regions above the air gap, i.e. the stator region. This flattening modelling would result in incorrect length representation, incorrect material use in the different machine regions with a consequent effect on the predicted machine performance.

Therefore, to overcome this inaccurate material representation and to obtain a more accurate results, 3D model was also built and solved. It is known that solving 3D machine model gives predicted solutions closer to the performance of the actual machine as it takes into account the windings' end effects, and leakage fluxes within the machine geometry. However, experience has found that the simulation time required to investigate the transient performance of a (4 degrees) sector of a linear machine model takes more than 48 hours per model operating at no-load. Different models with variable large mesh size have been tried to reduce the solution time, yet all did not reduce the solution time effectively. Therefore, 3D modelling with transient solution is not considered. Static solution of 3D model is still valid for comparison purposes as an alternate of transient solution. Static solution has a drawback in cancelling the phase inductance effects under loading conditions. Overall, 3D FEA was useful only in estimating the machine cogging force and no load flux linkage by performing static solution.

The 2D Axisymmetric (2DA) model, on the other hand, has a satisfactory representation of tubular geometry machine model in addition to its satisfactory processing time. Modelling the machine using this property would result in obtaining solutions closer to 3D modelling solutions, since the model counts for the actual length of each machine region with different parts.

Samples of the results of the different modelling techniques are shown in Figure A-2. It is clear that the 2D results show higher flux linkage values compared with those obtained using 2DA and 3D models. This is the first effect of the larger PM mass implemented in 2D model due to improper PM length representation. The maximum percentage deviation between 2D and 3D results is (6.63 %), (5.55 %) between 2D and 2DA results and (1.14%) between 2DA and 3D results.

Figure A-3 shows a comparison of no-load cogging force where it clarifies that 2D model show a force result lower than that of 2DA and 3D models results. This indicates that the improper length representation of different machine parts using 2D modelling has an incorrect prediction of various machine forces due to improper material representation.

Therefore, from these comparisons, the 2DA modelling technique was selected to perform the various optimisation procedure reported in Chapter 5 and so on, as it was found the most appropriate in predicting the performance of the machine, appreciating that the transient solving time per model does not exceed ≈ 30 minutes as similar as 2D model solving time.

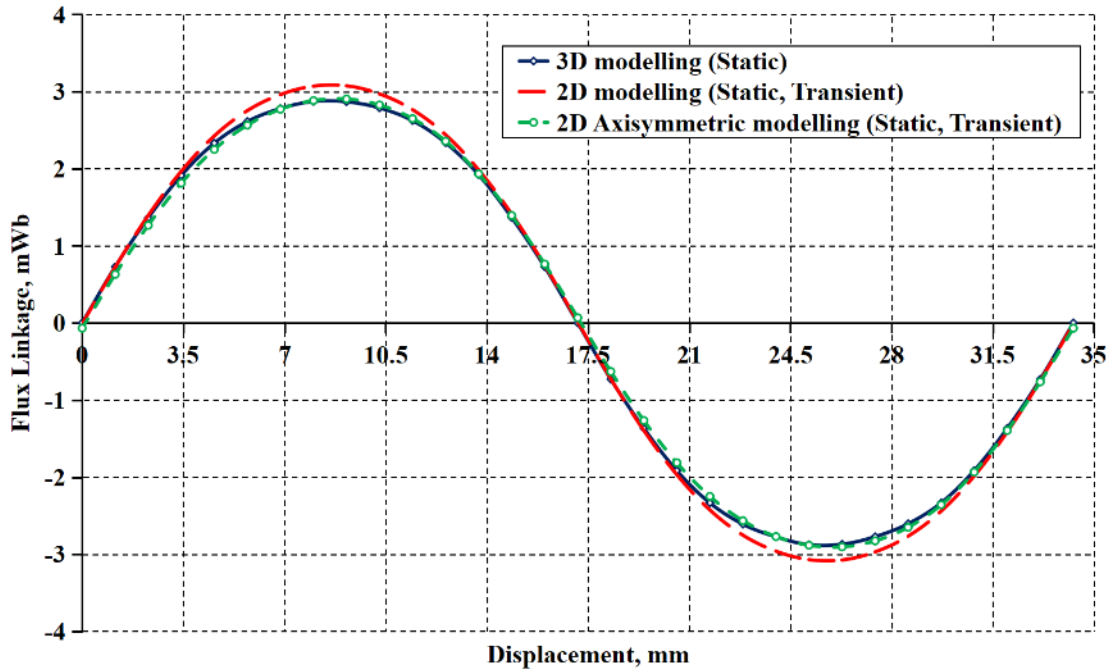


Figure A-2: Flux linkage variation over full electrical cycle

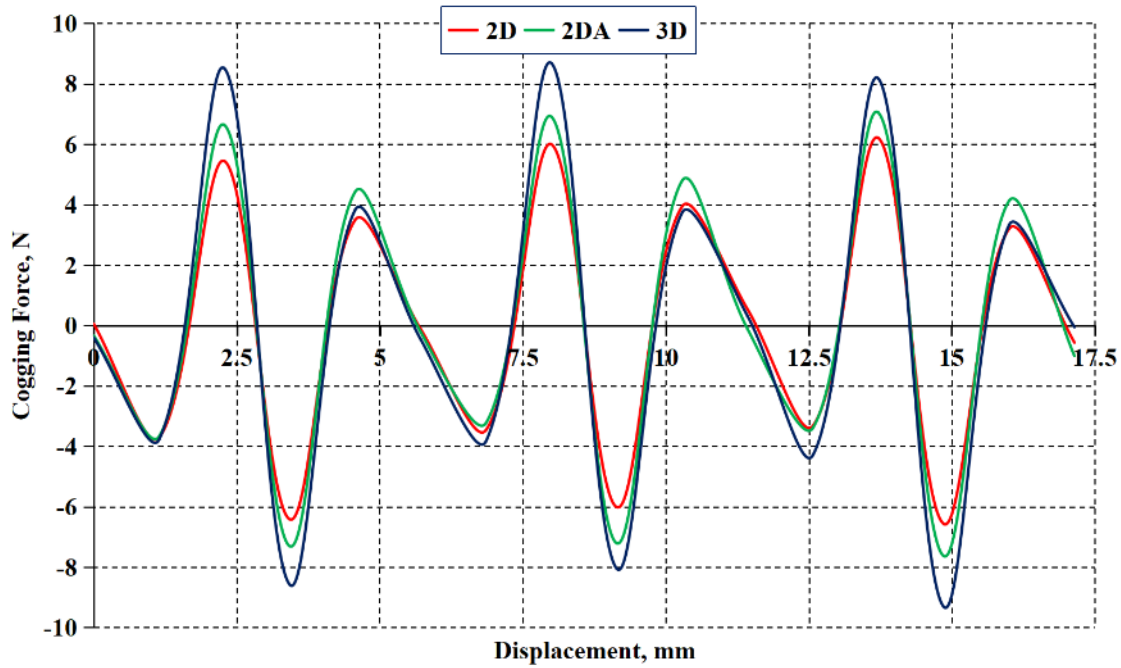


Figure A-3: Flux linkage variation over full electrical cycle

Appendix B: B-H curves of the Materials used in FEA modelling

The materials used in the magnetic circuit of the machine have the B-H characteristics as shown in Figure A-1.

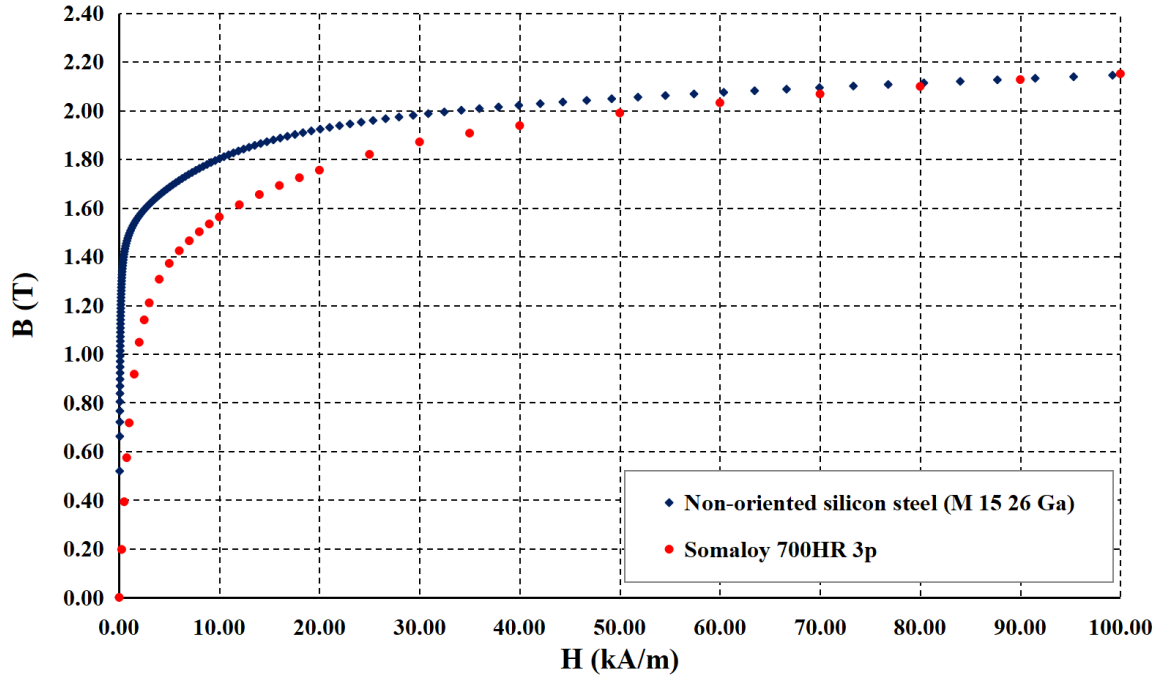


Figure B-1 : B-H curves of the materials used in FEA machine modelling

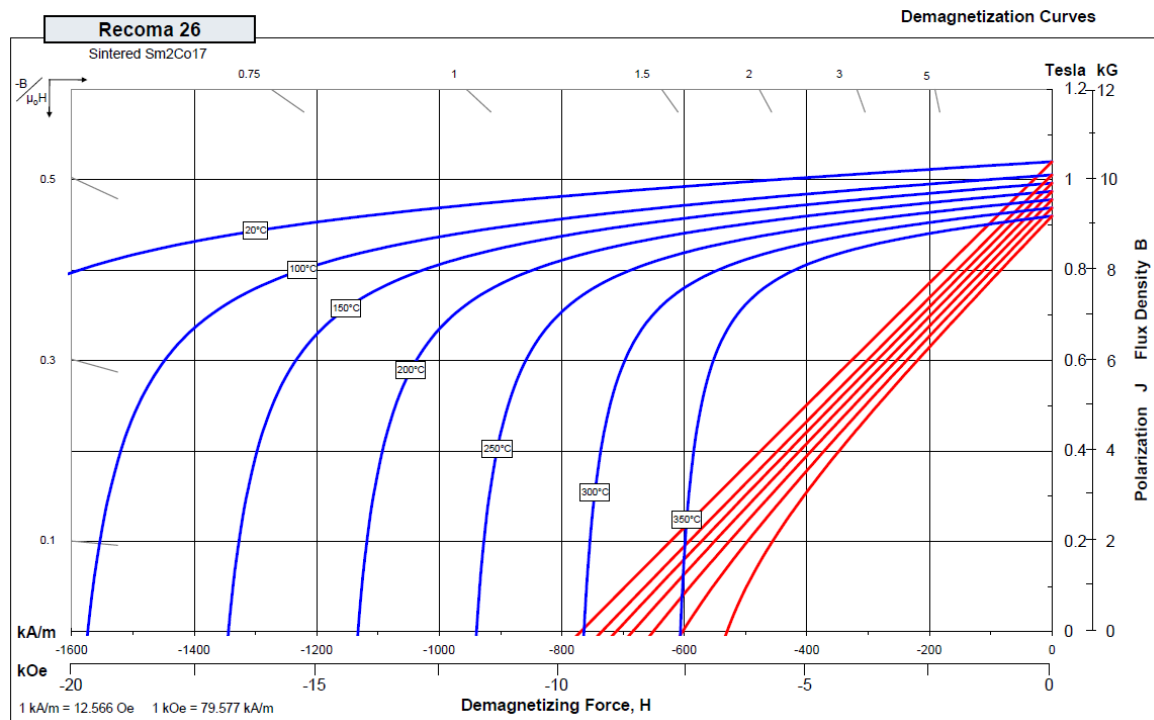
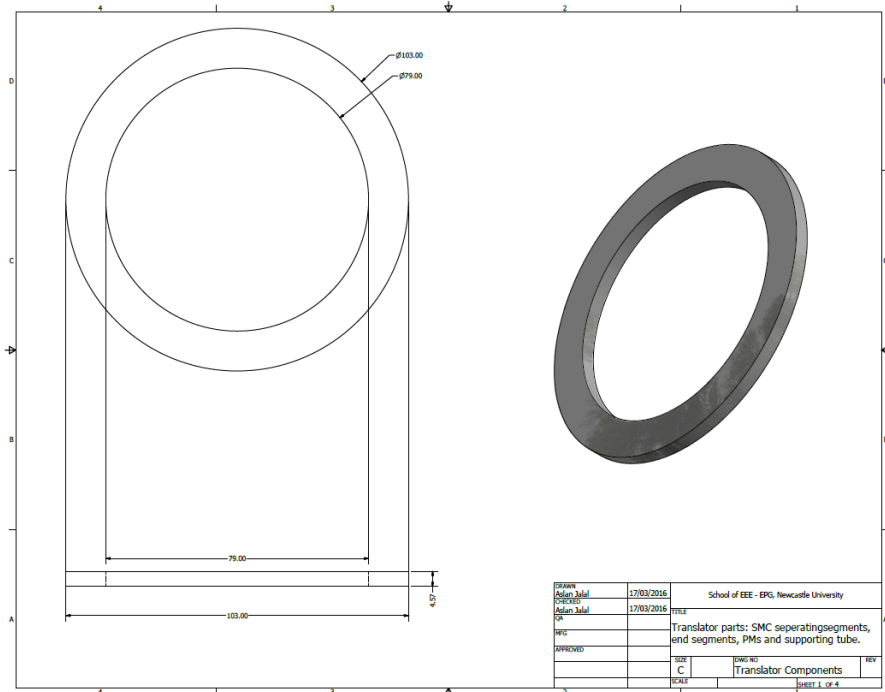


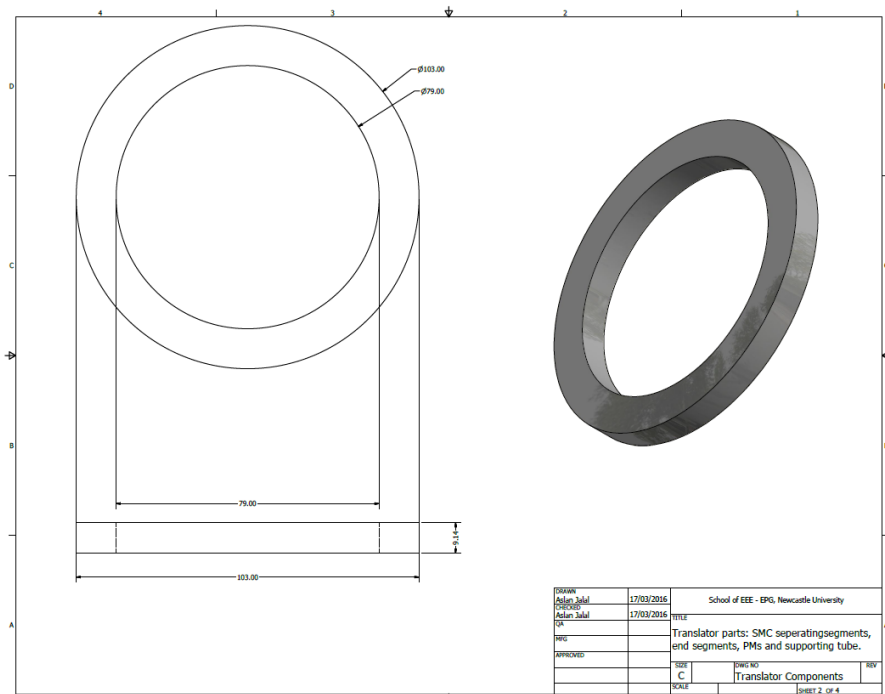
Figure B-2 : Demagnetisation curves of Recoma 26, Sintered Sm2Co17

Appendix C: Machine mechanical drawings

1- Translator iron pole piece components



(a)



(b)

Figure C-1 : Translator magnetic pole piece made from SMC material (a) Lateral; (b) Interior

2- PM dimensions and polarisation

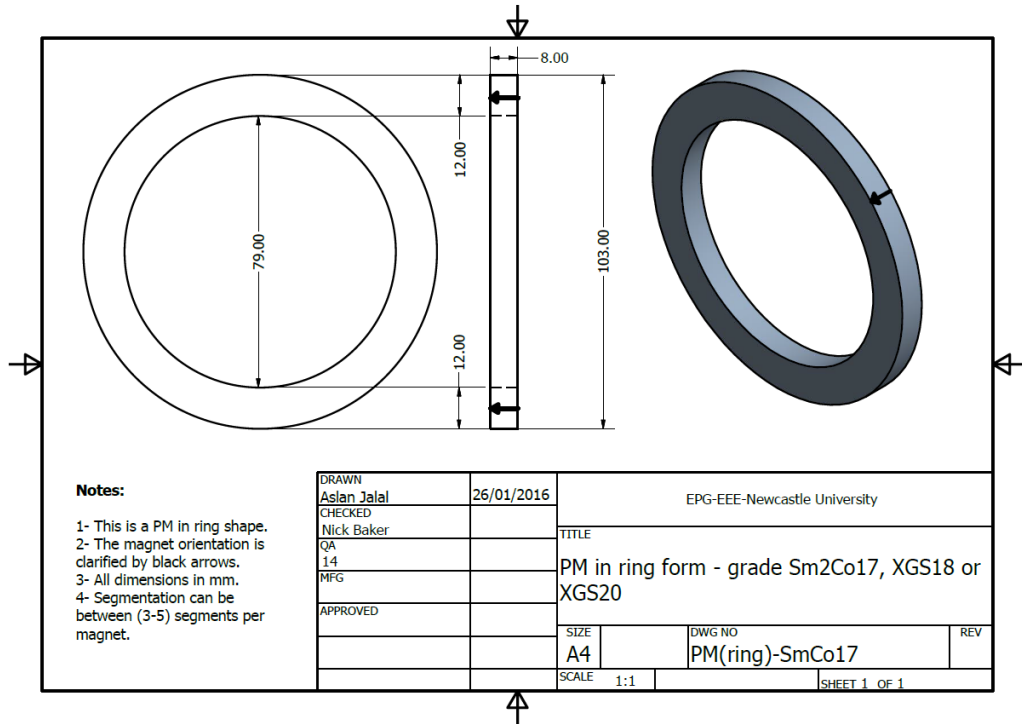


Figure C-2 : PM dimensions

3. Supporting tube dimensions

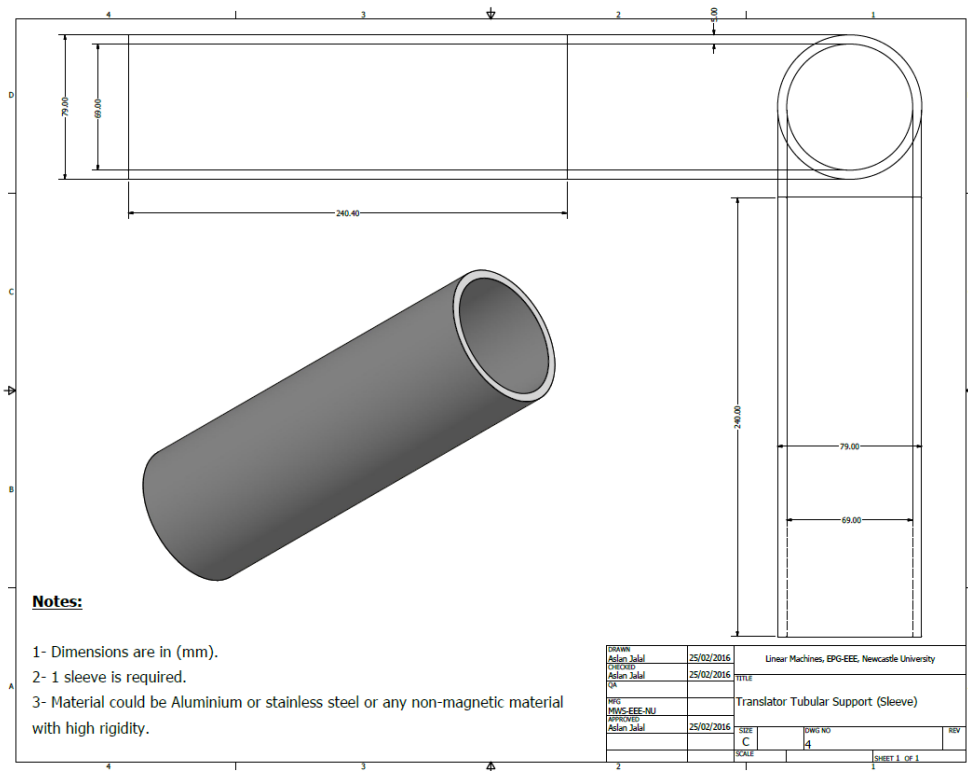
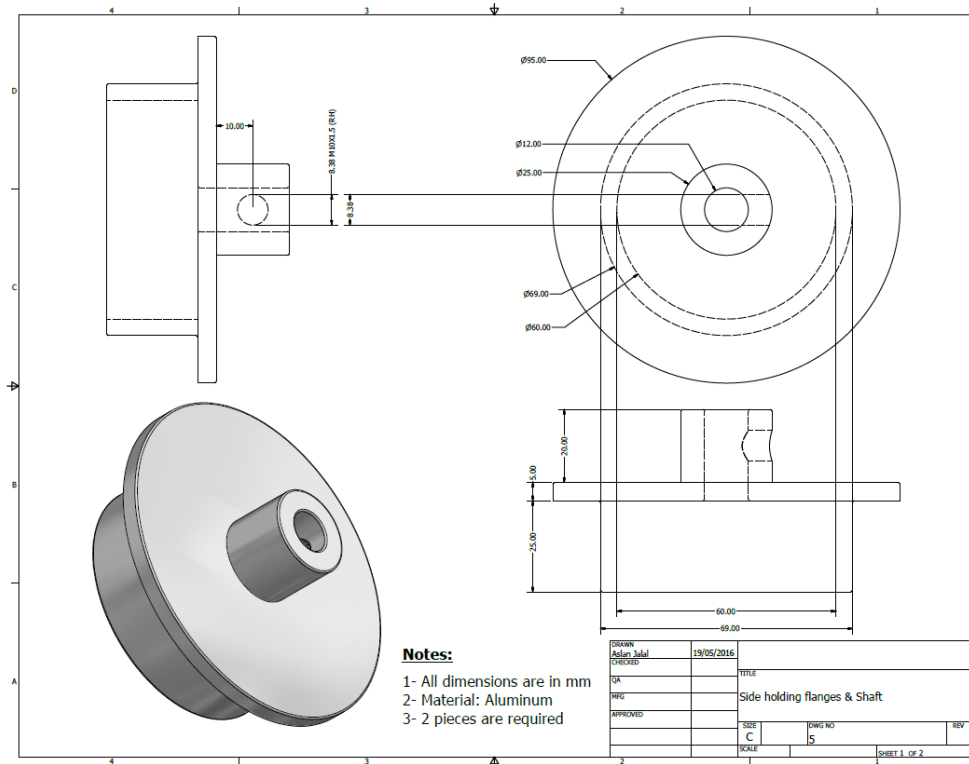


Figure C-3 : Translator supporting tube dimensions



(b)

Figure C-4 : Translator end caps

4. Shaft dimensions

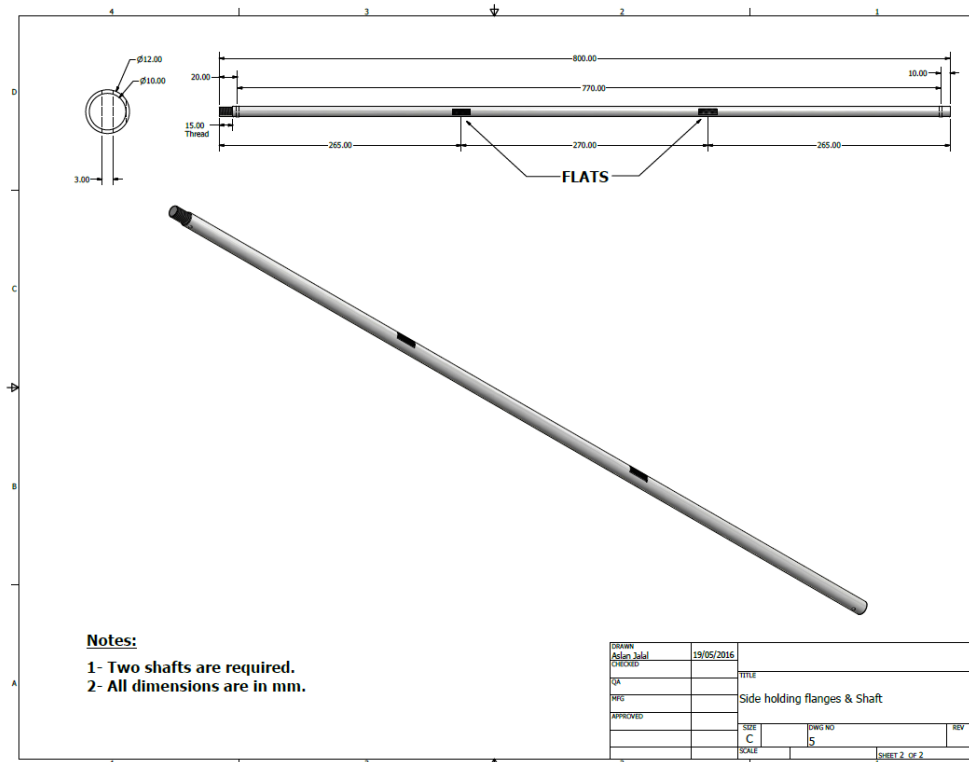
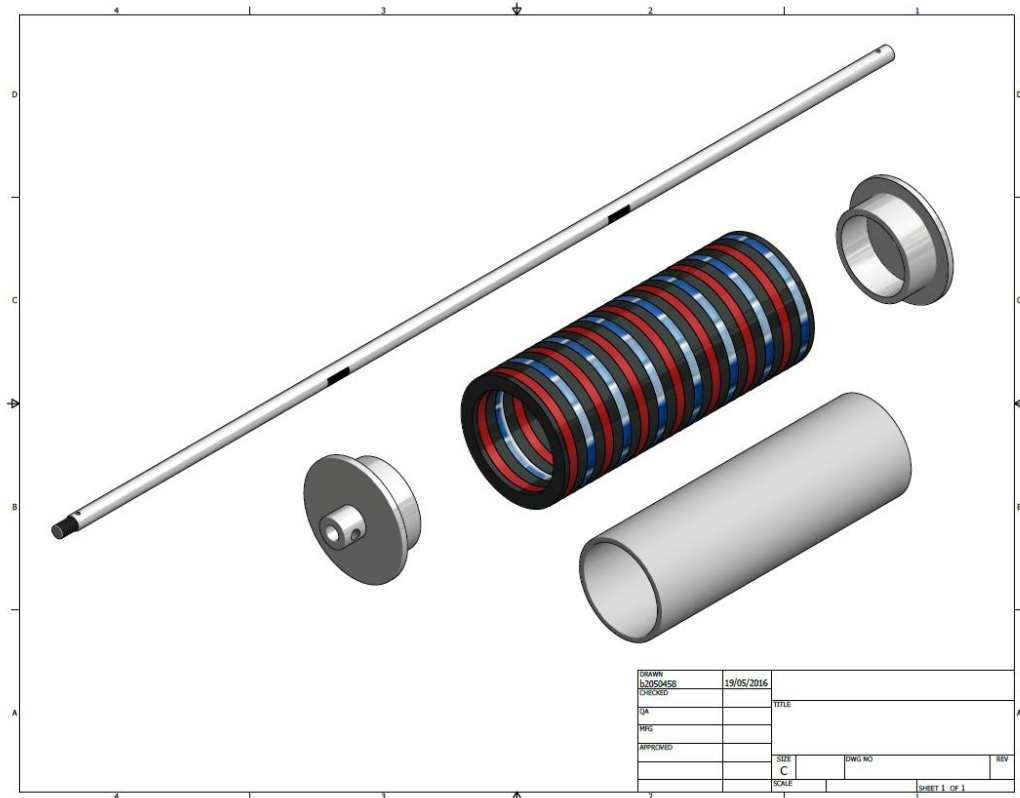
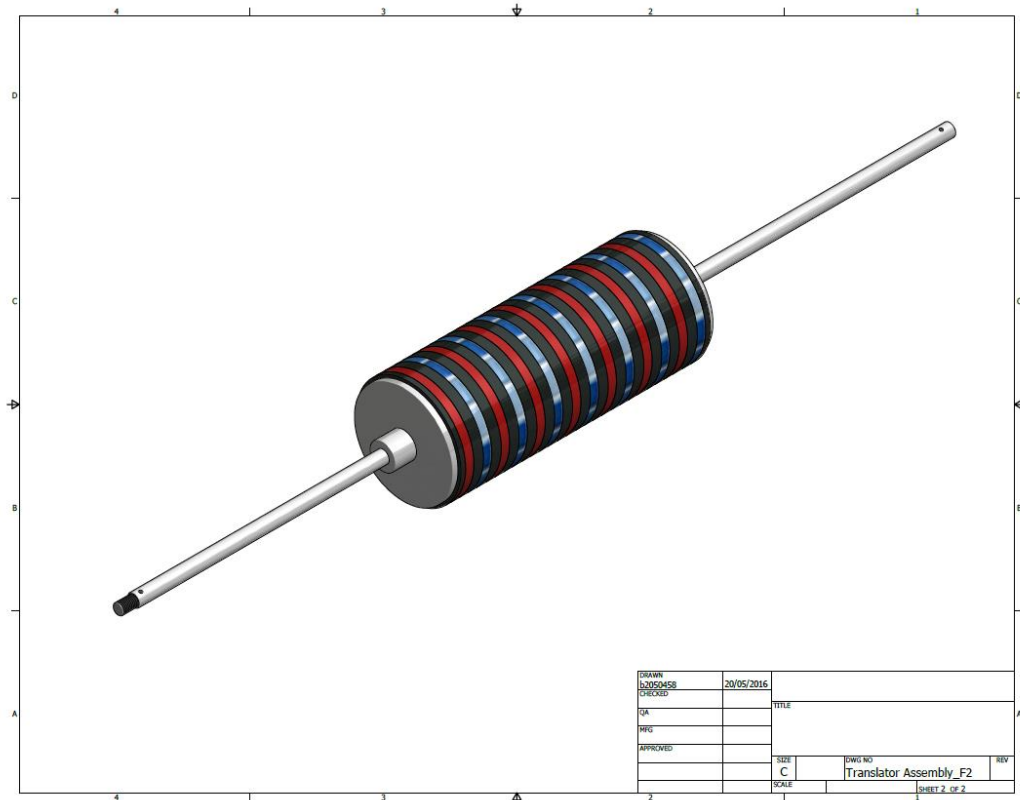


Figure C-5 : Translator shaft

5. Translator assembly steps and linear bushing holders



(a)



(b)

Figure C-6 : Translator assembly steps (a) Step 1; (b) Step 2

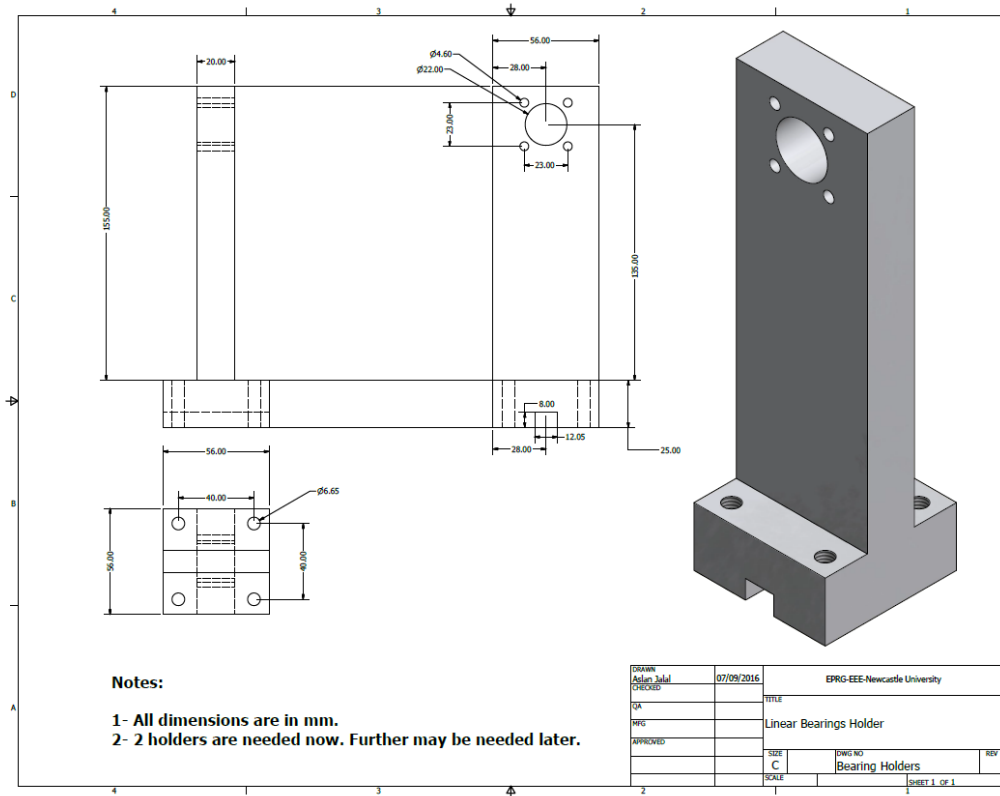


Figure C-7 : Linear bushings holder

6. Stator yoke segments

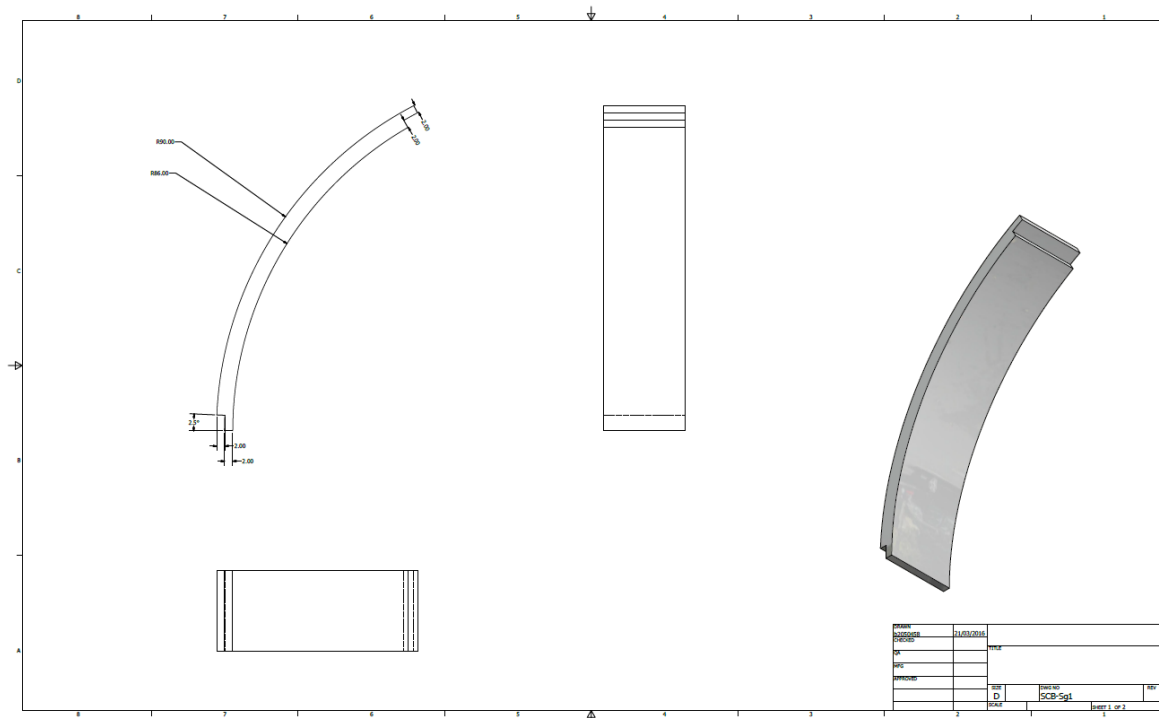


Figure C-8 : SMC stator yoke segments without punches

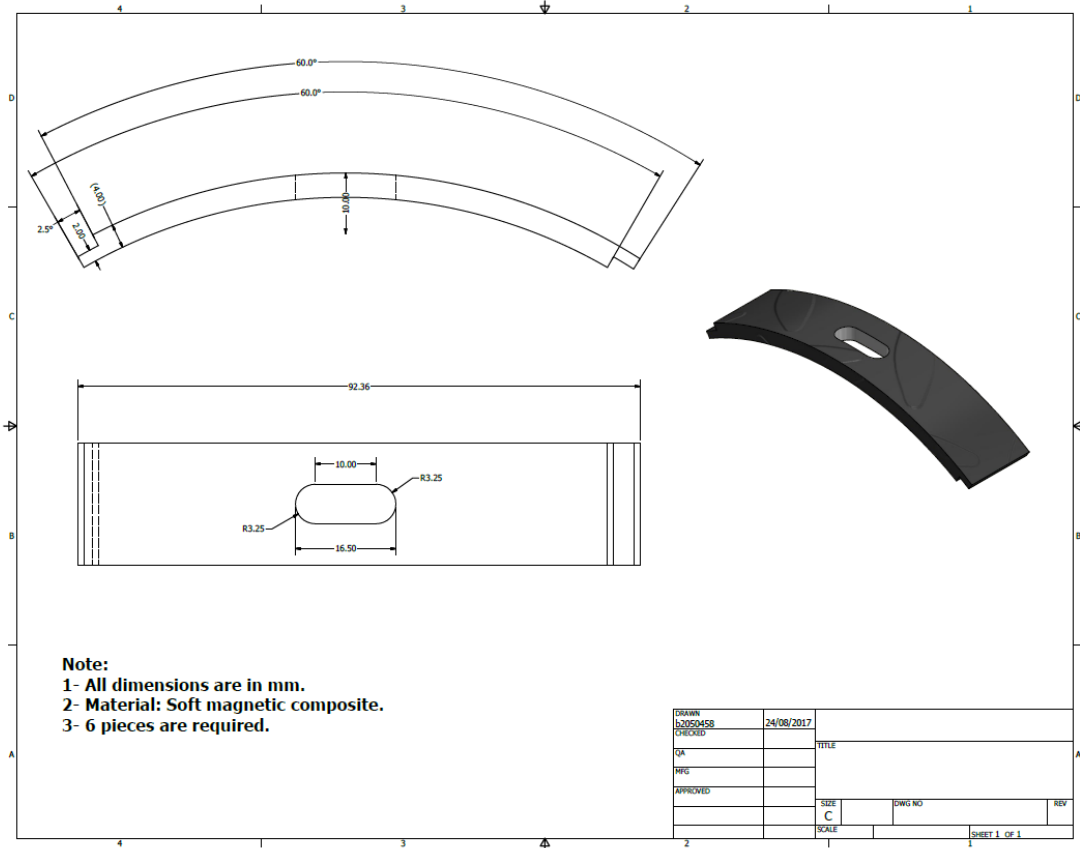


Figure C-9 : SMC stator yoke segments with punches

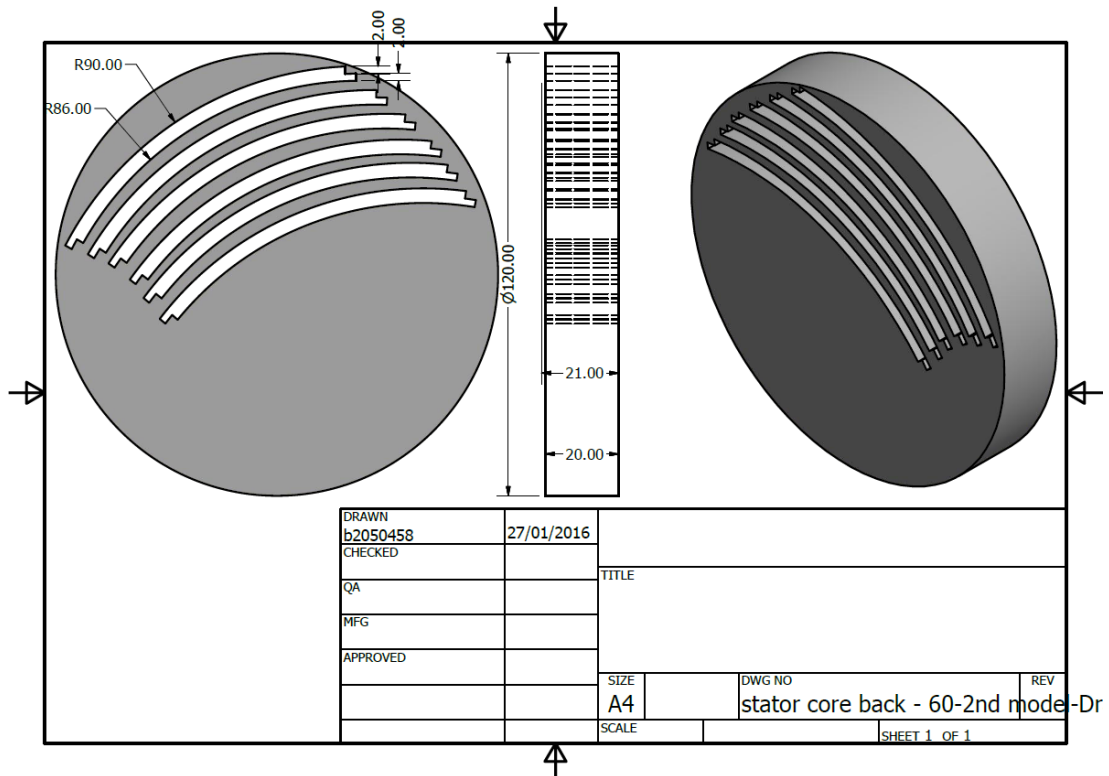
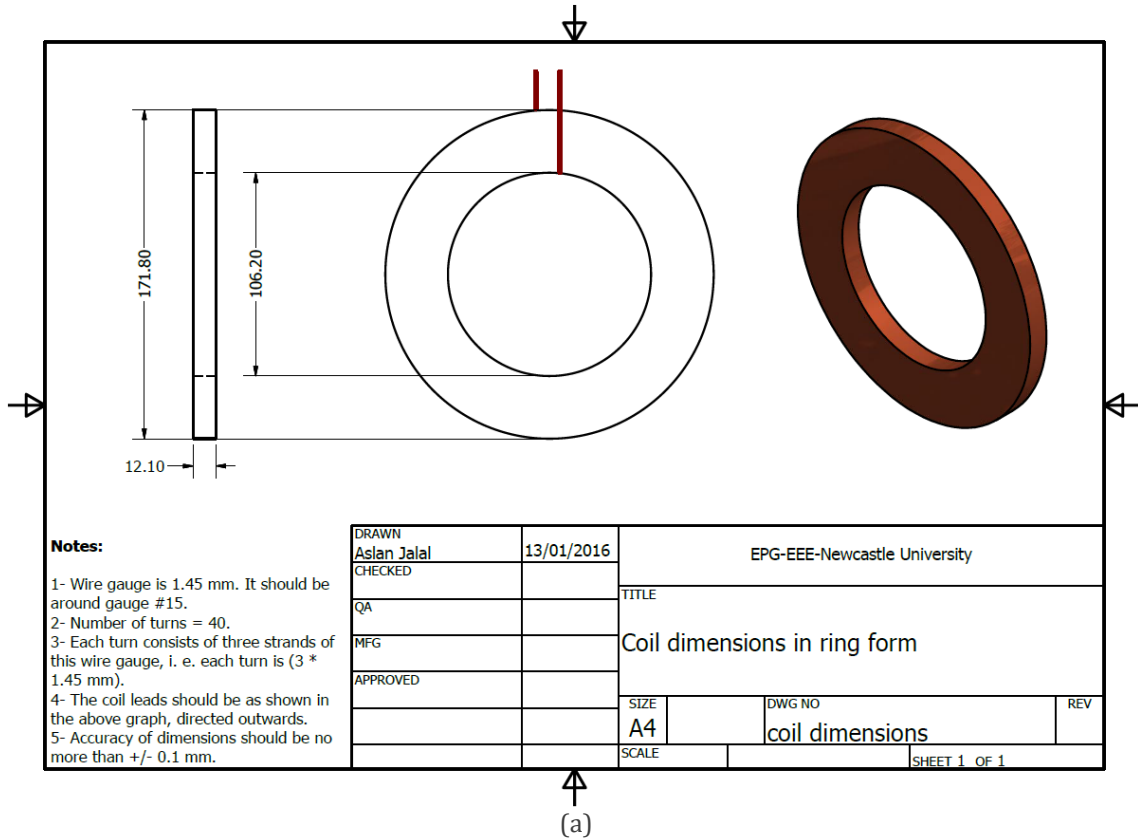


Figure C-10 : Stator yoke segments cut from SMC discs

7. Coils and mould



(b)

Figure C-11 : Machine coils (a) Dimensions; (b) Mould used to wind the coils

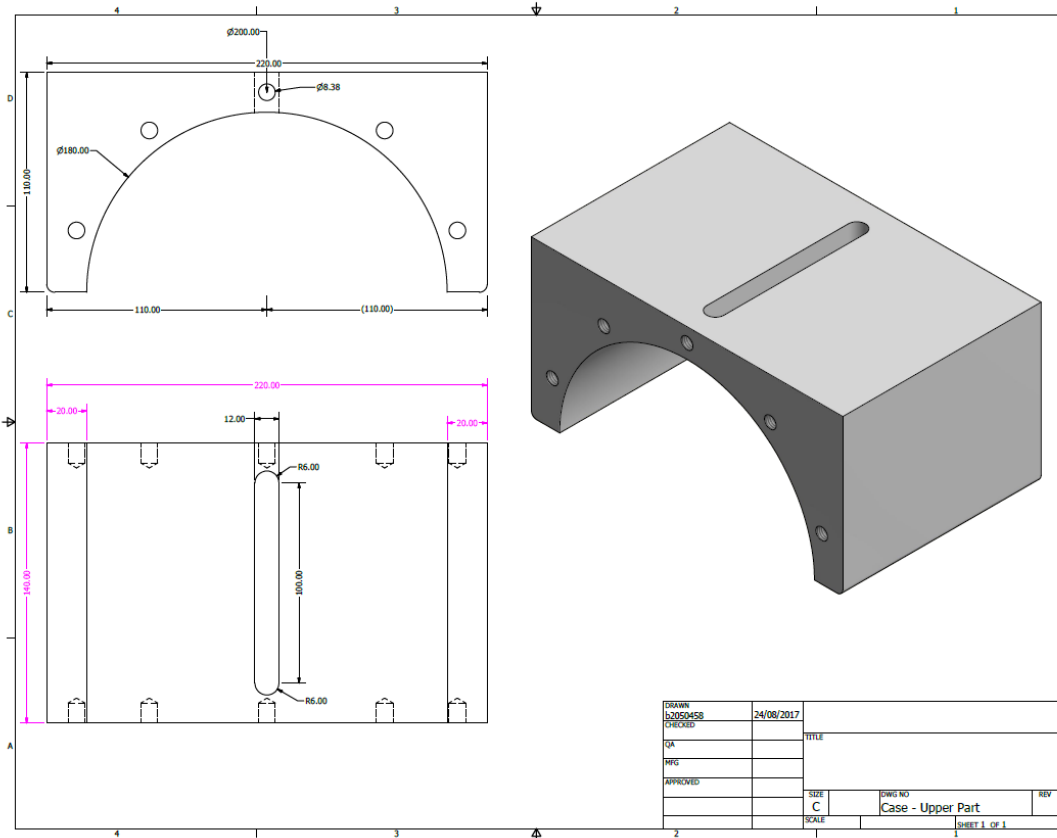


Figure C-14 : Machine housing – upper part

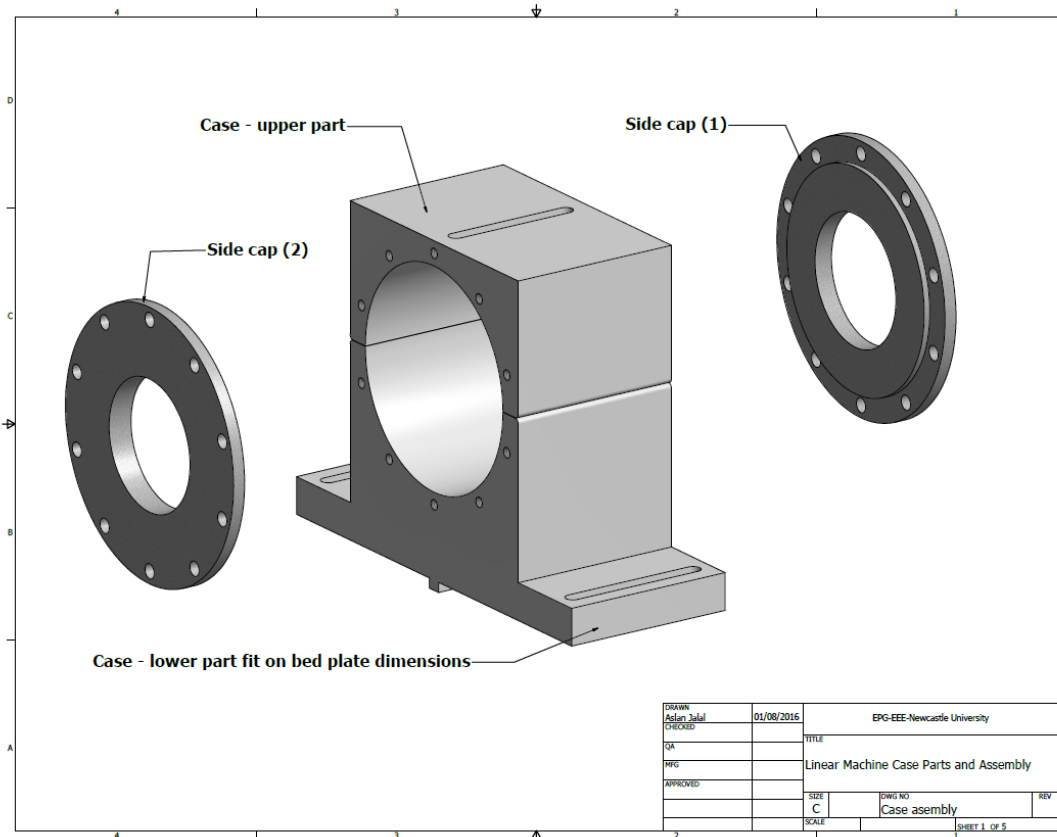


Figure C-15 : Machine housing assembly

9. Special equipment data sheets and measuring

LVDT: Test Calibration Certificate

Product : AML/EU10+/-100mm-R0R-02-024
 Serial Number : 530620
 Stroke : ± 100 mm
 Supply Voltage : 14 - 24 Volts DC (Regulated)
 Sensitivity : 49.980000 mV/mm
 Zero (Midpoint) : 5.046 Volts
 Span (High - Low) : 9.996 Volts
 Linearity : Better than ± 0.25%
 Cable Length : 2 Metres

Connection Details

Red : Supply Volts DC
 Blue : 0 Volts DC
 Green : Output(0-10V)
 (10V when core displaced towards cable exit)

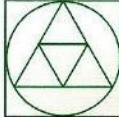
Test Equipment

ID	Type	Manufacturer	Cal Date	Re Cal Date
95	Power Supply	Thurlby Thandar	Ref Only	Ref Only
1	Multimeter	Thurlby Thandar	12/07/2016	12/07/2017
173	Slip Gauges	Yorichshire Gauges	11/08/2015	11/08/2017

Works Order No: 56758 Date: 25/07/2016
 Tested By: S.Bisseker Signature: *S. Bisseker*

Certified that the instrument has been calibrated using equipment certified and traceable to UK national standards carried out in accordance with the general requirements of BS EN ISO 10012-1. The instrument complies with the manufacturer's specifications.

Visit our website at: www.appmeas.co.uk


APPLIED MEASUREMENTS LIMITED
 3 MERCURY HOUSE
 CALLEVA PARK
 ALDERMASTON
 BERKSHIRE
 RG7 8PN
 UK
 Tel: (+44) 0118 981 7337
 Fax: (+44) 0118 981 9121
 e-mail: info@appmeas.co.uk
 Internet: www.appmeas.co.uk

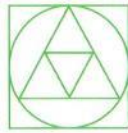
Directors:
 PETER LEWIS
 ROBERT DAVIES
 OLIVER MORCOM
 DARREN SKIPP
 Reg. No. 2583968

Figure C-16 : LVDT manufacturer calibration certificate

The LVDT was used in the translator position sensing. At the beginning a reference position was fixed and was chosen very close to the LVDT centre at which V_{ref} is recorded. When the position of the translator changes, the sensed position voltage V_{sen} changes from which the position can be calculated as:

$$x = \frac{V_{sen} - V_{ref}}{Sensitivity}, (\text{mm}) \quad \text{C-1}$$

Where: Sensitivity = 49.98 mV/mm



APPLIED MEASUREMENTS LTD.
 3 Mercury House, Calleva Park, Aldermaston, Berkshire, RG7 8PN
 Tel: +44 (0) 1189 817339 | Web: www.appmeas.co.uk
 Fax: +44 (0) 1189 819121 | Email: info@appmeas.co.uk

CALIBRATION CERTIFICATE

Calibration of Transducer with Instrumentation

Customer: Newcastle University
 Invoices
 PO Box 70613
 London
 E10 9DY

Date: 3rd August 2016

Customer Ref: 4200401003

AML Order Ref: 105703

Transducer Type: DDE-10kN-002-000 **Serial Number:** 40013

Instrumentation Type: SGA/A **Serial Number:** 17173410

Supply Voltage: 110 - 240 Vac

Instrumentation Calibration Engineering Units: kN

Number of Decimal Places: Three

Options Fitted: None

Calibration Carried Out By: BAD

AML Reference Standard: Asset No: TE138 - Load Reference Traceable to
 National Standards Certificate No: TD0242
 Calibration date: 27th August 2014

Calibration Results:

Load Applied N	Analogue Output Vdc	
	Tension	Compression
0	0.000	0.000
2	1.993	-1.993
4	3.994	-4.018
6	5.995	-6.037
8	7.999	-8.054
10	10.000	-10.069
0	0.001	-0.001

Electrical Connections:

DDE-250N Cable (2m)	SGA Input Terminal J2
Blue -ve Exc	(-) Strain Excite
Red +ve Exc	(+) Strain Excite (10V)
Screen	Shield (0V)
N/A	Ref (2.5V/5V)
Green -ve Sig	(-) Strain Input
Yellow +ve Sig	(+) Strain Input

Applied Measurements Limited hereby certifies that the above items have been inspected, tested and calibrated - using UKAS traceable test equipment - in all respects with the requirements of the customer's order.

Figure C-17 : Load cell calibration certificate

The force transducer measuring unit was used in sensing the force produced by, or applied to, the machine translator. The measured voltage out from the unit was simply transformed into force as follows:

$$F_{\text{force}} = \pm V_{\text{read}} \times F_{\text{ratio}}, \text{ (mm)} \quad \text{C-2}$$

Where F_{ratio} represents the Tension or Compression ratio of the measuring unit at the range given in the certificate table. This ratio has the value of (± 0.9965 KN/V).